0-dimensional modeling of the combustion of alternative fuels in spark ignition engines

Sabre Bougrine

Ecole Centrale Paris

THÈSE

présentée par

Sabre BOUGRINE

pour l'obtention du

GRADE DE DOCTEUR de l'Ecole Centrale Paris

Spécialité :	**Sciences pour l'Ingénieur**
Laboratoire de rattachement :	**Laboratoire d'Energétique Moléculaire et Macroscopique, Combustion (EM2C) du CNRS (UPR 288) et de l'Ecole Centrale Paris (ECP)**
Laboratoire d'accueil :	**IFP Energies Nouvelles (IFPEN)**

MODELISATION 0D DE LA COMBUSTION DES CARBURANTS ALTERNATIFS DANS LES MOTEURS A ALLUMAGE COMMANDE

Thèse soutenue le 22 juin 2012

devant un jury composé de :

Thierry POINSOT	Président, Rapporteur	Directeur de Recherche – CNRS / IMFT
Fabrice FOUCHER	Rapporteur	Maître de Conférence – PRISME
Sébastien CANDEL	Examinateur	Professeur – ECP
Xavier TAUZIA	Examinateur	Maître de Conférence – ECN
François-Alexandre LAFOSSAS	Examinateur	Ingénieur – TOYOTA Motor Europe
Vincent TALON	Examinateur	Ingénieur – RENAULT SA
Denis VEYNANTE	Examinateur	Directeur de Recherche – CNRS / ECP
Stéphane RICHARD	Examinateur	Ingénieur de Recherche – IFPEN

2012- 2012ECAP0031

Ecole Centrale Paris
Grande Voie des Vignes
92295 CHATENAY MALABRY Cedex
Tél. : +33 (0)1 41 13 10 00 (standard)
Fax : +33 (0)1 41 13 10 10

IFP Energies nouvelles
1 & 4, avenue de Bois-Préau
92852 Rueil-Malmaison Cedex
Tél. : 01 47 52 60 00
Fax : 01 47 52 70 00

À ma mère Touria, mon père Driss
et à mes sœurs Nada et Majdeline

Avant-propos

Quelles énergies pour le futur ?

Nombreux sont les ouvrages, les études, les conférences, les colloques, les discours politiques, les débats de bistrot, les émissions, les reportages, les articles qui tentent depuis plusieurs années de faire le témoignage de la situation énergétique actuelle, d'en dresser des bilans et d'apporter une nouvelle vision d'un monde plus efficient. Multiples sont les propositions et rares sont les certitudes. Beaucoup de réflexions plus ou moins structurées et de discussions de plus en plus engagées laissent cependant croire que la vraie énergie de demain est celle qui alimenta le monde depuis la nuit des temps et qui se trouve depuis ce même crépuscule en chacun de nous. Au service de la science, cette force intérieure a permis de produire des systèmes facilitant la vie de l'Homme. L'automobile revêt une place particulière parmi les inventions qui changèrent le fonctionnement de nos sociétés. Depuis le "Fardier à vapeur" de Joseph Cugnot au XVIIIe siècle jusqu'au milliard de véhicules du parc automobile mondial actuel, la route fût longue et nombreuses furent les avancées technologiques qui permirent d'améliorer en conséquence le rapport des individus à l'espace. La question initiale sur les énergies du futur intimement liée à la question des moyens de locomotion de demain n'est finalement qu'une manière de s'interroger sur l'avenir de nos sociétés. Au risque de décevoir le lecteur, aucun parti pris n'est formulé dans ce recueil pour répondre à cette question existentielle qui déchaine tant les passions. Le travail réalisé s'inscrit dans la philosophie de l'ingénieur consistant à penser et à étudier des propositions techniques pour en dégager des solutions concrètes. C'est d'abord en sachant ce qui est réalisable aujourd'hui qu'il est possible de réfléchir à ce qui pourra l'être demain. Ettore Bugatti disait : "Ce qui a déjà été inventé appartient au passé, seules les innovations sont dignes d´intérêt". J'espère donc que les travaux qui ont été réalisés lors de cette thèse permettront d'apporter un éclairage supplémentaire au développement de l'automobile et plus particulièrement à celui des moteurs. Puisse cette thèse contribuer à initier et faire progresser les innovations...

Remerciements

Je suis très reconnaissant à tous les membres du jury d´avoir accepté d´évaluer mon travail de thèse, en particulier: À Thierry Poinsot et Fabrice Foucher pour avoir assuré le rôle de président/rapporteur et de rapporteur. L´intérêt et le regard critique qu´ils ont porté à mon travail m´honorent. À Sébastien Candel pour m´avoir fait l´honneur d´accepter de faire partie de mon jury. Je m´en réjouis d´autant plus qu´il a été à l´origine de l´approche CFM et des modèles qui en ont découlé dont le CFMD1D développé lors de cette thèse. À Xavier Tauzia, Vincent Talon et François-Alexandre Lafossas pour avoir accepté de participer à mon jury de thèse en tant qu´examinateurs et pour leurs questions très constructives. Remerciements particuliers à F.-A. Lafossas qui est l´un des investigateurs du CFMD1D et qui m´avait passé le flambeau à l´époque où il était encore à l´IFP (et non IFPEN). J´en garde de très bons souvenirs.

À Maître Stéphane Richard très reconnaissant je lui suis pour avoir pris en stage puis en thèse le jeune padawan que j'étais en 2008. L´enseignement que j'ai reçu était de très haut niveau, j'ai énormément appris sur le plan technique, professionnel et humain. J'ai acquis grâce à lui des connaissances précieuses et indispensables pour la maitrise du Sabre. Je le remercie pour son dynamisme, sa grande motivation, son débit incroyable d´idées et de propositions. J'ai eu la chance d´avoir été encadré par l´un, voire LE meilleur d´entre tous.

Au grand Maître Denis Veynante très reconnaissant je lui suis pour avoir accepté de diriger mon travail de thèse. Ses remarques toujours très pertinentes et d´une extrême précision furent un atout incontestable pendant ces trois années. Je lui suis très redevable pour sa grande disponibilité et pour m´avoir fait profiter de sa maitrise de la force. Je garderai un souvenir doux et suave de ses corrections d´articles particulièrement incisives et qui m´ont donné tant de fil à retordre. A vrai-dire ce n´était qu´un juste retour de flamme bien mérité! Je le remercie enfin pour sa grande écoute, sa bonne humeur et pour ses anecdotes toujours très insolites.

Au garant de la République Antonio Pires da Cruz reconnaissant je lui suis pour le suivi qu´il a fait de ma thèse et pour son soutien. Toujours à l´écoute, il m´a permis de réaliser ma thèse au sein de son département dans les meilleures conditions. Un grand merci à maître Christian Angelberger pour son aide précieuse dans ma recherche de missions intergalactiques.

Au régiment d´élites Simulation Système mené par mes amis les maîtres Qui-Gon Fabrice et Obi-Wan Gregory toute ma gratitude j´exprime pour son dynamisme, son soutien et leur amitié. Mention spéciale à mes amis Dark Lionelor pour les longues discussions de vaisseau spatial et autres astuces et bons plans échangés pendant les veilles de Noel aux Lys, et Cécile Skywalker pour sa gentillesse et son transfert d´energie positive au service de la force. Au génial droide R3-D3 André à l´activité sur-humaine et pour les 14 579 articles qu´il m´a fait lire. La chimie n´a plus de secret pour moi (à condition d´avoir Chemkin 4 qui est beaucoup mieux que Chemkin 3 car on peut sortir les sensibilités mais d´un autre coté ... la suite dans son bureau). Je remercie enfin toutes les personnes que j´ai pu côtoyer de près ou de loin et qui m´ont été d´une aide précieuse, J.-B. M., Olivier C., Vincent K., Olivier L., Guix, Antoine A., Anthony V., Anthony D., Karine T., Eric W., et tous ceux que jai oublié.

À toute l´équipe de padawans du troisième étage qui m´ont fait perdre au moins 2 ans sur ma thèse, je vous suis très reconnaissant pour les bons moments passés à parler science (of course).

À tous mes amis, qui m´ont soutenu lors de ces 3 années et qui ont souvent dû supporter le fameux “je suis sur un paplar que je réécris pour la 15eme fois, je suis pas dispo désolé”. Mais disponible je le suis redevenu.

Enfin, mes plus chaleureux remerciements vont bien-sûr à mes parents et mes petites sœurs et à toute ma famille, pour leur aide et leur soutien.

Je n´oublis pas non plus mes fans, mon producteur Nasser Al-Khelafi, ma maison de disque et tous l´équipe technique, la r´gie, l´équipe son, les maquilleuses, etc.

Que la force soit avec vous !

Résumé

Pour satisfaire les exigences environnementales et d'agrément de conduite, le moteur automobile a évolué en une vingtaine d'années en un système très complexe combinant de nombreux composants de haute technologie avec des stratégies de contrôle très élaborées. L´optimisation et le contrôle de ce système sont alors devenus de véritables challenges pour les constructeurs automobiles. Ces derniers points sont aujourd'hui d'autant plus complexes que le contexte actuel de raréfaction des ressources impose de plus en plus le couplage ou le remplacement des carburants conventionnels par des carburants alternatifs tels que l´éthanol, le gaz naturel ou encore l´hydrogène. Ces nouveaux carburants présentent, en plus de leur intérêt économique, un certain nombre de propriétés physico-chimiques favorisant un meilleur rendement du moteur ainsi que la réduction des gaz à effet de serre. L´élaboration de ces nouveaux moteurs est finalement rendue possible par l'utilisation de dispositifs physiques et numériques de plus en plus sophistiqués. Dans ce contexte, les outils de simulation système destinés aux groupes moto-propulseurs se sont démocratisés et peuvent aujourd'hui être utilisés à toutes les étapes de développement des moteurs, du choix de l´architecture au développement des stratégies de contrôle et à la calibration. Cependant, l'efficacité de tels outils demande encore à être améliorée afin de fournir un haut niveau de prédictivité couplé à un temps de calcul proche du temps réel. Les travaux réalisés lors de cette thèse ont visé à contribuer au développement du modèle de combustion 0-dimensionnel CFM1D (Coherent Flame Model) afin d´améliorer la prédiction du dégagement d'énergie, des polluants et des phénomènes d'auto-inflammation (AI) dans les moteurs à allumage commandé lorsque des variations de la composition du carburant sont considérées. Le formalisme CFM distingue deux zones : les gaz frais et les gaz brûlés qui sont séparés par un front de flamme et qui sont entièrement décrits par leur masse, température et composition. Dans ce formalisme, le taux de consommation des espèces est directement lié aux processus de combustion et de post-oxydation assujettis aux mécanismes de chimie et de turbulence. Dans la version initiale du CFM1D, ces mécanismes sont représentés par des approches simples pouvant souffrir d'un manque de prédictivité. Ainsi, la prédiction de la formation de polluants peut être limitée par les chimies simples ou réduites la décrivant. Ces dernières sont en effet généralement définies dans des domaines de validité restreints en température, pression et composition. De la même manière, le calcul de la vitesse de flamme laminaire, de l'étirement de la flamme ou encore des éventuels délais d'auto-inflammation intervenant dans l'évaluation du dégagement d'énergie met en jeux des corrélations phénoménologiques initialement développées sur un nombre limités de points de validation. Toutes ces limitations peuvent finalement entraîner une mauvaise réaction du modèle de combustion à des variations thermodynamiques ou de compositions et ont donc nécessité un certain nombre d'améliorations présentées dans ce manuscrit. L'originalité des développements réside dans l'intégration de chimie complexe dans le modèle CFM1D en utilisant des méthodes inspirées de récents travaux de CFD (Computational Fluid Dynamics) 3D. Cela se traduit par:

• le développement d'une nouvelle approche inspirée du modèle PCM-CFM pour décrire la chimie dans la flamme,
• le développement de l'approche CORA (CO Relaxation Approach) inspirée du modèle de relaxation NORA pour les processus de post-oxydation dans les gaz brûlés (CO et NO),
• le développement de nouvelles corrélations de vitesse de flamme laminaire adaptées à la combustion de mélanges méthane-hydrogène et essence-éthanol,
• le développement d'une nouvelle fonction d'efficacité pour l'étirement de la flamme améliorant la prédiction des effets de composition sur les interactions flamme/turbulence,
• le développement d'un nouveau modèle type TKI pour la description des phénomènes d'AI.

Le nouveau modèle, CFM1D-TC, est finalement validé à partir d'une large gamme de données expérimentales concernant un ensemble de points de fonctionnement stabilisés d'un moteur à allumage commandé.

Mots Clés: CFM1D, Vitesse de flamme, Plissement, Étirement, Combustion turbulente, Polluants, DNS, TFLES, Calcul moteur, Tabulation de chimie complexe, Modélisation 0D

Thesis

THESIS

submitted by

Sabre BOUGRINE

for the

DOCTOR DEGREE of Ecole Centrale Paris

Specialty: Engineering Sciences

Host laboratories: Laboratoire d'Energétique Moléculaire et Macroscopique, Combustion (EM2C) du CNRS (UPR 288) et de l'Ecole Centrale Paris (ECP)

IFP Energies Nouvelles (IFPEN)

Thesis subject:

0-DIMENSIONAL MODELING of the COMBUSTION of ALTERNATIVE FUELS in SPARK IGNITION ENGINES

Defended in June 2012, 22nd

Composition of the jury:

Thierry POINSOT	President, Reviewer	Directeur de Recherche – CNRS / IMFT
Fabrice FOUCHER	Reviewer	Maître de Conférence – PRISME
Sébastien CANDEL	Examiner	Professeur – ECP
Xavier TAUZIA	Examiner	Maître de Conférence – ECN
François-Alexandre LAFOSSAS	Examiner	Ingénieur – TOYOTA Motor Europe
Vincent TALON	Examiner	Ingénieur – RENAULT SA
Denis VEYNANTE	Examiner	Directeur de Recherche – CNRS / ECP
Stéphane RICHARD	Examiner	Ingénieur de Recherche – IFPEN

Summary

A promising way to reduce green house gases emissions of spark ignition (SI) engines is to burn alternative fuels like bio-mass-derived products, hydrogen or compressed natural gas. However, their use strongly impacts combustion processes in terms of burning velocity and emissions. Specific engine architectures as well as dedicated control strategies should then be optimized to take advantage of these fuels. Such developments are today increasingly performed using complete engine simulators running in times close to the real time and thus requiring very CPU efficient models. For this purpose, 0-dimensional models are commonly used to describe combustion processes in the cylinders. These models are expected to reproduce the engine response for all possible fuels, which is not an obvious task regarding the mentioned CPU constraints. Works performed in this thesis aimed at developing the 0-dimensional combustion model CFM1D (Coherent Flame Model) to improve the prediction of heat release, pollutants emissions and auto-ignition phenomena in SI engines when fuel composition variations are considered. The CFM formalism distinguishes two zones : the fresh and the burnt gases, which are separated by a flame front and are both described by their temperature, mass and composition. In this formalism, the rate of consumption of species is directly linked to the combustion and post-oxidation processes highly dependent on chemistry and turbulence mechanisms. In the original version of CFM1D, these mechanisms are represented by simple approaches which can suffer from a lack of predictivity. The prediction of pollutant formation can therefore be limited by the simple or reduced chemistries used to describe kinetics in the chamber. These latter are indeed defined in very restrictive validity domains in terms of temperature, pressure and composition. In the same way, the flame velocity, wrinkling or potential auto-ignition delays stepping in the heat release computation are defined by phenomenological correlations initially developed under a limited number of validation points. All these limitations can finally lead to a wrong behavior of the combustion model to thermodynamic and compositions variations and therefore required a number of improvements presented in this manuscript. The originality of the model derives from the fact it is based on the integration of complex chemistry in CFM1D using methods inspired from recent 3D (Computational Fluid Dynamics) CFD works. It results in :

• development of a new approach similar to the PCM-CFM model to describe the flame chemistry,
• development of the CO relaxation approach (CORA) inspired from the NORA relaxation model to describe post-oxidation processes in burnt gases,
• development of new laminar flame velocity correlations adapted to the combustion of methane-hydrogen and gasoline-ethanol blend fuels,
• development of a new efficiency function for flame stretch inspired from the ITNFS function to improve the prediction of composition effects on flame/turbulence interactions,
• development of a new auto-ignition model inspired from TKI model to describe knock.

The new combustion model, CFM1D-TC (Tabulated Chemistry), is validated against a wide range of experimental data at several steady state operating points and fuel compositions for many IFPEn SI engines.

Keywords: CFM1D, Flame velocity, Wrinkling, Stretch, Turbulent combustion, Pollutants, DNS, TFLES, Engine simulation, Complex chemistry tabulation, Abnormal combustions, 0D modeling, System simulation.

Contents

Part I

Introduction

Chapter 1

Introduction

1.1 Context

With regards to the amazing growth of the vehicle number in the world, the development of new eco-aware and more efficient engine concepts have become in the last few years one of the main priorities to ensure environmental and health protections and to overcome the progressive depletion of oil resources. Pollutants emissions from piston engines are subjected to specific regulations which particularly concern carbon monoxide (CO), nitrogen oxides (NO and NO_2, referenced as NO_x), unburnt hydrocarbons (HC) and particles (PM). CO, HC and PM result from incomplete combustion whereas NO_x are products of reaction between oxygen and nitrogen at high temperature. Table 1.1 presents European standards for pollutants emissions. These emissions levels of car engines are assessed by a standardized test procedure, based on the so-called New European Driving Cycle (NEDC). It consists of four repeated urban driving cycles (ECE-15) and an extra-urban driving cycle (EUDC) and is supposed to represent the typical usage of a car in Europe. Carbon dioxide (CO_2) directly resulting from fuel combustion is also front and center of public debate. Contrary to other emissions which can be reduced thanks to exhaust gas aftertreatment systems, the only way to reduce CO_2 concentration is to reduce the fuel consumption or to propose low carbon content fuels.

Economical constraints due to the reduction of world energy resources, pollutant emissions regulation and fuel diversification policies have led car manufacturers to reinforce research and development in an other way than the one of pure improvement of vehicle performance and comfort. Cutting fuel consumption and greenhouse gases while allowing fuel composition variations have thus become central aims. To reach these goals, many developments were performed during last decades through different paths which mainly consisted on optimizing vehicle aerodynamics and lightening, reducing friction, improving mechanics and engine efficiencies, developing pollutant after-treatment devices or even using alternative fuels. Figure 1.1 presents an evaluation (performed at IFPEn) of the potential consumption gains of such developments and points out that the optimization of the engine unit is the most contributor to fuel consumption decrease (and thus also CO_2 emissions decrease).

This last figure demonstrates therefore that a special interest has to be devoted to the development of more efficient power-trains. Such developments today mainly concern the integration of new internal combustion engine technologies and on the other hand vehicle hybridization and electrification. At the same time car manufacturers have to face with the diversification of fuels. Both issues should be considered simultaneously to provide sustainable mobility solutions and are detailed in the two following sections.

		Euro 1	Euro 2	Euro 3	Euro 4	Euro 5	Euro 6
	mg/km	1993	1996	2000	2005	2009	2014
Diesel	Nitrogen oxides (NOx)	-	-	500	250	180	80
	Carbon monoxide (CO)	2720	1000	640	500	500	500
	Hydrocarbons (HC)	-	-	-	-	-	-
	HC + NOx	970	900	560	300	230	170
	Particles (PM)	140	100	50	25	5	5
Gasoline	Nitrogen oxides(NOx)	-	-	150	80	60	60
	Carbon monoxide (CO)	2720	2200	2200	1000	1000	1000
	Hydrocarbons (HC)	-	-	200	100	100	100
	HC + NOx	-	-	-	-	5(*)	5(*)
	Particles (PM)	-	-	-	-	68	68

Table 1.1: European pollutant emissions standards - (*) only for direct injection gasoline engines running under poor conditions (source : IFPEn).

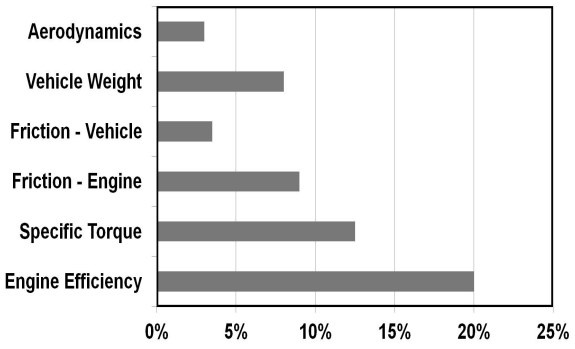

Figure 1.1: Potential consumption gain of main vehicle parameters optimization (source : IFPEn).

1.1.1 Technological paths for reducing greenhouse gases and pollutant emissions

This thesis focuses on spark ignition (SI) engines, therefore only this technology is considered in the following.

Conventionally called "gasoline engines", SI engines run thanks to a real-time control of the fuel-air mixture ignition as function of the operating point. Contrary to Diesel engines, the mixture is here electrically ignited and a flame front expanding from the spark plug to the cylinder walls turns fresh mixture in burnt gases. In such engines the mixture is commonly homogeneous and the equivalence air/fuel ratio is set around unity. As a consequence, soots emissions are negligible compared to Diesel engines and 3-ways catalytic converters are generally enough to reduce pollutant emissions to regulation standards. Nevertheless, the strengthening of these restrictions makes essential the development of less polluting technologies for SI engines. However, most improvements focus today on the engine efficiency. The main objective consists in reducing the gap with Diesel engines in term of consumption (and therefore in term of CO_2 emissions) keeping or improving in the same time performances and driving comfort. Restraining parameters in SI engines are pumping losses (due to the presence of a throttle valve) and knock. This latter is a phenomenon caused by the auto-ignition of one or several fresh gases pockets having not been reached by the flame yet. The shock wave generated from this detonation creates the characteristic metallic "pinging" sound, and cylinder pressure increases dramatically. Effects of engine knocking can therefore be highly destructive. At the engine bench, knock detection is often performed by ear. The operator catches therefore a knock onset temporal frequency and set in consequence the spark ignition advance (SA) considering a certain caution (around 3 crank angle degrees (CAD)). Thus, if the SA is increased by 5 CAD knock clearly appears. The choice of the optimal SA is done so that the engine efficiency is maximized. Generally, at low engine loads, thermodynamic conditions are not severe enough to make knock appear and the SA can be ideally set so that the maximum in-cylinder pressure is obtained at $\theta(P_{max}) \approx 373CAD =$ (where θ is the crank angle degree and P_{max} the maximum pressure). As soon as SA is reduced to prevent knock occurrence, $\theta(P_{max})$ increases and the engine efficiency decreases. In practice, that is how knock-limited engine operating points can be identified using bench data. Knock results from particular thermodynamic conditions. High temperatures and pressures will tend at intensifying the phenomenon while dilution of fresh gases will have an inhibitory effect. Among attractive perspectives answering to the issue of SI engines efficiency limitation, several technical solutions (preventing knock, reducing energy losses, consumption and emissions, etc..) can be mentioned here :

- Gasoline Direct Injection (GDI) – GDI engines use high pressure injectors ($100 - 200$ bars) introducing the fuel directly into the chamber. The idea here is to reduce the consumption by decreasing pumping losses linked to gas transfer. Furthermore, the spray evaporation cools the fuel-air mixture pushing back knock occurrence and enabling therefore the use of higher volumetric compression ratios improving thus the engine efficiency. This alternative to port fuel injection has also the advantage of allowing a precise control of the fuel quantity injected in each cylinder. An issue of such a technology development is to allow an homogeneous air-fuel mixing and to avoid interactions between the spray and the engine walls.

- Stratified Combustion – Another advantage of direct injection is the possibility of generating a stratification of the fuel/air equivalence ratio in the chamber. A fuel-air cloud is created around the spark plug while the rest of the chamber volume is mainly composed of air. This distribution is mainly controlled by the flow motion in the cylinder driven by the chamber design. Such chambers are characterized by a spherical cavity assigning to the air load a compact feature described by a vertical reversed flow maintained throughout the entire compression. In such a case, the equivalence ratio evolves from rich (mainly fuel) to poor (mainly air) values as function of the distance to the spark plug. For low

engine loads a little volume of fuel is injected and the overall equivalence ratio is too low to ensure the combustion of the fresh mixture. In this case, the stratification is sparked off by a late injection during the compression stroke just before ignition leading to a local equivalence ratio close to stoichiometry around the spark plug. For higher loads, the injection starts early enough to enable homogeneous and stoichiometric combustion. The interest of stratified combustion is finally to develop enough power minimizing in the same time the consumption. Potential consumption savings of such systems (stratified GDI) are estimated at between 10 and 15% on the NEDC cycle.

- Exhaust Gases Recirculation (EGR) – As for Diesel engines, recirculation of exhaust gases (EGR) is often considered to dilute the fresh gas mixture and to reduce the flame temperature. In stratified injection GDI engines, only the charge around the spark plug need to be at the stoichiometry and the global equivalence ratio is finally even lower than in classical SI engines. Finally, it should be noticed the dilution and temperature decrease induced by EGR also have the advantage of preventing knock occurrence. This last effect is true only if recirculating gases are sufficiently cold. Otherwise, the thermal effects take over on dilution effects in favor of knock. Typically, mass fractions of recirculated exhausted gases in SI engines can be ranged from 0 to 30%.

- Downsizing – Already integrated in Diesel engines for several years, downsizing is spreading in many SI engines units. It consists in reducing the engine capacity to promote the engine volumetric efficiency. The two key technologies used in this system are direct injection and turbocharging. This latter decreases pumping losses and improves exhaust gas scavenging which consequently allows a reduction of knock occurrence at high loads. This scavenging is made possible by direct injection which prevents any fuel loss. More generally, direct injection makes turbo-charging possible thanks to a better control of the injected fuel quantity as function of the trapped air level. Finally, downsized engines are characterized by higher high-pressure loops in the thermodynamic cycle leading to a better engine efficiency.

- Variable Compression Ratio (VCR) strategies – One of the main solutions to prevent knock is to reduce the volumetric compression ratio. Unfortunately, this solution drops efficiency and performances of operating points (defined by a load and an engine speed) which are not limited by knock (low engine loads for example). As a consequence a basic idea consists in developing a system able to automatically adjust the compression ratio as function of the operating point. With VCR systems, the compression ratio is limited at high loads where the probability of having knock is high and increased at low loads. No VCR engine is today available on the market but several prototypes were developed by MCE-5 (2000) or more recently by Lotus Engineering (2009) and by Saab (2000) who commercialized some vehicles with this technology.

- Variable Valve Actuation (VVA) – Technologies controlling intake and exhaust valves behaviors are more and more integrated in new engine units. The principle consists on the real-time calculation of valves opening and closing timings (VVT = Variable Valve Timing) via the Engine Control Unit (ECU). Some systems as BMW's Valvetronic allow also to control the valves lift (VVL = Variable Valve Lift). VVT approaches are generally performed geometrically adjusting the camshaft phasing. Nevertheless, common camshaft systems are mechanically linked to the crankshaft making the development of VVT strategies combined to VVL very difficult. Another system consists in dissociating both shafts and driving valves thanks to an electromagnetic system. Consumption savings of such a technology called "camless system" is estimated at between 7 and 13%.

- Controlled auto ignition (CAI) – CAI systems are similar to HCCI technology for Diesel engines where the fresh gas mixture is ignited by compression. The interest of using such a combustion process is to avoid throttling and then to decrease pumping losses. Consumption saving from CAI technology is estimated between 10 and 15%. As for direct injection SI engines, the combustion is also performed under poor and diluted conditions leading to low

levels of NO_x, CO and soots. However, pollutant emissions can be still high enough regards to legislation on gasoline engines and aftertreatement systems may be required. Moreover, as for HCCI engines, combustion takes place simultaneously everywhere in the chamber leading to an important noise and making combustion control strategies more complex. Finally, the main drawback of such engines is the limitation of the operating range. Indeed, at very high loads, main combustion can turn into intensive knock and contrary to SI engines where this phenomenon can be controlled through the spark advance, there is no direct way to prevent it in CAI engines. As a result, CAI technologies require to be technically able to switch from spark ignition to auto-ignition modes (and vice versa) which is not an easy task.

- High Research Octane Number (RON) fuels – Fuels with high RON values have the advantage of reducing the proclivity to detonate. Generally, alcohol compounds are integrated into conventional gasoline fuels to increase the RON but alternative fuels like biofuels or natural gas are also more and more used.

- Hybridization – A hybrid electric vehicle (HEV) combines a conventional internal combustion engine (ICE) with an electric propulsion system. The idea here is to partially dissociate the connection between the ICE and wheels allowing to use the ICE only on its optimal operating points. Elsewhere, an electrical system combining batteries and a motor-generator system takes over. In parallel hybrids systems, the ICE and the electric motor are thus both connected to the mechanical transmission and can simultaneously transmit power to drive the wheels, usually through a conventional transmission. However, some other varieties of HEVs (series hybrids) use their internal combustion engine to re-generate batteries by spinning the motor-generator system, to either recharge their batteries or to directly power the electric drive motors. In any case (parallel and series) the presence of the electric powertrain is therefore intended to achieve better fuel economy than a conventional vehicle as well as better performances and lower pollutant emissions.

1.1.2 Fuel diversification : Alternative fuels

Engine manufacturers work closely with oil companies to develop gasoline or Diesel formulations adapted and optimized to current technologies expected to respect pollution standards and to reduce consumption. However, with regards to the economical situation, the engine industry has to face a new challenge concerning diversification of energy sources to ensure a better energy independence of the states (European Union directive on renewable energy sources 2009/28/CE). A new philosophy is therefore considered and consists in developing engines technologies adapted and optimized to alternative fuels as CNG (Compressed Natural Gas), hydrogen or biofuels. A significant growth of incorporation rates of these compounds in fuels is envisaged in the next few years (Figure 1.2). This growth makes crucial an adaptation of current technologies and control strategies to take advantage of the physical and chemical properties of these new fuels (see Table 1.2). For example, ethanol is characterized by a high latent heat of vaporization implying a cooling effect of fresh gases which leads to a decrease of the intake temperature and fresh gas density. The air flow rate at the intake is therefore increased (Marriot et al. 2002) and the enrichment at high loads commonly proceeded to decrease the exhaust temperature is not needed anymore (Kapus et al. 2007). Moreover, ethanol is also defined by high octane number (RON, see Table 1.2) making the engine less sensitive to knock (Nakama et al. 2008, Starkman et al. 1964, Brinkman 1981, Salih and Andrews 1992, Castro et al. 1994, Maji et al. 2001). Therefore, although the combustion velocity of ethanol is high (Bayraktar 2005, Gülder 1982, Gülder 1984, Hara and Tanoue 2006, Farrell et al. 2004, Karpov et al. 1986), it allows to maintain optimal spark advances (SA) on a larger range of engine operating points compared to conventional gasoline. Nevertheless, ethanol has also a high boiling-point which leads to low vaporization rates inadequate for cold starting (Nakata et al. 2006, Kapus et al. 2007, Cowart and Boruta 1995, Stodart et al. 1998). Similarly, CNG mainly constituted by methane, has the advantage of having a low carbon content $H/C \cong 4$ (Table 1.2) making it one of the less polluting fuels in term of CO and CO_2. Moreover, its high stability,

its low density and its high auto-ignition temperature make it safer than conventional gasoline or diesel. However, contrary to ethanol, methane burns quite slowly leading to a lower efficiency and important cycle-to-cycle variations, both decreasing power and increasing fuel consumption. An efficient way to improve the burning velocity is then to dump natural gas by hydrogen, which is also a good candidate to reduce pollutant emissions by increasing the hydrogen/carbon atomic ratio. Moreover, this addition extends flammability limits, and improves, the engine thermal efficiency (Schefer 2003, Sankaran and Im 2006, Hawkes and Chen 2004). However, the hydrogen impact on combustion processes can be dramatic for high blending rates. In addition, contrary to liquid fuels, it is harder to obtain an homogeneous gas/air mixture making the control of combustion even more challenging. Natural gas-hydrogen mixtures need therefore specific system architectures and optimized control strategies to take advantage of fuel properties on combustion ensuring at the same time safe operation.

1.1.3 Research tools for powertrains developments

As previously mentioned, future engines are expected to be more and more complex and the development of innovative technologies for combustion will depend on the ability to understand the complex physical phenomena stepping in the combustion chamber but also to evaluate the potential of new engine technologies and strategies and new fuels. A short description of experimental and numerical tools directly or indirectly used during this thesis is proposed here :

- ***Experimental tools***
  In the past, engine developments were mainly based on experiments using engine test benches. These benches were used to support engine developments from concept design to powertrain control, calibration and test. A typical engine test bench could house several sensors, data acquisition features and actuators to control and to provide informations about the engine state (engine torque and speed, temperatures, pressures at several locations, air and fuels flow rates, equivalence ratio, pollutant concentrations, etc.). The increasing complexity and number of devices, the new pollutant regulation standards as well costs in term of facilities, human resources and time made such an approach more and more complemented by numerical simulations. However, engine test-benches are still in use today essentially for testing new engine control strategies, validating numerical engine simulations and finally optimizing the full engine design. The development of more efficient engines imply to be aware of the reality of phenomena occurring in the chamber. Single cylinder optical engines are therefore a very interesting tool to study in-cylinder flow, mixing, combustion and emissions phenomena by allowing the application of qualitative and quantitative non-intrusive diagnostic techniques. On the other hand, the physics description requires also to understand each single process defining more complex phenomena and more fundamental experimental set-ups (spherical bomb, Bunsen burners, rapid compression machines (RCM), etc.) are generally used to study for example flame propagation, auto-ignition, heat transfers or chemical processes.

- ***Numerical tools***
  Due to the expensive costs of experimental campaigns and to the few available informations allowing the understanding of interactions between components, engine development are more and more performed using dedicated numerical tools. Indeed, in the two last decades, consequently to the rapid progress in CPU performance and the large increase in data storage capabilities, numerical simulation has evolved quite significantly. These simulation tools can today be efficiently used at all stages of the engine development as described in a recent review by Drake and Haworth (2008) for GDI and HCCI engines. In particular, CFD (Computational Fluid Dynamics) allows a better understanding of physical phenomena taking place in combustion chambers such as spray development, heat transfer, combustion, pollutant formation, etc. All these phenomena are highly influenced by the flow motion. The

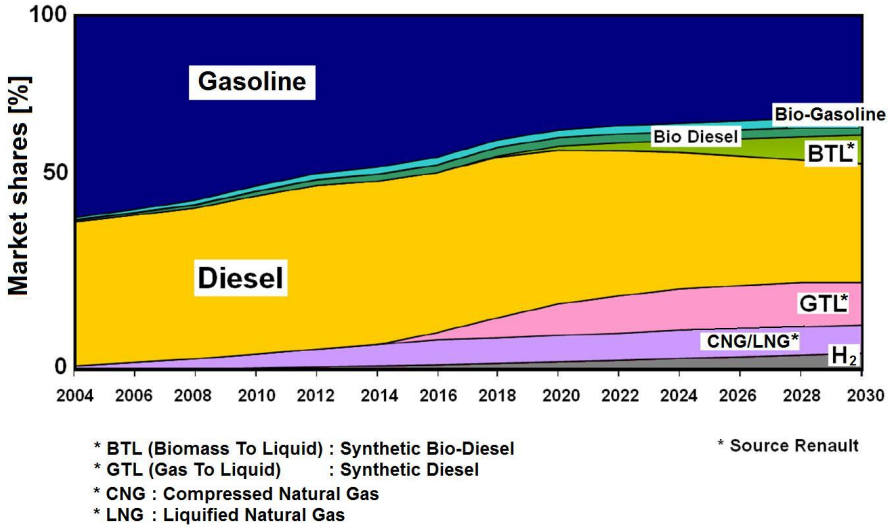

Figure 1.2: Diversification of fuels in the next 20 years.

Fuel	Density [kg/m3]	Air-Fuel Ratio at stoichiometry [-]	FHV [kJ/kg]	RON [-]	H/C [-]
Gasoline	700-750	14,7	42600	91-99	2,25
CNG	550	17,2	50000	130	≈4
LPG	510-580	15,5	46000	110	≈2,6
Ethanol	789	9	26900	106-130	3
Methanol	790	6,4	19937	136	4
Butanol	800	11,2	33075	94	2,5
Hydrogen (liquid)	70,79	34	120000	88-130	∞

Table 1.2: Chemical fuel properties. FHV = Fuel Heating Value – CNG = Compressed Natural Gas – LPG = Liquefied Petroleum Gas.

turbulent flow field is defined by all characteristic length scales and kinetic energies of the eddies describing the flow. Kolmogorov (1941) proposed a continuous distribution of the energy of turbulent eddies as function of their length. In such a representation, the flow energy is supposed to be transfered from largest eddies to smaller ones through division processes without dissipation. The range of scales is comprised between the integral length scale l_t (associated to the domain geometry) and the Kolmogorov scale from which the turbulent energy is dissipated as heat. During last years, numerical description of turbulent processes was subjected to several investigations to be able to solve a given problem considering available computational resources. A list of main numerical solutions considered in this thesis is given here :

- **CFD Tools**
  - *Direct Numerical Simulation (DNS) - Tool for understanding and modeling*
    In this case, all turbulent scales are resolved and meshes sizes are of the order of the Kolmogorov scale or smaller (when a flame is resolved for example). Such meshes require therefore an important number of grid points. Moreover, DNS need highly precise numerical discretization schemes to solve physical equations. As a consequence, direct numerical simulations are very expensive and appear thus difficult to address powertrain development, considering current computational resources. Indeed, considering a typical engine configuration, such an approach would require about $\approx 10^{12}$ grid points for the combustion chamber which makes it therefore not adapted to engine simulation. DNS are thus generally used to investigate fundamental aspects which can not be experimentally studied.
  - *Reynolds-Averaged Navier-Stokes (RANS) - Tool for engine components design*
    In such an approach, flow variables are split into an averaged part and a fluctuating one. Classical mass and momentum Navier-Stokes balance equations and combustion related variables are averaged and the whole turbulence spectrum is modeled. As a consequence, RANS is generally adapted to industrial configurations. Indeed, only the mean flow is solved and computational time requirements remain moderated. Nevertheless, in such an approach most physical phenomena are modeled which leads to a limited predictivity of RANS simulations.
  - *Large Eddy Simulation (LES) - Tool for understanding or for engine components design*
    This approach can be considered as a compromise between DNS and RANS. The global concept consists in solving physics of large eddies and modeling the behavior of small ones. This approach is based on the fact that all scales have not the same role within the flow. Indeed, large eddies hold most of the flow energy and directly depend on the domain geometry and fluid properties. Such eddies are therefore characterized by a high anisotropy and are very hard to model. On the contrary, smaller eddies which have a dissipative role, contain few energy and a short life-time and have a more isotropic behavior. The modeling of these scales is therefore easier. In practice, in such an approach, variables are split in a solved part corresponding to the effect of large eddies and in a modeled part corresponding to the effect of small ones. This separation is made at a cutting scale generally of the order of the mesh size. LES is thus a very interesting tool close to DNS in terms of information and to RANS in terms of computational cost. Nevertheless, LES remains a new approach and expensive for industrial problems such as engine simulations. As an example, the first multi-cylinder engine LES simulations were performed by Laget et al. (2011) in 2011 for twenty engine cycles.
- **Complex kinetics - Tool for chemical processes description**
  - *Complex chemistry - Tool for a precise chemical processes description*
    The complexity of chemical processes makes very hard the solving of both fluid dynamics and chemistry phenomena. In the past, only few computations have

been performed integrating direct resolution of complex kinetic mechanisms. Indeed, such mechanisms may involve hundreds of species and thousands of reactions leading for every more species to an additional balance equation, increasing in consequence the required computational time. Moreover, chemical reaction rates and transport coefficients are complex functions of species mass fractions and temperature. Therefore, increasing the number of chemical reactions also dramatically increases the computational time. Finally, solving chemistry in reactive flow problems requires also to be able to well-describe chemistry/turbulence interaction processes.

  * *Global chemistry - Tool for an efficient chemical processes description*
  To fix previously mentioned problems, a solution consists on using global schemes derived from complex chemical mechanisms. Generated schemes are thus build-up with a lower number of species and reactions. This derivation can be done "by hand" or using automatic reduction tools allowing to identify most influent reactions. Such a reduction is not a simple task and requires an expert knowledge of chemistry. Despite a lost of precision, these reduced schemes have the advantage of allowing a direct integration in CFD codes thank to a lower computational work compared to the direct resolution of complex chemical mechanisms.
  * *Tabulated chemistry - Tool for a precise and efficient chemical processes description*
  Tabulation approaches are based on *a priori* simulations of chemical processes (1D premixed flame, homogeneous reactors, etc.) using a complex kinetic scheme to generate a wide chemical database (of composition, characteristic times or burning velocities, etc.) which can thereafter be directly plugged in a CFD combustion model. Actually, integrating tabulation methods in combustion models requires an important modeling effort. However, such approaches appear today as a very interesting alternative to optimize computational times while accounting for complex chemical processes.

– **System Simulation - Tool for engine architecture design, control strategies development and calibration**
Based on 0D/1D models, system simulation tools have known rapid improvements in the past ten years and can today be used at all stages of the engine development from concept design to powertrain control development and calibration. Contrary to 3D approaches, these tools aim at replacing experimental engine benches providing only mean values of global variables such as temperature, pressure, pollutant concentrations, etc. 0-dimensional models are essentially based on empirical or phenomenological approaches which are mainly developed to reach very low computational times (≈real time). Nevertheless, such models are often characterized by very limited prediction levels. The challenge is therefore to develop more predictive 0D approaches (in terms of heat release, pollutant emissions, etc.) keeping at the same time the low computation resources requirements. This latter appears however as an hard task considering the nature of 0D modeling where no mesh is defined making complex the consideration of spatial geometry effects on physical phenomena. This last observations motivated the development of refined physical models based on the reduction of 3D approaches (RANS/LES) over a given domain volume as for example the combustion chamber (Mauviot et al. 2006, Dulbecco 2009, Lafossas et al. 2005, Richard et al. 2009, Kwon et al. 2011). The main difficulty of developing such models is to solve unclosed terms resulting from this reduction. This closure is generally performed either using 3D modeling concepts or by developing phenomenological or semi-phenomenological approaches.

1.2 Aim of the thesis

Because of the high complexity of engine operations, the high number of parameters (engine technologies and strategies, fuel composition, etc.) to be calibrated and the increasing cost of experimental campaigns, it seems crucial to develop accurate simulation tools able to support the engine development from design to control strategies development and calibration. In such a prospect, the system simulation approach appears today as an essential solution which has the advantage of allowing the integration of all technical skills previously presented :

- Academic experiments and detailed numerical simulations (DNS/LES/complex chemistry) to support the development of new modeling approaches.
- Engine test benches and efficient numerical simulations (RANS) for models calibration and validation.

This thesis aims at proposing a combustion chamber system simulation model able to accurately represent the different phenomena associated to all the technologies previously mentioned (GDI, EGR, downsizing, VCR, CAI, etc.) and to the use of alternative fuels (CNG, hydrogen, gasoline, ethanol and liquid or gaseous hydrocarbon mixtures). To this end a new 0D combustion model describing heat release, pollutant formation and auto-ignition processes is developed leaning on the set of experimental and numerical tools previously presented :

- Experimental data from IFPEn engine test benches measurements are post-processed and used to define initial and boundary conditions for the developed combustion model and on the other hand, to validate it by comparing simulation and experimental results (pressure traces, pollutant emissions, etc.);
- A wide range of experimental measurements of laminar flame velocities has been post-processed and used to validate the chemistry description of the developed combustion model and to propose new laminar flame velocity correlations;
- DNS analysis are achieved to improve the understanding of interactions between the flame and turbulence;
- RANS simulations are performed under engine conditions to evaluate the in-cylinder temperature distribution, a crucial parameter for the prediction of NO and CO formation
- Tabulation approaches are developed and integrated in the new 0D combustion model to improve the description of chemical processes in the flame front (oxidation), in the burnt gases (post-oxidation) and in the fresh gases (auto-ignition for knock or CAI combustion).
- The 0D combustion model developed in this work is based on the reduction of the 3D ECFM approach (Colin et al. 2003, Baritaud et al. 1996) and was implemented in the AMESim® system simulation software (Malbec et al. 2009) as a sub-model of the whole engine model.

The new combustion model is built on the association of several sub-models (describing heat release, turbulence processes, pollutant formation, etc.) which are linked together as displayed in Figure 1.3. This latter presents the global synopsis of the model development and will be reminded at the beginning of each chapter. Finally, all approaches proposed in this work were built to allow integration in current 3D models.

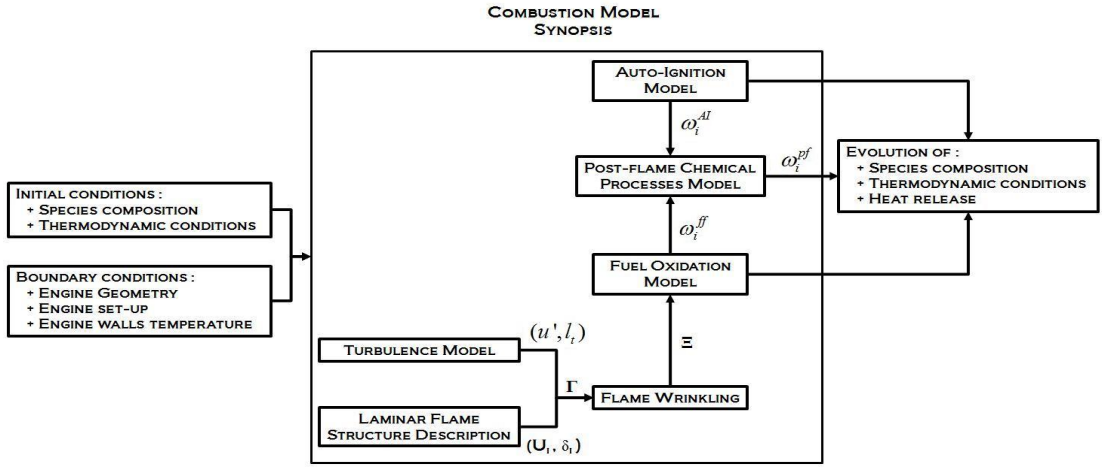

Figure 1.3: Combustion model global synopsis – ω_i^{ff},ω_i^{pf} and ω_i^{AI} refer to the rate of consumption/production of species i associated respectively to the combustion, post-oxidation and auto-ignition processes. U_l represents the laminar flame speed, u' the turbulent velocity fluctuation, δ_l the laminar flame thickness, l_t the integral turbulent length scale, Γ the stretch efficiency function and Ξ the flame wrinkling factor. All these parameters are defined in the different chapters of the thesis.

1.3 Organization of the manuscript

Works conducted in this thesis are organized as follow:

- **Part I – Introduction**
  - Chapter 1 (present chapter) presents the current environnemental, economical and technical contexts and defines the aim of the thesis.
  - Chapter 2 describes the physical basis of phenomena taking place in the combustion chamber which will be studied in this thesis.
  - Chapter 3 presents a review of previous and current 0-dimensional models adapted to engine simulation.
- **Part II – CFM1D model based on global chemistries**
  - Chapter 4 makes a state of the art of the current CFM1D model based on simple and reduced chemistries and phenomenological approaches to account for the effect of the fuel on combustion processes. Works described in this chapter were published in the *Oil & Gas Science & Technology* journal for gasoline case and in proceedings of the *SAE 9th International Conference on Engines and Vehicles* for gasoline-ethanol mixture case.
- **Part III – Integration of complex chemistry: the CFM1D-Tabulated Chemistry model**
  - Chapter 5 presents the tabulation approach used to integrated complex chemistry in the CFM1D model to describe the fuel oxidation process. A a new laminar flame correlation adapted to $CH4$–H_2–air–N_2 mixtures is proposed. This work is then extend to gasoline/ethanol blends. Works described in this section were published in the *International Journal of Hydrogen Energy* presented during the *33rd International Symposium on Combustion* in Beijing and selected for publication in the corresponding proceedings.

– Chapter 6 presents the new tabulation approach (CORA) devised to describe post-oxidation processes including complex chemistry in the CFM1D model. The final pollutant model named CFM1D-TC integrating developments presented in Chapter 5 and 6 is validated against a wide range of operating conditions of an IFPEn SI engine. Corresponding works were integrated in an article submitted to *Combustion and Flame*.

– Chapter 7 presents the new auto-ignition model for the prediction of controlled and uncontrolled auto-ignition phenomena in SI engines. This new model is based on the TKI approach initially developed for 3D simulations where auto-ignition delays and reaction rates of a progress variable are tabulated using *a priori* complex chemistry calculations.

– Chapter 8 investigates the effects of fuel composition on flame/turbulence interaction processes. DNS of flame/vortex interaction are performed to study the effect of fuel composition on the flame stretch and a new stretch efficiency function integrating Lewis number effects is proposed. Works described in this section were integrated in an article submitted to *Combustion and Flame*.

- **Part IV – Conclusion & Perspectives**

  – Chapter IV closes this manuscript by proposing a global conclusion of the thesis. It finally exposes the limitations of the new model and opens this work to new potential applications.

Figure 1.4 summarizes the organization of this manuscript.

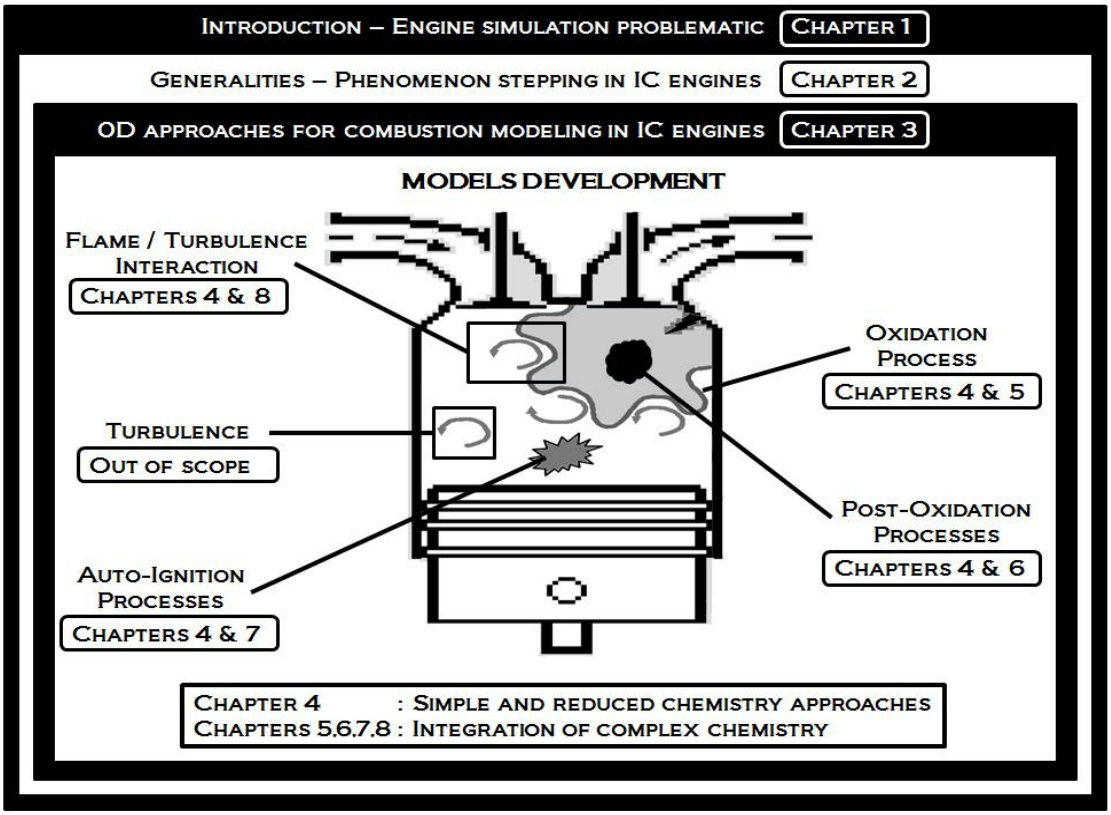

Figure 1.4: Schematic manuscript layout.

Chapter 2

General points

This chapter presents all basic concepts and vocabulary used in this thesis.

Gas motion within the engine cylinder is one of the major factors that controls the combustion process in IC engines. The initial in-cylinder flow pattern is set up by the intake processes. Indeed, relatively high characteristic flow velocities at the intake ($Re \approx 10^5$) combined to complex geometries of air-paths, combustion chamber and intake valves yield important turbulent flow motions characterized by a high anisotropy and high unsteadinesses of the mean flow. This flow pattern is also driven by the piston alternative travel which leads to pulsating motions within the flow amplified by the important differences between intake pipe and chamber pressures at the IVO (Intake Valve Opening). In IC engines, chemical phenomena occur therefore in highly turbulent conditions which promote species mixing and energy exchanges affecting in turn the combustion process. As a consequence, the understanding of flame/turbulence interaction mechanisms is of a crucial importance. In this chapter, a short description of laminar premixed flame structure and properties is presented. Classical turbulence concepts are then defined before studying interactions between combustion and turbulent flows. Short reviews of pollutant formation and auto-ignition mechanisms are also presented.

2.1 Laminar premixed combustion

Laminar flames are generally considered in many turbulent combustion models as the elementary building block of turbulent flames. In such models, fresh and burnt gases are assumed to be separated by a relatively thin continuous layer where chemical reactions take place, the turbulent flame, generally viewed as a collection of elementary laminar flames (flamelets) transported and stretched by the flow. With regards to premixed combustion, flamelet models showed in the past very good performances and proved that such an approach is well adapted to describe main phenomena (species and heat diffusion, transport, chemical reactions) occurring in the flame front. Moreover, the study of laminar flames is well-documented and quite simple in most cases. Besides, laminar flame is one of the few configuration where detailed comparisons between experiments, theory and computations can be performed. With regards to turbulent combustion modeling, the study of laminar flame mechanisms is therefore an important step before studying interactions between these mechanisms and flow aerodynamics processes.

The structure of a laminar premixed flame is displayed in Figure 2.1.

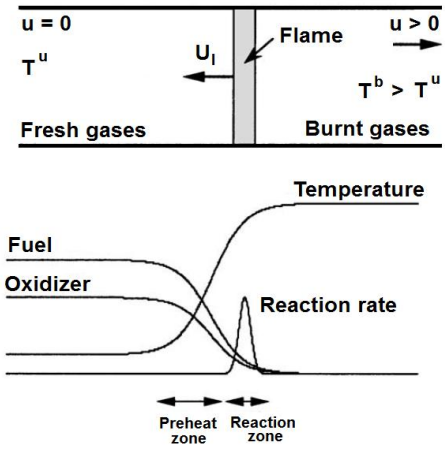

Figure 2.1: Structure of a laminar plane premixed flame.

Fresh gases (fuel and oxidizer mixed at the molecular level) and burnt gases (combustion products) are separated by a thin reaction zone. A strong temperature gradient is observed (typical ratios between burnt and fresh gases temperatures are about 5-7). Another characteristic of a premixed flame is its ability to propagate towards the fresh gases. Because of the temperature gradient and the corresponding heat fluxes, fresh gases are preheated and then start to burn. The local imbalance between diffusion of heat and chemical consumption leads to the propagation of the front. The difference between fresh and burnt gases temperature makes the density of burnt gases lower than fresh gases one leading to an acceleration of gases behind the flame due to the effect of heat expansion.

There are many ways to compute laminar flame structure and speed depending on the complexity of the chemistry and transport description. In Chapters 5 and 6 complex chemistry approaches based on a detailed kinetic scheme are used to describe the chemical processes in the flame but also in burnt gases. In such a case, no analytical solution to the problem can be found and numerical techniques are needed. However, simplified chemistry and transport descriptions can be considered as in Chapter 4 and analytical or semi-analytical solutions may be developed (Poinsot and Veynante 2001).

In all cases, the computation of a laminar flame means to solve:

- spatial and temporal species evolutions
- spatial and temporal temperature evolutions
- laminar flame velocity and reaction rate

All these variables can be tracked in turbulent combustion models such as flamelet models to finally compute the turbulent flame structure and velocity. In the following short descriptions of main macroscopic laminar flame characteristics are presented.

Laminar flame thickness

The laminar flame thickness generally determined from the temperature profile (Figure 2.1) is mainly used to characterized the turbulent combustion regime (see next section) and to size meshes used for simulations. Indeed, in most combustion approaches, the flame structure must be resolved and enough points must be localized within the flame thickness. Moreover, in some approaches as the ITNFS model (Meneveau and Poinsot 1991) this thickness is used as an input parameter characterizing the flame and helping at describing flame/turbulence interaction processes (see

Chapter 8). There are many ways to define thicknesses for premixed flames. Several of them are presented here:

- ***Total thickness*** δ_l^t: it is represented by the distance over which the temperature changes from $T^u(1+\varepsilon)$ and $T^b(1-\varepsilon)$ (Figure 2.2). δ_l^t is therefore always larger than δ_l^0 and δ_r^0 defined below.

- ***Diffusion thickness*** δ_l^0: it verifies :

$$Re_f = \frac{U_l^0 \cdot \delta_l^0}{D^u} = 1 \tag{2.1}$$

  where Re_f represents the flame Reynolds number, U_l^0 the laminar flame velocity defined in the following and D^u the laminar diffusivity in the fresh gases. δ_l^0 is generally approximated from the temperature profile as:

$$\delta_l^0 = \frac{T_b - T_u}{\max\left(\left|\frac{\partial T}{\partial x}\right|\right)} \tag{2.2}$$

  δ_L^0 requires here a first computation of the flame front (Figure 2.2).

- ***Reaction thickness*** δ_r^0 : it is generally linked to the diffusive thickness by a proportional law as $\delta_r^0 = \delta_l^0/\beta$, with β a proportionality parameter. β need then to be evaluated which is not a simple task considering complex chemical processes occurring within the flame. As a result the reaction thickness may have a different behavior than the diffusive thickness. A common way to estimate δ_r^0 from simulations is to consider that δ_r^0 is equal to the half-height width of the total heat release rate, by combustion (Q) (Figure 2.2). Indeed, if δ_r^0 is defined as:

$$\delta_r^0 = \frac{1}{Q_{max}} \int_{-\infty}^{+\infty} Q dx \tag{2.3}$$

  where Q_{max} denotes the maximal value of the total heat release rate Q across the flame front. In the particular case of a Gaussian evolution:

$$Q = Q_{max} \exp\left(-\left(\frac{x}{\delta}\right)^2\right) \tag{2.4}$$

  (with δ the Gaussian thickness), definition 2.3 gives:

$$\delta_r^0 = \int_{-\infty}^{+\infty} \exp\left(-\left(\frac{x}{\delta}\right)^2\right) dx = 2\delta \int_0^{+\infty} \exp\left(-\left(\frac{x'}{\delta}\right)^2\right) dx' = \delta\sqrt{\pi} \tag{2.5}$$

  while the half-weight thickness of the heat release is:

$$\delta_{1/2} = 2\delta\sqrt{\ln(2)} \tag{2.6}$$

  which finally lead to:

$$\delta_r^0 = \frac{\sqrt{\pi}}{2\sqrt{\ln(2)}} \approx \delta_{1/2} \tag{2.7}$$

  showing that Eq. 2.3 provides a relevant definition of the laminar flame reaction thickness.

- ***Correlations*** δ_l^0 : The essential drawback of previous expressions is that a first computation of laminar flame is needed to post-process temperature or heat release curves. Being able to evaluate it before computation can therefore be useful and time saving in particular when

mesh resolution has to be quickly determined. It will be seen latter that δ_l^0 can also be used as an input parameter in many turbulent combustion models to compute for example the turbulent flame velocity U_T. A typical scaling law generally used to estimate this thickness is the so-called Zel'dovitch expression (Poinsot and Veynante 2001) which writes:

$$\delta_l^{Zel'dovitch} = \frac{\lambda_u}{\rho_u Cp_u U_l} = \frac{D_{th}^u}{U_l} \tag{2.8}$$

where λ_u, ρ_u, Cp_u and D_{th}^u are respectively the fresh gases heat conductivity, density, heat capacity and heat diffusivity.

This thickness may be evaluated easily before any computation as soon as the flame speed U_l is known. In practice, this thickness may be too approximate and too small to be used for mesh determination. Blint (1986) proposed another correlation which is supposed to be closer to the thickness defined from the temperature profile 2.2. It includes a correction by the burnt gases properties considering a Sutherland law for λ_u (supposing a constant Prandtl number, $Pr = \nu/(\lambda/(\rho Cp)) = \mu Cp/\lambda$):

$$\delta_l^{Blint} = 2\frac{\lambda_u}{\rho_u Cp_u U_l}\left(\frac{T^b}{T^u}\right)^{0.7} \tag{2.9}$$

This correlation is more restrictive than the Zel'dovitch one because of the adiabatic flame temperature which is required to estimate the thickness. However, T^b can be easily approximated considering the enthalpy balance between fresh and burnt gas which finally leads to:

$$T^b = T^u + QY_F^0/Cp \tag{2.10}$$

where Y_F^0 is the initial fuel mass fraction and Q the heat of reaction per unit mass.

In Chapter 5 both correlations are compared to thicknesses obtained from complex chemistry calculations using Eq. 2.2. Results will show that Blint's correlation globally overestimates the results from complex chemistry while the Zel'dovitch one tends to underestimate them and is closer to the reaction thickness. In practice, Zel'dovitch correlation may thus be more appropriated to estimate meshing resolutions. Beyond meshing considerations, these correlations are also good approximations to characterized the turbulent combustion regime (see next section). Chapter 8 will show that a good estimation of the characteristic flame thickness is crucial to well describe the turbulent flame structure and propagation.

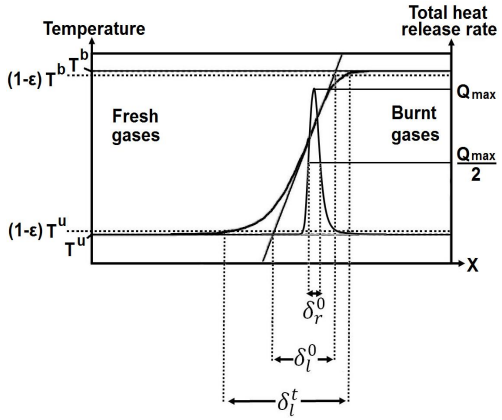

Figure 2.2: Premixed flame thicknesses.

Laminar flame characteristic velocity

If we consider the simple case of a 1D stationary laminar flame configuration in which all species k have the same molecular weight $W_k = W$, the same constant heat capacity $C_{p,k} = C_p$, the same molecular diffusion coefficient $D_j = D$ and the same Lewis number equal to $Le_k = Le = \lambda/(\rho C_p D) = 1$, the classical Navier-Stokes conservation equations can be simplified, leading to:

$$\rho u = constant = \rho_u u_u = \rho_u U_l \tag{2.11}$$

$$\rho_u U_l \frac{dY_F}{dx} = \frac{d}{dx}\left(\rho D \frac{dY_F}{dx}\right) + \dot{\omega}_F \tag{2.12}$$

$$\rho_u U_l \frac{dC_p T}{dx} = \frac{d}{dx}\left(\lambda \frac{dT}{dx}\right) - Q\dot{\omega}_F \tag{2.13}$$

where u_u is the velocity in the fresh gases in the flame reference frame, $\dot{\omega}_F$ is the fuel reaction rate (negative), λ is the heat conductivity and Q the heat of reaction per unit fuel mass.

Assuming a poor regime ($Y_F^b = 0$), if the two previous equations are integrated between $x = -\infty$ and $x = -\infty$ (see Figure 2.1), diffusive terms on both sides of the domain are zero so that the total burning rate Ω_F is written:

$$\rho_u U_l Y_F^u = -\int_{-\infty}^{+\infty} \dot{\omega}_F dx = \Omega_F \tag{2.14}$$

where Y_F^u is the mass fraction of fuel in the fresh gases.

In this particular example, the laminar velocity term U_l appears and need to be estimated to solve the system. More generally, the laminar flame velocity is a crucial parameter directly used in many combustion models (as in the previous example) and used as a base to describe the turbulent velocity. In addition, it is required in many models for non-dimensionalization of equations. Finally, it may be useful to estimate the physical burning time of a given problem and therefore to know approximately the computational time required to determine it. Many works proposed ways to analyze and compute the laminar flame velocity as the analysis of Zel'dovitch, Frank-Kamenetski and von Karman (asymptotic analysis) which is the basis of several analytical expressions for U_l (Clavin 1985, Williams 1985). Another solution to determine U_l is to measure it experimentally. In such a case, phenomenological correlations can be conjectured and parameters defining them will just need to be calibrated. These expressions are most of the time given as function of macroscopic variables such as pressure, fresh gases temperature and fresh gases composition parameters (air/fuel equivalence ratio[1], dilution rate, etc.) making them easier to use in practice. Many authors proposed expressions for U_l adapted to specific fuels. A review of most known laminar flame velocity correlations (used as references in this thesis) is presented here:

- **Isooctane** – The most used correlation results from Metghalchi and Keck (Metghalchi and Keck 1980, Metghalchi and Keck 1982) is written:

$$U_l = U_l^0(\varphi)\left(\frac{T^u}{T^0}\right)^{\alpha}\left(\frac{P}{P^0}\right)^{\beta} \tag{2.15}$$

with

$$U_l^0(\varphi) = 0.3422 - 0.13865\,(\varphi - 1.08)^2 \tag{2.16}$$

$$\alpha = 2.18 - 0.8\,(\varphi - 1) \quad | \quad \beta = -0.16 + 0.22\,(\varphi - 1) \tag{2.17}$$

[1] the fuel/air equivalence ratio is defined as: $\varphi = \frac{Y_F}{Y_{air}} / \left(\frac{Y_F}{Y_{air}}\right)_{stoichiometry}$ where Y_{air} represents the air mass fraction

where U_l^0 represents the laminar flame velocity under reference conditions $P^0 = 1$ bar and $T^0 = 298$ K (given in m/s), α and β calibrated functions of the equivalence ratio φ, T^u the fresh gases temperature and P the pressure. This function has been experimentally validated for: $298 < T^u < 700$ K, $0.4 < P < 50$ bar and $0.8 < \varphi < 1.5$.

- **Isooctane-ethanol blends** – The most used expression in such case is given by Gülder (Gülder 1982, Gülder 1984):

$$U_l = U_l^0(\varphi, V) \left(\frac{T^u}{T^0}\right)^c \left(\frac{P}{P^0}\right)^d \tag{2.18}$$

with

$$U_l^0(\varphi, V) = FA\varphi^a \exp\left(-b\left[\varphi - 1.075\right]^2\right) \tag{2.19}$$

where F, A, a, b and d are calibration parameters given in Table 2.1. In this Table V represents the volume fraction of ethanol in fuel and $T^0 = 350$ K. This function has been experimentally validated for: $300 < T^u < 600$ K, $1 < P < 8$ bar, $0.7 < \varphi < 1.3$ and $0 < V < 20\%$.

Fuel	C_2H_5OH	C_8H_{18}	$C_8H_{18} - C_2H_5OH$
F	1	1	$1 + 0.07V^{0.35}$
A	0.609	0.5924	0.5924
a	0.25	-0.326	-0.326
b	6.34	4.48	4.48
c	1.75	1.56	$1.56 + 0.23V0.46$
d if $\varphi > 1$	$-0.17\sqrt{\varphi}$	-0.22	$-0.22Y_{C_8H_{18}}$ $-0.17\sqrt{\varphi}Y_{C_2H_5OH}$ (Bayraktar 2005)
d if $\varphi \leq 1$	$\frac{-0.17}{\sqrt{\varphi}}$	-0.22	$-0.22Y_{C_8H_{18}}$ $\frac{-0.17}{\sqrt{\varphi}}Y_{C_2H_5OH}$ (Bayraktar 2005)

Table 2.1: Constants of Gülder's isooctane-ethanol blends laminar flame speed correlation (Gülder 1984) including Bayraktar's correction for the pressure dependency constant (Bayraktar 2005). Y_i corresponds to the mass fraction of component i in the fuel.

- **Methane and methane-hydrogen blends** – In the case of pure methane, Rahim et al. (2002) proposed an expression based on Metghalchi and Keck's one and writes:

$$U_l^0(\varphi) = 70.77\left[1 + 0.237(\varphi - 1) - 3.411(\varphi - 1)^2\right] \tag{2.20}$$

$$\alpha = 1.39 \;\; ; \;\; \beta = -0.016 \tag{2.21}$$

This function has been experimentally validated for: $298K < T^u < 650$ K, $1 < P < 40$ bar and $0.8 < \varphi < 1.2$.
In the case of methane-hydrogen mixtures, few correlations are available in literature. Recently, Hermanns (Hermanns 2007, Hermanns et al. 2010) proposed a correlation inspired by Gülder's one for isooctane-ethanol mixtures and validated for hydrogen volume fraction in fuel up to 40%. However, it is only defined for $298 < T^u < 418$ K and $P = 1$ bar. It is given here:

$$U_l = U_l^0(\varphi, \alpha) \left(\frac{T^u}{T^0}\right)^{\alpha_T} \tag{2.22}$$

with

$$U_l^0(\varphi,\alpha) = (1+\gamma\alpha)\, W \varphi^{\eta} e^{-\zeta(\varphi-\sigma-\omega\alpha)^2} \tag{2.23}$$

and

$$\alpha_T = \nu_0 + \nu_1\varphi + \nu_2\varphi^2 + \nu_3\alpha \tag{2.24}$$

where α is the hydrogen volume fraction in fuel and $\gamma, W, \eta, \zeta, \sigma, \omega, \nu_0, \nu_1, \nu_2$ and ν_3 calibration parameters.

Due to the complexity and cost of experimental campaigns, validity domains of such correlations are finally restricted to temperatures and pressures close to atmospheric conditions as previously mentioned. Moreover, for the same reasons, only few functions adapted to fuel blends are available. It will be shown latter (Chapter 8) that a bad description of the laminar flame velocity can have a significant effect on engine simulation results. In this work, a new approach based on complex chemistry calculation is presented and new correlations for U_l adapted to methane-hydrogen-air-nitrogen and isooctane-ethanol-air-nitrogen combustion are finally proposed (Chapter 5).

Stretched laminar flame velocity

The laminar flame velocity previously defined characterizes a laminar flame in its simplest configuration and presented correlations are developed to describe the propagation of 1D flame. However, in 3 dimensions, the flame may be subjected to spatial physical mechanisms as stretch and the real flame propagation velocity may finally differ from the planar unstretched laminar flame velocity. The velocity of the flame surface $\vec{U}$ may therefore be written as function of the unburnt gas velocity $\vec{u}_u$ and the displacement speed $u_d\vec{n}$ (where $\vec{n}$ is the unit vector normal to the flame surface pointing towards the fresh gases) as:

$$\vec{U} = \vec{u}_u + u_d\vec{n} \tag{2.25}$$

The flame stretch κ is a measure of strain and curvature effect induced by the flow to the flame. κ is defined by the fractal rate of change of a flame surface element A (Matalon and Matkowsky 1982, Candel and Poinsot 1990) as:

$$\kappa = \frac{1}{A}\frac{dA}{dt} \tag{2.26}$$

Another expression for κ can then be deduced from 2.26 and from kinematic considerations for a thin flame sheet (Candel and Poinsot 1990)[2]:

$$\kappa = -\vec{n}\vec{n} : \nabla\vec{U} + \nabla\cdot\vec{U} \tag{2.27}$$

which leads to:

$$\kappa = -\vec{n}\vec{n} : \nabla\vec{u}_u + \nabla\cdot\vec{u}_u + u_d(\nabla\cdot\vec{n}) \tag{2.28}$$

If both first terms are grouped, the last equation can be re-written:

$$\kappa = \nabla_t\cdot\vec{u}_u + u_d(\nabla\cdot\vec{n}) \tag{2.29}$$

$\nabla\cdot\vec{n}$ can be interpreted as the curvature of the flame front (linked to the flame radii of curvature R_1 and R_2) and $\nabla_t\cdot\vec{u}_u$ (the subscript t refers to the component of the ∇ operator tangential to the flame front) represents the flame strain related to the flow non-uniformity.

A steady spherical laminar flame fed centrally by a fresh gas source is therefore characterized by a stretch equal to zero. On the contrary an unsteady spherical laminar flame burning fresh gases outside is stretched through curvature mechanism (Figure 2.3).

As suggested by several asymptotic theories (Bush and Fendell 1970, Buckmaster and Crowley 1982, Williams 1985, Pelce and Clavin 1982, Clavin and Williams 1982), the stretch κ is a main parameter controlling the flame structure and the displacement velocity appearing in equation 2.25 can theoretically be linearly linked to the laminar flame velocity as (for small values of κ at least):

$$u_d = U_l - L_a^d \kappa \tag{2.30}$$

where L_a^d is the Markstein length which can be experimentally measured and which is linked to the Markstein number as $L_a^d = M_a^d \delta_l$ with δ_l the laminar flame thickness previously defined. Several expression for the M_a^d can be found in the literature as well as the important number of studies aiming at measuring it. Similarly, the consumption velocity u_c[3] is defined considering the respective Markstein length L_a^c and Markstein number $M_a^c = L_a^c/\delta_l$ as:

$$u_c = U_l - L_a^c \kappa \tag{2.31}$$

With regards to the present work aiming at studying effect of fuel composition on combustion processes, another parameter which would be interesting to integrate in relations 2.30 or 2.31 is the Lewis number $Le = \lambda/(\rho C_p D)$ measuring the ratio between heat and species diffusivities. In fact, the flame consumption speed u_c tends at growing due to the species diffusion mechanism (fuel mass fraction gradients are increased) and in the same time at decreasing because of the intensive induced flame cooling effect (temperature gradients are increased). Therefore, a competition between both effects takes place in the flame while the stretch is increasing. As a result, the Lewis number appears as an interesting parameter to evaluate which one of these two competing effects takes over. Thus, if $Le = 1$, u_c is supposed to be unchanged even if κ increases, if $Le < 1$ molecular diffusion takes over and u_c is supposed to grow when κ increases (and vice versa when $Le > 1$). These last assumptions are effectively observed in asymptotic results summarized by Poinsot and Veynante (2001) and presented in Figure 2.4 for a particular configuration of a stagnation flame exposed to two opposed fresh gases flows. Note that quenching is obtained only at very high stretch values. However if heat losses are accounted for (non adiabatic flame), quenching appears earlier. The Lewis number is therefore a crucial parameter to describe stretch effects especially at low values of Le (poor air-hydrogen mixtures for example) where thermo-diffusive instabilities can appear. It will be shown in Chapter 8 that such parameter should therefore be integrated in combustion models to account for fuel compositions effects.

Remark: Actually, the composition information is also supposed to be integrated in the Markstein length. As a result, the Markstein number can also be used instead of Le. Nevertheless, such a number comes from theories defined for low values of κ and is a global variable not well known contrary to the Lewis number which is clearly defined. Therefore, the Lewis number remains a good parameter to estimate the balance between heat and molecular diffusivities and is thus very useful for estimating thermodiffusive instabilities which can appear at very low values of Le. These instabilities existing in laminar modes and promoted by turbulent structures, are generally neglected. However, as presented in Chapter 8, these mechanisms could be the source of additional flame wrinkling in turbulent conditions and should then be studied in particular for engine applications.

[2]The operator $(\vec{n}\vec{n} : \nabla\vec{w})$ represents the gradient operator normal to the flame surface.

[3]The consumption speed, u_c, measures the speed at which the flame burns reactants while the displacement speed, u_d, measures the front speed relative to the flow. The first one is defined as function of the reaction rates as $u_c = -1/(\rho_u Y_F^0) \int_{-\infty}^{-\infty} \dot{\omega_F} dn$ while u_d is written as the difference between the flow speed, $\vec{u}_u$, and the front speed, $\vec{U}$, as $u_d = (\vec{U} - \vec{u}_u).\vec{n}$.

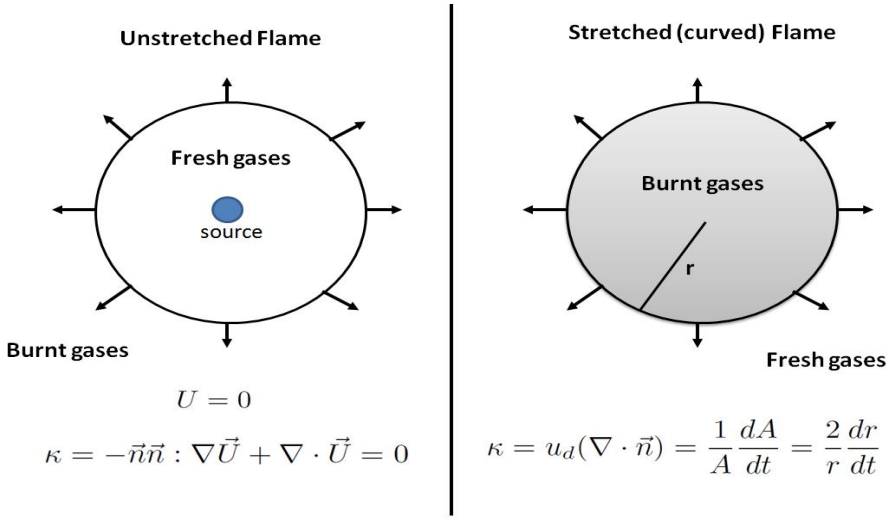

Figure 2.3: Examples of unstretched (left) and stretched (right) laminar flames. The first case (left) represents a steady flame propagation from a source providing fresh gases inside the sphere. The second case (right) represents an unsteady propagation of a flame burning inert fresh gases outside the sphere.

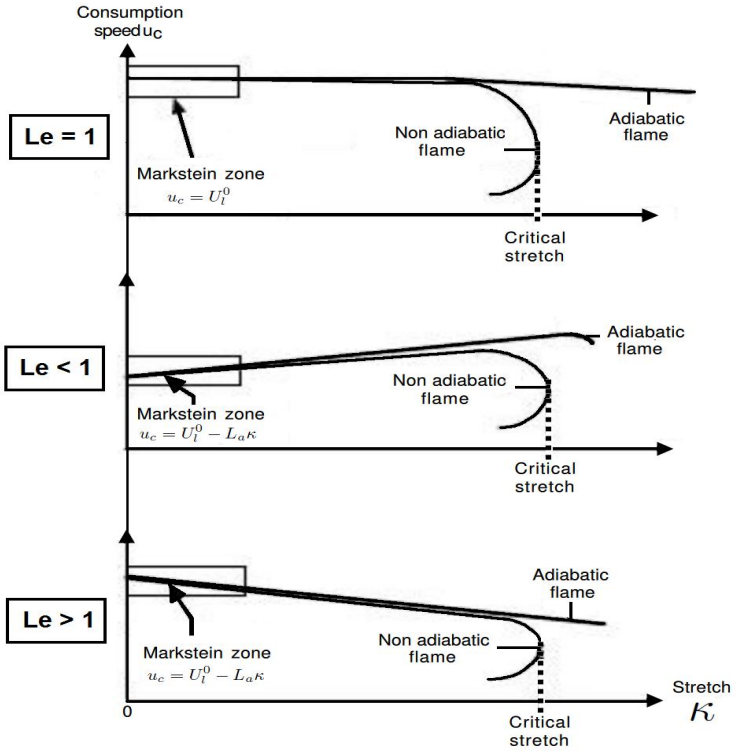

Figure 2.4: Stretch effect on laminar flames at different Lewis numbers (Poinsot and Veynante 2001).

Laminar flame characteristic numbers

This section summarized dimensionless numbers characterizing laminar combustion processes :

- *Flame Reynolds number* Re_f - introduced to define the diffusion thickness (section 2.1), it theoretically compares the flame front inertia to the fresh gases kinematic viscosity ν^u:

$$Re_f = \frac{U_l \delta_l}{\nu^u} \tag{2.32}$$

- *Schmidt number* Sc - compares the gases kinematic viscosity to the molecular species diffusivity D:

$$Sc = \frac{\nu}{D} = \frac{\mu}{\rho D} \tag{2.33}$$

  where μ is the dynamic viscosity.

- *Prandlt number* Pr - compares the gases kinematic viscosity to the heat diffusivity:

$$Pr = \frac{\nu}{\frac{\lambda}{\rho C_p}} \tag{2.34}$$

- *Lewis number* Le - compares the heat conductivity to the species diffusivity as previously presented:

$$Le = \frac{\frac{\lambda}{\rho C_p}}{D} = \frac{Sc}{Pr} \tag{2.35}$$

Finally, a characteristic flame time τ_{fl} can be defined here:

$$\tau_{fl} = \frac{\delta_l}{U_l} \tag{2.36}$$

Corresponding to the time needed by the flame to propagate over a distance equal to its thickness.

2.2 Turbulent premixed combustion

In the previous section, the main parameters describing a laminar premixed flame have been presented. Such mechanisms are crucial to understand how a given flame characterized by its laminar flame velocity, thickness and stretch (via its Markstein length) will be affected by the flow which is most of the time turbulent. This section aims therefore at presenting how the flame structure and properties are affected by turbulence.

Turbulence basics

In fluid dynamics, turbulence is a flow regime characterized by chaotic and stochastic property changes. Various time and length scales are involved and the structure and the description of turbulence remain open questions. Giving a precise definition of this phenomenon is therefore very difficult but some basic concepts can however be defined and are presented in this section. The stochastic and fluctuating processes defining turbulence makes the response of the flow highly dependent to initial and boundary conditions. With regards to numerical simulation, the strong

anisotropic three-dimensional nature of turbulent flows and the large distribution of length, temporal and velocity scales make the resolution of turbulent flow problems even more complex. In particular, the solving of such problems requires very consistent high order numerical schemes and highly resolved meshes and time steps. These last observations are even more true when dealing with reactive turbulent flows where a large range of chemical time and length scales are involved. However, considering current computational resources, direct resolution of a such problems (DNS) remains a hard task and alternative methods (RANS, LES, System simulation, see Chapter 1) based on modeling approaches are commonly used. In such approaches, every quantity Q is split into a mean part $\overline{Q}$ and a part Q' corresponding to fluctuations as:

$$Q = \overline{Q} + Q' \tag{2.37}$$

This decomposition allows such models to solve only averaged or spatially filtered variables while effects of turbulence are modeled. This modeling is generally based on the Kolmogorov's (Kolmogorov 1941) theory which main assumption states that the flow behaves such as fully developed and maintained homogeneous isotropic turbulence (HIT). In this theory a turbulent flow is composed by eddies of different sizes defined by characteristic length, velocity and time scales (turnover time) dependent on the length scale. The large eddies are unstable and eventually break up originating smaller ones. The kinetic energy of the largest turbulent structures is divided and transfered to the smaller ones. These smaller eddies undergo the same process, giving rise to even smaller structures which inherit the energy of their predecessors, and so on. In this way, the energy is passed down from the largest length scale of the motion – the integral length scal l_t – to smaller ones until reaching a sufficiently small length scale – the Kolmogorov length scale η_k – such that the viscosity of the fluid can effectively dissipate the kinetic energy into heat. Length scales r of the different flow structures are therefore such as:

$$\eta_k \leq r \leq l_t \tag{2.38}$$

The energy transfer process previously described defines the so-called $''$ Kolmogorov energy cascade$''$. A spectral representation of this energy contained in a HIT is plotted in Figure 2.5. The flow is supposed here to be composed by rotative eddies defined by a characteristic length scale r and velocity $u'(r)$. Each eddy is associated to a turnover time τ_r and a wave number K_r defined as:

$$\tau_r = \frac{r}{u'(r)} \quad ; \quad K_r = \frac{2\pi}{r} \tag{2.39}$$

In Figure 2.5, three zones can be distinguished:

- **Integral zone -** It corresponds to the lowest wave number and thus to the largest turbulent structures holding the most part of energy. These eddies obtain energy from the mean flow and also from each other. They have large velocity fluctuations ($u' = \sqrt{2/3k}$, where k is the turbulent kinetic energy) and low frequencies. The maximum length of these scales (l_t) is constrained by the characteristic length of the domain. As the turbulence level is supposed to be maintained, an equilibrium between energy production and dissipation is observed and the dissipation rate ε is written:

$$\varepsilon = \frac{k}{\tau_t} \tag{2.40}$$

  where $\tau_t = \tau_r(l_t)$. Using relation 2.39 it comes:

$$\varepsilon \approx \frac{u'^3}{l_t} \tag{2.41}$$

- **Inertial zone -** It concerns scales between η_k and l_t and corresponds to the range of eddies transferring energy without any loss. The dissipation rate is defined here as:

$$\varepsilon = \frac{u'(r)^2}{r/u'(r)} = \frac{u'(r)^3}{r} \tag{2.42}$$

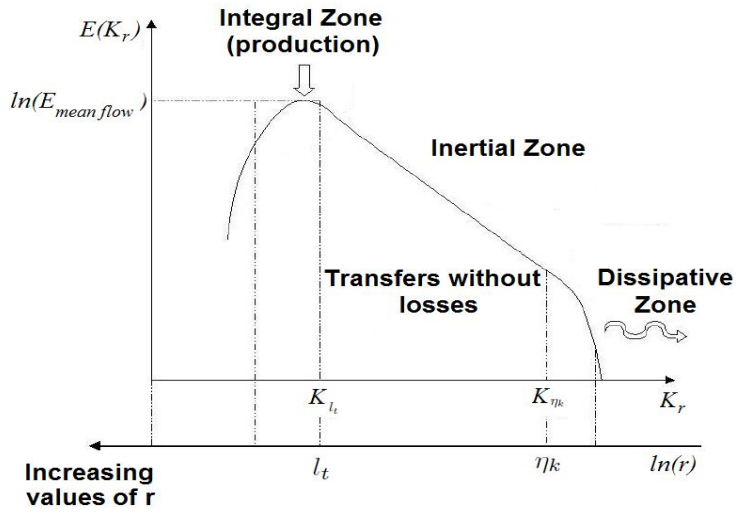

Figure 2.5: Flow energy distribution within an homogeneous isotropic turbulence.

- **Dissipative zone -** It corresponds to scales under the Kolmogorov scale. These are the smallest scales in the energy spectrum that form the viscous sub-layer range. In this range, the energy input from nonlinear interactions and the energy drain from viscous dissipation are in exact balance. The small scales are high in frequency, that is why turbulence is locally isotropic and homogeneous. In particular, at the Kolmogorov scale η_k, the dissipation rate given by Eq.2.42 can be written here:

$$\varepsilon = \frac{u'(\eta_k)^3}{\eta_k} \tag{2.43}$$

The turbulent Reynolds number $Re(r)$ is often used to characterize the turbulence of a given flow at $r = l_t$. $Re(r)$ is given by:

$$Re(r) = \frac{u'(r)r}{\upsilon} \tag{2.44}$$

Along the cascade, $Re(r)$ goes down from $Re_t = Re(l_t)$ to values close to unity where inertia and viscous forces balance. The Kolmogorov scale η_k controlled by viscosity and by the dissipation rate ε of the turbulent kinetic energy k can then be determined by this limit as:

$$\eta_k = \left(\upsilon^3/\varepsilon\right)^{1/4} \tag{2.45}$$

corresponding to a unity Reynolds number:

$$Re_k = Re(\eta_k) = \frac{u'_k \eta_k}{\upsilon} = \frac{\epsilon^{1/3}\eta_k^{4/3}}{\upsilon} = 1 \tag{2.46}$$

Generally, flows at turbulent Reynolds numbers Re_t larger than 10^3 are considered as turbulent, while those at low values of Re_t usually remain laminar. Actually, there is not a well-defined frontier between laminar and turbulent regimes and the turbulent Reynolds number is mostly used to quantify the size of the inertial zone in the turbulent energy spectrum. Indeed, from Re_t the ratio of the integral length scale, l_t, to the Kolmogorov length scale, η_k, can be expressed from Eqs. 2.44, 2.42 and 2.45:

$$\frac{l_t}{\eta_k} = \frac{u'^3/\varepsilon}{\left(\upsilon^3/\varepsilon\right)^{1/4}} = Re_t^{3/4} \tag{2.47}$$

A similar relation can be obtained for the ratio of the respective velocity scales u' and $u'(\eta_k)$:

$$\frac{u'}{u'(\eta_k)} = Re_t^{1/4} \tag{2.48}$$

Moreover, combining Eqs. 2.41 and 2.43, it comes:

$$\frac{u'(\eta_k)}{u'} = \left(\frac{\eta_k}{l_t}\right)^{1/3} \tag{2.49}$$

Turbulent combustion

The previous sections described the main mechanisms characterizing combustion and in the other hand turbulent processes. This section aims at understanding how these mechanisms are affected by each other within turbulent reactive flows. To do so the turbulent flow is treated like a set of eddies of different scales allowing to reduce the problem to the study of the interaction between a flame and a single turbulent structure. The total response of the flame to the global flow can finally be considered as a superposition of the responses of all the different structures. On the other hand, the flame also impacts the turbulent flow. The issue of turbulent combustion need therefore to be seen as the study of both effects of the turbulence on the flame and of the flame on the flow.

- ***Effects of turbulence on the flame -*** As it will be shown in next section, the effect of the flow on the flame is mainly dependent on the relative size and velocity of the different turbulent structures compared to the flame characteristics. Indeed, small eddies will enter the flame promoting mixing in the front and changing the chemical activity and therefore its structure. By contrast, large eddies (compared to the flame thickness) will affect the transport and stretching mechanisms finally leading the flame front to be wrinkled. By increasing the turbulent flame surface A_T, these processes are therefore supposed to increase also the combustion burning rate. As an extension of Eq. 2.14 to 3D turbulent combustion problems (assumed statistically 1D), this rate can be computed as:

$$-\int_{-\infty}^{+\infty} \dot{\omega} dV = S\rho_u U_T Y_F^u \tag{2.50}$$

  where V represents the volume of the domain considered, U_T is the turbulent flame speed and S is the projection in the propagation direction of the turbulent flame surface A_T.

  Damköhler (1940) explained that U_T and A_T growths are directly linked. Indeed, according to him, if the flame surface propagates locally at the laminar flame speed U_l, the local burning rate per unit area can therefore be given by Eq. 2.14 and the total reaction rate in a volume V can thus write:

$$-\int_{-\infty}^{+\infty} \dot{\omega} dV = A_T \rho_u U_l Y_F^u \tag{2.51}$$

  Using Eq. 2.50 and if the projected surface S is supposed to be equal to the laminar flame surface, it finally comes:

$$\frac{U_T}{U_l} = \frac{A_T}{A_l} = \Xi \tag{2.52}$$

  where Ξ is the flame wrinkling factor comparing the increase of the turbulent flame speed U_T due to the increase of the total flame surface A_T. As for the laminar case, the turbulent flame velocity appears as a crucial parameter for solving premixed turbulent combustion

problems[4]. Here also, many authors (Damköhler 1940, Zimont 2000, Peters 2000, Gülder 1990, Bradley et al. 1992, Driscoll 2008, Eickhoff 2002) proposed in the past dimensionless correlations for U_T/U_l generally defined as function of turbulent flow parameters (u', l_t, etc.) and flame properties (U_l, δ_l, Le, etc.). Considering the complexity of turbulent processes and the high dependency to the domain geometry and initial conditions, such functions often suffer from a lack of predictivity when dealing with complex problems and still need today more development. A short review of main correlations is given in Chapter 8. Finally, under certain turbulence conditions the induced stretch can become too strong for the flame which can break up. This quenching situation is not treated in this work.

- ***Effects of the flame on the flow field -*** The high temperature variations implied by the flame passage promote diffusion mechanisms and result in the increase of the kinematic viscosity through an increase of the turbulent energy dissipation downstream the flame. This phenomena can in some cases lead to a relaminarization of the flow. On the other hand, this temperature increase also lead to an increase of the dilatation of burnt gases which are accelerated increasing thereby the turbulence. As a result, the flame behavior is clearly not isotropic and the often supposed isotropic property of turbulence can not be considered any more when dealing with premixed combustion. As it will be shown in Chapter 3, these effects of the flame on the flow field are implicitly integrated by the 0D turbulence model through adjustable variables which are calibrated as function of the engine operating condition.

Combustion regimes

An important question in the study of premixed turbulent combustion is the determination of the combustion regime and the structure of the reactive flow. Indeed, as previously mentioned interaction processes between flame and turbulence are complex and different physical and chemical phenomena can be in competition. With regards to numerical simulation, it is therefore important to know which phenomena take over. It is crucial for characterizing the combustion regime and thus the modeling assumptions to consider. A continuous flame front will not be modeled in the same way as a flame broken into many small pockets and where combustion does not take place along a sheet but in a more distributed manner. Diagrams defining combustion regimes in terms of length and velocity scales ratios have been proposed in the past (Borghi. 1985, Peters 1986, Williams 1985, Poinsot et al. 1990, Poinsot et al. 1991) and are generally graphically represented as in Figure 2.6.

When the turbulence integral scale and the turbulent kinetic energy are known, these diagrams indicate whether the flow will contain flamelets, pockets, or distributed reaction zones. In such diagrams, the different regimes are limited by frontiers defined through dimensionless numbers as the Damköhler number Da, the Karlovitz number Ka and the turbulent Reynolds number Re_t expressed:

- *Damköhler number -* It compares the turnover time of an eddy at the integral length scale $\tau_t = l_t/u'$ with the characteristic flame time τ_{fl} (eq. 2.36) and is written:

$$Da = \frac{\tau_t}{\tau_{fl}} = \frac{l_t}{u'}\frac{U_l}{\delta_l} \tag{2.53}$$

- *Karlovitz number -* It compares turnover time of an eddy at the Kolmogorov length scale $\tau_k = \tau_r(\eta_k) = u'(\eta_k)/\eta_k$ (Eq. 2.39) with the characteristic flame time τ_{fl} (Eq. 2.36) and is

[4]It should be noticed here that the turbulent flame velocity is an important global parameter mainly used in simplified modelings of statistically 1D premixed flames but is generally expected to be a sub-product of the simulation.

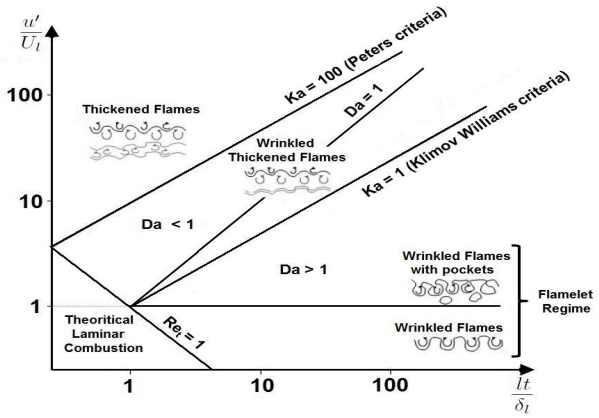

Figure 2.6: Peters's turbulent premixed combustion diagram (Peters 1999): regimes are identified as function of length scales ratios l_t/δ_l and velocity ratios u'/U_l.

written:

$$Ka = \frac{\tau_{fl}}{\tau_k} = \frac{u'(\eta_k)}{\eta_k}\frac{\delta_l}{U_l} \tag{2.54}$$

Using Eqs. 2.43, 2.45 and 2.1), it comes:

$$Ka = \left(\frac{u'}{U_l}\right)^{3/2}\left(\frac{\delta_l}{l_t}\right)^{1/2} = \left(\frac{\delta_l}{\eta_k}\right)^2 \tag{2.55}$$

A similar expression of the Karlovitz number can be given considering the flame reaction thickness δ_r. Indeed, in the cases where δ_r becomes larger than the Kolmogorov scale, η_k, the Karlovitz number reaches a transition value Ka_R, corresponding to $\delta_r = \eta_k$:

$$Ka_R = \left(\frac{\delta_l}{\eta_k}\right)^2 = \left(\frac{\delta_l}{\delta_r}\right)^2\left(\frac{\delta_r}{\eta_k}\right)^2 = \left(\frac{\delta_l}{\delta_r}\right)^2 \tag{2.56}$$

For most premixed flames, $\delta_l/\delta_r \approx 10$, corresponding to a transition for $Ka_R \approx 100$.

- *Reynolds number* - Using 2.1, 2.53 and 2.54 the turbulent Reynolds number $Re_t = Re(l_t)$ previously defined (Eq. 2.44) can finally be written:

$$Re_t = \frac{u' l_t}{\upsilon} = \frac{u'}{U_l}\frac{l_t}{\delta_l} = Da^2 Ka^2 \tag{2.57}$$

These last 3 numbers are used to characterize the different combustion regimes as shown is the following:

Limit of laminar/turbulent regimes - Considering that:

- the laminar regime corresponds to $Re_t \leq 1$
- the turbulent regime corresponds to $Re_t \geq 1$

and using Eq. 2.57, the limit between laminar and turbulent regimes can be defined as:

$$\frac{u'}{U_l} = \left(\frac{l_t}{\delta_l}\right)^{-1} \tag{2.58}$$

which corresponds in the combustion diagram of Figure 2.6 to a line with a slope equal to -1.

Turbulent regime analysis - Concerning turbulent regimes, two cases can be described:

- when $Da << 1$, turbulence characteristic times are much shorter than chemistry times. All turbulence structures are therefore small compared to the flame thickness and enter the front. The turbulent mixture becomes very important inside the flame while chemical reactions are very slow. Such regime is qualified as distributed combustion.
- when $Da >> 1$, chemical reactions are infinitely fast compared to turbulence characteristic speeds. The reaction rate can be here considered as mainly driven by turbulence which becomes the limiting factor. Moreover, the large turbulent structures are large compared to the flame thickness and can not enter inside. However, such structures will wrinkle the front and the topology of the flame is finally similar to a laminar flame. Such regime is thus qualified as flamelet regime. Using Eq. 2.53, the limit between laminar and turbulent regimes can be defined as:

$$\frac{u'}{U_l} = \frac{l_t}{\delta_l} \tag{2.59}$$

  which corresponds in the combustion diagram of Figure 2.6 to a line with a slope equal to 1.

Flamelet regime analysis ($Da > 1$) - A "perfect" flamelet regime would correspond to the case where all turbulent structures are large compared to the flame thickness and can only stretch the front. However, in such regimes, the smallest scales may be smaller than the flame thickness and finally can enter inside and change the chemical processes. The Karlovitz number Ka allows thus to distinguish three different regimes limited by two boundaries. The first one where $Ka = 1$ is the so-called "Klimov-Williams criteria" and the second one where $Ka_R = 1$ (and thus $Ka = 100$) is the so-called "Peters criteria":

- when $Ka < 1$, the flame thickness is lower than the Kolmogorov scale size. The smallest turbulent structures are therefore not able to enter the flame and the flamelet regime is "ideal". Such regime correspond to the thin wrinkled flames regime. Moreover, two sub-regimes can be distinguished:
  - $u'/U_l < 1$: It is the wrinkled flames regime. The velocity of largest turbulence structures is not strong enough to generate interactions between flamelets. Laminar propagation predominates.
  - $u'/U_l > 1$: It is the wrinkled flames with pockets regime. In this case, the velocity of the largest eddies is strong enough to allow interaction between two neighbor fronts leading to pockets generation.
- when $Ka > 1$, the flame thickness is higher than the Kolmogorov scale. Eddies able to change the flame internal structure exist. Actually, only a limited part of them which are sufficiently energetical can really affect the front. Indeed, because of the increase of viscosity in burnt gases, smallest structures are promptly dissipated through the front. Considering the reaction Karlovitz number Ka, two sub regimes can be distinguished:
  - $1 < Ka < 100$: It is the thickened wrinkled flame regime. It corresponds to the situation where $\delta_r < \eta_k < \delta_l$. Turbulence structures which enter the flame are small enough to penetrate into the preheat zone increasing the mixture inside but too large to affect the internal structure of the reaction zone.
  - $Ka > 100$: It is the thickened flame regime. In this case, Kolmogorov scales are lower than the reaction thickness and enter the reaction zone. The reaction zone is perturbed and diffusion effect are higher than in a laminar front. For this last case, the flamelet assumption can generally not be considered anymore.

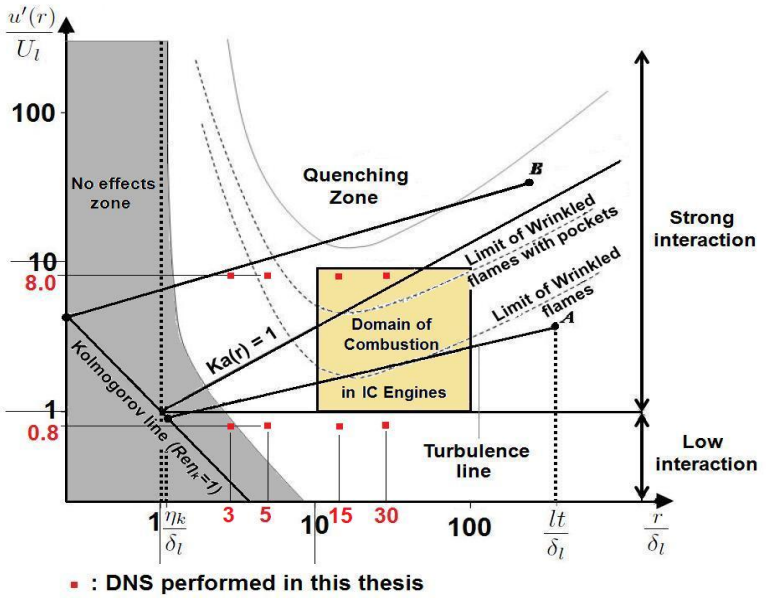

Figure 2.7: Spectral turbulent combustion diagram based on DNS results (Poinsot et al. 1990, Poinsot et al. 1991). The combustion domain in IC engines is approximately represented: it is globally located in the flamelet zone. A more precise evaluation of this domain is given in Figure 2.10.

Finally, if the integral length scale and Kolmogorov scale are known, these turbulent combustion diagrams can be used to have a rough estimation of the combustion regime. However, such diagrams are build on dimensional and phenomenological considerations and suffer therefore from a lack of precision. Poinsot et al. (Poinsot et al. 1990,Poinsot et al. 1991) improved limits between combustion regimes using results from DNS of interaction between a planar laminar flame and a pair of vortices. Previous diagrams were thus completed as presented in Figure 2.7. In this new classification, the flamelet zone is more extended and seems to be more represented by the Peters criteria. On the contrary to classical diagrams, this diagram represents the action of all turbulence scales and is called "spectral diagram". Indeed, according to Eq. 2.47, it easy to show that the turbulence spectrum can be represented in a log/log diagram by a line with a slope equal to 1/3 and with two extremities at the integral length scale $(u'; l_t)$ and at the Kolmogorov scale $(u'(\eta_k), \eta_k)$ located in the line $Re(r) = 1$. Two examples are plotted in Figure 2.7 (points A and B). Therefore, if theses two points are known, interactions between the flame and the turbulence structures at all intermediate scales can be described. In this thesis, DNS of flame-vortex interactions are performed using a detailed chemistry and considering the specific speed and length scale ratii ($u'(r)/U_l$ and r/l_t) identified in Figure 2.7 by square markers. Examples of achieved results are presented in Figure 2.8 which illustrates for four cases how a given pair of vortices wrinkles the flame. In particular, it can be observed that a fresh pocket is being creating for the cases $u'/U_l = 8.0$ while the flame seems to be less affected in the cases $u'/U_l = 0.8$. These results confirm previous DNS of Poinsot et al. (Poinsot et al. 1990, Poinsot et al. 1991) which were performed using a simple chemistry and allow to more precisely specify the limits of the flamelet regime displayed in the diagram of Figure 2.7. More details about this study will be given in Chapter 8.

Encountered regimes in IC engines - In IC engines, flow in the chamber can be generated by aerodynamic motions induced by the intake, the spray (in the case of direct injection) and the piston movements. These motions are therefore controlled by air-paths and chamber geometries and are generally classified into 3 main motions as shown in Figure 2.9: the tumble, the swirl

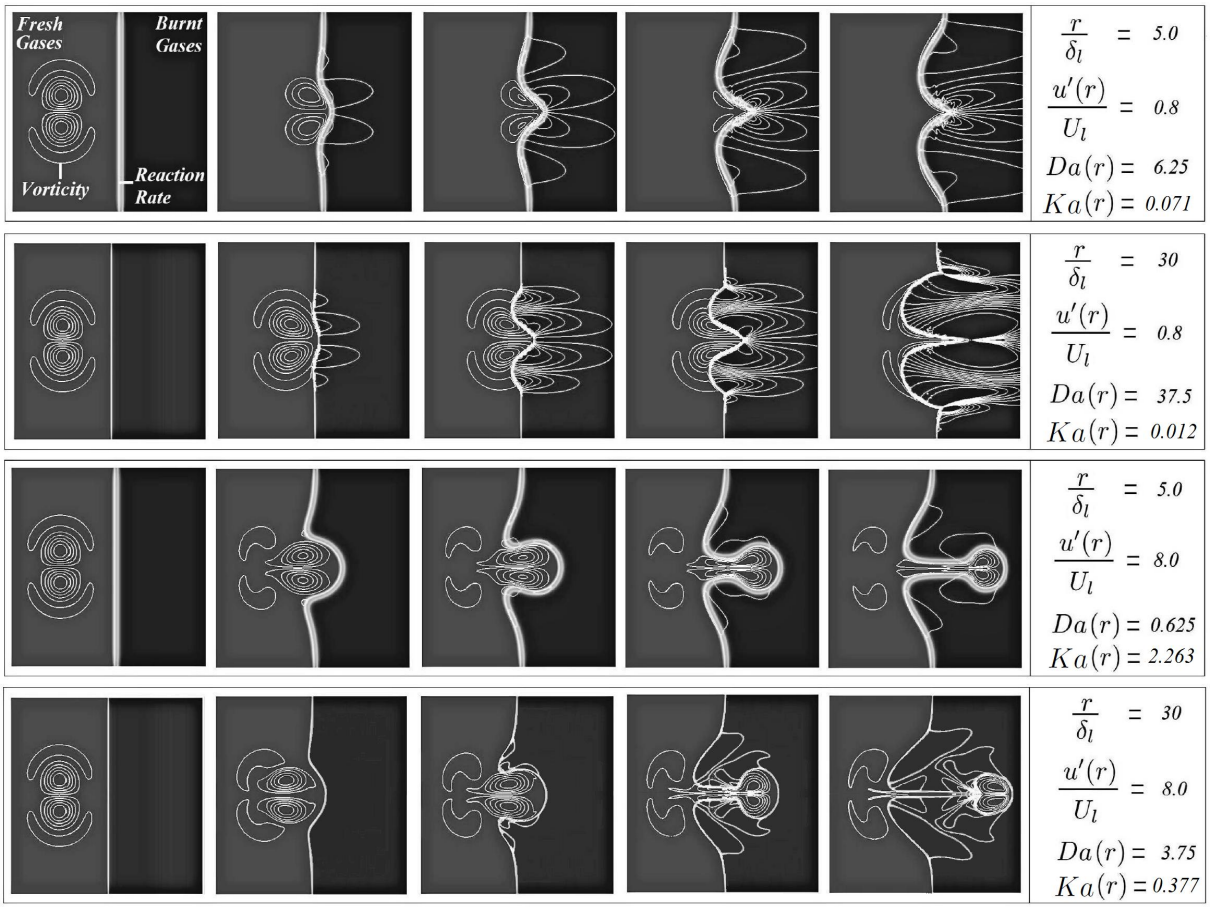

Figure 2.8: Snapshots of direct numerical simulations of flame-vortex interactions for different velocity and lenght scales ratii u'/U_l and r/l_t. Reaction rate and vorticity fields are superposed at different instants. Fuel = methane and fuel/air equivalence ratio $\varphi = 0.7$. Details of the study corresponding to these DNS results are presented in Chapter 8.

and the squish. These characterization of the main aerodynamic flow in the chamber is useful to develop mixing strategies and to globally identify the turbulence level in the chamber. As it will be presented in Chapter 3, in SI engines, swirl and squish contributions to the main aerodynamic flow can be generally neglected in favor of the tumble motion.

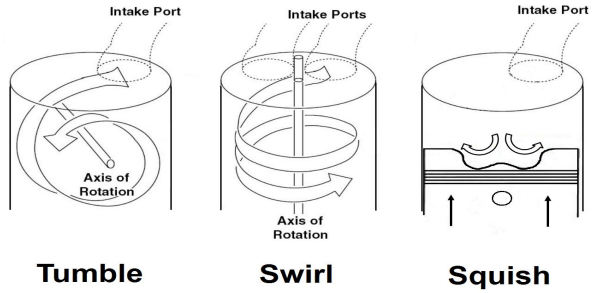

Figure 2.9: The three main aerodynamic motions identified in IC engine chambers.

From global geometrical considerations, the main turbulence characteristics u' and l_t are typically in the range: $1 < u'/U_l < 10$ and $10 < l_t/\delta_l < 100$. According to the spectral diagram displayed in Figure 2.7, it perfectly corresponds to the flamelet domain and more particularly to the thin wrinkled flame domain. In reality, u' and l_t can be higher as shown in Figure 2.10 which displays levels of $(l_t/\delta_l\ ,\ u'/U_l)$ for a IFPEn's SI engine burning gasoline. These results were obtained from engine simulation using the model presented in Chapter 3. The methodology used to estimate u' and l_t will be presented in Chapter 4. These last observations are very useful to set up combustion model assumptions and will be used to justify in the following that the flame can be supposed to be infinitely thin compared to all flow turbulence structures. However, as it can be observed in Figure 2.10 future engines with high downsizing levels are expected to run in operating zones not considered yet by current modeling functions describing U_T. Developments have therefore to be performed to describe the flame/turbulence interaction at high turbulence levels ($Da \approx 1$). Chapter 8 presents a new function aiming at improving the description of the turbulent flame stretch at high u'/U_l ratii when varying the fuel composition.

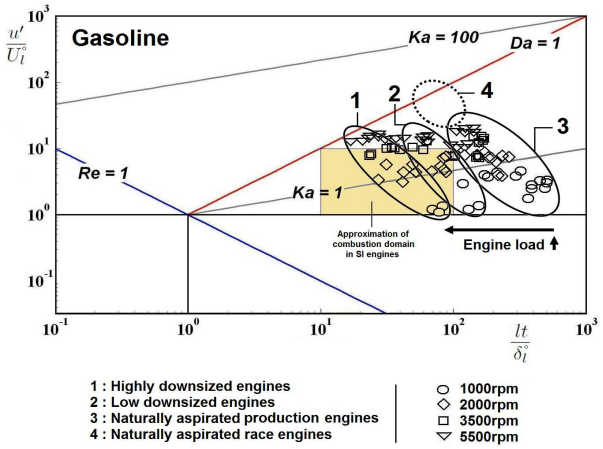

Figure 2.10: Operating domain of an IFPEn's SI engine burning gasoline at different engine speeds and loads. Min and max values of $(l_t/\delta_l\ ,\ u'/U_l)$ reached during an engine cycle are presented.

Remark: It should be noticed that although the combustion diagrams previously presented can be

very helpful to have an idea of interactions between the flame and turbulence, they should be taken with care as pointed out by Veynante and Vervisch (2009). Indeed, quantitative results should not be concluded from that diagrams for several reasons:

- *Frontiers between zones are only indicative. Transitions between regimes stay unclear.*
- *Physical variables used in these diagrams are not easy to define in real situations.*
- *The response time of the flame is not accounted for and the transitional behavior of the flame can be different from behaviors observed in diagrams in the same conditions.*
- *The turbulence is supposed to be homogeneous and isotropic (HIT) which is a strong assumption and which is generally not the case in IC engines.*

2.3 Auto-ignition

The auto-ignition (AI) of a turbulent mixing flow is a problem of fundamental importance and practical interest. Regarding IC engines, as mentioned in Introduction (Chapter 1), the development of SI engines limited by knocking phenomena (in term of performance, efficiency and pollutant emissions) can be significantly facilitated by a better understanding and ability to predict auto-ignition in the combustion chamber where thermodynamics, flow and composition conditions highly fluctuate.

Auto-ignition is a phenomenon in which a mixture of fuel and oxidizer brought at a sufficient temperature and pressure spontaneously ignites. In the last century many works aimed at determining the "autoignition temperature" of a combustible mixture. However, most studies use today the "auto-ignition delay time" associated with a set of initial conditions for the fresh gases temperature (T_u), pressure (P) and composition (equivalence ratio ϕ and dilution mass fraction Y^u_{res}). Auto-ignition can occur in both premixed and inhomogeneous conditions either in a stagnant field or in laminar or turbulent flow field. As a consequence, the development of numerical models aiming at solving auto-ignition physics requires a fine understanding of chemical processes, thermodynamics as well as turbulence mechanisms mixing and bringing together reactants and radical pool necessary for reaction. Despite a consistent number of works (Burwell and Olson 1965, Cowell and Lefebre 1987, Ducourneau 1974, Spadaccini 1977, Mizutani and Takada 1999, Stringer et al. 1969) studying the effects of the aforementioned processes, there is not a strong consensus regarding the effects of turbulence on auto-ignition. As an example Stringer et al. (1969) concluded that the influence of turbulence was insignificant on the contrary of Mizutani and Takada (1999) who state that autoignition delays were increased by strong turbulence, at least for a certain temperature range.

A simple Arrhenius formulation is often used to define the auto-ignition delay. This approach infers from the analysis of thermal explosion of a homogeneous mixture in a closed vessel (Semenov 1940). In such a configuration the combustion is supposed isobaric and the chemistry is assumed to be described by a one-step Arrhenius chemistry defined by a reaction rate term proportional to $\exp(-T_a/T)$. T_a is the activation temperature related to the activation energy of the reaction E_a by $T_a = E_a/R$, where R is the universal gas constant. From this definition, an auto-ignition delay τ_{AI} during which the rate of change of all scalars is exponential and can therefore be written as (Guibet and Fautre-Birchem 1996):

$$\tau_{AI} = f(P, Y_i) \exp\left(\frac{T_a}{T}\right) \tag{2.60}$$

where f is a function of pressure P and composition through the species mass fractions Y_i.

Formulation of Eq. 2.60 allows describing the slow evolution of chemistry at the beginning of combustion and the strongly self-accelerating behavior of the auto-ignition at later times (called as "thermal runaway"). Many works (Benson 1981, Griffiths and Scott 1987, McKay 1977, Simmie 2003) proposed approaches different from the single-step Arrhenius description of thermal explosions. In these studies emphasis rests on the study of the slow chemical paths and shifting explosion limits of the so-called "multiple ignitions" and "cool flames".

In this thesis two approaches are considered for the modeling of auto-ignition phenomena in SI engines. The first one is based on a phenomenological model computing an ignition delay through an Arrhenius formulation equivalent to 2.60 and a specific auto-ignition intensity through an empirical function. This model is presented in Chapter 4. The relative simplicity of the previous approach makes the prediction of AI phenomena limited to the study of knock occurrence (no specific heat release due to AI is computed) and cannot be used neither to precisely predict AI processes taking place in CAI applications (see Chapter 1) nor to account for fuel composition effects on these processes. A second approach has thus been developed in this thesis and is based on the tabulation of AI progress variable reaction rates and delays. This new model is presented in Chapter 7. Moreover, a short review of 0D auto-ignition models is proposed in Chapter 3.4.

2.4 Pollutants

Regarding environmental constraints and regulations (see Chapter 1), developing clean eco-aware power-systems has become one major and overarching challenge of the car industry. Considering the fast growth of numerical tools, the development of models able to predict emissions levels at the engine exhaust is today a crucial issue. In the case of SI engines, the gas composition at the exhaust is mainly constituted by N_2, CO_2, H_2O, oxides of nitrogen (nitric oxide, NO and small amounts of nitrogen dioxide, NO_2 - collectively known as NOx), carbon monoxide (CO), and organic compounds which are unburnt or partially burnt hydrocarbons (HC). This composition which depends on the engine design, operating conditions and fuel composition generally differ from composition calculated assuming the chemical equilibrium. As a consequence, the prediction of exhaust gases composition requires to finely describe kinetic processes involved in pollutant formation. Many complex chemistry schemes built-up with hundreds of species and hundreds or thousands of reactions are available and will be presented in the following (Chapters 5 and 6). Nevertheless, regarding the computational resources required to solve such systems, coupling these schemes with current fluid mechanics models (RANS, LES, DNS) is still impossible today. As a consequence, several alternative approaches are generally used to approximate the main chemical paths stepping in pollutant formation. These approaches are generally based on the reduction of complex mechanisms or on the direct use of simple chemistries. Finally, relatively new approaches consist in tabulating data (composition, characteristic times, etc.) obtained from *a priori* calculations of chemical reactors using complex kinetic schemes. These approaches are considered and developed in this thesis and are presented in Chapters 5 and 6. Whatever the approach used, well understanding physical and chemical mechanisms occurring in the combustion chamber to provide predictive models is essential. Indeed, for some species like CO the formation and destruction reactions are intimately coupled with the primary combustion process. Thus an understanding of the formation of these species requires knowledge of the combustion chemistry and its interaction with turbulence processes as seen in section 2.2. On the other hand, for species like NOx, the formation and destruction reactions are not part of the fuel combustion process but take place, in the case of SI engines, downstream the flame, in the burnt gases (post-oxidation process). However, the burnt gases zone being created by the flame propagation, post-oxidation, as all other processes in the chamber, is still directly linked to the combustion one. In the following, global descriptions of mechanisms implied in the formation of NOx, CO and HC in SI engines are briefly summarized.

Remark: With regards to numerical simulation, the challenge of emissions reduction also lies in the very low pollutant levels to predict (compared to the main species – $fuel$, O_2, N_2, CO_2,

H_2O– levels) which are for example of the order of hundreds ppm for NO molar fraction and some percents for CO.

CO formation

Carbon monoxide emissions are mainly controlled by the fuel/air equivalence ratio φ. As shown in Figure 2.11, the CO exhaust level is known in SI engines to be relatively constant (1% of molar fraction) for poor-fuel mixtures and increases steadily with increasing equivalence ratii for rich mixtures. Most SI engines are developed to operate close to stoichiometric conditions. Moreover, enrichment is often performed at high loads to decrease the exhaust temperature and to preserve thus exhaust systems. As a consequence CO emissions are often significant and must be controlled.

Carbon monoxide is produced during the combustion process from the partial oxidation of carbon-containing compounds when there is not enough oxygen to produce carbon dioxide CO_2. It is also produced in the high temperature products (post-oxidation), behind the flame through chemical dissociation mechanisms of carbon-containing molecules even in lean mixtures. Moreover, during the expansion stroke, the CO oxidation process also freezes as the burnt gas temperature falls and leaves CO concentrations far in excess compared to equilibrium at exhaust conditions. Actually, the levels of CO observed at the exhaust (i.e. at the exhaust valve opening (EVO)) are lower than the maximum values reached during combustion. Indeed, kinetic processes controlling the chemistry of CO, make these maximum levels finally decrease until the exhaust value which is higher than the equilibrium one as displayed in the schematic of Figure 2.12.

These kinetic processes are highly dependent on the temperature and pressure conditions. Therefore, as shown in Figure 2.12, at conditions close to peak cycle temperatures and pressure, kinetics is very fast and the equilibration times of CO are faster than characteristic times of changes in burnt gas conditions due to compression or expansion. Thus, the carbon-oxygen-hydrogen system is equilibrated which means in other terms that CO concentrations are close to equilibrium. Then, as the burnt gases cool during the expansion and exhaust strokes, the CO oxidation process is not equilibrated any more. The prediction of such kinetic mechanisms require adapted complex chemical schemes which need as inputs a precise estimation of local thermodynamic conditions at all locations of the chamber but also the knowledge of the CO formation history from ignition to the exhaust stroke. Indeed, as shown by dedicated studies (Delichatsios 1972, Keck and Gillespie 1971, Heywood 1988) the burnt gases zone can not be considered as an homogeneous domain. As shown in Figure 2.13, at the beginning of the combustion process first elements of fresh gases are consumed and change into burnt gases elements. These first elements, produced at high temperature and pressure, are characterized by relatively high levels of CO and burnt gases temperature T^b. Then, new elements of fresh gases are burnt and new burnt gases elements with lower levels of CO and T^b are produced behind the flame moving the previous elements and so on. As a consequence, if mixing between gas elements which burnt at different times is neglected, the burnt gases can finally be seen as a set of several part defined by a own composition and kinetic dynamics.

NOx formation

Among species constituting NOx (NO, NO_2, N_2O, etc.), nitric oxide NO is predominant inside the engine combustion chamber at stochiometry. As a consequence, in the following, NOx will be implicitly assimilated to NO. Similarly to CO, NO formation is strongly controlled by the equivalence ratio. As shown in Figure 2.14, a maximum is reached for a fuel/air equivalence ratio $\varphi \approx 0.9$ even if maximum in-cylinder temperatures are generally obtained for $\varphi \approx 1.1$. Indeed, NO is known to be highly dependent on the temperature but at this equivalence ratio the oxygen concentrations are low. $\varphi \approx 0.9$ represents therefore a compromise between temperature level and

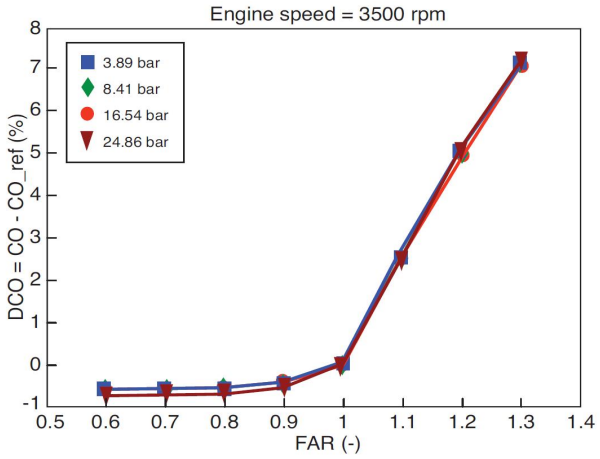

Figure 2.11: Typical evolutions of CO concentrations in SI engines as function of the fuel/air equivalence ratio (FAR) for different engine loads. Presented results were obtained from 0D simulations using the CFM1D model validated against a wide range of engine operating conditions. More precisions are given in Chapter 4. CO_{ref} corresponds to the level of CO at stoichiometry ($FAR = 1.0$).

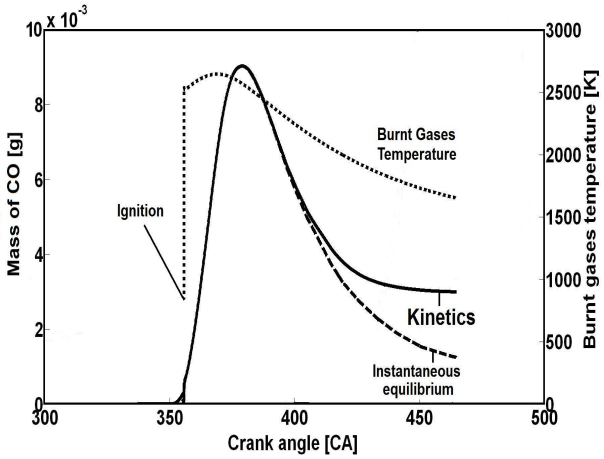

Figure 2.12: CO mass variations during an engine cycle when considering an actual evolution (kinetics) and an instantaneous CO oxidation process (equilibrium) as function of the crank angle. Indicated Mean Effective Pressure (IMEP) = 1.5 MPA, Engine speed = 3000 rpm. Presented results were obtained from 0D simulations using the CFM1D-TC model validated against a wide range of engine operating conditions. More precisions are given in Chapter 6.

available oxygen atoms.

Nitric oxide forms throughout the high-temperature burnt gases behind the flame through chemical reactions involving nitrogen and oxygen atoms and molecules, which do not attain chemical equilibrium. As for CO formation in the burnt gases, during the expansion stroke, as the burnt gases cool, reactions involving NO freeze and leave NO concentrations far in excess compared to equilibrium at exhaust conditions. As mentioned in the introduction of the section, there are several ways to form NO pollutants which can be summarized here:

- Flame-generated NO is produced in the flame front in short times. In IC engines, combustion occurs at high pressure so that the flame reaction zone is extremely thin and residence time within this zone is short.
- Fuel-bound NO is produced by nitrogen N_2 species in the fuel reacting with air during combustion. Regarding IC engines, both gasoline and diesel fuels contains only negligible amounts of nitrogen even if this level can be increased when the fuel is diluted (by nitrogen for example).
- Thermally-generated NO is formed by oxidation of nitrogen in air and requires sufficient temperature and time.

In SI engines, the main part of NO is produced in the burnt gases under high temperatures ($2000K < T^b < 3000K$) and the two first contributions can be neglected compared to the last one. This last assumption allows, in the case of NO modeling, to suppose that the combustion and post-oxidation processes can be decoupled. Besides, in comparison with CO formation mechanisms a similar description of kinetics in the burnt gases can be assumed here to understand NO formation processes (see previous paragraphs and Figure 2.13). As a consequence, a figure similar to Figure 2.12 can be presented here to show the differences between actual (kinetics) and instantaneous (equilibrium) chemical ways to produce NO. It can be noticed here that NO freezes earlier than CO.

The most common mechanism used for the description of NO formation is the so-called extended Zel'dovitch mechanism (Bowman 1975, Lavoie et al. 1970) based on a set of 3 reversible reactions:

$$\begin{aligned} O + N_2 &\rightleftharpoons NO + N \\ N + O_2 &\rightleftharpoons NO + O \\ N + OH &\rightleftharpoons NO + H \end{aligned} \tag{2.61}$$

This system is then solved using the kinetic constants $K_i^{+/-}$ of the different equations i, where indexs $+$ refers to the forward direction and $-$ to the reverse one. The evolution of NO molar concentration $[NO]$ is then estimated as:

$$\begin{aligned} \frac{d[NO]}{dt} &= K_1^+ [O][N_2] + K_2^+ [N][O_2] + K_3^+ [N][OH] \\ &\quad -K_1^1 [NO][N] - K_2^+ [NO][O] - K_3^+ [NO][H] \end{aligned} \tag{2.62}$$

Kinetic constants $K_i^{+/-}$ are taken from (Heywood 1988) and defined in Table 2.2 which also present temperature validation ranges for each reaction. The evolutions of N_2, N, O_2, O, H and

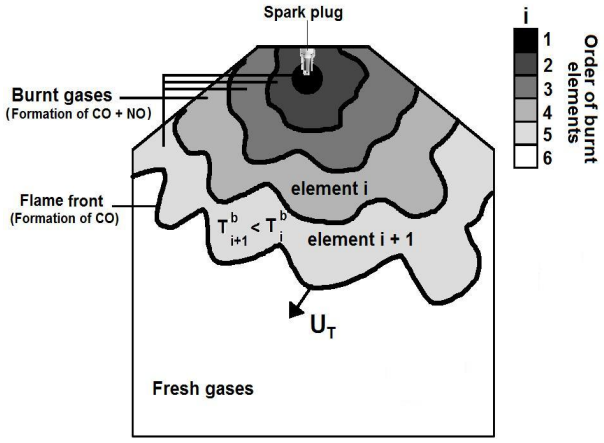

Figure 2.13: Schematic description of burnt gases heterogeneities formation.

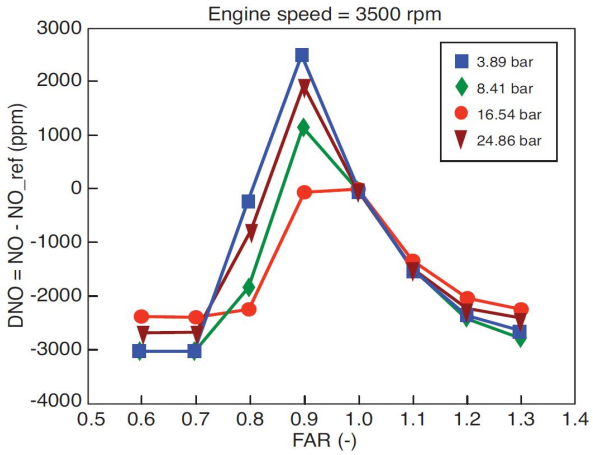

Figure 2.14: Typical evolutions of NO concentration in SI engines as function of the fuel/air equivalence ratio (FAR) for different engine loads. Presented results were obtained from 0D simulations using the CFM1D model validated against a wide range of engine operating conditions. More precisions are given in Chapter 4. NO_{ref} corresponds to the level of NO at stoichiometry ($FAR = 1$).

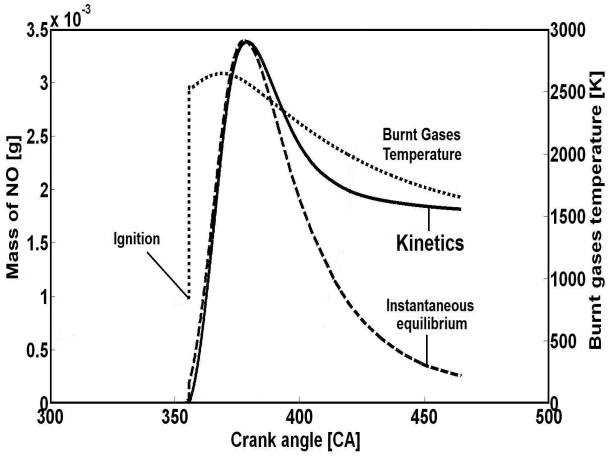

Figure 2.15: NO mass variations during an engine cycle when considering an actual evolution (kinetics) and an instantaneous NO oxidation process (equilibrium) as function of the crank angle. Indicated Mean Effective Pressure (IMEP) = 1.5 MPA, Engine speed = 3000 rpm. Presented results were obtained from 0D simulations using the CFM1D-TC model validated against a wide range of engine operating conditions. More precisions are given in Chapter 6.

OH are also taken into account using the set of equations 2.62. Considering that $[N]$ is much less than the concentrations of other species, the steady-state approximation can be considered and $d[N]/dt$ can be set to zero. Moreover, as combustion and post-oxidation processes can be decoupled, the concentrations of N_2, O_2, O, H and OH can be approximated to their equilibrium values at the local pressure and equilibrium temperature. Using both previous assumptions and K_1^+ value from Table 2.2, equations 2.62 lead to the expression for the initial NO formation rate (when $[NO]/[NO]_{eq} << 1$, with $[\cdot]_e$ denotes equilibrium concentration) as shown by Heywood (1988):

$$\frac{d[NO]}{dt} = \frac{6.10^{16}}{T^{1/2}} \exp\left(\frac{-69.09}{T}\right) [O_2]_e^{1/2} [N_2]_e \quad mol/(cm^3 \cdot s) \tag{2.63}$$

This expression allows a direct visualization of the strong temperature dependence of NO formation.

Coeff.	Value $[mol/(cm^3 \cdot s)]$	Temperature range [K]
K_1^+	$7.6 \cdot 10^{13} \exp[-38000/T^b]$	$2000 - 5000$
K_1^-	$1.6 \cdot 10^{13}$	$300 - 5000$
K_2^+	$6.4 \cdot 10^9 T^b \exp[-3150/T^b]$	$300 - 3000$
K_2^-	$1.5 \cdot 10^9 T^b \exp[-19500/T^b]$	$1000 - 3000$
K_3^+	$4.1 \cdot 10^{13}$	$300 - 2500$
K_3^-	$2.0 \cdot 10^{14} \exp[-23650/T^b]$	$2200 - 4500$

Table 2.2: Kinetic coefficients for NO formation.

To conclude this part, pollutant prediction finally appears as a strongly 3-dimensional problem, requiring a fine description of turbulent combustion mechanisms and kinetics processes. However,

as mentioned in the introduction of this section, computational constraints make very difficult the solving of turbulent reactive flows coupling 3D approaches and complex chemistry. However, many approaches based on the use of mean levels of main thermodynamical variables have been proposed in the past and generally showed reasonable results as it will be seen in Chapters 4 and 5. Nevertheless, the increasing constraints on pollutant regulation and the fuel diversification policies require an improvement of the accuracy and precision of these approaches. Therefore, precisely predicting pollutant emissions using only the mean levels is not a simple task and adapted models need to be developed to better represent the physics occurring in the chamber. A new approach for the prediction of CO and NO is proposed in this thesis and is presented in Chapter 6.

Chapter 3

0-dimensional approaches for combustion modeling in IC engines

As mentioned in introduction, engine developments as well as basic sizing, design optimization, control or calibration are allowed by the use of very compact simulation tools based on very fast models. Indeed, such developments are performed treating a high number of cases likely to represent most operating engine conditions and requiring therefore very short return times. On the other hand, another time constraint could be imposed by the direct use of these tools in HiL (Hardware-in-the-Loop) test benches where the whole vehicle operations are virtually played demanding thus that these models run exactly in real-time. As a result, using 3D CFD tools to solve this kind of problems remains impossible today motivating for a while the use of 0-dimensional models basically built on the resolution of 0D thermodynamic equations for enthalpy and mass conservation. This chapter aims at proposing a review of main 0-dimensional approaches for system simulation tools with regards to IC engines developments.

3.1 Heat release modeling

Applying the first principle of thermodynamics to an open system, the enthalpy balance for the combustion chamber can be written as:

$$\frac{dmh}{dt} = V\frac{dP}{dt} + \frac{dQ_{comb}}{dt} - \frac{dQ_{wall}}{dt} + \sum_{in,out} h_j \frac{dm_j}{dt} \tag{3.1}$$

where V is the cylinder volume, h is the mass enthalpy, m is the enclosed mass and P is the pressure which is linked to the mean temperature T by the perfect gas law. The last term of Eq. 3.2 refers to enthalpy exchanges at the inlets and outlets (valves, injector). Q_{wall} corresponds to heat losses at the walls which are generally described with the Woschni model (Woschni 1697) presented in Section 3.6 and Q_{comb} is the heat released by combustion processes. First heat release models were based on simple empirical mathematical laws. The reference of these models is the Wiebe empirical functions (Wiebe 1956). It provides a mathematical function defined through two parameters (Q_{pr}, premixed combustion reaction rate and Q_{df}, diffusion reaction rate) allowing to directly represent the combustion reaction rate Q_{comb} for both SI and Diesel applications and

leading to the following relation:

$$\frac{dQ_{comb}}{d\theta} = \frac{dQ_{pr}}{d\theta} + \frac{dQ_{df}}{d\theta} \tag{3.2}$$

with

$$\frac{dQ_{pr}}{d\theta} = f \cdot Q_{comb} \cdot \frac{1}{\Delta\theta} \cdot a_{pr} \cdot (m_{pr}+1) \cdot y^{m_{pr}} \cdot e^{-a_{pr}} \cdot y^{m_{pr}+1} \tag{3.3}$$

and

$$\frac{dQ_{df}}{d\theta} = (1-f) \cdot Q_{comb} \cdot \frac{1}{\Delta\theta} \cdot a_{df} \cdot (m_{df}+1) \cdot y^{m_{df}} \cdot e^{-a_{df}} \cdot y^{m_{df}+1} \tag{3.4}$$

where:

- f: mixture fraction,
- $Q_{comb} = Q_{pr} + Q_{df}$: total heat release computed as $Q_{comb} = LHV \cdot m_{fuel}$, where LHV is the lower fuel heating value and m_{fuel} is the total mass of fuel,
- $y = \frac{\theta - \theta_{ignit}}{\Delta\theta}$: reduced crank angle,
- θ: crank angle,
- θ_{ignit}: crank angle corresponding to the combustion beginning,
- $\Delta\theta$: combustion delay parameter fixed by the user,
- a_{pr} and a_{df}: Wiebe's coefficients respectively for the premixed and diffusion phase,
- m_{pr} and m_{df}: Shape factors respectively for the premixed and diffusion phase.

Such a model was initially developed to reach very low computational times but has the major drawback to be poorly predictive. Indeed, in this model, the heat release shape is fixed making difficult to reproduce very different engine operating conditions (engine speed, engine load, etc.) or set-up (equivalence ratio, ignition timing, etc.) which can lead to very different heat release evolutions. As an example, Figure 3.1 displays experimental measurement of heat release as function of crank angle highlighting the inability to use such a fixed heat released shape model as a generic tool for engine development. However, a solution consists in mapping or learning through acquisition methods (such as neuronal networks) the Wiebe's coefficients (a_{pr}, a_{df}, m_{pr}, m_{df}) as function of engine operating conditions and set-up. The problem of such methods is that they require a very high number of experimental data which can not be always available in advance. Moreover, resulting maps can be very different from an engine to another one thus increasing the number of needed experimental data. Finally, it should be noticed that the shape of the heat release remains nonetheless imposed and driven by the empirical law which is not based on physics and which is therefore not expected to be adapted to the modeling of highly complex phenomena taking place in engine combustion chambers.

In this context, phenomenological approaches have known a particular rise in the last decade. These approaches are built on models expected to reproduce macroscopic phenomena through simple equations or functions. In such models the heat release is described through physical variables representing for example the effects of turbulence on combustion or flame/walls interactions. A non-exhaustive list of main works on such models comprises Tabaczynski et al. (1977), Poulos and Heywood (1983), Bozza et al. (Bozza et al. 2001, Bozza and Gimelli 2004, Bozza et al. 2005), Nishiwaki (2008), for spark ignition (SI) engines or Chelma and Orthaber (1999), Barba et al. (2000), Arsie et al. (2005) and Rakopoulos and Hountalas (2000) for Diesel applications. Nevertheless, the description of fuel oxidation processes by these approaches is generally not based on

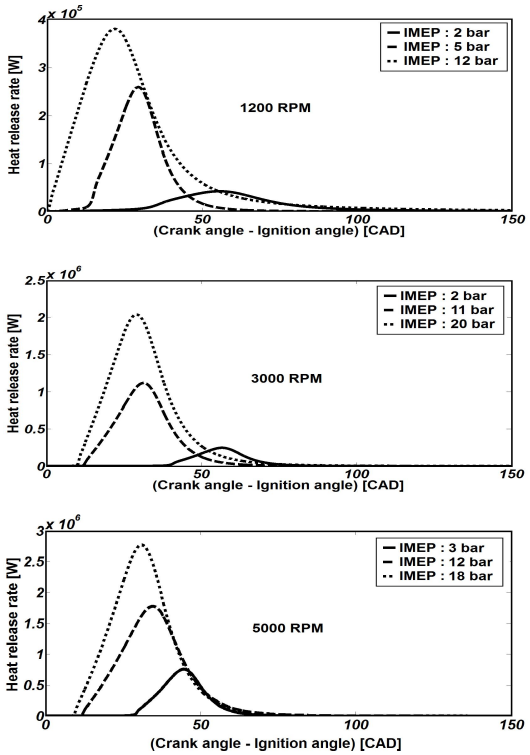

Figure 3.1: Experimental heat release evolutions as function of the crank angle and for different engine speeds and loads. Results were obtained from an IFPEn single-cylinder SI engine (internal source).

theoretical bases and cannot allow a precise description of combustion processes, like, for example, the evolution of the flame surface in SI applications, or the spray zone in Diesel ones. It can be cited here the "turbulent entrainment model" of Bozza et al. (2001) where the total burning rate due to the combustion process is written distinguishing laminar from turbulent processes as:

$$\left.\frac{dm_b}{dt}\right|_{tot} = \omega_1 \rho_u A_l U_l + \omega_2 \rho_u A_T U_l + \omega_3 \frac{m - m_b}{\tau_{turb}} \tag{3.5}$$

with

$$\tau_{turb} = l_t / u' \tag{3.6}$$

where m_b is the burnt mass of gases, m the total mass of gases, A_l and A_T respectively the laminar and turbulent flame surfaces, U_l the laminar flame velocity, l_t the integral length scale, u' the turbulent velocity fluctuation and $\omega_{1,2,3}$ adjustable parameters weighting the three contributions and which have to be fitted.

Such a model allows to describe the propagation of a flame front from a flame kernel growing at the laminar propagation velocity to a fully developed turbulent combustion. The turbulent flame velocity U_t is described through a model based on a fractal schematization of the flame surface (Bozza et al. 2005,Bozza et al. 2007,Matthews and Chin 1991,Barratta et al. 2005) (as presented in the following) where the turbulent flow field is supposed to wrinkle an infinitesimally thin flame front in a "self-similar" manner. The third term of Eq. 3.5 accounts for the burning rate decay at the end of the combustion process through a simple exponential law, function of turbulent main characteristics l_t and u'.

Thereafter, several works (Hiroyashu et al. 1983, Egnell 1998, Patriotis et al. 2006, Hountalas et al. 2002, Arregle et al. 2006, Jung and Assanis 2001, Assanis and Heywood 1986) introduce multi-zones approaches consisting in splitting the integration domain (combustion chamber) into several zones. These approaches allow to improve the modeling precision compared to a single zone model and are generally used to describe the charge inhomogeneities which can be significant in the case of Diesel or stratified combustion SI engines. The most famous works have been performed by Hiroyashu et al. (1983) who temporally discretized the injected spray into several iso-mass packets which are then individually followed in the chamber. Despite interesting results – the pollutant prediction are for example improved thanks to a better description of local thermodynamic conditions (temperature, equivalence ratio) – the multi-zone approaches remain not adapted to present engine development problems in particular because of the relatively high computational resources required. Indeed, such approaches often demand an important number of zones n (typically $n > 20$) all requiring the solving of energy, mass and species conservation equations. As a result, the corresponding CPU times can reach levels close to 2D or even 3D CFD simulation CPU times. Moreover, the high number of modeling parameters to adjust (such as $\omega_{1,2,3}$ in Eq. 3.5) makes difficult the use of such approaches in practical applications.

The high CPU times required by multi-zone models combined with the lack of predictivity of phenomenological approaches motivated the development of refined physical laws for the heat release derived from the reduction of 3D combustion models (Mauviot et al. 2006, Dulbecco 2009, Lafossas et al. 2005, Richard et al. 2009, Kwon et al. 2011). In the Diesel context, developments concerned the integration of tabulation approaches deduced from formalisms like the Tabulated Kinetics for Ignition method (TKI) (Colin et al. 2005) for auto-ignition phenomena or the Flame Prolongated of ILDM method (FPI) (Gicquel et al. 2000, Ribert et al. 2006) for species evolutions. These tabulation approaches are very efficient regarding 0D modeling since they allow to improve the description of chemistry decreasing required CPU times. However, these methods consider as inputs several parameters as the local temperature, pressure or composition and can finally lead to significant errors if only mean values of these variables are used especially in stratified combustion cases where heterogeneities are high. Developments were therefore achieved to account for inhomogeneities in combustion chambers integrating statistical methods initially developed for RANS or LES. These latter allow indeed to refine the representation of a physical variable Q describing its distribution by a presumed probability density function (PDF) $P(Q)$ (for example a Gaussian or a β-function (Vervisch et al. 1995) as function of the mean values of Q, $\tilde{Q}$, and its variance, $\tilde{Q}''^2$ (Bilger 1993, Klimenko 1995, Bradley et al. 1990, Peters 2000). These approaches have the advantage of being easy to couple with a 0D model since the mean values of variables such as temperature, pressure or composition are known. Nevertheless, modeling efforts are needed to estimate the variances of these parameters, which represent one of major challenges for future 0D combustion models. For SI applications, main works concerned the reduction of the Coherent Flame Model (CFM) (Candel and Poinsot 1990, Colin et al. 2003, Richard et al. 2007) dedicated to the flamelet regime (see Chapter 2) by Lafossas et al. (2005) and Richard et al. (2009) who derived the basis of the associated reduced combustion model CFM1D. This model - which will be detailed in Chapter 4 - is well adapted to premixed and partially premixed combustion processes, representing the main oxidation mechanisms in SI engines. The CFM formalism distinguishes two zones: fresh and burnt gases which are separated by a flame front propagating from the burnt gases towards the fresh mixture. Chemical reactions of fuel oxidation occurs in a very thin layer (the flame front) compared to all scales of the turbulent flow and post-flame chemistry takes place in the burnt gases. Each zone is described by its mass, volume, composition and temperature. Reduced equations of species and enthalpy conservation are solved and the total heat release Q_{comb} by chemical processes in the chamber is finally written:

$$\frac{dQ_{comb}}{dt} = \sum_i h_{f_i} \left(\left.\frac{dm_i}{dt}\right|_{ff} + \left.\frac{dm_i}{dt}\right|_{pf} \right) \tag{3.7}$$

where h_{fi} is the formation enthalpy of specie i, $dm_i|_{ff}$ and $dm_i|_{pf}$ are the mass variations of

this species respectively in the flame front and in the burnt gases due to post flame chemistry reactions. These variations are coupled with pollutant formation processes and will be detailed further in Chapters 4, 5 and 6. However, it can be noticed here that the first RHS term of Eq. 3.7 $dm_i|_{ff}$ – which is the main contributor to the calculation of dQ_{comb} – is explicitly dependent on the turbulent flame velocity U_T through the turbulent flame surface A_T as (for the fuel):

$$\left.\frac{dm_{fuel}}{dt}\right|_{ff} = \rho_u Y^u_{fuel} U_l A_T \tag{3.8}$$

where ρ_u is the fresh mixture density and Y^u_{fuel} is the mass fraction of fuel in the fresh gases (the mass fraction of fuel in the burnt gases Y^b_i is assumed here equal to zero).
Damköhler (Damköhler 1940) described A_T as function of U_T through the flame wrinkling Ξ as:

$$\Xi = \frac{U_T}{U_l} = \frac{A_T}{A_l} \tag{3.9}$$

where U_l and A_l respectively represent the laminar flame velocity and surface defined in Chapter 2.
A simple phenomenological law proposed by Damköhler (1940) is typically used to describe Ξ as function of the turbulent flow velocity fluctuation u' and laminar flame speed given by:

$$\frac{U_T}{U_l} \approx 1 + C\frac{u'}{U_l} \tag{3.10}$$

Zimont (2000), Peters (2000) or Gülder (1990), proposed to introduce the effect of turbulent length scales in their models, in order to account for the various combustion regimes (Peters 1999). For this purpose, the two latter directly implemented the Damköhler number Da in the U_T expression:

$$\frac{U_T}{U_l} \approx 1 + (Da)^{0.25}\frac{u'}{U_l} = 1 + \left(\frac{lt}{\delta_l}\frac{U_l}{u'}\right)^{0.25}\frac{u'}{U_l} \tag{3.11}$$

where l_t is the turbulent integral length scale and δ_l is the laminar flame thickness.

The previous expression, substituted in Eq. 3.8, allows to compute the mass burning rate, once the laminar flame velocity and surface are properly evaluated. The laminar flame velocity U_l is generally defined by empirical correlations as function of the fuel characteristics, in-cylinder pressure, unburnt gas temperature, air-fuel ratio and fraction of trapped burnt gas products (see Chapter 2). The laminar flame surface A_l can also be easily determined through a numerical procedure which computes the intersections between the inflamed volume, assumed of mean spherical shape, and the combustion chamber walls. This numerical procedure can be developed for simple geometries like a pancake, a hemispherical or a centered bowl-in-piston combustion chamber. When a more complex geometry has to be analyzed, a 3D representation of the actual chamber can be imported in parametric CAD software (see Figure 3.2) and an automatic procedure can be developed, which defines, at each crank angle, all the possible positions of the flame within the cylinder. At each piston position the intersections of the flame surface with the actual combustion chamber walls are identified by the CAD primitives for a number of flame radii, which also compute the inflamed volume and the burnt gases area. In this way a 2D (first direction : burnt gases volume ; second one : piston position) look-up table can be build once for the specified CAD geometry as shown in Figure 3.3. This table can be loaded by the numerical code and used on-line at each crank-angle to extract the flame surface as function of the current piston position and burnt gases volume (see Chapter 4).

Considering that U_l and A_l are well-defined, the above expression (Eq. 3.11) can nonetheless be insufficient to well-describe the flame wrinkling. Indeed, on the one hand, the description of

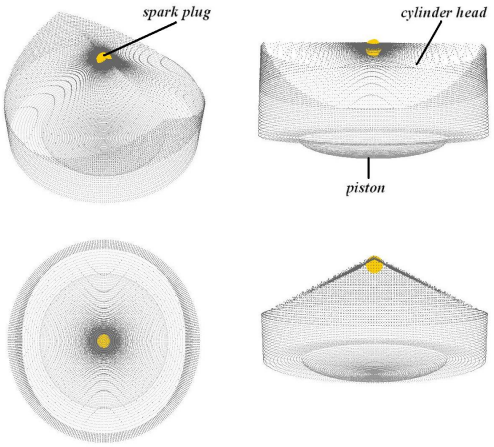

Figure 3.2: Simplified engine geometry obtained using a pre-processing tool developed at IFPEn for different burnt gases volumes and piston positions.

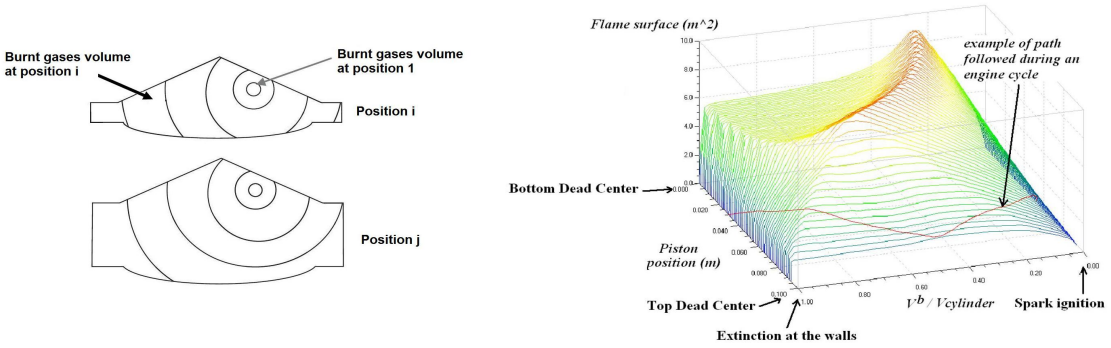

Figure 3.3: Principle of the mean flame surface tabulation.

interactions between the flame and turbulent flow can appear too simple compared to the high level of complexity of such processes and, on the other hand, it only depends on the turbulent flow and laminar flame properties although several experimental works (Lee et al. 1993,Wu et al. 1991,Goix and Shepherd 1993) suggests that flame stretch and differential diffusion have important effects on the local response and overall burning velocity of premixed flames. Such phenomenological descriptions of the flame wrinkling can therefore suffer from a lack of predictivity when dealing with engine applications where high turbulence levels and composition variations take place. A more physical description of the flame wrinkling represents therefore a missing link in the current heat release calculation and development of a more theoretical formulation for Ξ is therefore a crucial issue with regard to the present context of fuel diversification.
Under the assumption of a self-similar wrinkling within the length scales interval $L_{min} - L_{max}$, some authors (Bozza et al. 2005,Bozza et al. 2007,Matthews and Chin 1991,Barratta et al. 2005) proposed to describe Ξ through a fractal approach where the ratio A_T/A_l is written as:

$$\frac{A_T}{A_l} = \left(\frac{L_{max}}{L_{min}}\right)^{\alpha_{fractals}-2} \tag{3.12}$$

where $\alpha_{fractals}$ is the fractal dimension. In such an approach, the integral (l_t) and the Kolmogorov ($\eta_k = l_t/\left(u' l_t/\nu\right)^{3/4}$, see Chapter 2) length scales are usually chosen as the maximum (L_{max}) and the minimum (L_{min}) wrinkling scales (Bozza et al. 2006,Onorati et al. 2004). Bozza et al. (2006) written the fractal dimension $\alpha_{fractals}$ as function of the u' and U_l as:

$$\alpha_{fractals} = \frac{\alpha_1 u' + \alpha_2 U_l}{u' + U_l} \tag{3.13}$$

where $\alpha_1(\approx 2.35)$ and $\alpha_2(\approx 2.05)$ are adjustable parameters. Fractal approaches have the advantage of being easy to implement in engine codes and showed in the past promising results. However, the same reproach than phenomenological expressions previously presented (Eqs. 3.10, 3.11) can be made. Indeed, here also all mixture related effects are supposed to be only described by the laminar flame velocity U_l which is even more restrictive than expression of Eq. 3.11 which also accounts for the laminar flame thickness δ_l. Moreover, in such approaches, the flame wrinkling is considered to be at equilibrium i.e. the flame behaves as a fully developed turbulent flame. But, in engine combustion chambers, the ignition is almost laminar and the flame wrinkling growths during an important part of the flame propagation. Therefore, in order to account for this dynamics, severals authors (Bozza et al. 2007, D'Errico et al. 1996) add empirical transition functions depending on the flame kernel size or use weighting functions (as parameters $\omega_{1,2,3}$ in Eq. 3.5). Such approaches are not predictive especially when the engine load varies. In fact, these models are only valid at high loads where transitions between laminar and turbulent regimes are generally fast. To be more predictive, Nishiwaki (2008) proposed an equation to describe the evolution of the fractal flame surface for 3D CFD models but which could be adapted to 0D modeling. Another solution consists in deriving the CFM model to propose a reduced combustion model solving a transport balance equation for the unsteady turbulent flame surface. In this model called CFM1D model – developed at IFPEn (Richard et al. 2009) and presented in Chapter 4 – the flame wrinkling is deducted from the resolution of an equation for Ξ (see Chapter 8) obtained by reduction of the 3D CFD equation for the flame surface density balance (Richard et al. 2007) which writes:

$$\frac{1}{\Xi}\frac{d\Xi}{dt} = f_\Xi\left(l_t, u', U_l, \delta_l\right) \tag{3.14}$$

where f_Ξ is a function deducted from the 3D model and depending on l_t, u', U_l and δ_l. Regarding 0D modeling, no expression for f_Ξ have been developed yet to account for potential fuel composition effects (notably including thermo-diffusive instabilities) on the flame wrinkling. A particular attention need thus to be brought to the development of an accurate expression of f_Ξ. New approaches detailed in following chapters are therefore developed in the present thesis work and aim at integrating complex chemistry in the CFM1D model to improve the accuracy of the heat release calculated through Eqs. 3.8 and 3.14 to account for fuel composition variation effects.

3.2 Turbulence modeling

K-k model

As mentioned in Section 3.1, the determination of the flame wrinkling Ξ is a crucial issue regarding the prediction of the turbulent flame velocity and thus the heat release. Using simple phenomenological correlations such as Damköhler's one (Eq. 3.10) or a more physical description of Ξ (Eqs. 3.12 or 3.14) implies to be able to accurately estimate on the one hand the laminar flame characteristics (A_l, U_l and δ_l) and on the other hand the turbulence properties (u' and l_t). Considering that A_l, U_l, and δ_l are well-defined (see Sections 2.1 and 3.1) a particular attention has to be given to the evaluation of u' and l_t. For this purpose it is usual to introduce u'_{loc} the fluctuation of the local turbulent velocity u_{loc} defined as:

$$u_{loc} = < u_{loc} >_{V_{turb}} + u'_{loc} \tag{3.15}$$

where V_{turb} is a volume with a characteristic size l_t and the spatial filter $< \cdot >_{V_{turb}}$ is defined as:

$$< u_{loc} >_{V_{turb}} = \frac{1}{V_{turb}} \cdot \int_{V_{turb}} u_{loc} \cdot dV \tag{3.16}$$

If Eq. 3.15 is squared and filtered using operator 3.16, an equation for the kinetic energy density associated to the field u is obtained:

$$\underbrace{\frac{< u_{loc}^2 >_{V_{turb}}}{2}}_{total\ KED} = \underbrace{\frac{< u_{loc} >_{V_{turb}}^2}{2}}_{KED\ associated\ to\ the\ mean\ motion} + \underbrace{\frac{< u_{loc}'^2 >_{V_{turb}}}{2}}_{KED\ associated\ to\ the\ fluctuating\ motion} \tag{3.17}$$

(KED = kinetic energy density)

The second RHS term corresponds to the local turbulent kinetic energy density k_{loc} (see Figure 3.4):

$$k_{loc} = \frac{< u_{loc}'^2 >_{V_{turb}}}{2} \tag{3.18}$$

A characteristic dissipation rate can be associated to k_{loc} and will be noted ϵ_{loc}. Finally, the local kinetic energy density K_{loc} corresponding to the mean motion can be defined as (see Figure 3.4):

$$K_{loc} = \frac{< u_{loc} >_{V_{turb}}^2}{2} \tag{3.19}$$

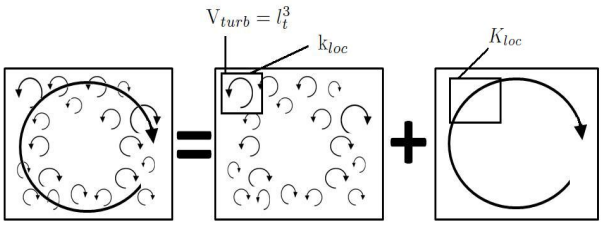

Figure 3.4: Schematic turbulence energy decomposition.

Finally assuming that the turbulent and mean kinetic energy densities are homogeneously distributed and that the gases density ρ is spatially constant, the total turbulent and mean kinetic energies in the combustion chamber write:

$$E_{kin,mean} = \int \rho K_{loc} dV = m_{tot} K_{loc} = m_{tot} K \tag{3.20}$$

$$E_{kin,turb} = \int \rho k_{loc} dV = m_{tot} k_{loc} = m_{tot} k \tag{3.21}$$

where m_{tot} is the total mass of gas in the combustion chamber, K and k ($= 3/2u'$) respectively the overall mean and turbulent kinetic energy densities in the combustion chamber.

These last two variables are generally computed considering a K-k approach (Poulos and Heywood 1983) based on a conservation equation of the mean flow and turbulent kinetic energies ($E_{kin,mean}$ and $E_{kin,turb}$ in the combustion chamber writing:

$$\frac{dE_{kin,mean}}{dt} = \underbrace{\frac{dE_{kin,mean,in/out}}{dt}}_{supplying\ term} - \underbrace{\frac{dE_{kin,transfer}}{dt}}_{transfer\ term} + \underbrace{\frac{dE_{kin,mean,density}}{dt}}_{density\ term} \tag{3.22}$$

$$\frac{dE_{kin,turb}}{dt} = \underbrace{\frac{dE_{kin,turb,in/out}}{dt}}_{supplying\ term} + \underbrace{\frac{dE_{kin,transfer}}{dt}}_{transfer\ term} + \underbrace{\frac{dE_{kin,diss}}{dt}}_{dissipation\ term} + \underbrace{\frac{dE_{kin,turb,density}}{dt}}_{density\ term} \tag{3.23}$$

The above relations allow to represent the 0D energy cascade as illustrated in Figure 3.5: mean flow kinetic energy is supplied to the cylinder through valves (supplying terms); mean kinetic energy is converted into turbulent kinetic energy through turbulent dissipation (transfer term), turbulent kinetic energy is converted to internal energy through viscous dissipation (dissipation term). Turbulent production terms (density terms) are finally integrated in Eqs. 3.22 and 3.23 to account for the in-cylinder density variation. In particular, in the Bozza et al. model (Bozza et al. 2005), the unburnt density variation is considered during the compression and combustion phases and the burnt gas one during the expansion stroke.

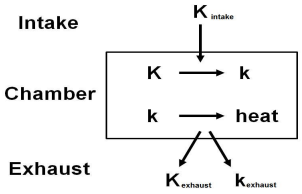

Figure 3.5: Turbulent energy cascade model. K: mean kinetic energy density; k: turbulent kinetic energy density

Then, defining:

- The rate of turbulent kinetic energy dissipation per unit mass $\epsilon =< \epsilon_{loc} >_{V_{0D}}$ linked to the dissipated energy (Eq. 3.23) as:

$$\epsilon \approx \frac{1}{m_{tot}} \cdot \frac{dE_{kin,diss}}{dt} \tag{3.24}$$

- A transfer function from the total kinetic energy into turbulent kinetic energy $T_{K \longrightarrow k}$ as:

$$T_{K \longrightarrow k} = \frac{1}{m_{tot}} \frac{dE_{kin,transfer}}{dt} \tag{3.25}$$

And assuming that:

- The mean kinetic energy supplied to the cylinder or lost through intake and exhaust valves can be expressed as:

$$\frac{dE_{kin,mean,in/out}}{dt} = c_{in} \frac{1}{2} \dot{m}_{in} {u_{in}}^2 + K \dot{m}_{out} \tag{3.26}$$

where $\dot{m}_{in}$ is the intake mass flow rate, u_{in} the gas velocity at the intake, $\dot{m}_{out}$ (< 0) is the exhaust mass flow rate and c_{in} a fitting parameter.

- The turbulent kinetic energy lost through exhaust valves can be expressed as:

$$\frac{dE_{kin,turb,in/out}}{dt} = (1 - c_{in})\,\frac{1}{2}\dot{m}_{in}{u_{in}}^2 + k\dot{m}_{out} \tag{3.27}$$

- The mean kinetic energy produced through density variations can be expressed as:

$$\frac{dE_{kin,mean,density}}{dt} = m_{tot}K \cdot \frac{\dot{\rho}}{\rho} \tag{3.28}$$

where $\dot{\rho}$ is the time derivative of the mean gas density ρ.

- The turbulent kinetic energy produced through density variations can be expressed as:

$$\frac{dE_{kin,mean,density}}{dt} = m_{tot}k \cdot \frac{\dot{\rho}}{\rho} \tag{3.29}$$

It results from Eqs. 3.22 and 3.23 the following system to solve for deducing u' from the turbulent kinetic energy density k (Eq. 3.18):

$$\begin{cases} \dfrac{dk}{dt} = T_{K\longrightarrow k} - \epsilon + k\dfrac{\dot{m}_{out}}{m_{tot}} + k \cdot \dfrac{\dot{\rho}}{\rho} \\ \dfrac{dK}{dt} = -T_{K\longrightarrow k} + \dfrac{1}{2}\dfrac{\dot{m}_{in}}{m_{tot}}{u_{in}}^2 + K\dfrac{\dot{m}_{out}}{m_{tot}} + K \cdot \dfrac{\dot{\rho}}{\rho} \end{cases} \tag{3.30}$$

To summarize, the solving procedure for u' and l_t (used as inputs of the calculation of the heat released by combustion, Q_{comb}, through the flame wrinkling Ξ (Eqs. 3.12 or 3.14)) directly depends on the way the production term $T_{K\longrightarrow k}$ (Eq. 3.25) and the dissipation rate ϵ (Eq. 3.24) are closed.

The most widespread 0D turbulence model was initially proposed by Mansouri et al. (1982) and developed by Poulos and Heywood (1983) and Bozza et al. (2005) who integrated the above equation system all over the engine cycle after having closed $T_{K\longrightarrow k}$ and ϵ as follow:

- The rate of turbulent kinetic energy dissipation per unit mass ϵ is closed considering the relation of Eq. 2.41 leading to:

$$\epsilon = \frac{(2/3k)^{\frac{3}{2}}}{l_t} \tag{3.31}$$

The integral length scale l_t was assumed proportional to a characteristic dimension of the combustion chamber as:

$$l_t = c_{l_t}V_{cyl}^{1/3} \qquad or \qquad l_t = c_{l_t}H \tag{3.32}$$

where V_{cyl} is the cylinder volume, H the instantaneous clearance height of the cylinder and c_{l_t} an adjustable parameter.

- Since the turbulence model does not spatially resolve the flow patterns, the production term, $T_{K\longrightarrow k}$, must be estimated from mean flow quantities. Assuming that turbulence production in cylinder is similar to turbulence production in a turbulent boundary layer over a flat plate, the works of Tennekes and Lumley (1972), Poulos and Heywood (1983) proposed to write $T_{K\longrightarrow k}$ as:

$$T_{K\longrightarrow k} \cdot m_{tot} = \mu_t \left(\frac{\partial u}{\partial y}\right)^2 \tag{3.33}$$

where $\mu_t = c_\mu k^2/\epsilon$ is the turbulent viscosity, $c_\mu = 0.09$ is a universal constant and u is the mean flow velocity defined as $\sqrt{2K}$. Since the velocity gradient in Eq. 3.33 is not known, they proposed to model it as:

$$\left(\frac{\partial u}{\partial y}\right)^2 = c_\beta \left(\frac{u}{l_t}\right)^2 \tag{3.34}$$

where c_β is an adjustable parameter. Combining Eqs. 3.19, 3.31, 3.33 and 3.34 results in the following expression for $T_{K \longrightarrow k}$:

$$T_{K \longrightarrow k} = 0.3307 \cdot c_\beta \cdot \frac{K}{l_t} \cdot \frac{k^{1/2}}{m_{tot}} \tag{3.35}$$

Using the 0D turbulence model previously presented coupled with the modeling closure of Eqs. 3.31 and 3.35, the turbulence characteristics u' and l_t required to estimate the flame wrinkling Ξ (Eqs. 3.11, 3.12, 3.14) can be finally computed. Nevertheless, this model requires to compute turbulent energy transfers all over the engine cycle solving a non-linear system (Eqs. 3.30, 3.31 and 3.35). Moreover considering the complexity of flow conditions in combustion chambers, the range of validity of such a model, based on the calibration of several fitting parameters (c_{in}, c_{l_t}, c_β), is often limited and is too heavy in practice.

A semi-predictive K-k model

An alternative to the previous model was developed by Lafossas et al. (2005) who proposed to compute the turbulent kinetic energy transfers only during the compression and expansion strokes. As a result, the supplying terms of Eqs. 3.22 and 3.23 can be removed since the valves are closed. Moreover, the density terms are neglected. Finally, the following modeling was used for ϵ and $T_{K \longrightarrow k}$ closures:

- A closure for the dissipation term ϵ of Eq. 3.19 was proposed by Chelma and Orthaber (1999) who considered that the kinetic energy injected in the combustion chamber is mainly dissipated by viscosity. Therefore, they closed ϵ by an empirical linear relaxation of the turbulent kinetic energy $E_{kin,turb}$ as:

$$\epsilon = C_{diss} \cdot E_{kin,turb}/m_{tot} = C_{diss} \cdot k \tag{3.36}$$

  where C_{diss} is a fitting parameter associated to the level of diffusion processes in the engine chamber.

- The production term $T_{K \longrightarrow k}$ can be written as function of the contributions of the 3 aerodynamic flow motions generally observed in IC engines (i.e. tumble, swirl and squish, see Section 2.2) and of the kinetic energy variation due to the spray injection (in case of direct injection engines). $T_{K \longrightarrow k}$ can therefore be expressed as:

$$T_{K \longrightarrow k} \cdot m_{tot} = \frac{dE_{kin,tumble}}{dt} + \frac{dE_{kin,swirl}}{dt} + \frac{dE_{kin,squish}}{dt} + \frac{dE_{kin,spray}}{dt} \tag{3.37}$$

  where notations *tumble*, *swirl*, *squish* and *spray* are respectively related to the contributions to the total kinetic energy of the tumble, swirl, squish and spray motions. In the case of SI engines, the three last contributions to the main aerodynamic flow can be generally neglected in favor of the tumble motion and Eq. 3.37 can finally be simplified as:

$$T_{K \longrightarrow k} \cdot m_{tot} = \frac{dE_{kin,tumble}}{dt} \tag{3.38}$$

$E_{kin,tumble}$ is generally computed assimilating the tumble motion to a cylinder turning around a rotation axis orthogonal to the piston displacement axis and defined by an equivalent inertia momentum J. $E_{kin,tumble}$ is then given as function of the engine speed ω_e as:

$$E_{kin,tumble} = \frac{1}{2} \cdot J \cdot \omega_{tumble}^2 = \frac{1}{2} \cdot J \cdot N_{tumble} \cdot \omega_e^2 \tag{3.39}$$

with

$$J = \frac{1}{2} \cdot m_{tot} \cdot \left(\frac{h}{2}\right)^2 \tag{3.40}$$

where h is the distance between the piston and the cylinder head and N_{tumble} the tumble ratio.

Finally, the evolution of the kinetic energy associated to the tumble motion is obtained assuming a linear decrease of the tumble motion from the intake valve closure (IVC) to the top dead centre and using the following expression:

$$\frac{dE_{kin,tumble}}{dt} = \frac{1}{8} \cdot m \cdot \omega_e \cdot \left[h^2 \cdot \frac{dN_{Tumble}}{dt} + 2N_{tumble} \cdot h \frac{dh}{dt}\right] \tag{3.41}$$

Remark: It should be noticed that in Diesel engine cases, the main contributor to the produced kinetic energy is the spray motion. Under this assumption, the production term of Eq. 3.30 becomes (Chelma and Orthaber 1999):

$$T_{K \longrightarrow k} \cdot m_{tot} = \frac{dE_{kin,spray}}{dt} = \frac{1}{2} \cdot U_f^2 \cdot \frac{dm_{inj}}{dt} \tag{3.42}$$

where U_f is the effective spray velocity at the injector exit and dm_{inj}/dt the fuel injection rate (Chelma and Orthaber 1999).

It results from Eqs. 3.22 and 3.23 and given modeling closure the following equation system to solve for deducing u' (from Eq. 3.18):

$$\begin{cases} \dfrac{dk}{dt} = C_{turb} \cdot T_{K \longrightarrow k} - C_{diss} \cdot k \\ \dfrac{dK}{dt} = -T_{K \longrightarrow k} \end{cases} \tag{3.43}$$

where C_{turb} is a turbulence parameter allowing to consider that only a given proportion of the total kinetic energy is associated to the fluctuating motions constituting the turbulence.

In such a model, N_{tumble} is a flow parameter corresponding to an initial conditions for the compression stroke and l_t is assumed to be constant during the whole combustion stroke. N_{tumble} could be captured at IVC using Eq. 3.30 and l_t could be computed using Eq. 3.32. However, the flame wrinkling and the corresponding flame velocity are highly sensitive to the estimation of u' and l_t. Then using such single estimations is too rough to yield an accurate description of the cylinder pressure trace. Indeed, as shown in Figure 3.6 errors on u' and l_t of 10% lead to high discrepancies in engine results. In addition, developping a more refined turbulence model was not in the scope of this thesis. For all these reasons, in this work, N_{tumble} and l_t were adjusted for each engine operating point to perfectly match experimental pressure traces. These quantities where then stored in look-up tables as function of the engine load and speed and used afterwards without being modified to predict the effect of engine settings and fuel composition variations on the engine behavior and to simulate transient operating conditions as well. The methodology used to generate these maps is detailed in Chapter 4.

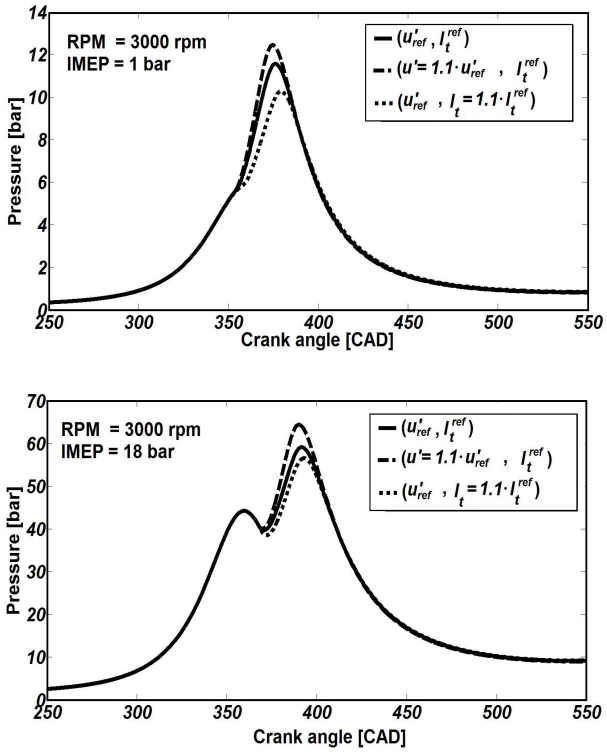

Figure 3.6: Simulated in-cylinder pressure evolutions as function of the crank angle at 3000 rpm and for different engine loads (IMEP = 1 and 18 bar). Results were obtained using the CFM1D combustion model presented in Chapter 4. The reference curve was obtained by calibrating the turbulence model to fit the corresponding experimental pressure trace. The other curves were obtained by perturbing the values of either u' or l_t from the reference ones u'_{ref} and l_t^{ref} in the turbulence model.

Remark: It should be noticed that presented approaches allow to estimate the turbulent characteristics u' and l_t which can then be used to compute the effect of turbulence on the flame wrinkling. Nevertheless, the effect of the flame on the turbulent flow (see Chapter 2) are not accounted for by these models and complementary developments need therefore to be performed to enhance the description of physical phenomena taking place in the combustion chamber.

3.3 Pollutants modeling

As mentioned in Chapter 2.4, main pollutants in IC engines are nitrogen oxides (NOx), carbon oxides (CO_2 and CO) and unburnt hydrocarbons (HC). CO_2 is mainly produced through fuel oxidation processes while NOx and CO are principally formed by post-oxidation mechanisms in the burnt gases zone. This zone is quite natural to define in premixed combustion cases but can be more difficult to identify in diffusion combustion cases. Historically in order to ensure a high computational efficiency, more or less complex reduced chemistry descriptions were used in 0D combustion models to predict pollutant formation in the burnt gases (Barba et al. 2000, D'Errico and Onorati 2004, D'Errico and Lucchini 2005, D'Errico et al. 2006, Heywood et al. 1979). However, the computational resources required by these ″pseudo complex″ chemistries (with regard to system simulation) combined to their low prediction level especially under engine conditions (pressures up to 13 MPA, temperatures up to 3000 K, equivalence ratii between 0.6 and 1.3 and dilution rates up to 30%) made crucial the developement of new modeling solutions allowing to decrease CPU time and improving at the same time the pollutants estimation. More

recently, some authors (Coble et al. 2011) directly integrated complex chemistry into stochastic reactors distributed in the combustion chamber in which chemical reactions are activated as soon as the associated reactors are reached by the flame. These approaches are then coupled to combustion models as for example the CFM1D (Lafossas et al. 2005) for SI engines applications. Nevertheless, here also, CPU time ($\approx 2000s/cycle$ which represent $\approx 10^4 - 10^5 times the real time(RT)$!, (Coble et al. 2011)) make these approaches limited with regard to system simulation. An interesting alternative to optimize computational times while accounting for complex chemical processes is the integration of tabulation methods as performed in recent 3D CFD simulations (Colin et al. 2005, Gicquel et al. 2000, Ribert et al. 2006, Vervisch et al. 2011). This solution is discussed in the present work and considered to develop new approaches improving NOx and CO prediction in SI engines (see Chapters 5 and 6). As regards hydrocarbon prediction, HC are considered as unburnt or partially burnt fuel (especially in Diesel cases) or estimated through specific models accounting for HC trapping in oil or in engines crevices (Schramm and Sorenson 1990, Cordiner and Rocco 1997). In both approaches, in the case of HC release in the burnt gases (especially in SI engine cases), simple post-oxidation chemistries are then used to compute HC consumption.

3.4 Abnormal combustion modeling

Abnormal combustion issue is mainly linked to SI engines and concerns knock phenomena caused by the uncontrolled auto-ignition of one or several fresh gases pockets having not been reached by the flame yet (see Chapter 2.3). With regards to system simulation, models dedicated to knock prediction generally aim at answering two questions:

+ Does an abnormal combustion appear ? Auto-ignition delay evaluation is here required.
+ If an abnormal combustion appears, which consequences have to be expected ? An auto-ignition intensity evaluation is here therefore required.

The two main approaches generally considered to fix the problem of auto-ignition prediction are:

- **Phenomenological approaches:** First models were based on the calculation of auto-ignition delays using correlations developed from rapid compression machines (RCM) measurements (AnB model from Guibet and Fautre-Birchem (1996)). This delay was then integrated using the approach of Livengood and Wu (1955) to predict the auto-ignition timing in the engine cycle. An auto-ignition intensity was finally computed as function of several parameters which main one was the energy quantity remaining available to release (Karim 2004, Ho and Kuo 1997, Attar and Karim 1998). These approaches have the advantage of being quite simple and requiring only few computational resources but the generated results quality are extremely dependent on the delay correlation accuracy as well as on the relevance of the intensity definition which are generally limited by covered conditions of RCM measurements. Moreover such phenomenological approaches are generally dissociated from the main combustion model and the simple intensity evaluation does not provide any information about auto-ignition heat release and can not finally precisely answer to the second question previously mentioned. The relative simplicity of this approach makes therefore the prediction of AI phenomena limited to the study of knock occurrence (no specific heat release due to AI is computed) and cannot be used neither to precisely predict AI processes taking place in CAI applications (see Chapter 1) nor accounting for fuel composition effects on these processes.
- **Chemical description approaches:** An alternative to AnB models is the direct integration of chemistry description in the fresh gases through a simple kinetic scheme as the Shell or Tananka models (Halstead et al. 1977, Noda et al. 2004) or a more complex one (D'Errico et al. 2007) allowing in both cases to directly access to the reaction rate related to the auto-ignition process. These approaches are sometimes coupled to a multi-zone description

(see Section 3.1) of fresh gases to account for temperature stratification but can then increase CPU times (Ho and Kuo 1997). In the case of a chemical description of auto-ignition processes, several issues have to be fixed :

- *Reduction of computational costs* – Similarly to pollutant modeling (see Section 3.3), an interesting solution to decrease CPU times of the direct resolution of complex chemistry processes consists in using tabulation approaches based on *a priori* simulations of chemical processes, in homogeneous reactors for example, using a complex kinetic scheme. A wide chemical database is then generated and can thereafter be directly plugged in the combustion model. Such approaches initially developed for 3D CFD applications appear today as a very interesting alternative to optimize computational times while precisely accounting for complex chemical processes. A non-exhaustive list of main works on such methods comprises the models FPI (Flame Prolongation of Intrinsic Low-Dimensional Manifolds) (Gicquel et al. 2000), FGM (Flamelet-Generated Manifold) (van Oijen et al. 2001) and TKI (Tabulated Kinetics for Ignition) (Colin et al. 2005). The two first methods are very similar and consist in representing the chemical path through a unique parameter for given thermodynamic conditions, the progress variable, which goes from 0 in fresh gases to 1 in fully burned gases. FPI was initially based on the tabulation of unstrained laminar premixed flames but was extended to AI cases (Michel et al. 2009). It was successfully applied to the simulation of combustion in a Diesel engine (Pera et al. 2009). The TKI model showed also good results in such an application (Knop and Jay 2006). In the case of system simulation, no equivalent approaches are currently available. In this thesis a 0D model, inspired from the PCM-CFM-I 3D model proposed by Lecocq (2010) in a LES framework, is developed. This model, based on the tabulation of AI progress variable reaction rates and delays, is presented in Chapter 7.
- *Definition of an AI intensity indicator* – A difficulty linked to the chemistry resolution is that an intensity indicator has to be specified. In the TKI model Colin et al. (2005) this intensity was evaluated by defining a ratio between the heat release by the main combustion and the one by the auto-ignition (Noda et al. 2004, Laget et al. 2010).
- *Post-processing of experimental data* – The use of post-processed experimental data is generally quite difficult since the achieved informations are not of the same nature than the model outputs. Indeed, the pressure signal provided by the bench is filtered by the engine and the sensor itself and locally measured for each cycle by an accelerometer through a transfer function which is generally unknown. By contrast, the auto-ignition model provides a mean pressure trace resulting from the main combustion and auto-ignition process which can only be compared to the average of local experimental pressures data measured over several engine cycles.

Developments have therefore to be performed to reduce the CPU cost, to improve the definition of an adequate indicator and to account for cycle-by-cycle instabilities in SI engines in the other hand.

In the present thesis work, both phenomenological and chemical descriptions of auto-ignition processes have been developed and tested against a wide range of operating condition in gasoline-ethanol burning engine. Approaches and results are presented in Chapters 4 and 7.

3.5 Modeling of fuel composition effects on combustion

Only few works studied in the past the description through 0D models of fuel composition effects on combustion processes. In these studies the heat release was generally described by a Wiebe model (see Section 3.1) which coefficients were adjusted as function of the fuel formulation (Cavalcante.Cordeiro.de.Melo et al. 2007). Regarding auto-ignition prediction, most of them aimed at

studying the impact of fuel composition on knock by coupling the Livengood (Livengood and Wu 1955) approach (see Section 3.4) for the integration of the auto-ignition delay with a Wiebe model estimating the fuel remaining to burn (Yates et al. 2005). In such an approach, the auto-ignition delay given by a AnB law which coefficients are also adjusted as function of the fuel formulation to fit results *a priori* obtained using complex chemistry calculations. As a result, for all approaches the effect of fuel composition on the total heat release is not predicted since a parameter adjustment step is always beforehand required. The aim of this thesis is precisely to develop a model based on the integration of complex chemistry able to account for these effects on flame propagation, pollutant and auto-ignition phenomena. It represents indeed the main objective of the present work in addition to the predictivity enhancement and CPU times decrease mentioned in the three last sections.

3.6 Heat losses at walls modeling

With regards to piston engines, the Woschni model (Woschni 1697) is commonly used to describe heat transfer across the engine walls. It provides an expression for the instantaneous thermal convective coefficient h_w stepping in the computation of the convective heat fluxes Q_{liner} , Q_{piston} and Q_{head} respectively through the cylinder liner, the piston and the cylinder head as given by Eqs. 3.44-3.46.

$$\frac{dQ_{liner}}{dt} = h_w \left(\pi D l_c\right) \left(T - T_{liner}\right) \tag{3.44}$$

$$\frac{dQ_{piston}}{dt} = h_w \left(\pi D^2/4\right) \left(T - T_{piston}\right) \tag{3.45}$$

$$\frac{dQ_{head}}{dt} = h_w \left(\pi D^2/4\right) \left(T - T_{head}\right) \tag{3.46}$$

where T is the in-cylinder temperature, T_{liner} , T_{piston} and T_{head} are respectively the cylinder liner, the piston and the cylinder head temperature, D the piston diameter, l_c the instantaneous liner height (see Figure 3.7). For the three equations, h_w is written as function of D , T, the cylinder pressure P and the piston instantaneous velocity v_p as:

$$h_w = 3.26 D^{-0.2} P^{0.8} T^{-0.55} v_p^{0.8} \tag{3.47}$$

The gas temperature T in Eqs. 3.44-3.47 is assumed to be the mean temperature of the gas under consideration (fresh or burnt).

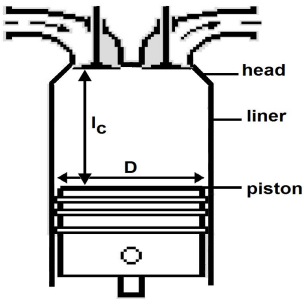

Figure 3.7: Engine scheme for Woschni model parameters definition.

3.7 Conclusion

In this Chapter, a review of main 0-dimensional approaches for system simulation tools with regards to IC engine developments have been proposed. These approaches are summarized in Table 3.1. A description of existing models for heat release prediction has been proposed distinguishing empirical from phenomenological and reduced models. A presentation of typical 0D turbulence models has been developed. Main approaches considered for the prediction of pollutants (NO, CO and HC) were evoked distinguishing simple and reduced chemistries from complex and tabulated kinetics. Widespread solutions for auto-ignition phenomena 0D modeling were described. It has been shown that only few works studied in the past the description of fuel composition effects on combustion processes through 0D models. Finally, a complementary sub-model (heat losses at walls) was presented. All these presentations aimed at explaining the evolution and the issue of 0D modeling developments and putting the basis of the 0D turbulent combustion model developed in this thesis and presented in the following chapters. Starting from the CFM1D physical combustion model (Part II), the new model CFM1D-TC integrates new complex chemistry approaches as well as new physics descriptions to improve heat release, pollutant formation and auto-ignition prediction (Part III) accounting at the same time for fuel composition variations.

Remark: As previously mentioned, developing a refined turbulence model was not in the scope of this thesis. As a result, the semi-phenomenological model presented in Eq. 3.43 was finally used.

APPROACH	ADVANTAGES	DRAWBACKS	CPU EFFICIENCY	EASE OF CALIBRATION / NUMBER OF VARIABLES	PREDICTION / EXTRAPOLATION	PRECISION
Global approaches						
Empirical mathematical models	easy to implement / low CPU cost	not based on physics / poorly predictive / high number of experimental data required	●●●●●	●○○○○	●○○○○	●○○○○
Phenomenological models	more physical than empirical models	not based on theoretical basis	●●●●○	●●●○○	●●●○○	●●○○○
Multi-zones models	improve the modeling precision compared to a single / inhomogeneities	demand an important number of zones / high computational resources required / high number of modeling parameters to adjust	●○○○○	●●●●○	●●●●○	●●●●○
3D reduced models	physical models	difficulty to close some terms	●●●●○	●●●●○	●●●●○	●●●●○
Tabulated chemistry methods	improve chemistry description / reduce CPU cost	requires precise inputs estimations	●●●●○	●●●●○	●●●●○	●●●●○
Statistical methods (PDF)	improve the description of heterogeneities/ easy to couple with a 0D model	difficulty to estimate the variable variances	●●●●●	●●●●●	●●●●●	●●●●●
Flame wrinkling closure						
Experimental correlation	easy to implement	lack of predictivity when dealing with engine applications / too simple to describe complex turbulence/flame processes and fuel composition effects / the flame wrinkling is considered to be at equilibrium	●●●●●	●●●●●	●●○○○	●●○○○
Fractal models	easy to implement	the flame wrinkling is considered to be at equilibrium	●●●●○	●●●●○	●●●○○	●●○○○
Transport equation for the flame wrinkling	physical model /precise description of turbulence flame interaction processes	requires to improve the description of fuel composition effects	●●●○○	●●●●●	●●●●●	●●●●●
Turbulence closure						
Full-predictive K-k model	Low model calibration required	highly dependent on geometry	●●●●○	●●●●○	●●○○○	●●○○○
Semi-predictive K-k model	Possibility to calibrate the model	a calibration step is required	●●●●●	●●●○○	●●●●○	●●●○○
Pollutants						
Global chemistry	allow the chemistry description	high computational resources required / low prediction level	●●●○○	●●●●●	●●●○○	●●○○○
Pseudo-complex chemistry	high level of prediction	very high computational resources required	●○○○○	●●●●●	●●●●●	●●●●●
Distributed stochastic reactors models	high level of prediction	very high computational resources required	●○○○○	●●●●●	●●●●○	●●●●○
Tabulated chemistry	high level of prediction / low CPU cost	requires precise inputs estimations	●●●●○	●●●●○	●●●●○	●●●●○
Auto-ignition						
Phenomenological correlations (AnB models)	easy to implement / low CPU cost	prediction of AI phenomena limited to the study of knock occurrence / no specific heat release due to AI is computed	●●●●●	●●●○○	●●○○○	●●○○○
Pseudo-complex chemistry	high level of prediction	very high computational resources required	●○○○○	●●●●●	●●●●●	●●●●●
Tabulated chemistry	high level of prediction / low CPU cost	requires precise inputs estimations / an efficient AI intensity indicator definition is required	●●●●○	●●●●○	●●●●○	●●●●○
CFM1D-TC model developed in this thesis						
+ 3D reduced model + phenomenological functions + flame surface density + tabulated chemistry + Semi-predictive K-k model	' ' ' ' ' ' ' '	' ' ' ' ' ' ' '	●●●●○	●●●●○	●●●●●	●●●●●

Table 3.1: Summary of common approaches considered in system simulation with the corresponding advantages and drawbacks.

Part II

CFM1D model based on global chemistries

Chapter 4

CFM1D model based on simple & reduced chemistry approaches

This chapter presents the CFM1D 0-dimensional model solving the physical phenomena occurring in SI engines as described in Chapter 1 and Figure 1.4. This model will serve as a basis for developments performed in this thesis. It is based on simple and reduced descriptions of chemistry in the flame front and in the burnt gases and on phenomenological approaches to solve the turbulent flame propagation and auto-ignition phenomena. Each physical phenomenon is associated to a sub-model considering specific inputs (temperature, pressure, composition, etc.) and leading to the description of thermodynamics and species temporal evolutions in the engine chamber. Figure 4.1 gives an overview of the global definition of these sub-models and can help to have a global visualization of works conducted here. As presented in Figure 1.3, four main sub-models are therefore considered (combustion in the flame, post-oxidation, flame propagation, auto-ignition) and will be presented in this chapter.

Works presented in this chapter are organized as follow :

- **Section 4.1 : Presentation of the CFM1D model with an application to gasoline fuel** – Works described in this section were published in the **Oil & Gas Science & Technology** journal.
- **Section 4.2 : Model enhancement for gasoline-ethanol blends combustion** – Works described in this section were subjected to an article presented in the **SAE's 9th International Conference on Engines and Vehicles** and selected for publication in proceedings.
- **Section 4.3 : Complementary comments** – Complementary results are presented for methane-hydrogen blends combustion. Additional comments are brought and global conclusions are given. These conclusions are at the base of the developments described in the following chapters aiming at improving the ability of the model to account for fuel composition.

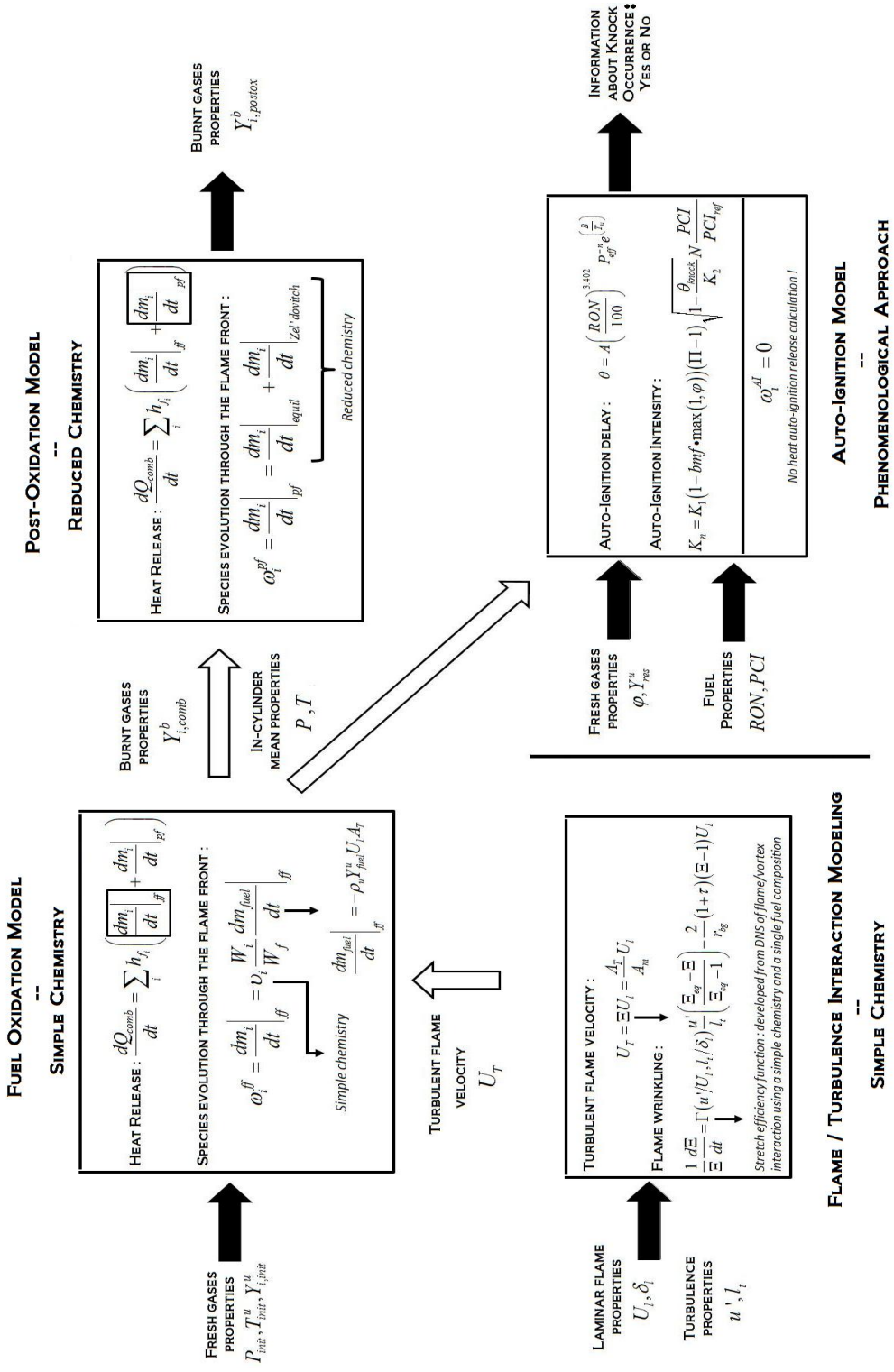

Figure 4.1: Sub-models global description – All parameters will be defined in the following sections – ω_i^{ff}, ω_i^{pf} and ω_i^{AI} refer to the rates of consumption/production of species i stepping in Figure 1.3.

4.1 0D modeling of heat release, pollutants and knock in SI engines : application to gasoline combustion

---

- **Title**: On the Reduction of a 3D CFD Combustion Model to Build a Physical 0D Model for Simulating Heat Release, Knock and Pollutants in SI Engines
- **Authors**: S. Richard*, S. Bougrine*, G. Font*, F.-A. Lafossas* and F. Le Berr*
  * IFP Energies nouvelles
- **Reference**: Oil & Gas Science and Technology, 2009, 64:3:223-242

4.1.1 Abstract

In the automotive industry, todays major objectives concern the reduction of pollutant emissions and fuel consumption while improving performance and driveability. For this purpose, during the last decade, the classical engine has evolved towards a very complex system combining many hi-tech components with advanced control strategies. Optimizing the whole engine system and controlling its behavior has then become a real challenge for car manufacturers. In this context, powertrain simulation tools have been shown to be an undisputable support during all stages of the engine development from concept design to control strategies development and calibration. However these tools require sophisticated models to be efficient, especially in the combustion chamber where combustion and pollutant formation processes take place. This paper presents a 0D physical combustion model devoted to the prediction of heat release, knock and pollutants in SI engines. The originality of the model derives from the fact it is based on the reduction of the 3D CFD E-CFM (Extended Coherent Flame Model) model developed at IFP. The CFM formalism distinguishes two zones: the fresh and the burnt gases, which are separated by a flame front and are both described by their temperature, mass and composition. The proposed model is an important evolution of the CFM-1D model previously published. It computes the rate of consumption of the fresh gases and is based on the calculation of the flame front surface using the real engine geometry and a 0D derivation of the flame surface density approach. Pollutants (CO and NOx) are computed both through the flame front an within the burnt gases using a reduced kinetic scheme and a classical extended Zeldovitch mechanism. The knock timing calculation is performed in the fresh gases zone describing the evolution of an auto-ignition precursor and a simple correlation is used to estimate the corresponding knock intensity. The whole model is validated against experimental data at several steady state operating points for a single-cylinder engine. Parametric variations around optimal engine settings are also performed. A good agreement with experiments is observed, showing the interest of reducing 3D CFD models to build predictive 0D models for engine system simulations.

4.1.2 Introduction

In the two last decades, piston engines specifications have greatly evolved. Indeed, main challenges nowadays concern the reduction of pollutant and CO_2 emissions. To satisfy these new requirements, powertrains have become very complex systems combining many high technology components (high pressure injectors, 2-stage turbocharger, EGR loop, after-treatment devices, variable valve actuators, energy recovery and storage systems, etc.) with advanced control strategies. In the past, engine developments were mainly based on experiments using engine test benches. This approach is not adapted to the complexity of new engines: on the one hand, tests are very expensive and on the other hand they do not give enough information to permit the understanding

of interactions between components. Today, a promising alternative to experimental tests may be the use of 0D/1D simulation tools. These tools have known rapid improvements in the past ten years and can today be used at all stages of the engine development, from concept design to powertrain control development and calibration. However, they are generally based on empirical models (Tabaczynski et al. 1977, Heywood et al. 1979) and often suffer from a lack of predictivity, especially when dealing with in-cylinder phenomena. A solution for extending the range of application of the system simulation consists of developing more physical models including a detailed description of combustion and pollutants formation processes. Such models can be obtained using 0D phenomenological approaches (Matthews and Hall 1996, D'Errico et al. 2002) or reducing 3D CFD combustion models (Lafossas et al. 2005, Emery et al. 2003). The second method is used in this work to derive a 0D physical combustion model dedicated to the prediction of heat release, knock and pollutant emissions in SI engines.

4.1.3 Combustion modeling

The model proposed in this paper is an important evolution of the CFM-1D model already presented in (Lafossas et al. 2005). It includes a more precise approach for computing the turbulent flame surface evolution and describes the formation and evolution of pollutants in the cylinder. It is also coupled to a simple autoignition model to predict the onset of knock in the engine.

Principle and assumptions

This work is based on the 3D CFD CFM model initially developed for RANS (Colin et al. 2003) and LES (Richard et al. 2007) calculations. The coherent flame model (CFM) is a combustion model dedicated to the flamelet regime. This approach is well adapted to premixed and partially premixed combustion processes, which represent the main oxidation mechanism in SI engines. As presented in Figure 4.2, the CFM formalism distinguishes two zones: fresh and burnt gases which are separated by a flame front propagating from the burnt gases towards the fresh mixture. Chemical reactions of fuel oxidation occurs in a very thin layer (the flame front) compared to all scales of the turbulent flow and post-flame chemistry takes place in the burnt gases. The different equations of the model, initially written for 3D simulations, are reduced by integration over the cylinder to obtain a 0D physical model called the CFM-1D model as it accounts for the radial propagation of the flame. This reduction of the 3D model is based on several assumptions:

- The gaseous mixture consists of 15 species ($Fuel$, $N2$, $O2$, $H2$, $H2O$, CO, $CO2$, NO, $NO2$, HC, $NH3$, $soot$, O, H, OH) considered as perfect gases.
- The mixture composition is considered as homogeneous in each zone (fresh and burnt gases).
- Fuel can be found in both liquid and gaseous phases in the combustion chamber. In this case, liquid fuel is treated as a separated thermodynamic system exchanging mass and enthalpy by vaporization with the fresh gases.
- The pressure is assumed to be the same in both zones.
- Each zone is described by its mass, volume, composition and temperature (Colin et al. 2003).
- The turbulent kinetic energy field is assumed to be uniform in the cylinder.

Heat release calculation

The enthalpy balance for the combustion chamber is:

$$\frac{dmh}{dt} = V\frac{dP}{dt} + \frac{dQ_{comb}}{dt} - \frac{dQ_{wall}}{dt} + \sum_{in,out} h_j \frac{dm_j}{dt} \tag{4.1}$$

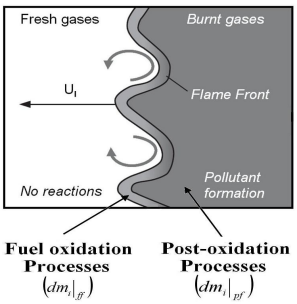

Figure 4.2: The coherent flame approach (subscripts u and b respectively refer to fresh and burnt gases)

where V is the cylinder volume, h is the mass enthalpy, m is the enclosed mass and P is the pressure which is linked to the mean temperature T by the perfect gas law. The last term of Eq. 4.1 refers to enthalpy exchanges at the inlets and outlets (valves, injector). Q_{wall} corresponds to heat losses at the walls which are described with the Woschni model (Woschni 1697). Q_{comb} is the heat released by combustion processes and can be expressed as:

$$\frac{dQ_{comb}}{dt} = \sum_i h_{f_i} \left(\left.\frac{dm_i}{dt}\right|_{ff} + \left.\frac{dm_i}{dt}\right|_{pf} \right) \tag{4.2}$$

where h_{fi} is the formation enthalpy of specie i, $dm_i|_{ff}$ and $dm_i|_{pf}$ are the mass variations of this species respectively in the flame front and in the burnt gases due to post flame chemistry reactions. These variations are coupled with pollutant formation processes and will be detailed further in the paper. $dm_i|_{ff}$ can be expressed as a function of the fuel consumption rate:

$$\left.\frac{dm_i}{dt}\right|_{ff} = \upsilon_i \frac{W_i}{W_f} \left.\frac{dm_{fuel}}{dt}\right|_{ff} \tag{4.3}$$

where υ_i is the stoichiometric coefficient of specie i, W denotes the molecular weight and $dm_{fuel}|_{ff}$ is defined as:

$$\left.\frac{dm_{fuel}}{dt}\right|_{ff} = \left.\frac{dm^u_{fuel}}{dt}\right|_{ff} - T^{u\to b}_{fuel} \tag{4.4}$$

where $\left.dm^u_{fuel}\right|_{ff}$ is the fuel lost by the fresh gases zone through the flame and $T^{u\to b}_{fuel}$ is the transfer of fuel from fresh to burnt gases in very rich cases. In the CFM model, $\left.dm^u_{fuel}\right|_{ff}$ depends on the turbulent flame surface A_T and the fresh gases properties:

$$\left.\frac{dm^u_{fuel}}{dt}\right|_{ff} = -\rho_u Y^u_{fuel} U_l A_T \tag{4.5}$$

where ρ_u is the fresh gases density, $Y^u_{fuel} = m^u_{fuel}/m_u$ is the fuel mass fraction in the fresh gases and U_l is the laminar flame speed computed with Metghalchi and Kecks correlation (Metghalchi and Keck 1982):

$$U_l = U^0_l(\varphi) \left(\frac{T^u}{T^0}\right)^{\alpha} \left(\frac{P}{P^0}\right)^{\beta} (1 - 2.1 X_{rgb}) \tag{4.6}$$

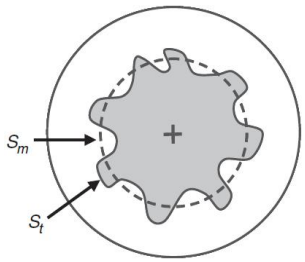

Figure 4.3: Definition of the mean and turbulent flame surfaces.

where U_l^0 is the reference laminar flame speed at P^0 and T^0, α and β are coefficients depending on the fuel air equivalence ratio, X_{rbg} is the molar fraction of residuals in the fresh gases and T^u is the fresh gases temperature. The turbulent flame surface A_T is written as the product of a mean surface A_m and the flame front wrinkling Ξ (Figure 4.3):

$$A_T = \Xi A_m \tag{4.7}$$

Finally, the mass evolution of specie i is:

$$\begin{aligned} \frac{dm_i}{dt} &= \left.\frac{dm_i}{dt}\right|_{inlet/exhaust} + \left.\frac{dm_i}{dt}\right|_{ff} + \left.\frac{dm_i}{dt}\right|_{pf} \text{ for i } \neq \text{ fuel} \\ \frac{dm_{fuel}}{dt} &= \left.\frac{dm_{fuel}}{dt}\right|_{inlet/exh} + \left.\frac{dm_{fuel}}{dt}\right|_{ff} + \left.\frac{dm_{fuel}}{dt}\right|_{pf} + \left.\frac{dm_{fuel}}{dt}\right|_{evap} \end{aligned} \tag{4.8}$$

where $dm_{fuel}|_{evap}$ is defined below.

Fresh and burnt gases properties computation The fresh gases composition at IVC is obtained from the fresh charge composition at the intake and the amount of residual burnt gases in the cylinder. The fresh gases mass then evolves due to combustion reactions in the flame front and to the injection of fuel when dealing with GDI engines. In this case, the rate of gaseous fuel production by evaporation is estimated as:

$$\left.\frac{dm^u_{fuel}}{dt}\right|_{evap} = \left.\frac{dm_{fuel}}{dt}\right|_{evap} = \frac{m^{liq}_{fuel}}{\tau} \tag{4.9}$$

where m^{liq}_{fuel} is the current mass of liquid fuel in the combustion chamber and $\tau = 10^{-3}s$ is a time scale. After IVC, the mass evolution of specie i in the fresh gases can then be written as:

$$\begin{aligned} \frac{dm^u_i}{dt} &= \left.\frac{dm^u_{fuel}}{dt}\right|_{ff} \frac{m^u_i}{m^u_{fuel}} \\ \frac{dm^u_{fuel}}{dt} &= \left.\frac{dm^u_{fuel}}{dt}\right|_{ff} + \left.\frac{dm^u_{fuel}}{dt}\right|_{evap} \end{aligned} \tag{4.10}$$

The fresh gases temperature T_u is obtained by inversion from the fresh gases composition and the fresh gases enthalpy h_u (Lafossas et al. 2005). h_u is computed after IVC using a 0D equation reduced from the 3D balance equation for the fresh gases enthalpy (Colin et al. 2003, Baritaud et al. 1996):

$$\frac{dmh_u}{dt} = \frac{\rho}{\rho_u}\frac{dP}{dt}V + \frac{dQ^u_{wall}}{dt} \tag{4.11}$$

The right hand side terms correspond respectively to the compression work and to heat transfer at the walls. Q^u_{wall} is computed with Woschnifs correlation. The fresh gases density is obtained from the fresh gases volume V_u and m_u: $\rho_u = m_u/V_u$. V_u can be computed with P, T_u and the fresh gases composition using the perfect gas law. Following the CFM formalism, a progress variable c is defined to account for the evolution of chemical reactions in the flame front:

$$c = 1 - \frac{m_u}{m} \tag{4.12}$$

The burnt gases enthalpy can then be deduced from the mean and fresh gases enthalpies:

$$mh = (1 - c)\, m_u h_u + c\, m_b h_b \tag{4.13}$$

where $m_b = \sum_i m_i^b$ and $m_i^b = m_i - m_i^u$

The burnt gases temperature T_{bg} is deduced by inversion from the burnt gases composition and h_{bg}. Finally, the burnt gases volume V_{bg} is written as: $V_{bg} = V - Vu$. The algorithm used to solve equations 4.1 to 4.13 is presented in detail in (Lafossas et al. 2005).

Mean flame surface calculation The mean evolution of the flame surface over many engine cycles has been investigated by Baritaud (1989). These experiments suggest that the mean flame front grows spherically in the cylinder. A_m is then computed assuming a spherical flame propagating from the spark plug position in a realistic geometry for the combustion chamber (Figure 4.4). For this purpose, A_m is a priori tabulated as a function of the piston position and the burnt gases volume (Figure 4.5). The mean flame surface is then obtained at each time step by interpolation from the look-up table using the current piston position and burnt gases volume. This look-up table can be built with a 3D CAD software by computing intersections between the spherical inflamed volume and the combustion chamber walls to retrieve the enclosed flame surface (Bozza et al. 2005, Bozza and Gimelli 2004). However, as the 3D engine geometry is not always available, a pre-processing tool based on the main geometrical characteristics of the engine (bore, stroke, roof angle, bowl dimensions, compression ratio, spark plug position) has been developed in this work. This tool provides a slightly simplified engine geometry and can deal with pent-roof and flat cylinder heads as well as flat and bowled pistons. The tool then computes the mean flame surface in the same way as in (Bozza and Gimelli 2004).

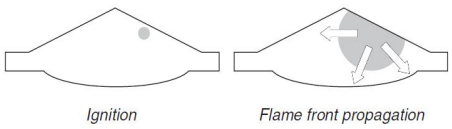

Figure 4.4: Mean flame surface evolution in a realistic combustion chamber.

Flame front wrinkling computation A simple way to compute the flame wrinkling is the use of a classical Damkholrer's formulation based on an equilibrium assumption for Ξ (Lafossas et al. 2005, Boger et al. 1998):

$$\Xi = \Xi_{equ}\, g(r_b) = \left(1 + 2\frac{u'}{U_l}\sqrt{\frac{\Gamma C}{Sc}}\right) g(r_b) \tag{4.14}$$

where u' is the instantaneous velocity fluctuation, Γ is the efficiency function of the turbulent flow on the flame strain (Charlette et al. 2002), C is a modeling constant, Sc is the Schmidt number, r_b is the current mean flame radius and g a function accounting for the laminar-turbulent transition of the flame front. This approach is very close to those proposed in the literature

which are commonly based on a fractal description of the flame front (Matthews and Hall 1996) combined with a phenomenological description of the transition from the laminar flame kernel to a fully developed turbulent flame front (Bozza et al. 2005, Bozza et al. 2001). The major drawback of a such model for the laminar-turbulent transition is its lack of predictivity (Bozza et al. 2005, LeBerr et al. 2006). Indeed, a tunable transition flame radius is often used to match experimental cylinder pressure curves. However, the transition process depends strongly on the current thermodynamic and flow conditions (Baritaud 1989), thus the flame surface evolution is difficult to reproduce correctly for all engine operating conditions without modifying this radius. A promising alternative to this method can be the use of a physical equation for the temporal evolution of the flame wrinkling. This equation can be obtained by reduction of the 3D CFD equation for the flame surface density (Richard et al. 2007):

$$\frac{1}{\Xi}\frac{d\Xi}{dt} = \Gamma\left(u'/U_l, l_t/\delta_l\right)\frac{u'}{l_t}\left(\frac{\Xi_{equ}-\Xi}{\Xi_{equ}-1}\right) - \frac{2}{r_b}\left(1+\tau\right)\left(\Xi-1\right)U_l \tag{4.15}$$

where l_t is the integral length scale, $\tau = \rho_u\ \rho_b$is the thermal expansion rate, $r_b = (3V_b/4\pi)^{1/3}$ is the current burnt gases mean radius and δ_l is the laminar flame thickness estimated using Blint's correlation (Blint 1986). The first RHS term of Eq. 4.15 corresponds to the flame strain by all turbulent structures while the second describes the effect of the thermal expansion which limits the flame front wrinkling by imposing a positive curvature on the flame front.

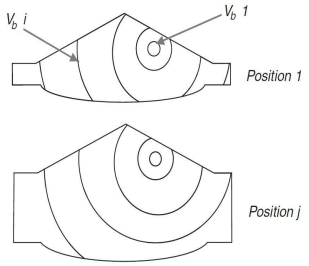

Figure 4.5: Principle of mean flame surface tabulation.

0D turbulence model It can be observed in Eq. 4.15 that the flame development strongly depends on the turbulence characteristics (u', l_t). These characteristics are very sensitive to the combustion chamber and intake pipes geometry and to the engine operating point. Therefore the reduction of a 3D turbulence model to build a 0D physical model is not obvious and strong geometrical assumptions are generally made to close the unknown terms. For example, in the K-k 0-dimensional model (Meintjes and Morgan 1987), lt is assumed to be exactly the distance between the piston and the cylinder head. An adjustable parameter is then often incorporated to the turbulent kinetic energy production term to fit experimental results. For these reasons, a simple phenomenological turbulence model (Lafossas et al. 2005) is retained in this work. This model is expected to be less predictive than a reduced one, but has the advantage of being easy to control while remaining based on physical quantities. In this model, l_t is assumed to remain constant and equal to its value at spark timing during the whole combustion stroke, while the evolution of $u' = \sqrt{2/3k}$ is described by a 0D equation for the turbulent kinetic energy k:

$$k = C_{turb} \cdot \frac{E_{kin,diss}}{m} \tag{4.16}$$

where $E_{kin,diss}$ is the dissipated kinetic energy and $C_{turb} = 1$ is a modeling constant. $E_{kin,diss}$ is computed using the kinetic energy in the combustion chamber E_{kin} as follows:

$$\frac{dE_{kin,diss}}{dt} = \frac{dE_{kin}}{dt} - C_{diss} \cdot E_{kin,diss} \tag{4.17}$$

where $C_{diss} = 150$ is a modeling constant. Finally, the evolution of the kinetic energy is obtained assuming a linear decrease of the tumble motion from the intake valve closure (IVC) to the top dead centre and using the following expression:

$$\frac{dE_{kin}}{dt} = \frac{dE_{kin,tumble}}{dt} + \frac{dE_{kin,swirl}}{dt} + \frac{dE_{kin,squish}}{dt} + \frac{dE_{kin,spray}}{dt} \tag{4.18}$$

with L the distance between the piston and the cylinder head and ω_{eng} the engine speed in rad.s-1. N_{tumble} is the tumble number at IVC and corresponds to an initial condition for the compression stroke.

Pollutants formation model

As a first step towards pollutant emissions prediction, models for CO and NO creation based on the 3D ECFM approach (Colin et al. 2003, Baritaud et al. 1996) have been developed. These models are presented below. Unburnt hydrocarbons modeling is still in development at IFP Energies nouvelles and will not be discussed in this paper.

CO formation and oxidation In premixed combustion, CO can be created both through the flame and in the burnt gases. CO formation in the flame front mainly occurs in rich mixtures. In this case, instead of using a classical stoichiometric chemical reaction for the fuel oxidation, a set of two equations is used to account for CO and H_2 production:

$$\begin{cases} C_xH_y + \left(x + \frac{y}{4}\right) \cdot O_2 \rightarrow x \cdot CO_2 + \frac{y}{2} \cdot H_2O, & \varphi < 0.98 \\ \alpha_r \cdot \left(C_xH_y + \left(x + \frac{y}{4}\right) \cdot O_2 \rightarrow x \cdot CO_2 + \frac{y}{2} \cdot H_2O\right) + & \\ (1 - \alpha_r) \cdot \left(C_xH_y + \frac{x}{2} \cdot O_2 \rightarrow x \cdot CO + \frac{y}{2}H_2\right) & \varphi \geq 0.98 \end{cases} \tag{4.19}$$

These reactions are weighted using a parameter α_r which can be expressed considering the atomic conservation of C, H and O, as:

$$\alpha_r = \left(0.98 \cdot \frac{4x + y}{\varphi} - 2x\right) \Big/ 2x + y \tag{4.20}$$

If the fuel/air equivalence ratio φ is equal to 0.98, α_r is equal to 1, and both equations of set 4.19 are equivalent. Then, if φ increases, α_r decreases correspondingly and the amount of CO produced increases. This set of equations allows the definition of the stoichiometric coefficients υ_i used in Eq. 4.3. Due to the high level of the burnt gases temperature, chemical reactions influencing CO emissions also occur in this zone. Indeed, the burnt gases composition evolves towards chemical equilibrium concentrations. In order to account for this mechanism, an equilibrium scheme is adopted (Meintjes and Morgan 1987):

$$\begin{cases} N_2 \leftrightarrow 2 \cdot N \\ O_2 \leftrightarrow 2 \cdot O \\ O_2 + 2 \cdot CO \leftrightarrow 2 \cdot CO_2 \\ H_2 \leftrightarrow 2 \cdot H \\ O_2 + H_2 \leftrightarrow 2 \cdot OH \\ O_2 + 2 \cdot H_2O \leftrightarrow 4 \cdot OH \end{cases} \tag{4.21}$$

This set of 6 equations is based on 10 species and must be completed by 4 conservation equations for C, O, H and N to be solved. Then, using a Newton method for the system inversion, the equilibrium concentration $[i]^{equil}$ of each specie i can be computed. As this concentration is not reached instantaneously, a pseudo kinetics is used in the burnt gases as long as $T_u > 1700K$:

$$\left.\frac{dm_i}{dt}\right|_{equil} = \frac{m_i^{equil} - m_i}{\tau_{chem}} \tag{4.22}$$

where τ_{chem} is the time necessary to relax the current burnt gases composition towards the chemical equilibrium. Furthermore, chemical kinetics being strongly dependent on the temperature level, τ_{chem} is expressed as a linear function of the burnt gases temperature.

NO formation Nitrogen oxides are mainly produced at high temperature levels. NO formation is then only described in the burnt gases zone using an extended Zeldovitch mechanism (Heywood 1988) based on a set of 3 reversible equations:

$$\begin{cases} N_2 + O \leftrightarrow NO + N \\ O_2 + N \leftrightarrow NO + O \\ OH + N \leftrightarrow H + NO \end{cases} \tag{4.23}$$

This system is solved using the kinetic constants Ki of the different equations i, with indexes + for the forward direction and for the reverse one. The evolution of NO is then computed as:

$$\left.\frac{d[NO]}{dt}\right|_{Zel'dov} = K_1^+ [O][N_2] + K_2^+ [N][O_2] + K_3^+ [N][OH] - K_1^- [NO][N] - K_2^- [NO][O] - K_3^- [NO][H] \tag{4.24}$$

The evolution of N_2, O_2, N, O, H and OH is also taken into account using set 4.23. Kinetic constants Ki are taken from (Heywood 1988) and defined in Table 2.2. This set of constants is only valid for temperatures higher than 2200 K. Moreover, reactions of NO formation are known to be rapidly frozen during the expansion stroke (Heywood 1988). Consequently, in this work, the Zeldovitch mechanism is only solved for $T_b > 2500K$.

Finally, the mass evolution of the species due to post flame chemistry reactions in the burnt gases is:

$$\left.\frac{dm_i}{dt}\right|_{pf} = \left.\frac{dm_i}{dt}\right|_{equil} + \left.\frac{dm_i}{dt}\right|_{Zel'dov} \tag{4.25}$$

Knock modeling

During spark ignition engines operation, spontaneous autoignition of fresh gases pockets can occur before the arrival of the flame front. This phenomenon, known as knock, produces a distinctive noise and is characterised by a rapid rise of the energy release, pressure and heat transfer in the cylinder. When persisting, this uncontrolled combustion process can even lead to serious mechanical and thermal damages. Knock is known to be very sensitive to the fresh gases composition and temperature. Its occurrence can be prevented by limiting the compression ratio, the spark advance or the boost level when dealing with supercharged engines. However, these solutions have a negative impact on the engine performances and thermodynamic efficiency. Optimizing the engine behaviour from its initial design to its control strategies development can then not be performed without predicting the onset of knock.

Knock timing calculation Knock timing is computed as in the 3D ECFM model using a simple AnB expression to estimate the instantaneous auto-ignition delay θ (Lafossas et al. 2002). This formulation is based on an Arrhenius law and accounts for the research octane number (RON) of the fuel, the fuel/air equivalence ratio φ, the residual burnt gases molar fraction in the fresh gases zone $Xrbg$, the pressure P and temperature of the fresh gases T_u:

$$\theta = A \left(\frac{RON_{eff}}{100}\right)^{3.402} P_{eff}^{-n} e^{\left(\frac{B}{T^u}\right)} \tag{4.26}$$

where, $RON_{eff} = RON\ e\left(0.1\, K_{far}(\varphi - 1)^2\right)$, $P_{eff} = \frac{P}{1+K_{gbr}Y_{gbr}}$ and A, n, B are modeling constants (Table 4.1). The proposed delay expression has the advantage of being low CPU consuming

while providing results close to those obtained by complex chemistry calculations for a large range of operating conditions (Figure 4.6). During the compression and combustion strokes, thermodynamic conditions strongly evolve so that the knock delay can not be given directly by Eq. 4.26. For this purpose, a model describing the evolution of an auto-ignition precursor is used (Lafossas et al. 2002). This precursor P is described by its mass fraction in the fresh gases which can be computed as:

$$\frac{dY_p}{dt} = Y^0_{fuel} F(\theta) \tag{4.27}$$

where $Y^0_{fuel} = m^0_{fuel}/m^0_u$ is the fuel mass fraction in the fresh gases before the start of the combustion and $F(\theta)$ is a function of the delay:

$$F(\theta) = \frac{\sqrt{\alpha^2\theta^2 + 4\,(1-\alpha\theta)\,\frac{Y_p}{Y^0_{fuel}}}}{\theta} \tag{4.28}$$

where $\alpha = 1s^1$ is a constant. When $Y_P = Y^0_{fuel}$, auto-ignition occurs and the corresponding knock intensity is computed.

A	$0,01931s$
n	$1,7$
B	$3800K$
K_{far}	1
K_{gbr}	10

Table 4.1: Default parameters of the Arrhenius law used for the auto-ignition delay calculation.

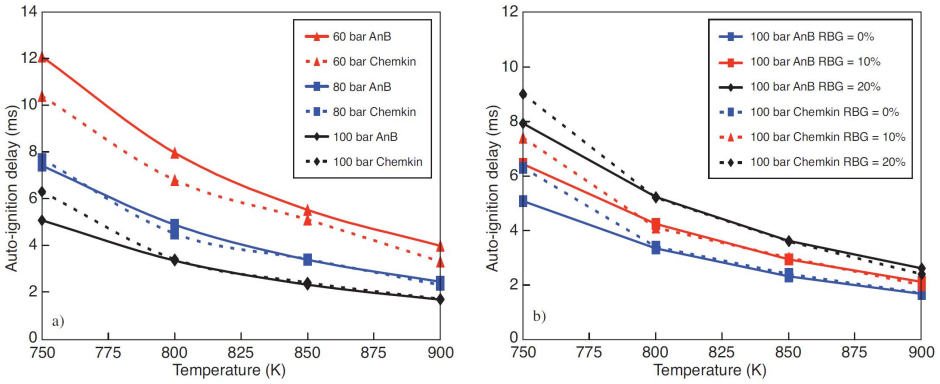

(a) (b)

Figure 4.6: Comparisons between results from the AnB model and complex chemistry calculations (chemical scheme from DCPR 500 species and 2500 reactions (Bounaceur et al. 2004)): a) Delay evolution for different pressures and temperatures and no residual burnt gases – b) Delay evolution for different residual burnt gases rates at 100 bars.

Knock intensity estimation The quantification of knock intensity has enjoyed a great attention in the research literature and many different ways to estimate it have been proposed (Karim 2004, Noda et al. 2004, D'Errico et al. 2007, Teraji et al. 2005, Halstead et al. 1977, Ho and Kuo 1997). The first one consists in simulating the auto-ignition process itself, using reduced or

detailed chemical schemes to compute the corresponding heat release rate (HRR) (Noda et al. 2004, D'Errico et al. 2007, Teraji et al. 2005, Halstead et al. 1977). In this case, a knock intensity should then be calculated from the cylinder pressure or the HRR signal following the same procedure as in experiments. However, using 0D models, it is not obvious to have a fine prediction of the heat release rate for a wide range of operating conditions as knock is strongly dependent of the temperature, fuel and residual burnt gases distribution in the combustion chamber (Castagne et al. 2003). Moreover, for engineering applications, accounting for the influence of auto-ignition processes on the cylinder pressure evolution or the engine work is not of primary importance. What engineers want to know is the degree of spark retard required to avoid severe knock. For this reason, the heat release rate due to knock is not taken into account in this work and knock intensity is simply computed using a correlation. The idea of using a criterion for knock onset has been proposed in previous publications (Karim 2004, Noda et al. 2004, D'Errico et al. 2007, Teraji et al. 2005, Halstead et al. 1977, Ho and Kuo 1997). This criterion K_n is generally based on the energy released by spontaneous auto-ignition of the remaining fresh charge at knock timing normalized by the total energy to be released by combustion through flame propagation. K_n can then be written as:

$$K_n = \frac{m_{fuel^u}}{m_fuel^0} = 1 - bmf \tag{4.29}$$

This formulation has to be corrected in rich cases as combustion may not be complete: $K_n = 1bmf.max(1, \varphi)$. Some authors (Karim 2004, Noda et al. 2004, D'Errico et al. 2007, Teraji et al. 2005, Halstead et al. 1977, Ho and Kuo 1997) also propose to account for the influence of the cylinder volume at the instant of knock occurrence. For this purpose, we propose here a correction based on the compression ratio Π and the knock phasing in the expansion stroke θ_{knock}:

$$K_n = (1 - bmf \cdot max(1, \varphi))\,(\Pi - 1)\sqrt{1 - \frac{\theta_{knock}}{K_2}} \tag{4.30}$$

K_2 corresponds to the maximum crank angle for which knock is still audible and is generally set to 40-50 cad. Finally, it is important to note that knock limited spark advances are often tuned for a given temporal frequency at the engine bench. Then knock margin is not the same at every engine speed and is higher at high rpm levels. Therefore, assuming that knock intensity is directly linked to the knock cyclic frequency, the indicator of Eq. 4.30 can be considered as an image of this frequency. To compare the proposed knock indicator to the experimental one, the engine speed N_{eng} should then be taken into account:

$$K_n = K_1\,(1 - bmf \cdot max(1, \varphi))\,(\Pi - 1)\sqrt{1 - \frac{\theta_{knock}}{K_2}}N_{eng} \tag{4.31}$$

where K_1 is a parameter for tuning the global knock intensity level and expressed in rpm-1. Using Eq. 4.31, four levels of intensity are distinguished:

- $K_n < 0.5$: no knock,
- $0.5 \leq K_n < 1$: trace knock,
- $1 \leq K_n < 1.5$: medium knock,
- $1.5 \leq K_n$: strong knock.

4.1.4 Model validation

The combustion model proposed in this paper has been implemented in the AMESim® simulation software (LeBerr et al. 2006, Albrecht et al. 2005). It has then been used to simulate many steady state operating points of a GDI single cylinder prototype. Experimental data were used for the

boundary conditions (pressure, temperature) and the engine settings (spark advance, injection timing and duration). The main characteristics of the single cylinder engine are summarized in Table 4.2 and the simplified geometry obtained from the pre-processing tool is presented in Figure 4.7.

$Bore\ (mm)$	69
$Stroke\ (mm)$	80.5
$Compression\ ratio$	9.5
$Connecting-rod\ length(mm)$	139

Table 4.2: Single cylinder engine characteristics

Cylinder pressure and engine work

Calibration process methodology The proposed CFM-1D combustion model is based on the reduction of 3D CFD equations and on weak assumptions for the mean flame geometry. It is thus expected to give an accurate description of physical processes without modifying any combustion parameter. Hence, only the turbulence model parameters (N_{tumble} at IVC and l_t) are adjusted to obtain a correct description of the flame front evolution and to match the experimental cylinder pressure curve. These parameters are then tabulated as a function of the volumetric efficiency and the engine speed and can be re-used to simulate transient operating conditions (Lafossas et al. 2005, LeBerr et al. 2006, Albrecht et al. 2005). The engine model used in this study is presented in Figure 4.8. The calculation time for a whole engine cycle was about 1s and 57 operating points covering nearly the entire engine operating range were simulated (engine speed from 1000 to 5500 rpm and IMEP from 2.5 to 30 bars). The turbulence parameters N_{tumble} and l_t were adjusted using an automatic calibration tool, IFP-Optilab. This tool performs a sequence of runs with AMESim® for each operating point and uses optimization methods to minimize differences between experimental and simulated cylinder pressure curves. As IFP-Optilab is dedicated to the combustion stroke calibration, calculations begin at IVC (245 CAD) and end at EVO (475 CAD). Then, an accurate estimation of initial conditions is required to obtain a correct behaviour of the models. These conditions concern the mass fractions of air, fuel and residual burnt gases (Y_{air}^{IVC}, Y_{fuel}^{IVC}, Y_{rbg}^{IVC}) and the mean temperature Y^{IVC} and mean pressure P^{IVC} in the cylinder at IVC. Mass fractions of air and fuel are computed using the measured mass flow rates. However, air or fuel included in residual gases (rg) from the previous engine cycle should not be forgotten, especially if the mixture is not stoichiometric. Moreover, burnt gases contained in residuals have a huge influence on combustion processes (heat release rate, knock, pollutants). Consequently, the residual gas mass fraction at IVC Y_{rbg}^{IVC} has to be precisely estimated to obtain reasonable values for the initial mass fractions of fuel, air and burnt gases. For this purpose, a two step procedure is followed for the model calibration (Figure 4.9).

First step

For each operating point, Y_{rg}^{IVC} is computed using an iterative procedure which stops when convergence is reached ($Y_{rg}^{IVC^n}$ - $Y_{rg}^{IVC^{n-1}} < 10^9$). First, the residual gas temperature at IVO Y_{rg}^{IVO} is calculated assuming an adiabatic expansion of the residual burnt gases at intake valve opening:

$$\frac{T_{gbr}^{IVO}}{T_{gbr}^{EVC}} = \left(\frac{P^{EVC}}{P^{IVO}}\right)^{\frac{\gamma-1}{\gamma}} \tag{4.32}$$

P^{IVO}, P^{EVC} and Y_{rg}^{EVC} are provided by the engine bench and are assumed to be equal to the intake pressure at IVO, exhaust pressure at EVC and exhaust mean temperature respectively.

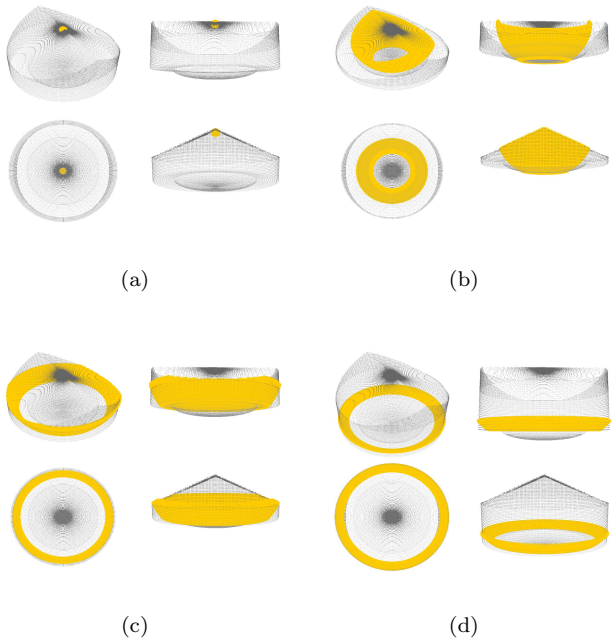

Figure 4.7: Simplified engine geometry obtained using the developed pre-processing tool for different burnt gases volumes and piston positions.

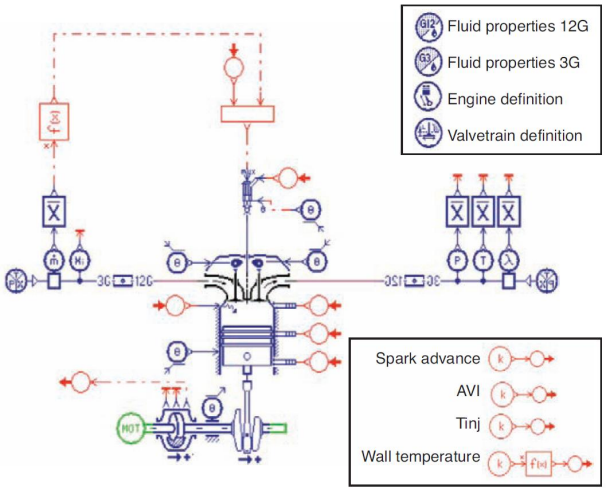

Figure 4.8: Presentation of the single cylinder engine model.

T^{IVC} is then computed following:

$$\underbrace{h\left(T^{IVC}, Y_i^{IVC}\right)}_{mixture\ at\ IVC} = \underbrace{Y_{gbr}^{IVC^{n-1}} \cdot h\left(T_{gbr}^{IV0}, Y_i^{IV0}\right)}_{residual\ gases} + \underbrace{\left(1 - Y_{gbr}^{IVC^{n-1}}\right) \cdot h\left(T_{intake}, Y_i^{intake}\right)}_{fresh\ charge} \tag{4.33}$$

where h is the sensible enthalpy, $Y_{rg}^{IVC^{n-1}}$ is the residual gas mass fraction at iteration $n1$ and subscript i denotes either air, fuel or burnt gases. The intake temperature T_{intake} and composition T_{intake}^{i} are given by experiments, while compositions at IVC Y_i^{IVC} and at IVO Y_i^{IVO} are calculated using the intake composition and residuals mass fraction at iteration $n1$. The enclosed mass at IVC m_{IVC} is then:

$$m_{IVC} = \frac{P^{IVC} V^{IVC}}{r^{IVC} T^{IVC}} \tag{4.34}$$

where V_{IVC} is the cylinder volume at IVC and where the mixture constant at IVC r_{IVC} is estimated from the composition at IVC at iteration $n1$:

$$r_{IVC} = Y_{air}^{IVC} \cdot r_{air} + Y_{fuel}^{IVC} \cdot r_{fuel} + Y_{gbr}^{IVC} \cdot r_{gbr} \tag{4.35}$$

Finally, the residual gas mass fraction at iteration n, $Y_{rg}^{IVC^n}$, is given by the perfect gas law at EVC:

$$Y_{gbr}^{IVC^n} m_{IVC} = \frac{P^{EVC} V^{EVC}}{r^{gbr} T^{EVC}} \tag{4.36}$$

where V^{EVC} is the cylinder volume at EVC and r_{rg} is estimated using the residual composition at iteration $n1$. A first calibration is then performed with IFP-Optilab to build maps for the tumble number and the integral length scale.

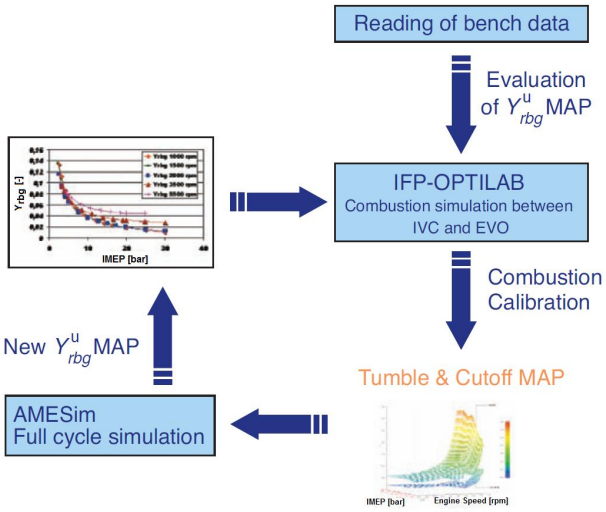

Figure 4.9: Combustion model calibration procedure.

Second step

In order to get a finer estimation of Y_b^{IVC}, multi-cycle simulations are performed on the single cylinder engine model using maps for N_{tumble} and l_t from the first step. When convergence is reached for Y_b^{IVC}, *i.e.* after approximately 5 cycles, the calculation is stopped. The residual gases mass fractions, pressure and temperature at IVC obtained from these simulations are then reused as initial conditions in IFP-Optilab for a second calibration of the combustion model (Figure 4.2).

Differences between Y_{rbg}^{IVC} computed in both steps are almost the same for all engine speeds and are presented in Figure 4.10 for $N = 3500rpm$. It is shown that the residual gas mass fraction at IVC is larger at low load when using the multi-cycle simulation. This is because the back-flow phenomenon occurring at IVO is neglected in the first step, while it is taken into account in the second step. These results then show the advantage of using a two-step procedure to obtain reliable initial conditions for the combustion model calibration.

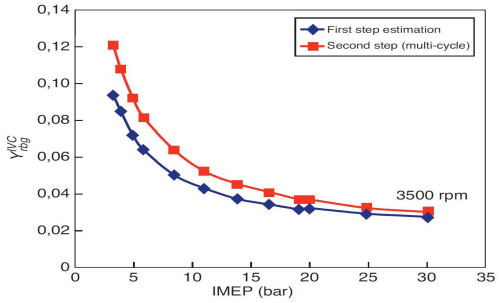

Figure 4.10: Comparison between $Y_r^{IVC}bg$ evaluated in the first step and $Y_r^{IVC}bg$ simulated in the second step.

Simulation results First simulations concern optimal engine settings for 57 points (Figure 4.11) covering a large range of operating conditions and for which experimental data were available.

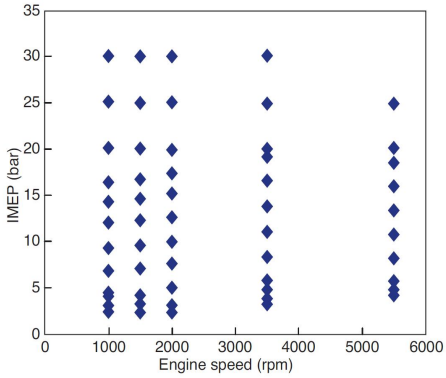

Figure 4.11: Presentation of the 57 steady state operating points used in the combustion model calibration process.

Examples of simulated cylinder pressure curves are presented in Figure 4.12. Uncertainties about the real compression ratio and measured air mass flow rate on this experimental configuration leads to small errors in the compression stroke, especially at high engine speed. For example, the simulated cylinder pressure is underestimated at high load and 5500 rpm. However, results from simulations are globally in good agreement with experimental data, showing that the evolution of the heat release rate is described well for all operating conditions. In particular the maximum cylinder pressure level is correctly reproduced (Figure 4.13) with relative errors less than 1% for 90% of the simulated points. Similarly, good precision is obtained on the IMEP with absolute errors below 0.3 bar for 90% of the points. Moreover, the largest errors on the IMEP are only found at high load, where they do not have any considerable influence on the simulated engine torque.

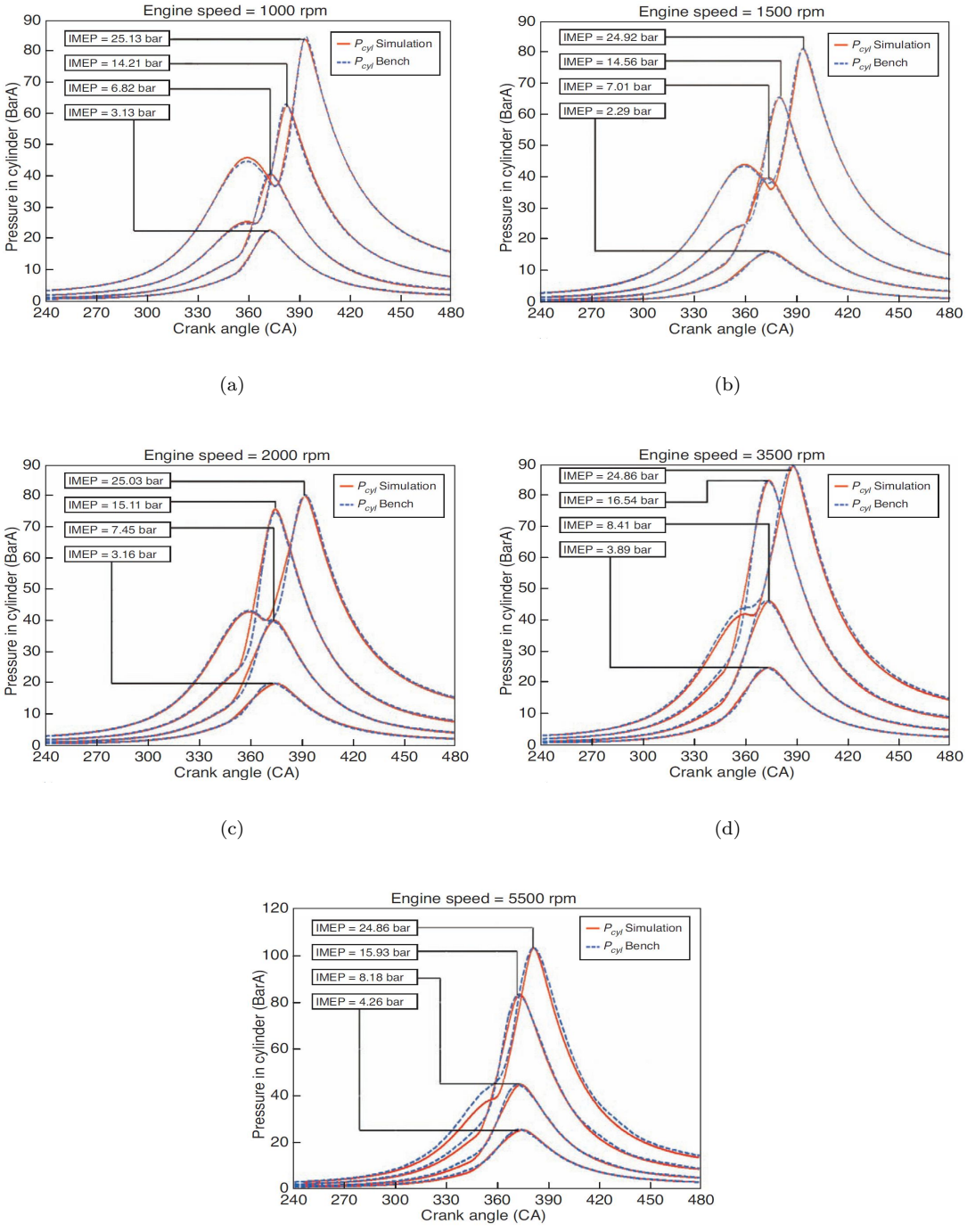

Figure 4.12: Comparison between experimental and simulated cylinder pressure curves for different operating points.

The maps obtained for the tumble number and the integral length scale are presented in Figure 4.14. It is encouraging to note that the evolution of these variables is smooth when varying the load or the engine speed. It should therefore be possible to obtain reasonable values of N_{tumble} and l_t by interpolation of data in look-up tables, for simulating transient engine operations. It is also interesting to note that the integral length scale decreases with the IMEP. As the spark advance is also reduced when increasing the engine load and as l_t represents the integral length scale at spark timing, this means that l_t evolves as expected theoretically: it decreases with the piston-cylinder head distance.

In order to check the behavior of the modeling approach, spark advance variations around optimal settings also called reference settings provided by the engine bench have been simulated. Unfortunately, no experimental data were available for the comparison with calculations. However, these variations concern operating points not limited by knock and for which trends are well known. The results obtained are almost the same for all engine speeds and are presented in Figures 4.15 and 4.16 for $N_{eng} = 3500rpm$. As expected, the maximum pressure level increases with the spark advance and a bell curve is obtained for the IMEP. The maximum of this bell curve should be exactly located at the reference spark advance ($dSA = 0$), corresponding to the experimental SA, if the turbulence model was perfectly predictive.

Indeed, the combustion heat release depends on the turbulent flame surface evolution which is mainly controlled by the turbulence level after ignition. Then the cylinder pressure and IMEP prediction are strongly influenced by the turbulence intensity found at spark timing. Depending on the load, it can be observed in Figure 4.15 that an error ranging from 0 to 3 crank angle degrees is obtained on the best spark advance timing (BSAT) for $N_{eng} = 3500rpm$. This error does not exceed 10 CAD on the whole engine operating map(Figure 4.17) and is less than 5 CAD for 95% of the points. Considering the relative simplicity of the turbulence model used in this work, these results are satisfactory.

The influence of spark timing on the exhaust temperature is presented in Figure 4.16 for $N_{eng} = 3500rpm$. A correct trend is obtained with an increase of the temperature level when decreasing the spark advance. This is due to the fact that the main part of the fuel is burnt in the expansion stroke, so that heat losses at the walls and energy transferred to the piston are smaller. Most of the operating points from the engine map have been set with a unity fuel-air equivalence ratio (FAR). However, in real conditions, the engine can run with non-unity FAR, especially during transients. Hence, it is crucial to have a good behavior of the combustion model when varying the FAR. All the points have then been simulated with FAR ranging from 0.6 to 1.3. Once again, trends are the same at all engine speeds and results are shown in Figures 4.18 and 4.19 for $N_{eng} = 3500rpm$. A high increase of the IMEP is correctly observed for FAR from 0.6 to 1 as more and more energy is released by combustion processes. On the contrary, the IMEP tends to decrease slightly on the rich side with a maximum value situated around FAR = 1.1, which is known to be the fuel air ratio corresponding to maximum engine power. This is due to reactions of dissociation at high temperature involving CO and CO2. These reactions allow to free a small amount of oxygen atoms which can be reused in the burnt gases to oxidize a part of the exceeding fuel. The exhaust temperature T_{exh} evolution is presented in Figure 4.19. A correct decrease is observed on the rich side, with a classical reduction of about 50 K for a FAR increase of 0.1. This reduction is due to the dissociation of CO_2 into CO and O in the burnt gases. The behavior observed on the lean side is more complex. First, the temperature decreases from 1 to 0.8 because the energy released by combustion is reduced while the combustion speed does not vary much (see the fuel burnt mass fraction evolution at IMEP = 8.41 bar). Further, for FAR = 0.7, the combustion speed decreases and the main part of the fuel is burnt during the expansion stroke, so that T_{exh} increases. Finally, when decreasing the FAR to 0.6, the flame speed is very slow leading to a final BMF of less than 5% at EVO and a very low level of the exhaust temperature.

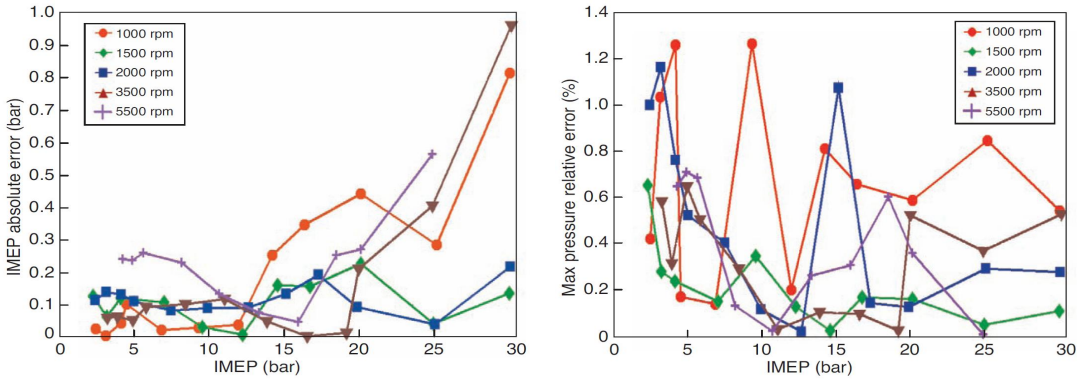

(a) (b)

Figure 4.13: Errors on the IMEP and the maximum cylinder pressure level from the simulations.

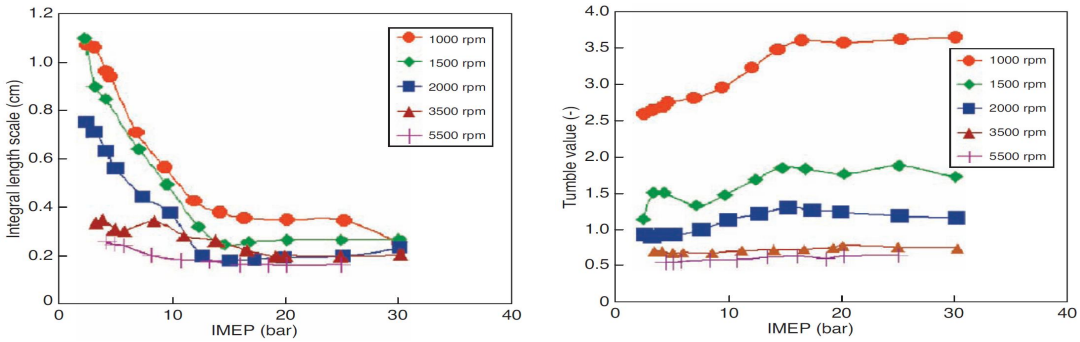

(a) (b)

Figure 4.14: N_{tumble} and l_t maps obtained from the automatic calibration tool.

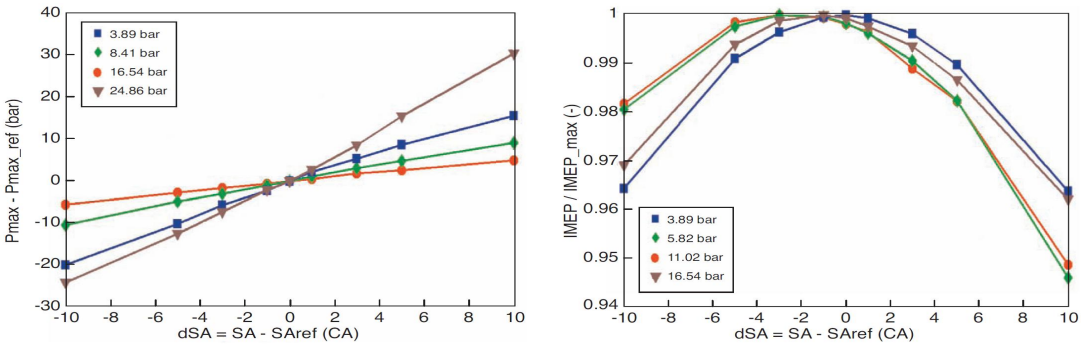

(a) (b)

Figure 4.15: Spark advance variation around optimal engine settings at 3500 rpm for different loads (results from simulations): a) differences between the maximum pressure levels at the optimal spark advance (SAref) and at spark advance SA – b) differences between the maximum IMEP and the IMEP at spark advance SA.

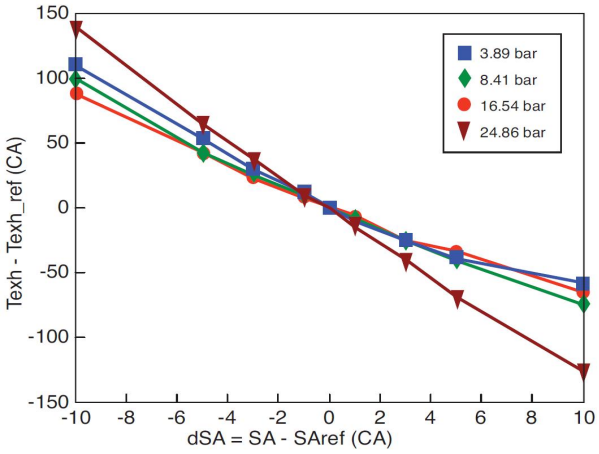

Figure 4.16: Spark advance variation around optimal engine settings at 3500 rpm for different IMEP (results from simulations): differences between the exhaust temperature at the optimal spark advance (SAref) and at spark advance SA.

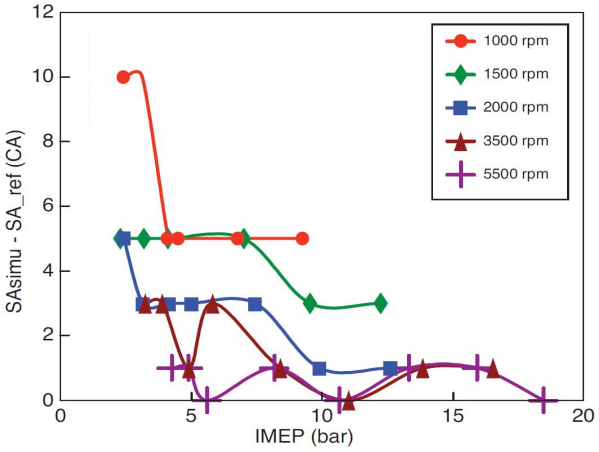

Figure 4.17: Errors on the optimal spark advance from simulations. Results concern only operating points not limited by knock.

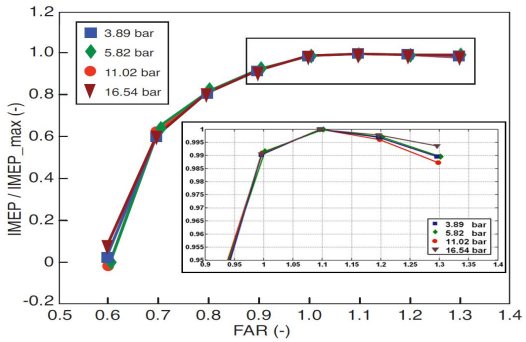

Figure 4.18: Fuel air equivalence ratio variation around stoichiometry at 3500 rpm for different loads (results from simulations): differences between the current IMEP and the maximum IMEP at a given load.

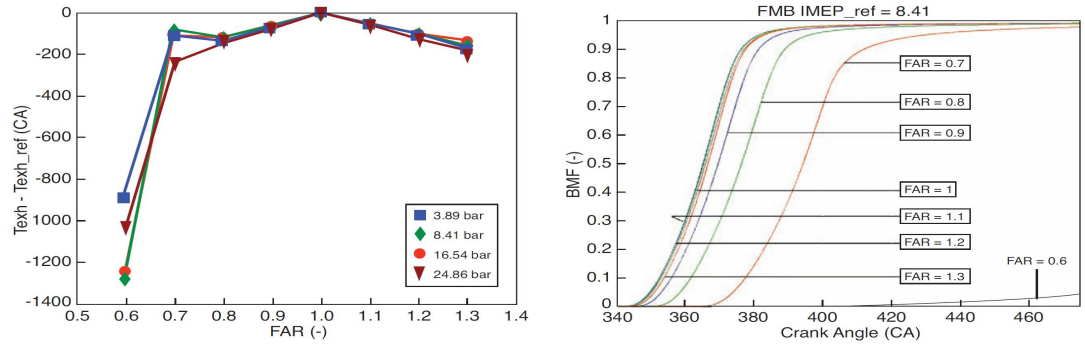

(a) (b)

Figure 4.19: Fuel air equivalence ratio variation around stoichiometry at 3500 rpm (results from simulations): a) differences between the current exhaust temperature and the exhaust temperature at stoichiometry (Texh_ref) – b) fuel burnt mass fraction (BMF) evolution for an engine load corresponding to IMEP = 8.41 bar at stoichiometry.

Pollutant emissions

Simulations of pollutant formation (CO and NOx) have been performed using a linear law for the chemical time scale which is defined as: $t_{chem} = 102s$ at 2500 K and $t_{chim} = 105s$ at 3000 K. Results of calculations for the 57 steady state operating points are presented in Figure 4.22. Emission levels and trends are correctly predicted for most of the engine operating points. In particular, at low rpm, the NO production increases at low load and is stabilized at a value about 2500 ppm at medium and high load. A different behavior is observed at 5500 rpm, where a bell curve is obtained. This evolution is due to a large increase of the fuel-air equivalence ratio at high engine speed and high load. This strategy, used to limit the burnt gases temperature level in order to avoid severe mechanical and thermal damages at the exhaust, also causes an increase of CO emissions. For all the other operating points, CO levels are quite constant with the IMEP and about 0.5 to 1% for all engine speeds. This trend is similar to the experimental one, but it can be observed that the production of CO is slightly underestimated, probably due to the fact that inhomogeneities of fuel and residual burnt gases distributions are not taken into account in the model. Pollutant emissions are known to be experimentally very sensitive to the fuel-air ratio. This behavior is well recovered when using the proposed model (Figure 4.20). Indeed, CO

emissions begin to grow for FAR > 0.9, because of CO_2 dissociation in the burnt gases. Further, for FAR > 1, an increasingly greater quantity of CO is produced in the flame front (Figure 4.21), followed by a very slow post-oxidation in the burnt gases leading to a significant increase of CO concentrations at the exhaust. The NOx evolution also shows a correct behavior with a peak situated at FAR = 0.9, a classical value found in the literature.

Knock

Auto-ignition processes are mainly influenced by thermodynamic conditions in the fresh gases and by the time spent at given values of these conditions. Hence, all operating points do not favour the onset of knock to the same extent. For example, low load and high engine speed operating points have less tendencies to reach auto-ignition than high load and low engine speed points. As explained previously, operating points not affected by knock are set with a spark advance aiming at maximize the IMEP. For this purpose, the SA is tuned to obtain a maximum pressure crank angle of 373 CAD (bottom part of Figure 4.23). For all other operating points, the use of an optimal spark advance would imply severe knock and the spark advance is then set to a limited value called border line spark advance (BLSA) in order to limit the knock level. Indeed, decreasing the spark advance leads to corresponding reductions in the maximum cylinder pressure (Figure 4.15) and knock tendency. In this case, the crank angle at maximum pressure is higher than 375 CAD and increases with a reduction of the spark advance and consequently with the IMEP (Figure 4.23). Experimentally, the BLSA is often determined by engineers for a given knock cyclic frequency which remains small and corresponds to trace knock.

In order to validate the knock model, a procedure similar to the experimental one has been followed: first simulations have been performed using engine settings provided by the bench; subsequently spark advance variations around optimal settings have been studied to check the model sensitivity to the SA. For all calculations the knock intensity constant was set to $K_1 = 67rpm^1$. Defining the dimensionless knock delay θ^* by the ratio between the precursor mass fraction in the fresh gases and the initial fuel mass fraction, knock is supposed to occur when $\theta^* = 1$. Results from the simulations of the 57 steady state operating points are presented in Figure 4.24. As expected, θ^* does not reach unity at low load, especially for high engine speeds. This is coherent with Figure 4.24, where the no-knock zone is larger at high N_{eng} values. The knock intensity, K_n also increases correctly with the IMEP and reaches values between 0.5 and 1, corresponding to trace knock, in the so called "knock limited zone". The limit of this zone, represented by a vertical red line and defined by an IMEP level (I^*) for each engine speed, is quite well predicted by the model as knock mainly appears ($K_n > 0.5$) for IMEP levels higher than I^*. The knock intensity is underestimated only at very high load and engine speed (for example $IMEP = 20.08bars$ and $N_{eng} = 5500rpm$). This is probably due to the fact the cylinder pressure evolution is not well reproduced for these points (Figure 4.12) so that the knock delay is overestimated. In this case, the BMF at spark timing and then the knock intensity are underestimated.

One objective of a knock model is to be able to predict borderline spark advances in the "knock limited zone". Following the modeling approach chosen in this work, for each operating point of the "knock limited zone", the BLSA can be determined by varying the spark advance to reach a fixed knock intensity K_n^{BLSA} situated between 0.5 and 1. Results of simulations for SA variations from 10 CAD to +10 CAD are very similar for all engine speeds and are presented in Figure 4.25 for $N_{eng} = 2000rpm$. Expected trends are obtained: when decreasing (resp. increasing) the SA, Kn correctly decreases (resp. increases). Moreover, a high sensitivity of the knock intensity to the SA can be observed. For example, starting from the experimental spark advance (SA_ref), a decrease of 3 to 6 CAD is sufficient to go from medium knock ($Kn > 1$) to no knock ($Kn < 0.5$). In order to compare the experimental and simulated BLSA, it is supposed that BLSA is experimentally tuned exactly at the same knock intensity level, corresponding to $K_n^{BLSA} = 0.75$, for every points of the "knock limited zone". However, in reality, a margin of about +/-1 CAD can be considered. Prediction of the BLSA from simulations are shown in Figure 4.26. A quite good estimation is obtained for the whole knock limited zone, as the absolute error is below 2 CAD for 80% of the

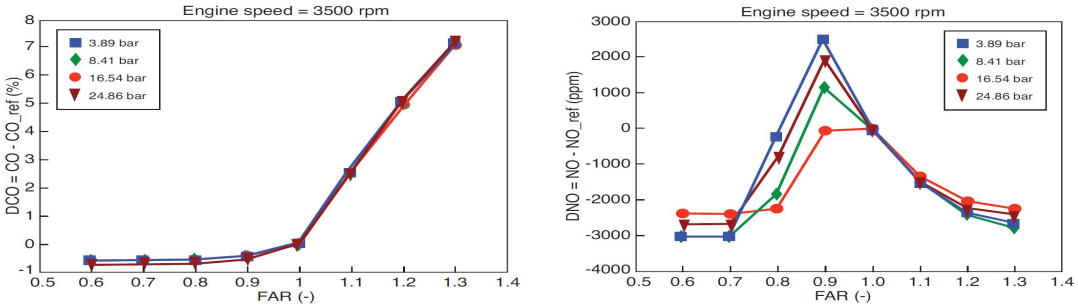

(a) (b)

Figure 4.20: Fuel air equivalence ratio variation around stoichiometry at 3500 rpm for different loads (results from simulations): a) differences between NO emissions at the current FAR and at stoichiometry (NO_ref) – b) differences between CO emissions at the current FAR and at stoichiometry (CO_ref).

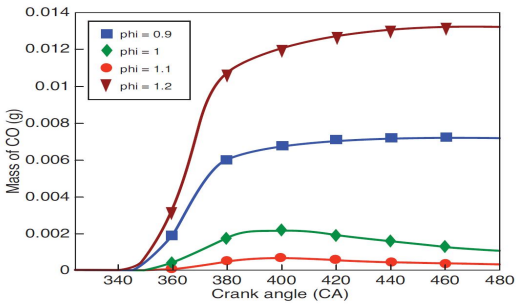

Figure 4.21: Evolution of the mass of CO in the cylinder at 3500 rpm for a given load corresponding to IMEP = 8.41 bars.

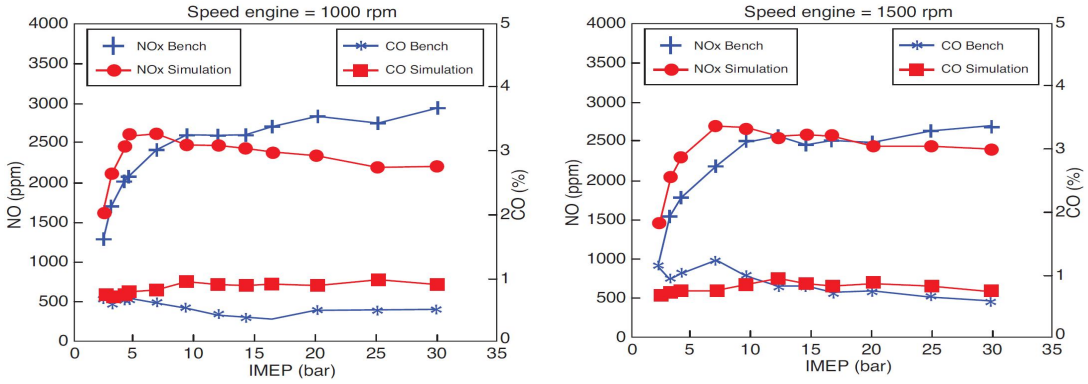

(a)

(b)

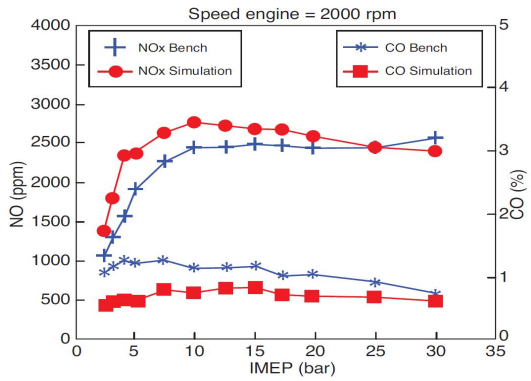

(c)

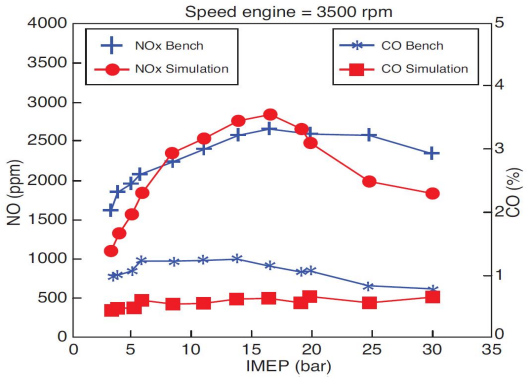

(d)

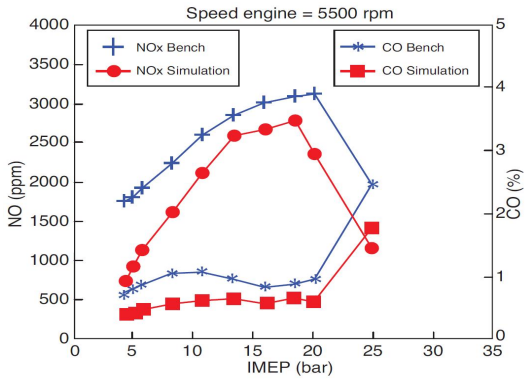

(e)

Figure 4.22: Comparison between experimental and simulated pollutant emissions for the engine optimal operating points.

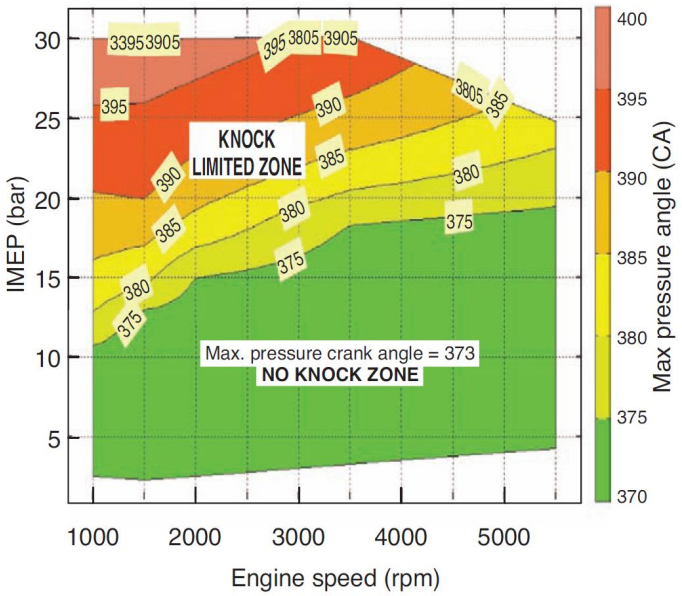

Figure 4.23: Maximum cylinder pressure angle as a function of the engine speed and the IMEP (load). Isolines correspond to operating points which have the same maximum pressure crank angle.

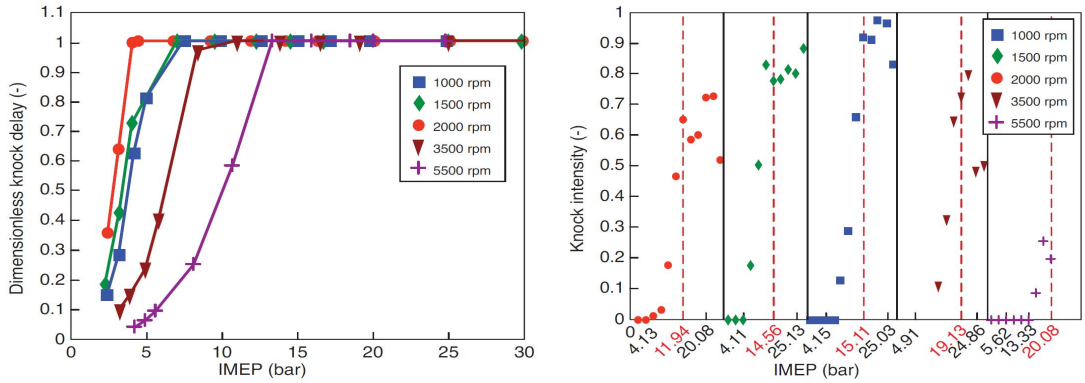

(a) (b)

Figure 4.24: Results from knock simulations. a) Dimensionless knock delay at EVO – b) Knock intensity at knock timing for increasing IMEP. Black lines represent the limit of an iso-engine speed and red ones, the first IMEP for which knock is detected.

operating points. In certain conditions knock can not be avoided only by decreasing the SA, as it causes a very high increase of the exhaust temperature (Figure 4.16) and can lead to severe damages to the engine. In this case, the fuel-air ratio is augmented to typical values of 1.1-1.2 in order to delay the occurrence of auto-ignition. It is then important to check the behavior of the knock model in these conditions. It is shown in Figure 4.27 that the knock intensity decreases of about 0.6-0.8 when increasing the fuel air ratio from 1 to 1.2, which is in good agreement with what is usually obtained experimentally.

4.1.5 Conclusion

In this paper, the latest evolutions of the CFM1D combustion model have been presented. These evolutions concern a better description of the turbulent flame surface evolution and the prediction of knock and pollutant emissions in SI engines. For this purpose, the different transport equations of the 3D CFD E-CFM combustion model were reduced and a new set of 0D balance equations for the fresh gases enthalpy, the species and the flame wrinkling was obtained. The 0D combustion model was then coupled to a simple phenomenological 0D turbulence model. This turbulence model uses the integral length scale at ignition and the tumble number at IVC as initial conditions for the calculation. Pollutant emissions were then described exactly in the same way as in the 3D model: indeed, the model accounts for reactions both in the flame front and in the burnt gases zone. Finally, a knock model based on the description of the evolution of an auto-ignition precursor in the fresh gases coupled with an estimation of the knock intensity was proposed. The CFM-1D model was then implemented in the AMESim® simulation software and used to simulate a wide range of steady state operating conditions comprising 57 points from the optimal engine map provided by experiments and variations of the spark advance and fuel air equivalence ratio around optimal engine settings. A correct description of the engine performances (IMEP, cylinder pressure curve) was obtained in terms of trends and levels for all the points of the engine map. The optimal spark advance was also correctly predicted in the no knock zone. An overall good estimation of pollutant emissions was also achieved and variations of the FAR showed a correct evolution of simulated CO and NOx. Finally, the knock model was used to predict the knock limited zone frontiers as well as the border-line spark advances in this zone. A good agreement was obtained with experiments, with errors close to experimental uncertainties. In conclusion, the proposed model is able to give at the same time a good prediction of performances, pollutant emissions and knock onset on a large range of operating conditions. Nevertheless, it should be noticed that our turbulence modeling is based on a simplified approach. Consequently, without any experimental results (cylinder pressure), the proposed model can only give an estimation of the IMEP by using default values for the integral length scale (typically about 0.5 cm) and the tumble value (typically about 1), but can not provide a good prediction of the maximum cylinder pressure. Therefore, future work will be devoted to the reduction of a 3D turbulence model. The advantage of the CFM- 1D is that this model is compatible with all submodels developed for the 3D E-CFM model (HC emissions, ignition, stratified combustion). Further studies will then be dedicated to the implementation of these models in the CFM-1D model.

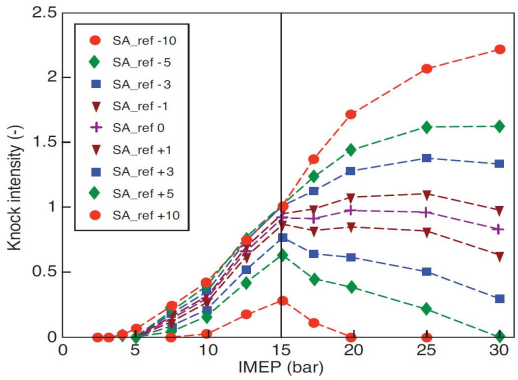

Figure 4.25: Evolution of the knock intensity as a function of the spark advance at 2000 rpm for different loads (results from simulations). SA_ref corresponds to the experimental spark advance. Variations of the SA are given in CAD.

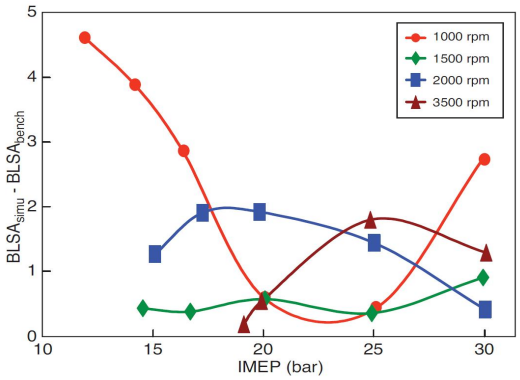

Figure 4.26: Errors on the knock borderline spark advance (BLSA) from simulations.

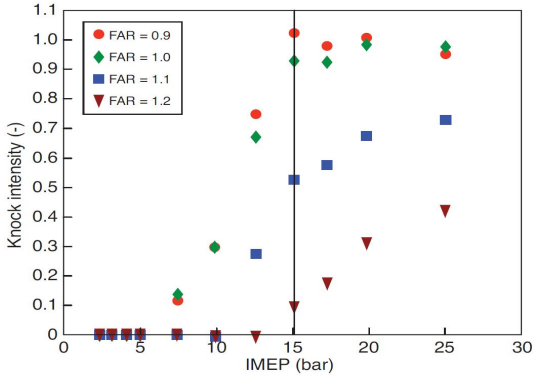

Figure 4.27: Evolution of the knock intensity as a function of the fuel air equivalence ratio at 2000 rpm for different load levels (results from simulations).

4.2 Model enhancement for gasoline/ethanol blends combustion

- **Title**: Modeling and Simulation of the Combustion of Ethanol blended Fuels in a SI Engine using a 0D Coherent Flame Model
- **Authors**: S. Bougrine* **, S. Richard*, Denis Veynante**
  * IFP Energies nouvelles
  ** Laboratoire EM2C, CNRS Ecole Centrale Paris
- **Reference**: SAE paper 2009-24-0016

4.2.1 Abstract

Motor fuels are today increasingly blended with oxygenate components to reduce global CO2 emissions. Among these components, biomass-derived ethanol is very popular for spark ignition engine operation as it is not only a renewable source of energy, but it also allows to increase the engine power and thermal efficiency. Indeed, ethanol has the advantage of a high latent heat of vaporization leading to the so-called "cooling effect" which allows to increase the air-mass flow rate in the engine while reducing the charge temperature. This last property of ethanol combined with its high octane index make the engine less sensitive to knock. Then, although ethanol is characterized by high combustion speeds, optimal values of spark advance can be maintained on a larger range of engine operating conditions and high compression ratios as well as increased levels of downsizing can be used, all these aspects contributing to improve fuel consumptions. However, the real potential of ethanol blended fuels still has to be explored and their impact on engine control strategies has to be investigated, especially considering the possible fuel composition variability during the engine life. Both issues can nowadays be addressed at low cost using system simulations of the whole engine, provided that the models used correctly account for the effect of the fuel composition on combustion processes. This paper deals with the extension of a 0-dimensional coherent flame model to the combustion of ethanol blended gasoline for the simulation of heat release, knock and pollutants in SI engines. This extension mainly relies on the combination of a new laminar flame speed correlation, a modified set of chemical reactions in the flame front and an adapted correlation for the knock delay. The proposed developments are validated on a wide experimental database including many engine operating conditions as well as ethanol volume fractions ranging from 0% to 30%. Parametric variations in terms of spark advance and fuel/air ratio are also performed to compare optimal engine settings obtained from the simulations and at the engine bench. A good agreement is observed, showing the interest of using system simulations to predict the influence of the fuel composition on SI engines operation.

4.2.2 Introduction

Nowadays, mathematical and physical modeling and simulation are an absolute necessity for industrial design applications and especially for powertrain systems which always become more and more complex. Experimental campaigns being often expensive and impossible or prohibited in some fields, are indeed increasingly replaced by numerical simulations. Within the framework of piston engines, the challenge is to develop new eco-aware and cost-efficient systems while improving performances and using experiments on engine benches as little as possible. A promising alternative to experimental tests may be the use of 0D/1D simulation tools. These tools remain today mainly based on mathematical (Wiebe 1956) or simple phenomenological (Tabaczynski et al.

1977, Heywood et al. 1979) approaches. Therefore, they often suffer from a lack of predictivity especially when dealing with complex fluid mechanics problems like combustion and pollutants formation processes taking place in the combustion chambers. It is then essential to develop new models including more physics while remaining low CPU consuming, a crucial issue for an extensive use at all stages of the engine development, from concept design to powertrain control development and calibration. The need for efficient 0D combustion models is today all the more important since regulations on fuel consumption and emissions become always more stringent everywhere in the world. In this context, in many countries, motor fuels are increasingly blended with oxygenate components to reduce global CO2 emissions. Among these components, biomass-derived ethanol is one of the most popular for spark ignition engine operations and is used either as a fuel in pure-ethanol and flex-fuel engines or as an additive in standard gasoline engines (Figure 4.28). One reason explaining the growing success of ethanol is that it is not only a renewable source of energy, but it also allows theoretically to increase the engine power and thermal efficiency (Nakata et al. 2006, Kapus et al. 2007). Indeed, ethanol is characterized by a high latent heat of vaporization leading to a "cooling effect" which reduces the charge temperature and increases the air-mass flow rate in direct injection engines (Marriot et al. 2002). This last property of ethanol combined with its high octane index make the engine less sensitive to knock (Nakama et al. 2008, Starkman et al. 1964, Brinkman 1981, Salih and Andrews 1992, Castro et al. 1994, Maji et al. 2001). Then, although its use leads to high combustion speeds (Bayraktar 2005, Gülder 1982, Gülder 1984, Hara and Tanoue 2006, Farrell et al. 2004, Karpov et al. 1986), optimal values of spark advance can be maintained on a larger range of engine operating conditions contributing to improve both engine performances and fuel consumption. In addition, enrichment at high load usually performed to prevent knock can be avoided allowing interesting gains on oil dilution and HC emissions (Kapus et al. 2007).

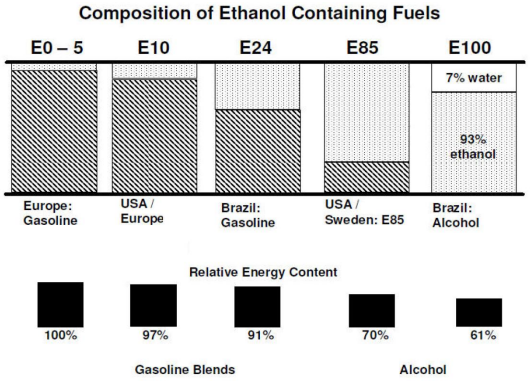

Figure 4.28: SI engines ethanol blended fuels composition around the world (Kapus et al. 2007) (dotted area: ethanol / hatched area: gasoline). EXX is the ethanol volume fraction in the fuel.

However, ethanol also has a high boiling point leading to low evaporating rates and cold start problems [Nakata, Kapus, Cowart, Stodart, Pontoppidan]. Furthermore, in order to take full benefits from the advantageous properties of this component, engines should be re-optimized or even redesigned, using for example high compression ratios or increased levels of downsizing. Today's use of ethanol being generally limited to simple adaptations in terms of injected quantities and spark advances, the real potential of ethanol as a fuel or as an additive combined with new technologies still has to be explored. For this purpose, engine simulations can be used as long as predictive 0D combustion models are available. This paper presents developments performed in the CFM-1D model, originally dedicated to gasoline applications (Lafossas et al. 2005, Richard et al. 2009), in order to predict the effect of ethanol addition in SI engines. This model, based on the reduction of the 3D ECFM model (Colin et al. 2003, Richard et al. 2007, Vermorel et al. 2007), has already shown to be able to reproduce heat release, knock and pollutants in gasoline

engines over the full engine operating map. The aim of these developments is to integrate the influence of ethanol on the turbulent burning rate, pollutant emissions and knock occurrence.

4.2.3 Combustion modeling

The model used here was already presented (4.1.3) and will not be described again in this section. However, some adaptations required to account for fuel properties effects need to be integrated and are presented here.

Laminar flame velocity The laminar flame speed U_l previously computed using Metghalchi and Keck's correlation (Metghalchi and Keck 1982) is only valid for non-oxygenated fuels and has to be replaced for ethanol blends. The measure of the laminar flame speed of ethanol has enjoyed a quite great attention in the research literature (Gülder 1982, Gülder 1984, Hara and Tanoue 2006, Farrell et al. 2004, Karpov et al. 1986), but only Gülder (Gülder 1982, Gülder 1984) and Hara et al. (Hara and Tanoue 2006) worked on simple alkane-ethanol mixtures. In this work, the correlation proposed by Gülder for ethanol-iso-octane blends is retained as iso-octane is quite close to gasoline in terms of laminar flame speed:

$$U_l = U_l^0(\varphi, V) \left(\frac{T_u}{T^0}\right)^c \left(\frac{P}{P^0}\right)^d \tag{4.37}$$

with

$$U_l^0 = FA\varphi^a \exp -b\left[\varphi - 1.075\right]^2 \tag{4.38}$$

where U_l^0 is the reference laminar flame speed at $P^0 = 10^5\ Pa$ and $T^0 = 350K$, T_u is the fresh gases temperature and φ is the fuel air equivalence ratio. F, A, a, b, c and d are coefficients depending on the liquid volume fraction V of ethanol in the fuel. The expression of d also varies with the fuel air equivalence ratio. These 6 coefficients have been calibrated by Gülder Table 4.3 using an experimental database in the range: $300K < T_u < 600K$, $10^5 Pa < P < 8.10^5 Pa$, $0.7 < \varphi < 1.3$ and $0 < V < 20\%$. It should be noticed that the proposed correlation might not be adapted to all engine operating conditions, as the pressure and the fresh gases temperature can respectively exceed $140bar$ and $800K$. In addition the ethanol volume fraction V can reach unity in pure-ethanol or flex-fuel engines applications. Simulation results should then be analysed with care.

Fuel	C_2H_5OH	C_8H_{18}	$C_8H_{18} - C_2H_5OH$
F	1	1	$1 + 0.07V^{0.35}$
A	0.609	0.5924	0.5924
a	0.25	-0.326	-0.326
b	6.34	4.48	4.48
c	1.75	1.56	$1.56 + 0.23V0.46$
d if $\varphi > 1$	$-0.17\sqrt{\varphi}$	-0.22	$-0.22Y_{C_8H_{18}}$ $-0.17\sqrt{\varphi}Y_{C_2H_5OH}$ (Bayraktar 2005)
d if $\varphi \leq 1$	$\frac{-0.17}{\sqrt{\varphi}}$	-0.22	$-0.22Y_{C_8H_{18}}$ $\frac{-0.17}{\sqrt{\varphi}}Y_{C_2H_5OH}$ (Bayraktar 2005)

Table 4.3: Constants of Gülder's iso-octane-ethanol blends laminar flame speed correlation (Gülder 1984) including Bayraktar's correction for the pressure dependency constant (Bayraktar 2005). Y_i corresponds to the mass fraction of component i in the fuel.

In (Gülder 1982, Gülder 1984), Gülder does not provide any expression for the dependency of the laminar flame speed on pressure when varying the fuel composition. Therefore, the correction proposed by Bayraktar (Bayraktar 2005) (Table 4.3) is adopted here. Figure 4.29 presents variations of the laminar flame speed with the fuel air equivalence ratio for 4 ethanol-iso-octane mixtures in engine-like conditions. U_l rapidly increases when adding ethanol and then reaches an asymptotic value for $V \approx 0.2$.

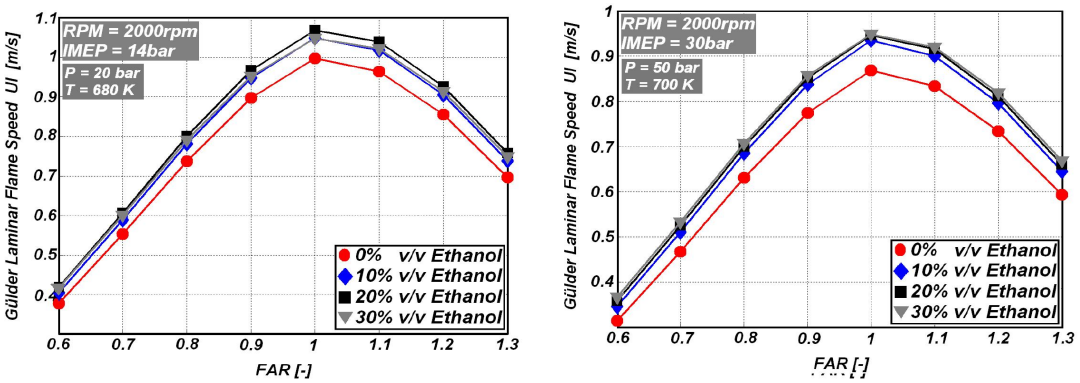

(a) (b)

Figure 4.29: Variation of the laminar flame speed obtained by Gülder's correlation with the fuel air equivalence ratio (FAR) for 4 ethanol-iso-octane mixtures and 2 engine loads (IMEP = 14 and 30 bar) at 2000 rpm. The fresh gases temperature and cylinder pressure used for the calculation are the same for all mixtures and are representative of in-cylinder conditions at spark timing.

Fuel oxidation - Global reaction equation
In the case of oxygenate fuels, Eq. 4.19 turns on :

$$\begin{cases} C_xH_yO_z + \left(x + \frac{y}{4} - \frac{z}{2}\right) \cdot O_2 \rightarrow x \cdot CO_2 + \frac{y}{2} \cdot H_2O, & \varphi < 0.98 \\ \alpha_r \cdot \left(C_xH_yO_z + \left(x + \frac{y}{4} - \frac{z}{2}\right) \cdot O_2 \rightarrow x \cdot CO_2 + \frac{y}{2} \cdot H_2O\right) + & \\ (1-\alpha_r) \cdot \left(C_xH_yO_z + \frac{x-z}{2} \cdot O_2 \rightarrow x \cdot CO + \frac{y}{2}H_2\right) & \varphi \geq 0.98 \end{cases} \tag{4.39}$$

These reactions are weighted using a parameter α_r which can be expressed considering the atomic conservation of C, H and O, as:

$$\begin{aligned} \alpha_r &= 1, & \varphi < 0.98 \\ \alpha_r &= \frac{\frac{0.98 \cdot (4x+y-2z)}{\varphi} - 2 \cdot (x-z)}{2x+y}, & \varphi \geq 0.98 \end{aligned} \tag{4.40}$$

As a reminder, this set of equations allows the definition of the stoichiometric coefficients υ_i used in Eq. 4.3.

Knock intensity quantification The knock phenomenological model presented in section 4.1.4 was developed considering only one fuel formulation. In order to account for the effect of fuel composition on knock occurrence, a new factor is added to the knock intensity correlation (Eq. 4.31 to account for the energy content variation when modifying the fuel formulation. Indeed, one of the advantages of ethanol blended fuels is to decrease the knock intensity thanks to a reduction

of the fuel low heating value (LHV in kJ/Kg). The knock intensity correlation is finally written as:

$$K_n = K_1 \left(1 - bmf \cdot max(1, \varphi)\right) (\Pi - 1) \sqrt{1 - \frac{\theta_{knock}}{K_2}} N_{eng} \cdot \frac{LHV}{LHV_{ref}} \tag{4.41}$$

The ratio between the fuel low heating value of the working fuel and a reference fuel (here iso-octane), LHV/LHV_{ref} , allows also to normalize K_n.

Ethanol-blended fuels properties Parameterization of the fuel properties is a crucial point in combustion simulations. The model retained in this work considers an equivalent chemical formulation for the fuel written as:

$$X_{ref} \cdot C_{x_{ref}} H_{y_{ref}} + X_{C_2H_6OH} \cdot C_2H_6OH \rightleftharpoons C_xH_yO_z$$

x, y and z are also expressed considering the atomic conservation of C, H and O and must be filled in the simulator. The temperature dependency of the heat capacity is determined using a Janaf formulation based on a polynomial expression whose coefficients depend on each fuel component. In practice, two sets of coefficients are used depending on the temperature range ($200K < T < 1000K$ and $1000K < T < 6000K$):

$$C_p(T) = r \left(a_i + b_iT + c_iT^2 + d_iT^3 + e_iT^4\right) \tag{4.42}$$

where $i = 1, 2$ is an index distinguishing high and low temperature levels, C_p is the heat capacity [J/kg/K] and r is the mass ideal gas constant.

No table directly provides the fuel heat capacity as a function of the ethanol proportion in oxygenate fuels. Equivalent polynomial coefficients are then computed considering a weighted average of the fuel components coefficients to obtain the Janaf heat capacity expression of a given gasoline-ethanol mixture.

4.2.4 Model validation

Similarly to the gasoline case (sec. 4.1.4), the combustion model has bee tested on a wide range of steady state operating conditions of the same IFP Energies nouvelles GDI single cylinder prototype (Table 4.2). An extended experimental database of 476 operating points was available. It comprised results for 16 oxygenated fuel formulations, 4 engine speeds from 1000 to 5500 rpm and loads from idle to Wide Open Throttle (Indicated Mean Effective Pressure (IMEP) from 3 to 30 bar). For a better clarity, simulation results for only 116 operating conditions (Figure 4.30) corresponding to 4 fuels A, B, C and D are presented in this paper. Fuels differ by their ethanol fraction ranging from 0% for fuel A to 30% for fuel D. Table 4.2 gives their main characteristics.

The simulator is the same than the one presented in Figure 4.8. The initial conditions (T^{IVC}, P^{IVC}, Y^{IVC}_{air}, Y^{IVC}_{fuel} and Y^{IVC}_{rbg}) are set using the methodology presented in section 4.1.4. Indeed, fuel and air mass fractions are estimated from the measured mass flow rates while the residual gas mass fraction at IVC Y^{IVC}_{rbg} are computed using the procedure described section 4.1.4 leading to the values displayed in Figure 4.31. It should be however noted that scavenging and back-flow processes in the combustion chamber are complex phenomena and uncertainties on the exact value of Y^{IVC}_{rbg} remain. The possible error is estimated at an absolute maximum level of +/- 5%.

Simulation results

A calibration step presented in (Richard et al. 2009) is first performed to adjust the turbulence parameters, considered as the main unknowns of the problem. Indeed 0D models can hardly

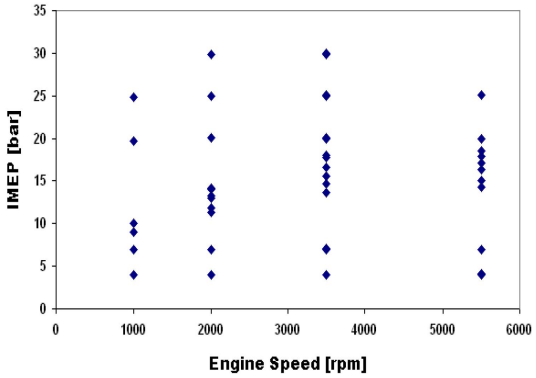

Figure 4.30: Distribution of the 116 operating points used in the simulation process over the engine map

	A	B	C	D
Available experimental operating points data	24	32	32	28
Ethanol volume fraction [%]	0	10	20	30
RON [-]	98.2	100	100.5	100.5
Fuel low heating value (LHV) [kJ/kg]	43102	38500	37192	36054
Density [kg/m3]	744	730.1	756	758.8

Table 4.4: Main characteristics of working ethanol blended fuels

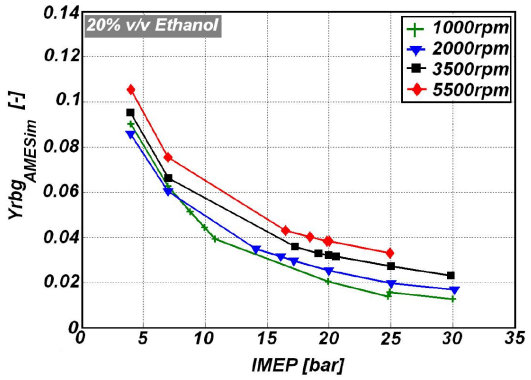

Figure 4.31: Estimates of the residual burnt gases mass fraction of the 20% ethanol blended fuel (C) as function of the engine speed and load.

give a precise description of the in-cylinder turbulent flow which is complex and highly geometry-dependant in SI engines. Then 0D turbulence models always require such a calibration to account for the influence of the air-path and combustion chamber geometry. Results in terms of cylinder pressure trace, pollutant emissions levels and knock prediction are presented in the following.

Cylinder pressure trace and IMEP The turbulence parameters N_{tumble} and l_t are adjusted using an automatic calibration tool, IFP-Optilab. This tool performs a sequence of runs with AMESim® for each operating point and uses optimization methods to minimize differences between experimental and simulated cylinder pressure curves. It then provides an optimized value of the set (N_{tumble} , l_t) for each operating point. These parameters are then tabulated in a map as a function of the volumetric efficiency and the engine speed and can be re-used to simulate transient operating conditions (Lafossas et al. 2005, Albrecht et al. 2005).

One of the objectives of this work was to use the same (N_{tumble} , l_t) map for all the fuel formulations. Indeed, N_{tumble} and l_t are an image of the turbulence level in the chamber which is not supposed to vary a lot with the fuel composition since the aerodynamic conditions at IVC should be similar. However, this last assumption is strong as:

- the latent heat of evaporation which is greatly affected by the presence of ethanol could slightly modify the intake process
- the energy released by combustion which depends on the amount of ethanol in the fuel, has a strong impact on the residual gases temperature level and then on scavenging and back-flow phenomena

In order to confirm these statements, a dedicated calibration process has been performed for each fuel. Results are almost the same for all the engine speeds and the (N_{tumble} , l_t) maps obtained at 3500 rpm are presented in Figure 4.32 for the 4 fuels. A good agreement between the different fuels is shown, indicating that flow motions in the engine are very close from one fuel to another. Therefore, in this study, the reference fuel (A) map is retained for all the following simulations.

It is also encouraging to recover levels quite common for SI engines and to note that the evolution of these variables is smooth when varying the load or the engine speed (not shown here) foreshadowing reasonable interpolated values of N_{tumble} and l_t . In addition, it is interesting to see that the integral length scale decreases with the IMEP. As the spark advance is also reduced when increasing the engine load and as l_t represents the integral length scale at spark timing, this means that lt evolves as expected theoretically: it decreases with the piston-cylinder head distance.

Examples of simulated cylinder pressure curves are presented in Figure 4.33. The use of a single (N_{tumble} , l_t) map for all the fuels combined with a laminar flame speed correlation which is not validated for all engine conditions lead to small errors on the maximum cylinder pressure level ($pmax$). However, results are globally in good agreement with experimental data, showing that the evolution of the heat release rate - and then the turbulent flame speed - is well-described for all operating conditions and all fuels. Relative errors on $pmax$ are indeed lower than 3% for 80% of the simulated points and the IMEP is reproduced with an error less than 1 bar for 75% of the simulated points (Figure 4.34). Moreover, the largest errors on the IMEP are only found at high load (IMEP > 20-25bar), where they do not have any considerable influence on the simulated engine torque.

An other way to look at the combustion model predictivity consists in performing spark advance (SA) variations around the optimal settings - also called reference settings or best settings - provided by the engine bench and which have been used in the previous simulations. Experimental data for these variations were not available. However for operating points not limited by knock, trends are well known: a parabolic curve for the IMEP centered at the optimal SA is expected.

Once again results obtained are similar for all engine speeds and all fuels considered. Some of them are presented in Figure 4.35 for an $N_{eng} = 3500$ rpm and $V = 20\%$. As expected, a bell curve is obtained for the IMEP, approximately located at the reference spark advance (dSA=0 as shown in Figure 4.36 where the errors made on the best spark advance timing (BSAT) for all fuels and operating conditions are displayed. These errors do not exceed 5 CAD on the whole engine operating map and are lower than 3 CAD for 98% of the points. All these results demonstrate the ability of the model to predict the heat release rate evolution and optimization when varying the fuel composition. Moreover, adjusting the turbulence parameters for a reference fuel seems to be sufficient to obtain reliable estimations of the maximum cylinder pressure, IMEP and optimal spark advance for different fuel formulations. In addition, the above simulations indicate that the laminar flame speed correlation proposed in this study (Eq. 4.37) is well-adapted to SI engines operations.

Pollutants emissions This section is dedicated to the evaluation of the pollutant model response when varying the fuel composition. Indeed, experimental data (Figure 4.37) show that there is no simple law to forecast NO and CO formation as a function of the ethanol volume fraction. The challenge is also to predict realistic pollutant levels using the same parameterization of the chemical time scale for all operating points and all fuels.

As in a previous study (Richard et al. 2009), simulations have been performed using a linear law for this time scale defined as: $\tau_{chem} = 10^{-2}s$ at $T_b = 2500K$ and $\tau_{chem} = 10^{-5}s$ at $T_b = 3000K$. Results are once again similar for all engine speeds and fuels and are displayed in Figure 4.37and 4.38 for conditions representative of the whole database in terms of fuel composition, speed and load. Figure 4.37 indicates that no trends on NO and CO emissions can be clearly identified in the simulations when increasing the amount of ethanol in the fuel, which is in good agreement with experimental data. In Figure 4.38, vertical bars represent the modification of the NO level for a +/- 5 absolute variation of the initial residual burnt gas mass ratio (Y_{rg}^{IVC}) in order to account for uncertainties about the real amount of burnt gases in the combustion chamber at IVC as discussed previously. For values of Y_{rg}^{IVC} lower than 5%, an absolute variation of -5% corresponds to $Y_{rg}^{IVC} = 0$. It should be noticed that the residual burnt gases level has a strong impact on the NO level and should be precisely estimated to obtain fully predictive simulations. It then appears as a key point in pollutant emissions prediction. The variations of CO with Y_{rg}^{IVC} are not presented because of the low level of concentrations. Indeed, CO levels are quite constant with the IMEP and about 0.5 to 1% for all engine speeds and a +/- 5% absolute variation of Y_{rg}^{IVC} doesn't have a huge impact on them. Finally, simulation results are globally satisfactory with a good prediction of the emissions levels and trends. It can also be observed that the production of CO is slightly underestimated, probably because of inhomogeneities of fuel and residual burnt gases distributions which are not accounted for in the model.

Knock Increasing the ethanol rate in the fuel leads to a reduction of the fresh gases temperature. Combined with the high octane index of ethanol, this phenomenon strongly reduces the probability of knock occurrence in the engine. This advantage of ethanol blended fuels can be verified on Figure 4.39 which shows the experimental maximum cylinder pressure angle (αP_{max}) as a function of the engine speed and load for the 4 fuels of this study.

It should be noticed that the bottom part of the graphs increases with the ethanol volume fraction. This area represents operating points which are not limited by knock and which SA allows to maximize the IMEP. In this case, an optimized maximum pressure angle of 373 CA is generally adopted. This is not possible when increasing the engine load at a given engine speed as knock may appear and the spark advance is then retarded to a limited value - called border line spark advance (BLSA) - leading to higher αP_{max} levels. Experimentally, knock is often ear-detected and the spark advance is chosen to reach trace knock, which corresponds to a knock

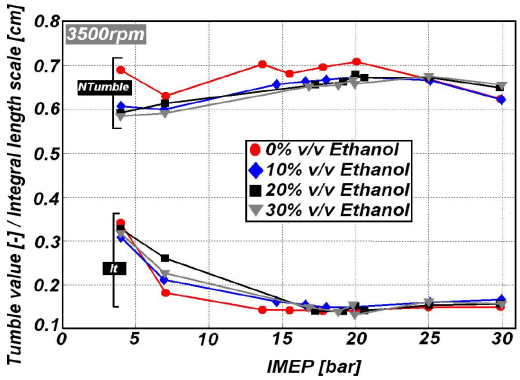

Figure 4.32: N_{tumble} and lt maps obtained from the automatic calibration tool for the 4 fuels.

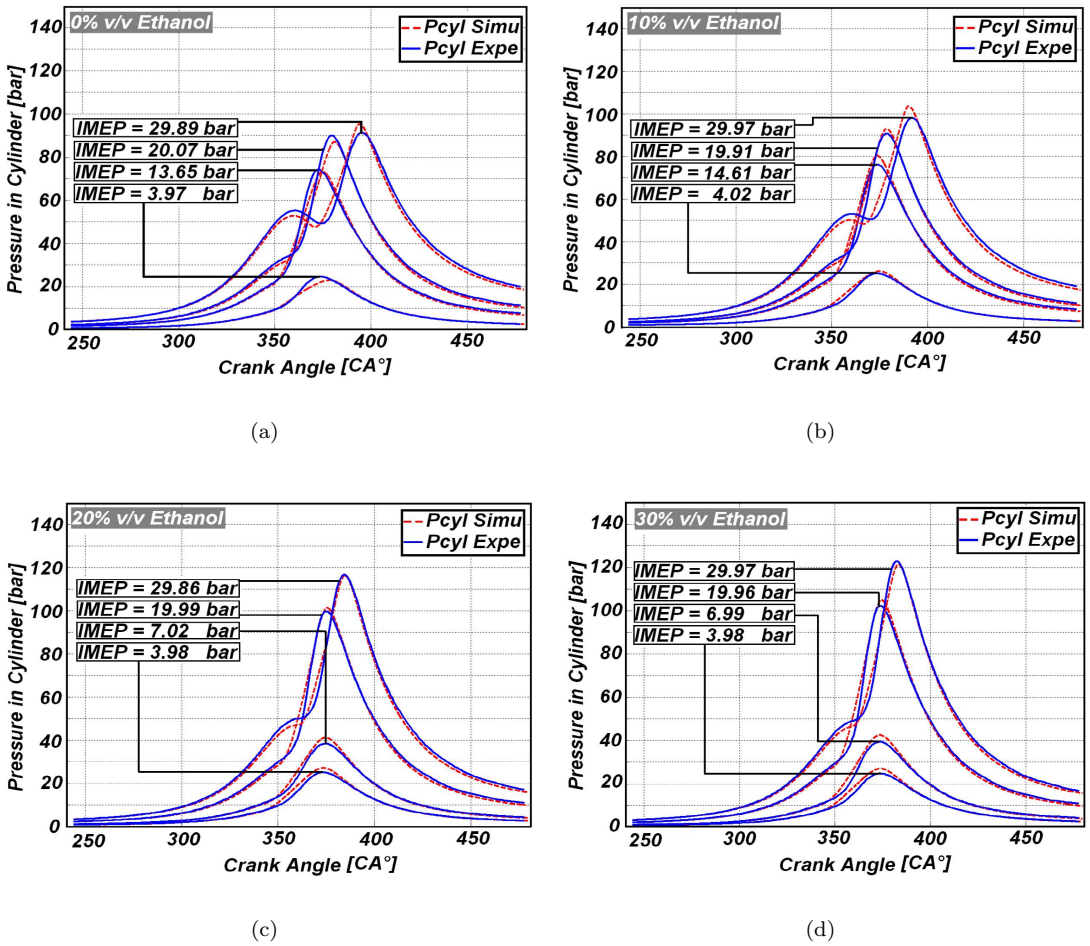

Figure 4.33: Comparisons between experimental and simulated cylinder pressure curves for different engine loads and fuels at 3500 rpm.

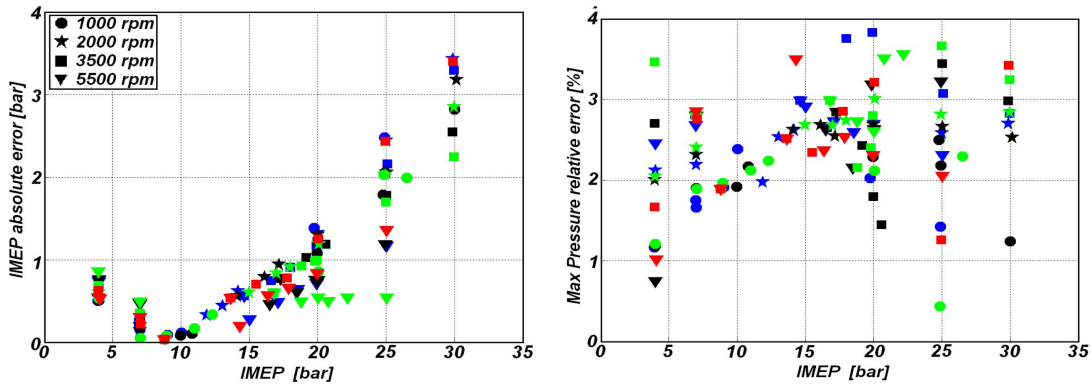

(a) (b)

Figure 4.34: Errors on the IMEP and the maximum cylinder pressure level from the simulations for the 116 operating points.

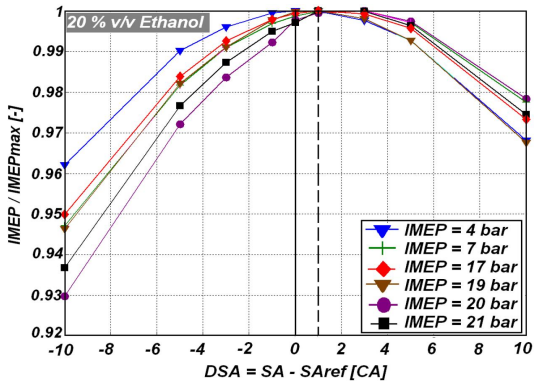

Figure 4.35: Spark advance variation around optimal engine settings at 3500 rpm for different loads (results from simulations): differences between the maximum IMEP and the IMEP at spark advance SA.

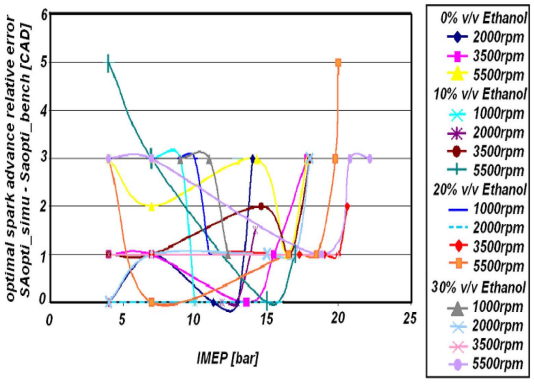

Figure 4.36: Errors on the optimal spark advance from simulations. Results concern only operating points without knock.

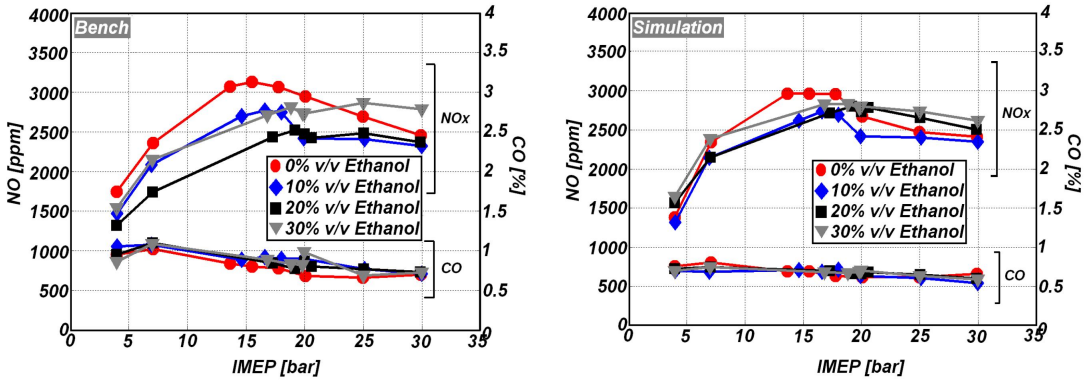

(a) (b)

Figure 4.37: NO & CO emissions levels for 4 ethanol rates at $N_{eng} = 3500rpm$. a) experiment – b) simulation.

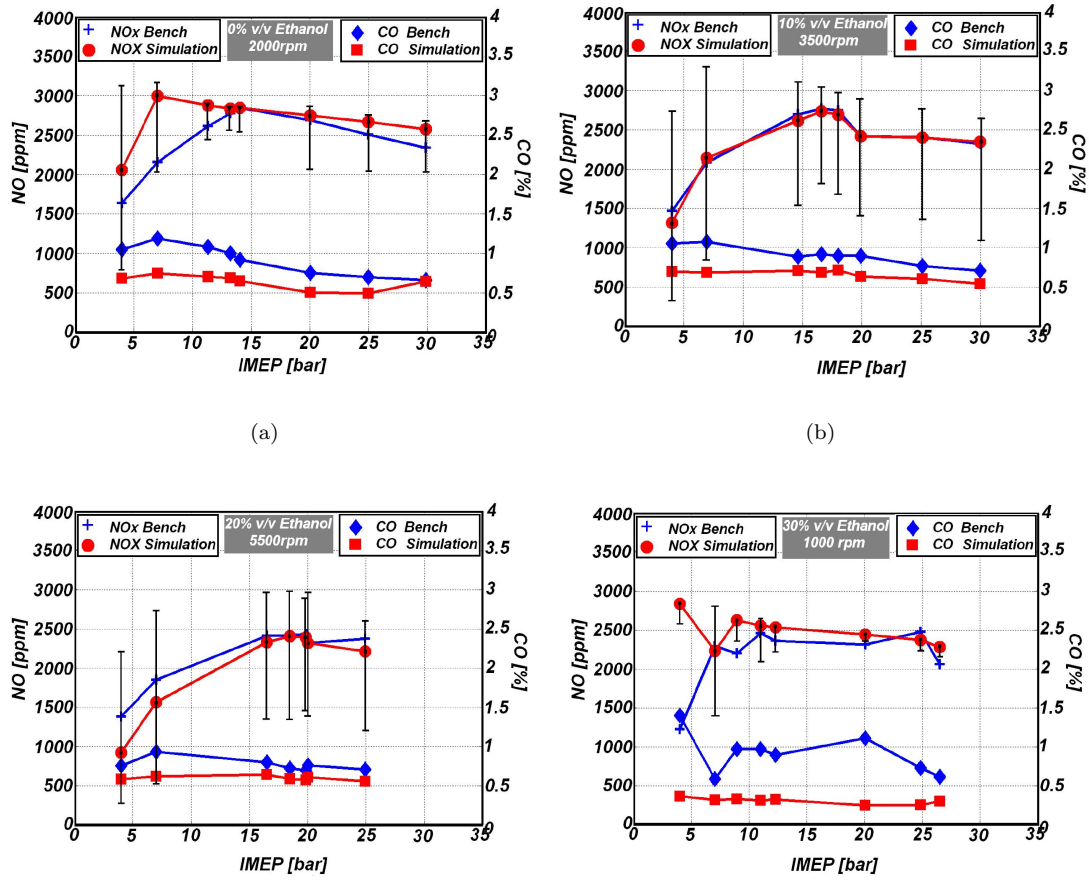

(a) (b)

(c) (d)

Figure 4.38: Comparison of simulated and experimental pollutant emissions for different operating conditions and fuels.

intensity of $0.5 < K_n < 1$ in the proposed model. This simple method of detection however leads to uncertainties on the experimental BLSA which could be about 1-2 CA. As auto-ignition process is influenced by thermodynamic conditions in the fresh gases and by the time spent at given values of these conditions, it is also logical to see that knock is more severe for high loads and low engine speeds.

The aim of this section is to present results on knock delays and intensities when varying the ethanol volume fraction. The different parameters of the knock model are kept constant and the fuel formulation is taken into account via the fuel heating value correction and the research octane number. Results from the simulations are presented in Figures 4.40-4.44.

Considering the simplicity of the proposed knock model, results are satisfactory as they are coherent with the previous experimental maps (Figure 4.39) where the no-knock zone is larger at high N_{eng} values. Indeed, the dimensionless knock delay θ^* does not reach unity at low load, especially for high engine speeds (Figure 4.40). Moreover, it can be noticed that θ^* reaches faster unity when decreasing the ethanol volume fraction which joins up with the previous description of αP_{max} maps.

Knock intensity results are almost the same for all fuels and are presented in Figure 4.41 for fuel C. K_n correctly increases with the IMEP and reaches levels corresponding to trace knock in the knock limited zone. Indeed, simulations show that points which intensities are higher than I^* - colored vertical strips representing the knock limited zone already shown in Figure 4.39 - are globally ranged between 0.5 and 1.

In order to go further in the analysis, a second validation step has been performed to check the knock model sensitivity to a SA or a FAR variation. Experimentally, engineers tune SA up to find the knock borderline spark advance ($BLSA$). The principle of the following simulations is thus to reproduce this experimental procedure to assess the ability of the knock model to predict the experimental $BLSA$ for each operating points of the "knock limited zone" (Figure 4.39). Therefore, SA variations have been performed around experimental settings from -10 CAD to 10 CAD. Results of simulations are very similar for all engine speeds and fuels and are displayed in Figure 4.42 for $N_{eng} = 2000$ rpm and $V = 20\%$. Expected trends are obtained: when decreasing (resp. increasing) the SA, K_n correctly decreases (resp. increases). A high sensitivity of the knock intensity to the SA can also be observed. The associated resolution is about +/-3 CAD for most of the simulated points. Considering the uncertainty of experimental measures, this result is satisfactory. In order to have global view of the knock model ability to predict $BLSA$, a comparison between experimental and simulated $BLSA$ is performed. For the analysis, the experimental $BLSA$ is supposed to be exactly tuned at the same knock intensity level, corresponding to a fixed knock intensity $K_n^{BLSA} = 0.75$. Varying the SA in the simulations to reach an exact intensity of 0.75 then allows to recover values for BLSA. If the model was perfectly predictive and without experimental uncertainties, the BLSA obtained by the simulation should be exactly the one provided by the engine bench and used in the previous simulations (Figure 4.40 and 4.41). Differences between the simulated and experimental BLSA are plotted in Figure 4.43. A fairly good estimation is obtained for the whole knock limited zone, with absolute errors bellow 2 CAD for 75% of operating points.

Finally, the sensitivity of the knock model to a FAR variation is tested. Experimentally, FAR is indeed often increased at high engine speeds and high loads to avoid severe thermal damages downstream of the combustion chamber which could be caused by the high temperature levels reached at the exhaust when retarding the SA. Using rich mixtures allows to increase the knock delay and consequently, to avoid auto-ignition. Figure 4.44 shows that the knock intensity decreases of about 0.8 when increasing the fuel air ratio from 1 to 1.2, a classical value retained in enrichment periods. It can also be observed that a reduction of the FAR from 1 to 0.9 has not a strong impact on the knock intensity because the flame speed is also reduced leading to the same amount of remaining fresh gases at knock timing as for $FAR = 1$. To conclude, the knock model

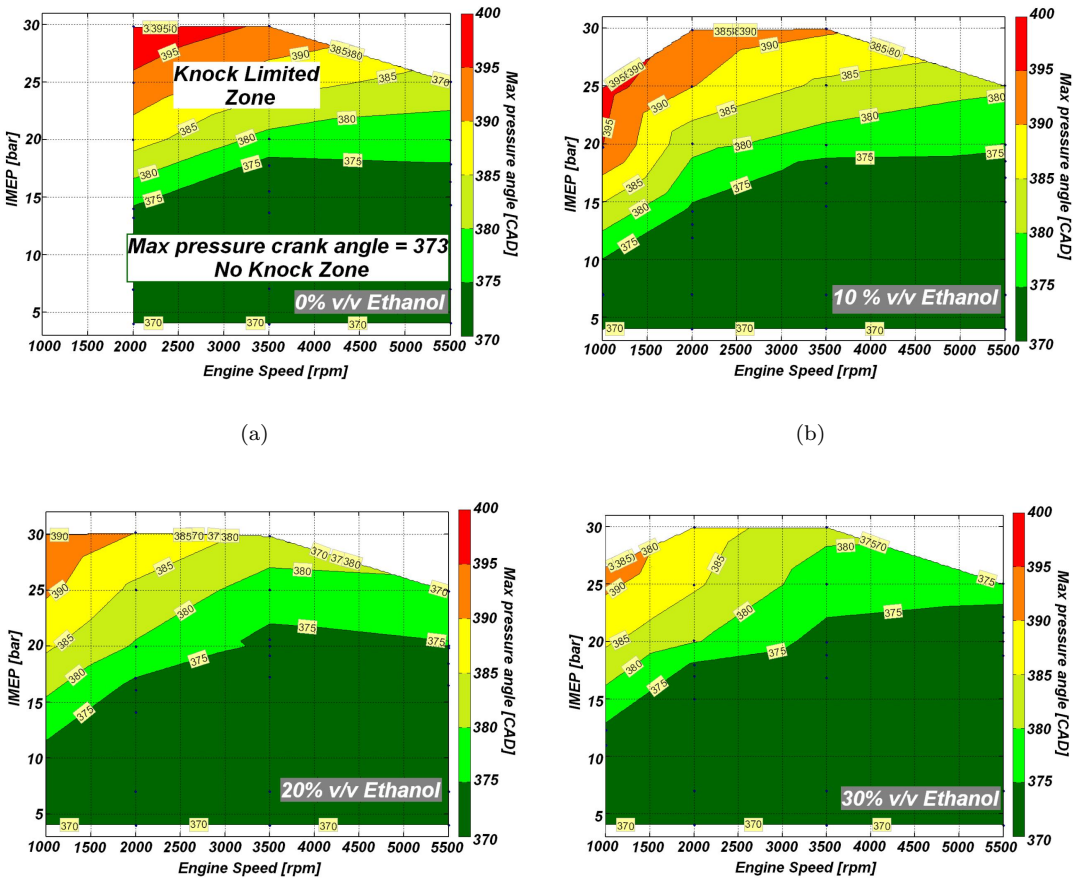

(a) (b)

(c) (d)

Figure 4.39: Isolines of maximum cylinder pressure crank angle as a function of the engine speed and load.

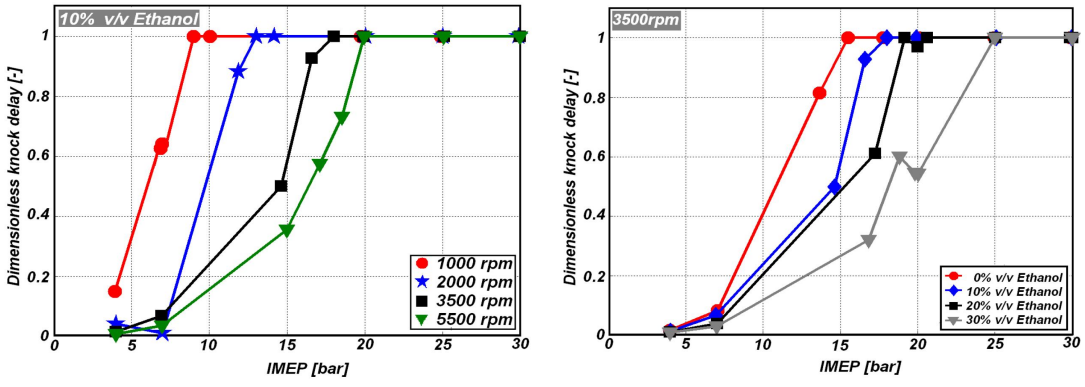

(a) (b)

Figure 4.40: Results from knock simulations. Top: dimensionless knock delay at EVO as a function of the IMEP for each engine speed (fuel C), Bottom: dimensionless knock delay at EVO as a function of IMEP for each fuel.

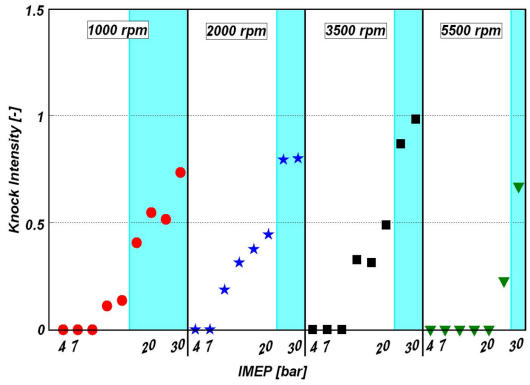

Figure 4.41: Knock intensity at knock timing as a function of the engine speed and the IMEP for fuel C. Black lines represent the limit of an iso-engine speed and colored zones to the knock limited SA area.

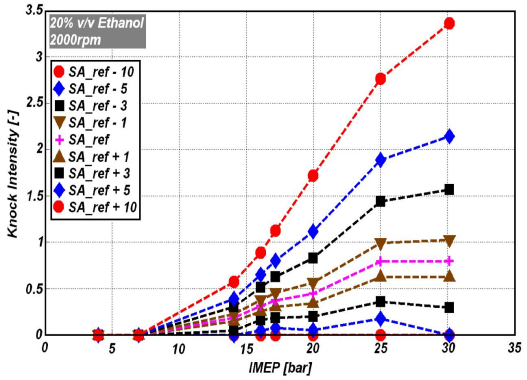

Figure 4.42: Evolution of the knock intensity as a function of the spark advance at 2000 rpm for different loads and for $V = 20\%$ (results from simulations). SA_ref corresponds to the experimental spark advance. Variations of the SA are given in CAD.

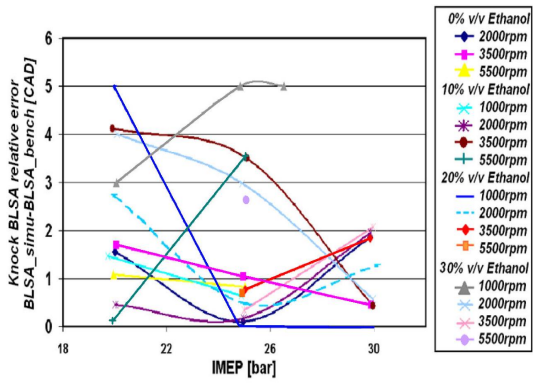

Figure 4.43: Errors on the knock borderline spark advance ($BLSA$) in CAD from simulations.

correctly allows to recover BLSA and the influence of the FAR for most of the engine operating conditions and all fuels. It can then be used for design and control purposes, especially when optimizing an engine for ethanol blended fuels applications.

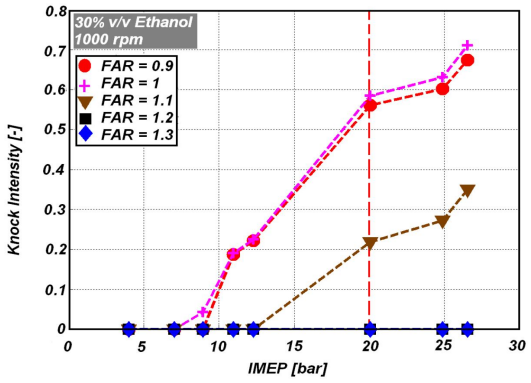

Figure 4.44: Evolution of the simulated knock intensity as a function of the fuel air equivalence ratio at 1000 rpm for different load levels and for $V = 20\%$.

Effect of ethanol on the engine efficiency Effect of Ethanol on the Engine Efficiency It is known that when used in existing gasoline engines configurations, ethanol blended fuels only allow to reduce fuel consumption at high load by allowing higher spark advances than gasoline (Kapus et al. 2007, Marriot et al. 2002, Nakama et al. 2008, Starkman et al. 1964, Brinkman 1981, Salih and Andrews 1992). This trend is correctly recovered in Figure 4.45, showing that the model developed in this work provides reliable engine efficiency levels.

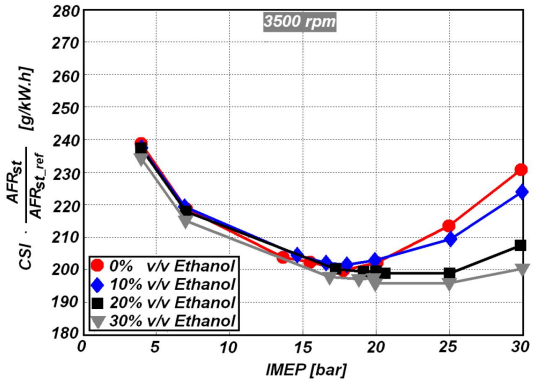

Figure 4.45: Specific fuel consumption corrected by the stoichiometric FAR ($FARst$) as a function of the IMEP for the different fuels. $FARst_ref$ corresponds to case 0% v/v Ethanol.

4.2.5 Conclusion

The aim of this paper was to evaluate the predictivity of the CFM-1D combustion model already presented in Richard et al. (2009) when dealing with ethanol blended fuels. Some evolutions have been brought to this model initially dedicated to gasoline applications and were presented. First, the laminar flame speed previously estimated using Metghalchi and Keck's correlation is here obtained by Gülder's one which has been experimentally calibrated considering iso-octane-air-ethanol mixtures. Regarding the turbulence model, the integral length scale at ignition and the tumble number at IVC are still used as initial conditions for the calculation. Considering that initial aerodynamic conditions in the chamber do not significantly vary when changing the fuel composition, the integral length scale and the tumble number have been fixed for all the fuel formulations. Pollutant emissions equations have been adapted including the oxygen contained in the fuel. Finally, the knock model has been updated to account for the heating value of each fuel in the knock intensity calculation. Simulation results presented in this paper have been obtained for 4 ethanol blended fuels with ethanol volume fractions ranging from 0% to 30%. The CFM-1D model calibration and validation process were the same as in a previous work (Richard et al. 2009). In spite of a single turbulence parameters map without distinction of the fuel formulation, a correct description of the engine performances (IMEP, cylinder pressure curve) was obtained in terms of trends and levels for all the points of the engine map. The optimal spark advances were also correctly predicted.

Considering a unique parameterization of the knock model for all fuels and operating conditions, knock simulations provided satisfactory results. Notably, the knock limited zone frontiers were correctly described as well as the border-line spark advances in this zone. Potential errors on the burnt gases mass fraction evaluation at IVC has led to small errors on the estimation of pollutant emissions. However, trends and levels were globally well-predicted and variations of the FAR showed a correct evolution of the simulated CO and NO levels.

Finally, all these results demonstrate the ability of the model to predict the impact of the fuel formulation on performances, consumption and emissions of a given engine. The proposed model then appears as an interesting tool to evaluate the potential of ethanol blended fuels combined with new technologies as high downsizing or variable compression ratio devices. This model can also be used in the learning process of neural network based models (LeBerr et al. 2006) to build real-time combustion models for engine control applications.

4.3 Complementary comments

According to conclusions of both previous sections, the CFM1D model appears as an efficient tool to describe physical phenomena occurring in SI engines such as combustion, post-oxidation and knock. Indeed, good agreements between simulation and experimental data are shown for both pure gasoline and gasoline-ethanol blends. This last observation demonstrates also the ability of the model to account for fuel composition variation effects. Besides, simulations on the same engine configuration confirmed that the model leads to similar results (compared to gasoline and gasoline-ethanol blends cases) in term of heat release and pollutant prediction when burning methane. Indeed, as presented in Figures 4.46 and 4.47 experimental pressure traces and NO and CO levels at the exhaust are globally well-recovered. Results on knock prediction are not available for methane case because of the high RON level which prevents knock occurrence. That is why in Figure 4.46 every pressure curves have a maximum around 373 CA : no operating point is limited by knock. Note that the correlation of Rahim (Rahim et al. 2002) for the laminar flame velocity described in Eq. 2.20 is used here for methane case.

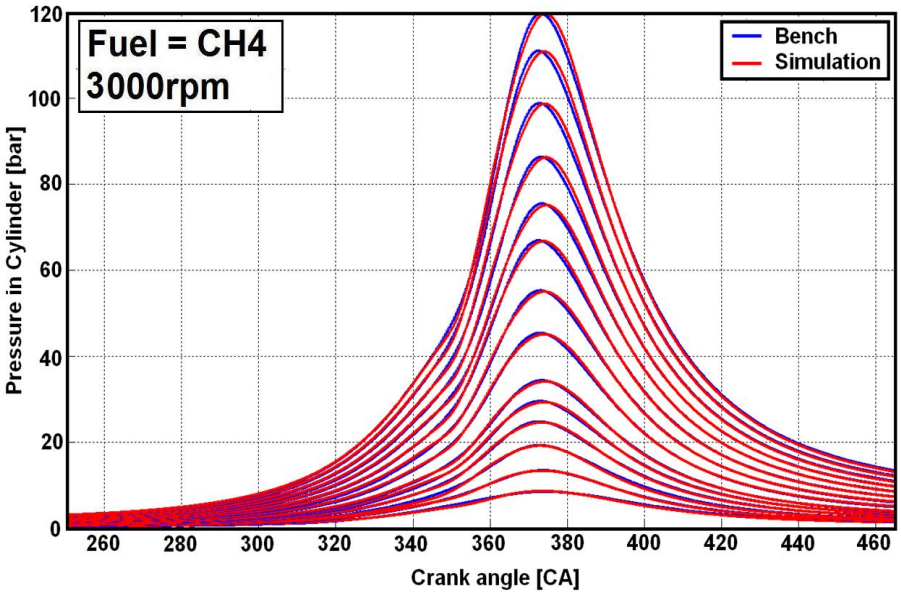

Figure 4.46: Comparisons between experimental and simulated cylinder pressure curves for different engine loads at 3000 rpm. Fuel = methane.

Even if all these conclusions are satisfying, some developments are still required to improve the predictivity and performance of the model :

- **Pollutants** – As shown in Figures 4.20,4.21,4.22,4.38 and 4.47, the prediction of NO and CO levels is well-described and an improvement of present results seems to be tricky. However, with regard to emissions restrictions (Table 1.1), the precision on pollutants prediction is more and more severe and observed differences between experimental data and simulation finally remain significant, notably in term of CO prediction. Moreover, focusing on system simulation, it should be pointed out that the chemistries solved to account for species evolution (Eqs. 4.19, 4.21 and 4.23) require significant computational resources. Indeed, as previously mentioned, the calculation time for a whole engine cycle is about 1s. This order of magnitude is satisfying regarding engine development and evaluation of the potential of new strategies. It is also low enough to allow an use in the learning process of neural network based models (LeBerr et al. 2006) to build real-time combustion models for engine control

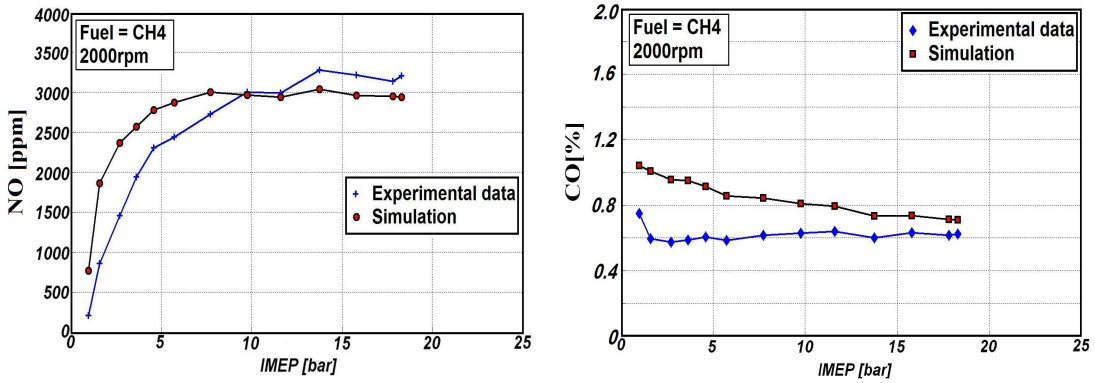

(a)

(b)

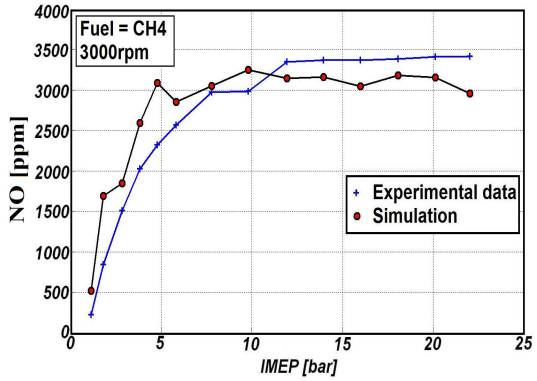

(c)

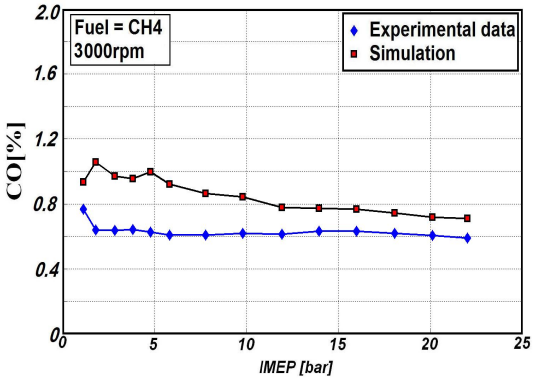

(d)

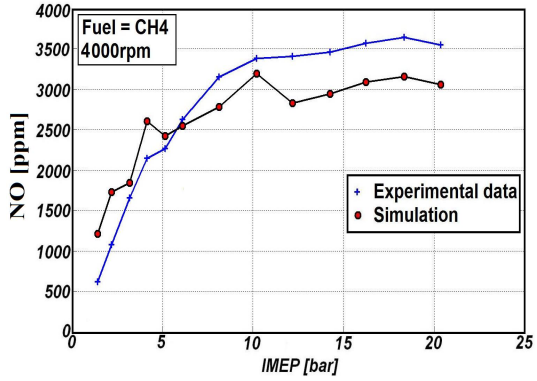

(e)

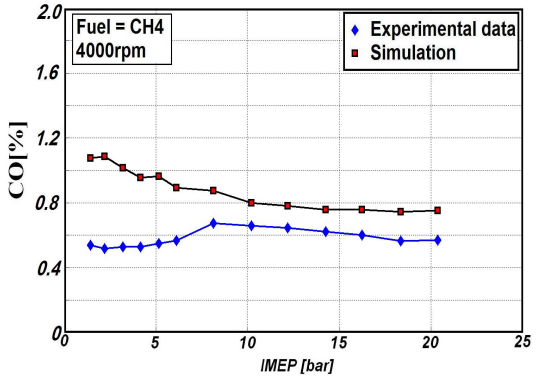

(f)

Figure 4.47: NO and CO evolutions as functions of engine load. Fist column: NO evolutions – Second column: CO evolutions – First row: 2000rpm – Second row: 3000rpm – Third row: 4000rpm. Fuel = methane.

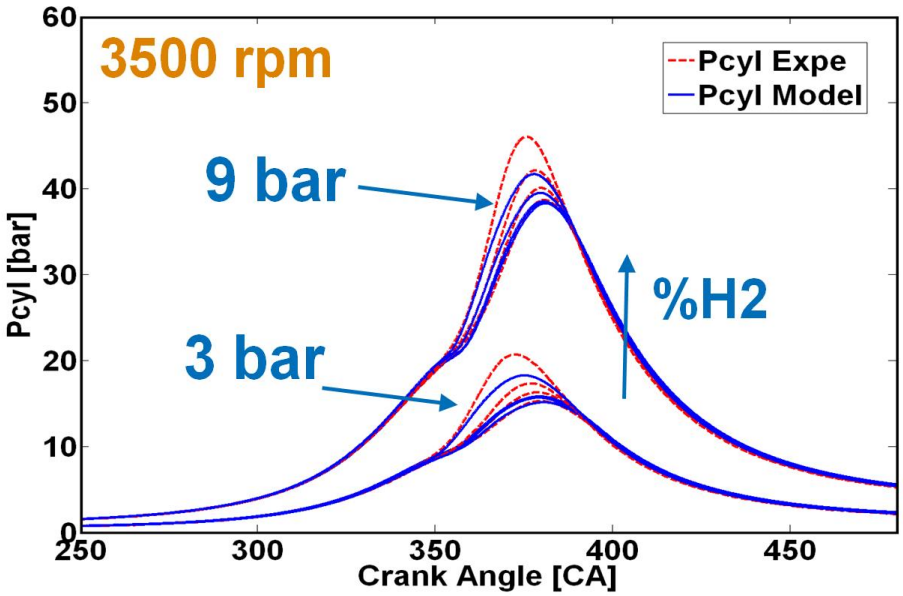

Figure 4.48: Comparisons between experimental and simulated cylinder pressure curves for different engine loads (IMEP = 3bar and 9bar) at 3500 rpm and for different hydrogen ratii (α) in methane ($\alpha = 0\%; 10\%; 20\%; 40\%$).

applications. Nevertheless, a computational time of 1s per cycle is still too high to allow direct real-time calculation. Considering that the most consuming part of the model is the solving of chemistry, solutions need therefore to be found to decrease the computational time of the reduced chemistries used for NO and CO prediction. In other terms, the question is to improve the description of species evolution when varying the fuel composition decreasing at the same time the computational time. An answer to this question is found in Chapters 5 and 6 and consists in integrating in the model complex chemistry through tabulation approaches to describe fuel oxidation (Chapter 5) and post-oxidation processes (Chapter 6).

- **Auto-ignition** – As previously mentioned, knock is the most efficiency limiting phenomena in SI engines. In this regard, its prediction is a crucial issue in the context of SI engine developments and the simple phenomenological model previously presented (Eqs. 4.26 – 4.31 and 4.41) appears as a promising tool to predict with a correct precision occurrence of knock in particular when varying the fuel composition (Figures 4.40–4.44). However, such a model requires a specific parameters calibration and above all is totally independent from the combustion model. Indeed, this model does not allow to compute an auto-ignition specific consumption rate which would have a direct impact on the global species evolution and heat release. Regarding knock occurrence, this last point is not really important since this phenomena is not expected to appear. However, in the case of CAI technology (Chapter 1) the species evolution is mainly driven by the auto-ignition species consumption rate and a simple phenomenological model is not sufficient anymore. To fix this problem, a similar approach to the one used for pollutants prediction is used and presented in Chapter 7.

- **Flame propagation** – Results on mean in-cylinder pressures prediction (Figures 4.12–4.19, 4.33–4.36 and 4.46) are quite satisfying showing that the evolution of the heat release rate - and therefore the turbulent flame speed - is well-described. However, looking at Figure 4.33, small deviations can be found when increasing the ethanol ratio in the fuel mixture. The error levels which are relatively low in the case of gasoline-ethanol blends (Figure 4.33), can become more significant when dealing with methane-hydrogen fuels. Indeed, as shown in Figure 4.48 simulations on the same engine basis confirmed this last point showing that

cylinder pressure levels are more and more underestimated when increasing the hydrogen ratio in methane. Then, three questions can be drawn here :

- Are physical phenomena (turbulence/flame interaction, thermo-diffusive instabilities, etc.) which are not well-accounted by the present model?
- Is the present description of turbulent flame velocity ($U_T = U_l \cdot \Xi A_m$, Eq. 4.5) well-defined?
- If not, is the flame wrinkling (Eq. 4.15) and flame stretch $\Gamma(u'/l_t)$ well-defined?

Answers to these questions are given in Chapter 8 where two studies dealing with effects of fuel composition on flame/turbulence interaction processes are investigated using DNS coupled with complex chemistry.

Part III

Integration of complex chemistry: The CFM1D-Tabulated Chemistry model

Chapter 5

Fuel burning process – Laminar flame velocity & Oxidation chemistry

This chapter presents the tabulation approach used to integrated complex chemistry in the CFM1D model to describe the oxidation process (Figure 5.1). As a first part of the new pollutant model development (second part in Chapter 6), the present approach consists in re-writing the first RHS term of Eq. 4.2 ($dm_i|_{ff}$) directly as function of the equilibrium compositions Y_i^{eq} and of the turbulent flame velocity $U_l \cdot \Xi$ (Figure 5.2). Y_i^{eq} are deduced from *a priori* calculation of 1D premixed flames using a detailed kinetic scheme. A database of laminar flame velocity is also generated and a new expression for U_l is developed to complement and improve common correlations which are generally restricted to low pressures and temperatures levels and often defined for a single fuel (see Section 2.1).

Works presented in this chapter are organized as follow :

- **Section 5.1 : Development of a new laminar flame correlation adapted to** CH_4–H_2–*air*–*diluent* **mixtures** – Works described in this section were published in the **International Journal of Hydrogen Energy**.
- **Section 5.2 : Integration in the CFM1D model of tabulation approach to describe the oxidation process with an application to methane fuel** – Works described in this section were subjected to an article presented in the **33rd International Symposium on Combustion** in Beijing and selected for publication in proceedings.
- **Section 5.3 : Complementary comments** – Additional comments are brought and global conclusions are given.

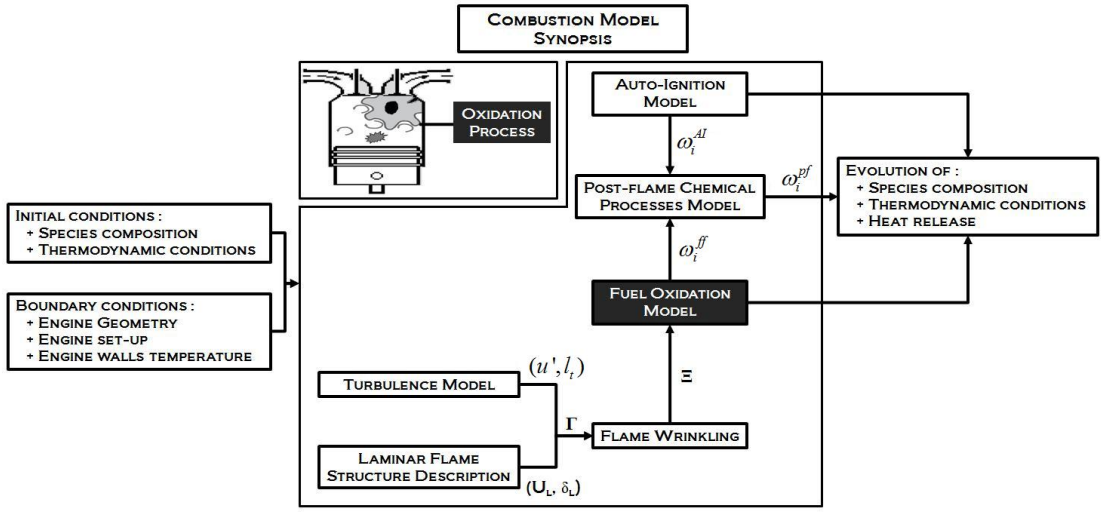

Figure 5.1: Combustion model global synopsis: **focus on the fuel oxidation model**. ω_i^{ff},ω_i^{pf} and ω_i^{AI} refer to the rates of consumption/production of species i associated respectively to the combustion, post-oxidation and auto-ignition processes stepping in Figures 1.3 and 1.4.

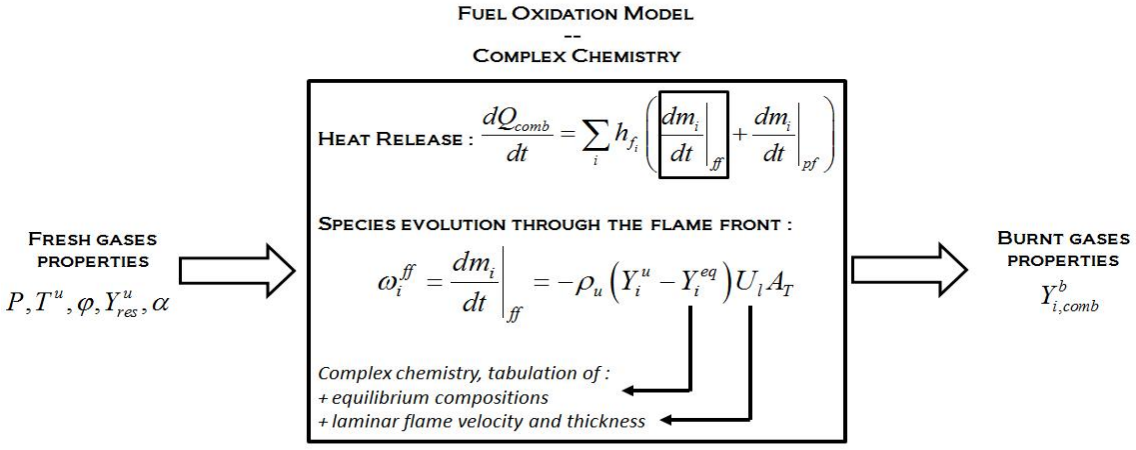

Figure 5.2: The new fuel oxidation model global description (see Figure 4.1 for the old one) – All parameters will be defined in the following sections – ω_i^{ff} refers to the rate of consumption/production of species i stepping in Figure 1.3.

5.1 Development of a new laminar flame velocity correlation for methane-hydrogen-air-diluent mixtures using detailed chemistry

---

- **Title**: Numerical study of laminar flame properties of diluted methane-hydrogen-air flames at high pressure and temperature using detailed chemistry
- **Authors**: S. Bougrine* **, S. Richard*, André Nicole*, Denis Veynante**
  * IFP Energies nouvelles
  ** Laboratoire EM2C, CNRS Ecole Centrale Paris
- **Reference**: Int. J. Hydrogen Energy, 2011, 36:18:1203547

5.1.1 Abstract

Technical limits of high pressure and temperature measurements as well as hydrodynamic and thermo-diffusive instabilities appearing in such conditions prevent the acquisition of reliable results in term of burning velocities, restraining the domain of validity of current laminar flame speed correlations to few bars and hundreds of Kelvin. These limits are even more important when the reactivity of the considered fuel is high. For example, the high-explosive nature of pure hydrogen makes measurements even more tricky and explains why only few correlations are available to describe the laminar flame velocity of high hydrogen blended fuels as $CH_4 - H_2$ mixtures. The motivation of this study is thereby to complement experimental measurements, by extracting laminar flame speeds and thicknesses from complex chemistry one-dimensional simulations of premixed laminar flames. A wide number of conditions are investigated to cover the whole operating range of common practical combustion systems such as piston engines, gas turbines, industrial burners, etc. Equivalence ratio is then varied from 0.6 to 1.3, hydrogen content in the fuel from 0 to 100%, residual burned gas mass ratio from 0 to 30%, temperature of the fresh mixtures from 300 to 950 K, and pressure from 0.1 to 11.0 MPa. Many chemical kinetics mechanisms are available to describe premixed combustion of $CH_4 - H_2$ blends and several of them are tested in this work against an extended database of laminar flame speed measurements from the literature. The GRI 3.0 scheme is finally chosen. New laminar flame speed and thickness correlations are proposed in order to extend the domain of validity of experimental correlations to high proportions of hydrogen in the fuel, high residual burned gas mass ratios as well as high pressures and temperatures. A study of the H_2 addition effect on combustion is also achieved to evaluate the main chemical processes governing the production of H atoms, a key contributor to the dumping of the laminar flame velocity.
Keywords: laminar flame speed, laminar flame thickness, premixed flame, correlation, methane, hydrogen, detailed chemistry.

5.1.2 Introduction

The fuel composition is an important element in the development of current combustion systems. Nowadays, common fuels such as gasoline or Diesel are more and more replaced by alternative fuels, which have raised a growing interest these last years because of economical and technical advantages. Natural gas, mainly constituted by methane, takes a particular status among these fuels thanks to its low carbon level $H/C \approx 4$ making it one of the less polluting fuels in term of CO_2. However, methane burns quite slowly leading to, in the case of piston engines, a lower thermal efficiency and important cycle-to-cycle variations (Wang et al. 2008,Huang et al. 2009), both

decreasing power and increasing fuel consumption. It also promotes combustion instabilities in gas turbines. An efficient way to improve the burning velocity is then to dump natural gas by hydrogen, which is also a good candidate to reduce pollutant emissions by increasing the hydrogen/carbon atomic ratio. Moreover, this addition extends flammability limits (Schefer 2003, Sankaran and Im 2006, Hawkes and Chen 2004), and improves, for example, the thermal efficiency of piston engines or gas turbines. However, the hydrogen impact on combustion processes can be dramatic for high blending rates. Natural gas-hydrogen mixtures need therefore specific system architectures and optimized control strategies to take advantage of fuel properties, ensuring in the same time on safe operation. Developments of such systems are today increasingly performed using simulation tools. Indeed, experimental campaigns, being often expensive, technically-limited or even prohibited in some fields, are more and more replaced by numerical simulations. The main difficulty is then to develop predictive models accounting for reacting flows including both chemistry and turbulence effects. The evaluation of the laminar flame speed and thickness is consequently crucial as these data are among the most critical parameters of turbulent combustion models. Generally, values of laminar flame speed are provided to the models through look-up tables or phenomenological functions which are mostly deduced from experiments. Current experimental correlations are usually based on low pressure, temperature and hydrogen rate measurements, and are thus often not representative of conditions encountered in realistic combustion systems. In the case of spark ignition engines for example, the in-cylinder pressure can reach more than 10.0 MPa and the fresh gases temperature can be higher than 1000 K. This issue is all the more relevant when dealing with high hydrogen blended fuels, as it is more sensitive to thermo-diffusive and hydrodynamic instabilities than common hydrocarbons leading to increase the flame wrinkling and leads to cell formation under certain conditions. In order to complement experimental measurements, an approach based on detailed kinetic calculations is presented and followed in this paper (section 5.1.3). A benchmark of available kinetic schemes of the literature is first realized and several of them are tested against a wide database of laminar flame speed measurements from the literature in order to evaluate and to choose the more relevant mechanism in terms of accuracy, robustness, precision and CPU-efficiency (section 5.1.4). The present results confirmed that the GRI 3.0 (Smith et al. 2000) mechanism has a good behavior compared to measurements of laminar premixed flames at low pressure and temperature regarding flame velocities. A database of laminar flame speeds and thicknesses is then generated from 1D premixed flames simulations using the Premix code from Sandia (Kee et al. 1989) and considering methane-hydrogen-air-diluent mixtures. A detailed study of the H_2 addition effect on the combustion is also achieved to understand the different regimes stepping in the methane-hydrogen flames propagation (Sarli and Benedetto 2007)and to explain the non-linear evolution of the laminar flame velocity (section 5.1.5). A new laminar flame speed expression, is then developed using an optimization algorithm (section 5.1.6). The phenomenological function presented in this paper is deeply inspired by previous works on experimental correlations for gasoline-ethanol-air-diluent and methane-hydrogen-air-diluent mixtures. Current laminar flame thickness correlation from the literature are also compared to simulation results leading to the conclusion that the Zel'dovitch (Poinsot and Veynante 2001)correlation describes well this quantity when the laminar flame velocity is well-predicted (section 5.1.7).

5.1.3 Description of the approach

This section describes the laminar burning velocity (U_l) determination process from detailed chemistry computations.

Methodology

The present approach is based on one-dimensional premixed flames computations using Premix (Kee et al. 1989). The first step is to choose an adapted chemical kinetics mechanism among available schemes. This choice is governed by 4 main factors:

- Relevance of the scheme for methane-hydrogen-air-diluent mixtures combustion
- Accuracy of the results and agreement with experimental data
- Numerical consistence and stiffness of the calculations
- CPU-cost which is directly linked to the number of species and reactions

In this work, reference mechanisms (GRI 3.0 (Smith et al. 2000), USCII (Wang et al.), Konnov 0.5 (Konnov 2011), Princeton (Li et al. 2011)) were tested against an extended database of laminar flame speed measurements from the literature. This validation step is presented in section 5.1.4. The second step is then to develop an adapted strategy to automate calculations. A very wide range of thermodynamic conditions (fresh gas temperature T^u and pressure P) and fresh mixture compositions (hydrogen rate in fuel α, equivalence ratio φ and diluent mass fraction Y^u_{res}) are considered to cover the whole range of operating conditions in SI engines, gas turbines, industrial burners, etc. For this purpose, an automated procedure, described in Figure 5.3, is followed.

Several parameters are set in the Premix input file for flame definition, like T^u, P and reactant mole fractions, depending on α, φ and Y^u_{res}, according to Eq. 5.1 (Figure 5.3).

$$(1-\alpha)C_xH_yO_z + \alpha H_2 + \left(x + \frac{y}{4} - \frac{z}{2} + \frac{1}{2}\right) O_2 \rightarrow xCO_2 + \left(\frac{y}{2} + 1\right) H_2O \tag{5.1}$$

Moreover, Premix requires an estimate of some other parameters like the surface mass flow rate through the burner, the peak mole fraction for intermediate species, the mole fraction values of flame products and the temperature profile through the flame front. The main difficulty is to set these initial conditions as precisely as possible to converge calculations, minimize failures and optimize the computational time required to generate all tables. To this end, products mole fractions and equilibrium temperature (T^{eq}) are deduced from equilibrium state calculations using the Equil module (Kee et al. 1989) (Figure 5.3, step 1). The mass flow rate is estimated from measurements, when existing, and approximately computed otherwise. Continuation runs are also pre-set to converge calculations in case of high pressures and poor or rich mixtures (Figure 5.3, step 2). Failed cases are detected by comparing the burned gas temperature reached at the end of the calculation (Figure 5.3, step 2') with the equilibrium one obtained by Equil (Figure 5.3, step 1), and are then recomputed refining inlet conditions. Finally, results are post-treated using Matlab®(Matlab) to extract laminar burning velocity (U_l) and temperature tables (Figure 5.3, step 3). Temperature profiles can be used to estimate laminar flame thicknesses defined from the maximum gradient between fresh and burned gases $(T^{eq} - T^u)/max(dT/dx)$. An analytical expression of U_l is then presumed (see section 5) and fitted from the Premix's table using the *lsqnonlin* function of Matlab®which solves nonlinear least-squares curve fitting problems.

Assumptions

Simulations were performed in the conditions presented in Table 5.1 , leading to the generation of a database containing more than 62244 points. To reduce computation times, pressure and fresh gas temperature have been chosen according to conditions currently met in common industrial applications (SI engines, gas turbines, industrial burner, etc.). andT^u and P ranges considered in this work are displayed in Figure 5.4.

Another assumption is to consider diluent as additional N_2 . In many combustion systems, such as piston engines or gas turbines, diluent are often composed by products of combustion (CO_2, H_2O, N_2), as well as residual reactants (fuel, O_2, N_2) in non-stoichiometric cases. In practice, diluent can be approximated at the first order as N_2. This assumption can be justified knowing that CO_2 and H_2O have opposite effects on the burning velocity and that N_2 is prevalent in mass

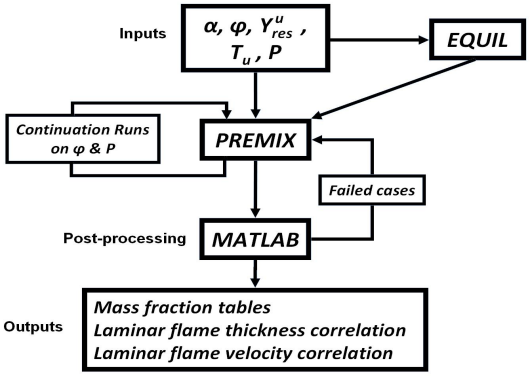

Figure 5.3: Global procedure for generating tables of mass fractions at equilibrium and laminar flame thickness and velocity correlation.

	Range of variation	Number of points
α [v/v%]	0.0 – 100	13
φ [-]	0.6 – 1.3	9
Y^u_{res} [m/m]	0.0 – 0.25	7
$(T^u \times P)$ [K] $\times$ [0.1MPa]	(300–950) $\times$ (1–110)	76
		Total = 62,244

Table 5.1: Characteristics of the 1D-premixed flames database.

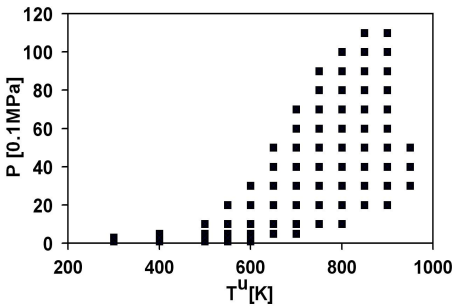

Figure 5.4: Map of pressure & fresh gases temperature used for Premix calculations.

on CO_2 and H_2O. Figure 5.5 compares burning velocities of diluted stoichiometric mixtures when considering residuals as additional N2 or as additional N_2, CO_2 and H_2O for several fuel compositions and thermodynamic conditions. In this last case, the residual composition is computed assuming a stoichiometric combustion of the fuel. Except in the case of pure hydrogen, the impact of taking CO_2 and H_2O into account is not significant, which confirms the validity of the previous assumption.

Finally, the last assumption concerns the modeling of molecular diffusivity. In the present work, the multicomponent diffusion has not been considered preferring the mixture-averaged diffusion model, neglecting then Soret and Dufour effects. These two effects respectively appear in species and heat flux vectors and only play a minor role on diffusion mechanisms when dealing with first-order expansion of the flame speed (Ern and Giovangigli 1998). However, it should not be neglected in case of the combustion of hydrogen which is highly sensitive to thermo-diffusive instabilities (Gerke et al. 2010). Nevertheless, the impact of thermal diffusion on hydrogen flame speed is mainly visible for rich mixtures (Greenberg 1980). Moreover, current thermo-chemical models cannot reproduce the impact of instabilities on laminar burning velocity like acceleration at high pressure (Gerke et al. 2010). The impact of using multicomponent model including Soret effect is presented Figure 5.6 for stoichiometric mixtures in atmospheric conditions. For high hydrogen blending rates accounting for the Soret effect has only a slight impact on simulation results, while no significant impact is observed at low hydrogen levels. Considering the possible reduction of computational costs when generating tables with an important size, it appears thus reasonable to neglect these effects. Indeed, the computational cost due to adopting the multicomponent diffusion model in the flame computations could be approximately estimated to be twice or thrice the time required to simulate a case without considering these diffusion effect. Moreover, activating the multicomponent diffusion model leads to more important number of failed cases when the presented approach is used which significantly increases the global time required to treat all the cases of Table 5.1.

5.1.4 Mechanism validation

The aim of this section is to compare experimental laminar flame velocities with Premix simulation results to choose the best chemical scheme (in term of prediction, robustness and CPU-efficiency) among four mechanisms (Table 5.2) adapted to the combustion of $CH_4 - H_2$ mixtures. For this purpose, an important process of gathering experimental measurements has been carried out (not extensively presented here) and collected data (Dong et al. 2002, Vagelopoulos and Egolfopoulos 1998, Gu et al. 2000, Bakali et al. 2004, Kishore et al. 2008, Fairweather et al. 2009, Elia et al. 2001, Tahtouh et al. 2009, Hu et al. 2009, Halter et al. 2005, Dyakov et al. 2001, Bosschaart and de Goey 2004, Rozenchan et al. 2003, Ali 1995, Aung et al. 1995, Clarke et al. 1995, Vagelopoulos and Egolfopoulos 1994, Maaren et al. 1994, Taylor 1991, Tanoue et al. 2003, Miao et al. 2008, Ilbas et al. 2006, Sun et al. 1999, Dowdy et al. 1991, Takahashi et al. 1983, Coppens et al. 2007a, Miao et al. 2009, Yu et al. 1986, Liao et al. 2004, Barassin et al. 1967, Babkin and Kozachenko 1966, Dugger 1952, Halpern 1958, Johnston 1947, Hassan et al. 1998, Egolfopoulos et al. 1989, Stone et al. 1998) were compared to Premix simulation results using the different chemical schemes. Many studies (Gerke et al. 2010, Greenberg 1980, Dong et al. 2002, Vagelopoulos and Egolfopoulos 1998, Gu et al. 2000, Bakali et al. 2004, Kishore et al. 2008, Fairweather et al. 2009, Elia et al. 2001, Tahtouh et al. 2009) reported a good behavior of these mechanisms compared to experimental results of laminar premixed flames at low pressures and temperatures, especially regarding flame velocities.

Figs. 5.a-g compare experimental and simulated laminar flame speeds for single parameter variations. Results from simulations are globally in good agreement with experimental data, showing that the impacts of with α, φ, $Y_r^u es$, T^u and P are satisfactorily captured by all schemes. However, calculations using the GRI 3.0 scheme seems to slightly overestimate U_l. Compared to the other simulations using higher resolution settings, errors remain nevertheless acceptable. It is then noticeable that GRI 3.0 behaves similarly than Konnov 0.5 or USCII mechanisms which are build-up with respectively nearly twice as many species and with twice to four times more

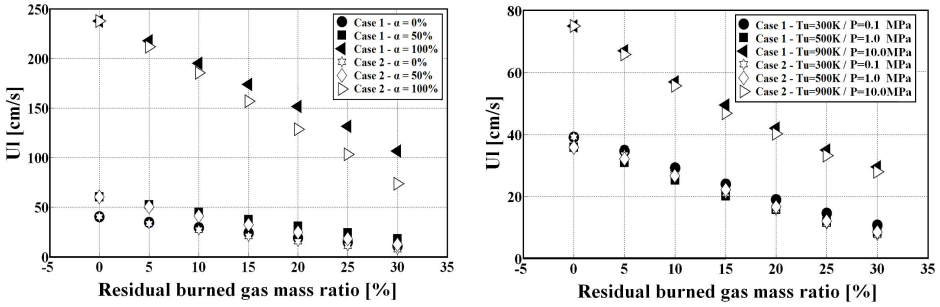

(a) (b)

Figure 5.5: Comparison of laminar flame speed variations with the residual burned gas rate for different hydrogen rate, pressures and fresh gas temperatures when considering diluent as additional N_2 (Case 1) or as additional N_2, CO_2 and H_2O (Case 2) - (GRI 3.0 scheme) - (a) $\varphi = 1$, $T^u = 300K$, $P = 0.1MPa$ - (b) $\alpha = 0\%$, $\varphi = 1$.

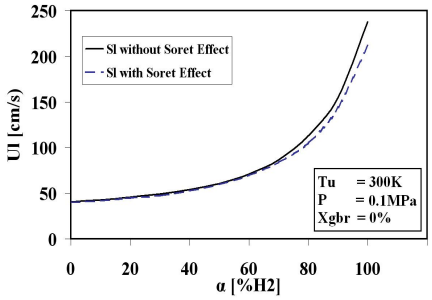

Figure 5.6: Comparison of laminar flame speed variations with the hydrogen rate ($\varphi = 1$) when using a diffusion model with or without Soret effect - (GRI 3.0 scheme).

	SPECIES	REACTIONS
Princeton (Li et al. 2011)	21	93
GRI 3.0 (Smith et al. 2000)	53	325
USCII (Wang et al.)	111	784
Konnov 0.5 (Konnov 2011)	127	12017

Table 5.2: Characteristics of the 1D-premixed flames database

reactions. On the other hand, Figs. 5 (a-g) show that the Princeton mechanism seems to systematically underestimate U_l pointing out that a minimum level of detail is all the same required to guarantee the computations accuracy. Finally, using the approach presented in section 2, the GRI 3.0 appears also more robust than Konnov 0.5; the first shows less than 20% of failed cases against more than 60% for the second. All these points comfort GRI 3.0 as a good compromise to predict laminar flame speeds at high pressure and temperature despite a lack of experimental data to validate the scheme over a wider range of pressure and fresh gas temperature T^u.

5.1.5 Detailed study of the effect of hydrogen addition

The evolution of the laminar burning velocity with α, the H_2 proportion in the fuel mixture, presented in Figure 5.7.d can be explained by non-linear chemical kinetics processes. Di Sarli and Di Benedetto (Sarli and Benedetto 2007) noticed that three regimes in methane-hydrogen flames propagation could be identified. The first ($0 < \alpha < 50\%$) and the third ($0 < \alpha < 50\%$) ones are characterized by a linear increase of the laminar burning velocity. These linear evolutions were attributed by the authors in the first case to the promoting effect of hydrogen addition in methane and in the last case to an inhibition due to the addition of methane to hydrogen. In the intermediate regime ($50 < \alpha < 100\%$), the evolution is strongly non-linear reflecting a complex kinetics behavior. Di Sarli and Di Benedetto showed that there is a clear coupling in stoichiometric conditions between the burning velocity and maximum concentration of H which is a key radical in chain branching. Preliminary sensitivity analyses (see Figure 5.8) performed in stoichiometric conditions using GRI 3.0 and Konnov 0.5 mechanisms confirm that the most sensitive reactions involve H atoms. Both mechanisms appear to show similar behaviors with respect to the addition of hydrogen in fuel. For example, according to both schemes, the maximum value of the flame speed sensitivity with respect to reaction (3) (Figure 5.8) rate constant is obtained for $\alpha = 50\%$. The importance of reaction (3) in the GRI 3.0 mechanism seems to be higher than in the Konnov scheme.

Working under very different operating conditions (jet stirred reactor versus premixed flame propagation), several groups (Sabia et al. 2007, de.Ferrires et al. 2007) concluded that H_2 substitution to natural gas enhances the oxidation pathway (C_1 sequence). However, their results concerning the impact of H_2 on recombination (C_2) pathway cannot be directly compared because they study very different fuel compositions: CH_4 (Sabia et al. 2007) versus CH_4-C_2H_6-C_3H_8 blends (de.Ferrires et al. 2007). In the present section, the effects of fuel decarbonization by H_2 addition on H production from C_1-C_2 species are investigated using GRI 3.0 in order to further elucidate H_2 addition effects on flame propagation.

Figure 5.9 shows the H production or consumption rates from the most significant C_1-C_2 species in stoichiometric conditions at the location of the maximum H concentration. As can be noticed, the production or consumption of H is mainly determined by C_1 species which appear to contribute more and more to H production as α is increased. It is important to note that H production rate from reactions involving CO is only slightly affected by H_2 addition, whereas some others pathways are strongly affected.

Figure 5.10 shows the evolution of the molar production and consumption rates of H for important reactions and for three hydrogen amounts in the fuel at stoichiometric and atmospheric conditions. Moreover, in order to numerically isolate the thermal and kinetic effects of H_2 addition, complementary calculations were carried out by imposing the temperature profile as well as the inlet mass flow rate corresponding to $\alpha = 50\%$ while at the same time keeping the inlet composition at $\alpha = 0\%$ (Figs. 8,9). It turns out that the complex evolution of the rate of reaction (1) (Figure 5.8) can be attributed to a competition between thermal and chemical effects (Figure 5.10.a). Looking at Figure 5.11.b, it appears that the promoting thermal effect is only partially compensated for by the chemical effect of increasing from 0 to 50%. As a result, the overall effect

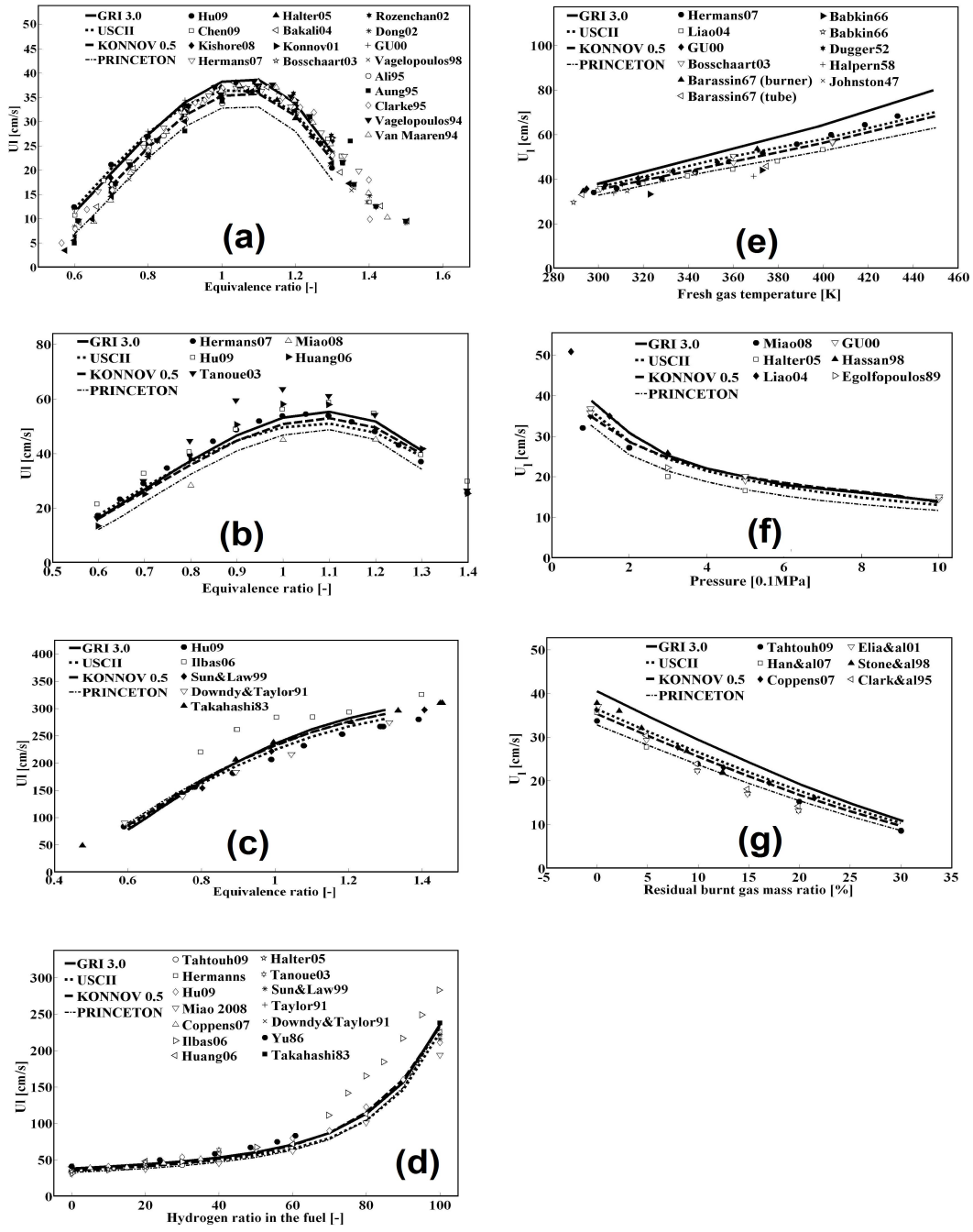

Figure 5.7: Figure 5: Comparison of experimental and simulated laminar flame speed variations as a function of the equivalence ratio (a-c) - hydrogen rate (d) - fresh gases temperature (e) - pressure (f) - residual burned gas rate (g) - Operating conditions: (a) $\alpha = 0\%$, $Y^u_{res} = 0\%$, $T^u = 300K$, $P = 0.1MPa$ – (b) $\alpha = 40\%$, $Y^u_{res} = 0\%$, $T^u = 300K$, $P = 0.1MPa$ – (c) $\alpha = 100\%$, $Y^u_{res} = 0\%$, $T^u = 300K$, $P = 0.1MPa$ – (d) $\varphi = 1$, $Y^u_{res} = 0\%$, $T^u = 300K$, $P = 0.1MPa$ – (e) $\alpha = 0\%$, $\varphi = 1$, $Y^u_{res} = 0\%$, $P = 0.1MPa$ – (f) $\alpha = 0\%$, $\varphi = 1$, $Y^u_{res} = 0\%$, $T^u = 300K$ – (g) $\alpha = 0\%$, $\varphi = 1$, $T^u = 300K$, $P = 0.1MPa$.

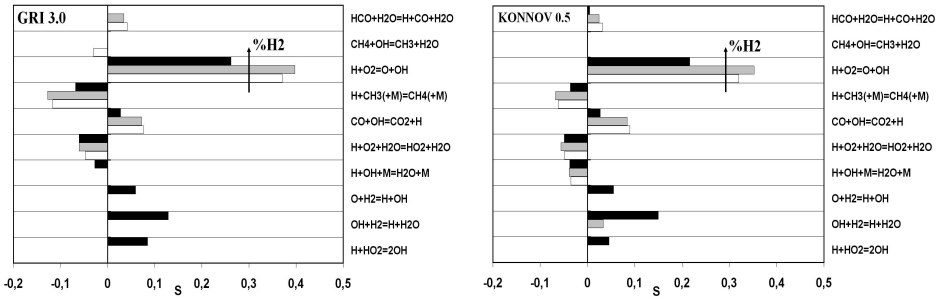

(a) (b)

Figure 5.8: Normalized sensitivity coefficients for U_l stoichiometric methane-hydrogen-air flames. The normalized sensitivity is defined by $S_j = k_j/U_l \cdot \partial U_l/\partial k_j$ where k_j is the reaction rate associated to step j - Operating conditions: $\alpha = 0/50/90\%$ (respectively white-grey-black), $\varphi = 1$, $Y^u_{res} = 0\%$, $T^u = 300K$, $P = 0.1MPa$ – (a) GRI 3.0 mechanism – (b) Konnov 0.5 mechanism.

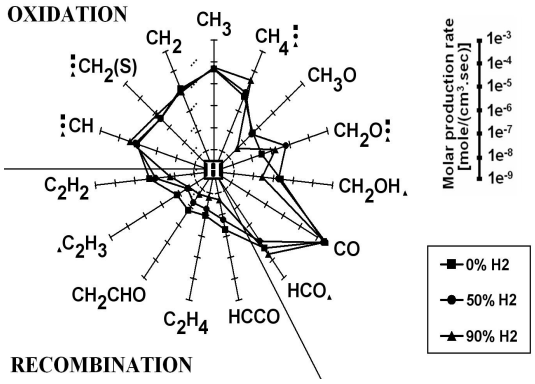

Figure 5.9: Main H production or consumption rates according to several species at H peak location, species with symbols correspond to species inhibiting H production at the corresponding H_2 rate – Operating conditions: $\alpha = 0/50/90\%$, $\varphi = 1$, $Y^u_{res} = 0\%$, $T^u = 300K$, $P = 0.1MPa$.

of H_2 addition on HCO profile is promoting, which results in an increase of the corresponding rate of reaction. In contrast, the extent of the chemical effect of H_2 addition on CO concentration profile (Figure 5.11.c) becomes lower than that of its thermal effect, so that the global effect on CO concentration becomes inhibiting. However, the rate of reaction (5) (Figure 5.8) is still enhanced when increasing α from 0 to 50% (Figure 5.10.b) due to the stronger impact of H_2 addition on OH concentration level. Concerning reaction (4) (Figure 5.8) consuming H radicals, the effect of H_2 addition on CH_3 species concentration (Figure 5.11.d) appears of minor importance compared to its leading promoting effect on H radical concentration.

This analysis carried out in stoichiometric conditions and at atmospheric pressure should help to understand the non-linear impact of H_2 addition on the laminar flame propagation as α is increased. In the next session, a correlation for the laminar burning velocity is then proposed for a large range of compositions and thermodynamic operating conditions, considering this non-linear behavior through the 3 regimes identified by Di Sarli and Di Benedetto (Sarli and Benedetto 2007).

5.1.6 Laminar flame speed correlation

The analytical expression for the laminar flame speed proposed here is inspired by previous works from Gülder (1984), Han et al. (2007), Rahim et al. (2002), Coppens et al. (2007b), Hermanns et al. (2010, **?**), Huang et al. (206), Tahtouh et al. (2009), Gerke et al. (2010), Bougrine et al. (2011) and Verhelst et al. (2011). The primary aim of the present study was to extend the current validity range of these correlations to high pressure and temperature levels and to propose a generic expression for any fraction of hydrogen content in the fuel, from 0 to 100%. The general form of U_l is written:

$$U_l(\alpha, \varphi, Y^u_{res}, T, P) = U_l{}^{\circ}(\alpha, \varphi) \cdot \left(\frac{T^u}{T^{\circ}}\right)^{\alpha_T} \cdot \left(\frac{P}{P^{\circ}}\right)^{\alpha_P} \cdot (1 - \alpha_{res} \cdot f(Y^u_{res})) \tag{5.2}$$

where U_l^0, α_T, α_P, $\alpha_r es$ and f are functions defined in the following, $P^0 = 10^5$ and $T^0 = 300K$ are the reference pressure and temperature respectively. This form was introduced by Metghalchi and Keck (Metghalchi and Keck 1980, Metghalchi and Keck 1982) for mixtures of air with propane, methanol, iso-octane and indolene. It was then widely extended to account for temperature, pressure and dilution effects. The work then consists in well-defining U_l^0, α_T, α_P, $\alpha_r es$ and f and by parametric functions, which coefficients have to be calibrated. For this purpose, the present correlation is based on the work of Hermanns (Hermanns et al. 2010, Hermanns 2007). Hermanns et al. (2010) indeed reviewed most studies of the literature dealing with burning velocity correlation for methane and methane-hydrogen combustion and proposed an expression valid over the following range: $0\% < \alpha < 40\%$, $0.6 < \varphi < 1.5$, $0 < Y^u_r es < 25\%$, $298K < T^u < 418K$, and $P = 1atm$.

Effect of equivalence ratio & hydrogen addition

U_l has not the same response to equivalence ratio variations when varying the fraction of hydrogen in the fuel. Indeed, Figure 5.7.a-c show that the flame speed promotion is more pronounced to hydrogen addition in rich mixture than in lean ones. The maximum of the curve is therefore shifted from 1.1 for pure methane (Figure 5.7.a) to more than 1.4 for pure hydrogen (Figure 5.7.c). This behavior makes thus correlations necessarily complex. Coppens et al. (2007b) and Hermanns et al. (2010) improved the Gülder expression (Gülder 1984) for U_l^0 by adding terms accounting for hydrogen addition effects up to $\alpha = 40\%$. The resulting correlation is here adapted to an hydrogen substitution level up to 100% and is presented in Eq. 5.3 below. For this purpose, Hermanns et al. coefficients have been re-adjusted. The optimization is however limited by the form of the expression which can hardly reproduce the shift of the optimum equivalence ratio burning velocity notably over $\alpha \approx 90\%$. A correction term (Λ_1), presented in Eq. 5.4, is thereof added to capture the hydrogen addition effect over $\alpha = 70\%$ by function A, presented in Eq. 5.5,

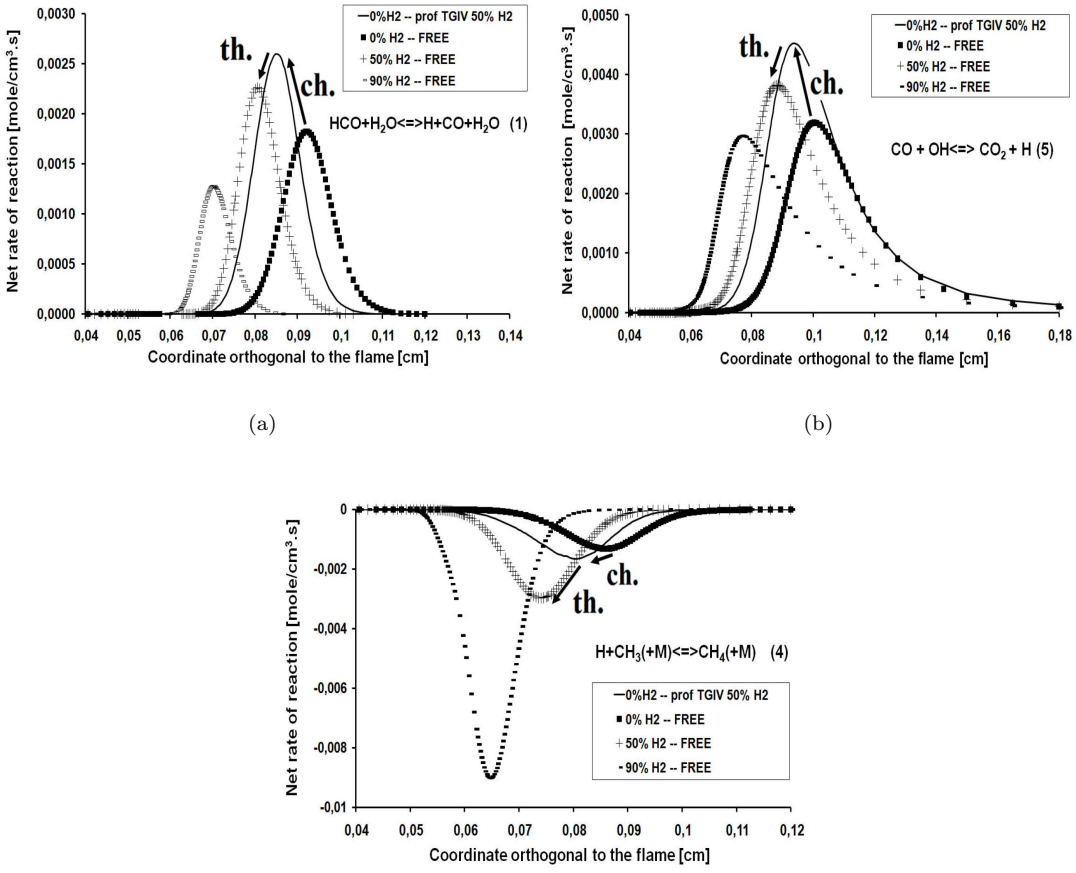

Figure 5.10: Evolution of the molar production and consumption rates of H for the most important C_1 reactions - Operating conditions: $\alpha = 0/50/90\%$, $\varphi = 1$, $Y^u_{res} = 0\%$, $T^u = 300K$, $P = 0.1MPa$ – *th.* : thermal effect, *ch.* : chemical effect.

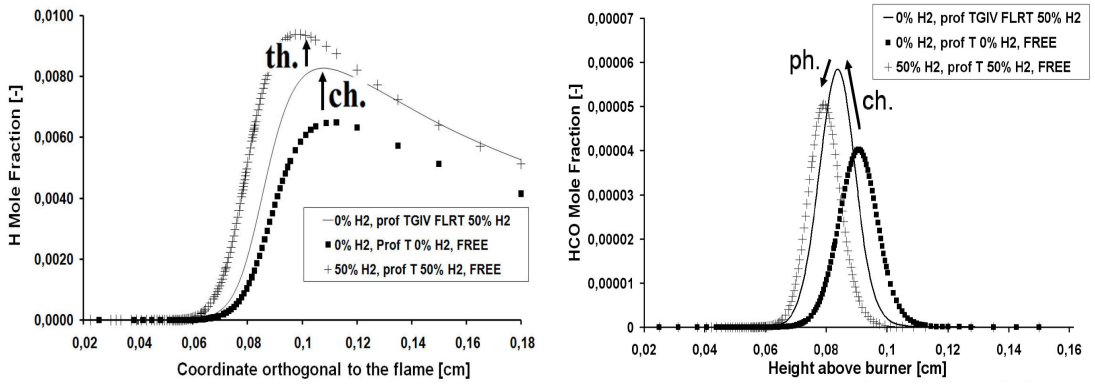

(a)

(b)

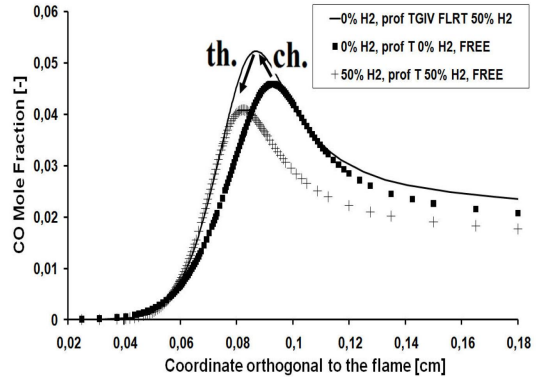

(c)

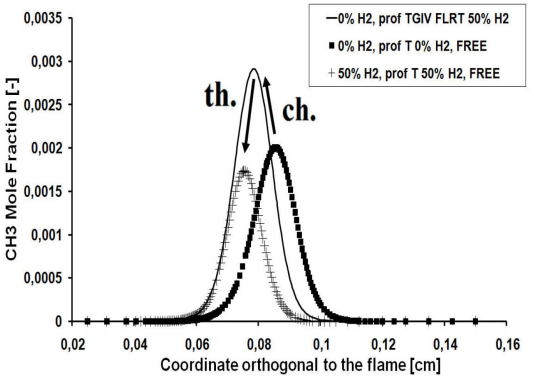

(d)

Figure 5.11: Mole fraction profiles in the direction orthogonal to the flame. Operating conditions: $\alpha = 0/50/90\%$, $\varphi = 1$, $Y^u_{res} = 0\%$, $T^u = 300K$, $P = 0.1MPa$ – *th.* : thermal effect, *ch.* : chemical effect.

and the equivalence ratio effect over $\alpha = 90\%$ by function Φ, presented in Eq. 5.6 , and inspired by Gerke et al. (2010) and Huang et al. (206) correlations for hydrogen/air flames. Function Λ_1 allows thus to capture the velocity behavior over $\alpha = 70\%$ which corresponds to the two last regimes evocated in section 4. The continuity of U_l^0 between the three regimes is then ensures by the function g presented in Eq. 5.7. The U_l^0 function, corresponding to the laminar flame speed for T^0, P^0 and $Y_r^u es$, is written:

$$U_l{}^\circ(\alpha, \varphi) = \left[\left(1 + a_0 \alpha^{a_1}\right) a_2 \varphi^{a_3} e^{a_4(\varphi + a_5\alpha + a_6)^2} \right] \bullet \Lambda_1 \tag{5.3}$$

where a_i are calibrated coefficients given in Table 5.3 and Λ_1 is a function defined as:

$$\Lambda_1 = [1 + g\,(\alpha, 70, 10) \cdot (\mathrm{A}(\alpha) - 1)] \bullet [1 + g\,(\alpha, 90, 10) \cdot (\Phi(\varphi) - 1)] \tag{5.4}$$

with

$$\mathrm{A}(\alpha) = \lambda_0 + \lambda_1\alpha + \lambda_2\alpha^2 + \lambda_3\alpha^3 + \lambda_4\alpha^4 + \lambda_5\alpha^5 \tag{5.5}$$

$$\Phi(\varphi) = \phi_0 + \phi_1\varphi + \phi_2\varphi^2 + \phi_3\varphi^3 + \phi_4\varphi^4 \tag{5.6}$$

$$g(\alpha, \alpha_0, \Delta_\alpha) = {}^1\!/_2 \left(1 + \tanh\left(\frac{(\alpha - \alpha_0)}{\Delta_\alpha}\right)\right) \tag{5.7}$$

where λ_i and ϕ_i are calibrated coefficients given in Table 5.3. Function g ensures the continuity of U_l^0 at $\alpha = \alpha_0$ and a smooth transition between $\alpha = \alpha_0$ - Δ_α and $\alpha = \alpha_0 + \Delta_\alpha$.

Effect of temperature and pressure

The expression of the fresh gas temperature exponent in Eq. 5.2 α_T and presented in Eq. 5.8, is adapted from Hermanns et al. (2010). It takes into account equivalence ratio and hydrogen addition effects when varying temperature but also integrates a new term to better fit with Premix results. However, Hermanns et al. do not consider a pressure effect in U_l. Similarly, the pressure exponent in Eq. 5.2, α_p, is then determined as function of φ and α (Eq. 5.9). Moreover the modeling of hydrogen effects is inspired by Gülder correlation on iso-octane-ethanol-air flames (Gülder 1984). Finally, correction terms (Λ_2, Λ_3), presented in Eq. 5.10 and 5.11, are thereof added to capture hydrogen addition effects when varying temperature and pressure when $\alpha = 90\%$.

$$\alpha_T = \left[\alpha_{T0} + \alpha_{T1}\varphi + \alpha_{T2}\varphi^4 + \alpha_{T3}\alpha + \alpha_{T4}\left(\frac{T_0^2}{T^2}\right) \cdot \varphi^2\right] \bullet \Lambda_2 \tag{5.8}$$

$$\alpha_P = \left[\alpha_{P0} + \alpha_{P1}\varphi + \alpha_{P2}\varphi^4 + \alpha_{P3}\alpha \cdot \left(\sqrt{\varphi + \frac{1}{\varphi}}\right) + \alpha_{P4}\left(\frac{T}{T_0}\right) \cdot \left(\frac{P}{P_0}\right) \cdot \varphi^2\right] \bullet \Lambda_3 \tag{5.9}$$

where α_{Pi} and α_{Ti} are calibrated coefficients given in Table 5.3 and are functions defined as:

$$\Lambda_2 = 1 + g\,(\alpha, 90, 10) \cdot \left(e^{\left(\lambda_{T1}\left(\frac{T}{T_0}\right)^{\lambda_{T0}} - 1\right)} - 1\right) \tag{5.10}$$

$$\Lambda_3 = 1 + g\,(\alpha, 90, 10) \cdot \left(e^{\left(\lambda_{P0} + \lambda_{P1}\frac{P}{P_0} + \lambda_{P2}\left(\frac{P}{P_0}\right)^2\right)} - 1\right) \tag{5.11}$$

where λ_{Pi} and λ_{Ti} coefficients are given in Table 5.3.

Dilution Effect

Concerning the influence of residual burned gases, Metghalchi and Keck (Metghalchi and Keck 1980) noticed a linear decrease of the flame speed when increasing the dilution rate while Hermanns et al. (2010) recommended to introduce an equivalence ratio dependency. The present expression of α_{res} (Eq. 5.12) integrates hydrogen fraction, temperature and pressure terms leading to a slight improvement of the results. Moreover, considering that over $Y_r^u es \approx 35\%$ the influence of residual burned gases is not linear anymore, a polynomial function f is introduced (Eq. 5.13):

$$\alpha_{res} = \alpha_{res0} + \alpha_{res1}\varphi + \alpha_{res2}\varphi^4 + \alpha_{res3}\alpha + \alpha_{res4}\left(\frac{T}{T_0}\right)\cdot\left(\frac{P}{P_0}\right)\cdot\varphi^2 \tag{5.12}$$

$$f(res) = Y_{res}^u + f_1 \cdot Y_{res}^{u^2} + f_2 \cdot Y_{res}^{u^3} \tag{5.13}$$

where α_{resi} and f_i coefficients are given in Table 5.3.

All functions previously presented are summarized in Table 5.4. Figs. 10.a-d compare Premix results and the present correlation over the whole simulated database. A very good agreement is observed showing that the influence of α,φ,P,T^u and $Y_r^u es$ is well reproduced. Results exhibit relative errors lower than 10% for about 83% of handled points and lower than 5% for about 60% of the points when $0\% < \alpha < 70\%$ (Figs. 10.d). Figs. 10.a-d show that errors are more important over 80% of hydrogen in the fuel pointing out the difficulty to well-describe the three regimes of the methane-hydrogen flame propagation by a single global continuous correlation. Globally, the mean error is about 6%. Considering the large number of cases treated and the accuracy of chemical mechanisms together with experimental errors that can lead to uncertainties of 10%, these results can however be considered as satisfactory.

5.1.7 Laminar flame thickness correlation

Different correlations have been proposed for the laminar flame thickness δ in the literature. These correlations generally describe the diffusive thickness corresponding to $Re_f = \delta_l U_l / D_{th} = 1$, where Re_f is the flame Reynolds number and the diffusion coefficient. Two of these correlations are tested here against Premix simulations : the first one is the so-called Zel'dovitch expression depending on the laminar flame speed and fresh gases properties (Poinsot and Veynante 2001):

$$\delta_l^{Zeldovitch} = \left(\frac{\lambda}{\rho \cdot c_p}\right)_u \frac{1}{U_l} \tag{5.14}$$

where λ is the thermal conductivity and C_p the heat capacity of the fresh gases. Blint (Blint 1986) proposed another correlation including a correction by the burned gases properties, a Sutherland law for λ and a constant Prandtl number:

$$\delta_l^{Blint} = \left(\frac{\lambda}{\rho \cdot c_p}\right)_u \frac{2}{U_l} * \left(\frac{T^b}{T^u}\right)^{0,7} \tag{5.15}$$

where T^b is the burned gases temperature.

Lafay et al. (2008) showed that the flame thickness is predicted well by the GRI 3.0 mechanism by comparing simulated results with experimental measurements for poor cases and for hydrogen rates in the fuel up to 40%. Their observations comfort then the GRI 3.0 mechanism as a well-adapted mechanism to predict the laminar flame thickness. The two correlations (14,15) have been therefore compared to 1D premixed flame results (Figure 5.13), the thickness from the Premix simulations being estimated from the temperature gradients between fresh and burned

α_{T0}	$3,2466$	α_{P0}	$-0,5406$	α_{res0}	$4,157$	ϕ_0	$1,750$
α_{T1}	$-1,0709$	α_{P1}	$0,1347$	α_{res1}	$-1,744$	ϕ_1	$-1,750$
α_{T2}	$0,1517$	α_{P2}	$-0,0125$	α_{res2}	$0,5124$	ϕ_2	$0,625$
α_{T3}	$-3,201.10^{-4}$	α_{P3}	$-5,174.10^{-4}$	α_{res3}	$-0,0047$	ϕ_3	$-0,038$
α_{T4}	$-1,0359$	α_{P4}	$2,289.10^{-4}$	α_{res4}	$-8,694.10^{-4}$	ϕ_4	$0,138$
a_0	$2,72.10^{-6}$	λ_0	$1,4$	λ_{T0}	$0,5$		
a_1	$2,897$	λ_1	$3,39.10^{-7}$	λ_{T1}	$0,58$		
a_2	$150,817$	λ_2	$-1,17.10^{-6}$	λ_{P0}	$-1,9026$		
a_3	$4,539$	λ_3	$-1,17.10^{-7}$	λ_{P1}	$3,556.10^{-2}$		
a_4	$-2,448$	λ_4	$-3,75.10^{-9}$	λ_{P2}	$-1,62.10^{-4}$		
a_5	$-0,0017$	λ_5	$1,4.10^{-10}$	f_1	$-1,115$		
a_6	$-0,2248$			f_2	$1,323$		

Table 5.3: Parameters of the new laminar flame speed correlation Eqs. 5.2-5.13

$U_l(\alpha,\varphi,Y^u_{res},T,P) = U_l{}^\circ(\alpha,\varphi)\cdot\left(\frac{T^u}{T^\circ}\right)^{\alpha_T}\cdot\left(\frac{P}{P^\circ}\right)^{\alpha_P}\cdot(1-\alpha_{res}\cdot f(Y^u_{res}))$
$U_l{}^\circ(\alpha,\varphi) = \left[(1+a_0\alpha^{a_1})\,a_2\varphi^{a_3}e^{a_4(\varphi+a_5\alpha+a_6)^2}\right]\bullet\Lambda_1$ $\Lambda_1 = [1+g(\alpha,70,10)\cdot(\mathrm{A}(\alpha)-1)]\bullet[1+g(\alpha,90,10)\cdot(\Phi(\varphi)-1)]$ $\mathrm{A}(\alpha) = \lambda_0+\lambda_1\alpha+\lambda_2\alpha^2+\lambda_3\alpha^3+\lambda_4\alpha^4+\lambda_5\alpha^5$ $\Phi(\varphi) = \phi_0+\phi_1\varphi+\phi_2\varphi^2+\phi_3\varphi^3+\phi_4\varphi^4$ $g(\alpha,\alpha_0,\Delta_\alpha) = {}^1\!/_2\left(1+\tanh\left(\frac{(\alpha-\alpha_0)}{\Delta_\alpha}\right)\right)$ $\Delta_\alpha = \alpha-\alpha_0$
$\alpha_T = \left[\alpha_{T0}+\alpha_{T1}\varphi+\alpha_{T2}\varphi^4+\alpha_{T3}\alpha+\alpha_{T4}\left(\frac{T_0^2}{T^2}\right)\cdot\varphi^2\right]\bullet\Lambda_2$ $\Lambda_2 = 1+g(\alpha,90,10)\cdot\left(e^{\left(\lambda_{T1}\left(\frac{T}{T_0}\right)^{\lambda_{T0}}-1\right)}-1\right)$
$\alpha_P = \left[\alpha_{P0}+\alpha_{P1}\varphi+\alpha_{P2}\varphi^4+\alpha_{P3}\alpha\cdot\left(\sqrt{\varphi+\frac{1}{\varphi}}\right)+\alpha_{P4}\left(\frac{T}{T_0}\right)\cdot\left(\frac{P}{P_0}\right)\cdot\varphi^2\right]\bullet\Lambda_3$ $\Lambda_3 = 1+g(\alpha,90,10)\cdot\left(e^{\left(\lambda_{P0}+\lambda_{P1}\frac{P}{P_0}+\lambda_{P2}\left(\frac{P}{P_0}\right)^2\right)}-1\right)$
$\alpha_{res} = \alpha_{res0}+\alpha_{res1}\varphi+\alpha_{res2}\varphi^4+\alpha_{res3}\alpha+\alpha_{res4}\left(\frac{T}{T_0}\right)\cdot\left(\frac{P}{P_0}\right)\cdot\varphi^2$ $f(res) = Y^u_{res}+f_1\cdot Y^{u^2}_{res}+f_2\cdot Y^{u^3}_{res}$

Table 5.4: Proposed laminar flame speed correlation ($\varphi[-]$, $\alpha[v/v\%]$, $Y^u_{res}[K]$, $P[0.1MPa]$)

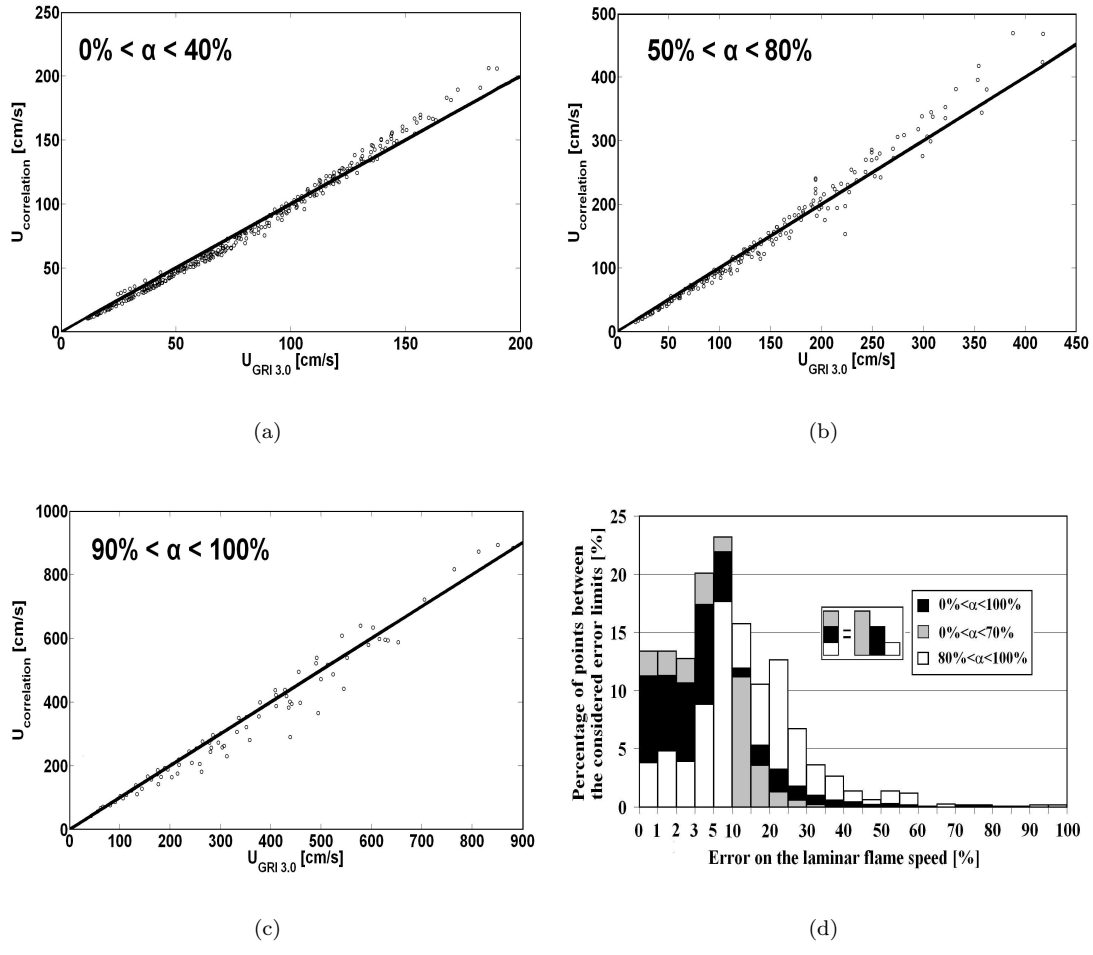

(a) (b)

(c) (d)

Figure 5.12: Errors on the laminar flame speed for all the 62244 operating points: (a) results for $0\% < \alpha < 40\%$ – (b) results for $50\% < \alpha < 80\%$ – (c) results for $90\% < \alpha < 100\%$ – (d) error on the laminar flame speed for the whole database.

gases zones $(T^{eq} - T^u)/max(dT/dx)$, which corresponds to the diffusive thickness ($Re_f \approx 1$). The Zel'dovitch correlation shows a better agreement than the Blint's one with complex chemistry results. Moreover, Figure 5.14 shows an improvement of results when the Zel'dovitch correlation is slightly modified by a factor $c = 1.2$. It should be noticed that various flame thickness definitions are available and the one based on the temperature gradient may be not optimal as implicitly assuming that temperature profiles have the same shape for all conditions, which is not the case, especially around flammability limits (see Figure 5.15). Complex chemistry results should then be analysed with care even if the Zel'dovitch correlation seems to be more adapted to define the thermal flame thickness.

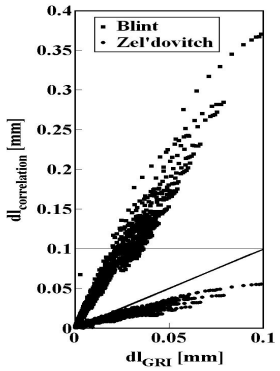

Figure 5.13: Comparison between Blint's and Zel'dovitch's laminar flame thickness correlations for all the 62244 operating points.

5.1.8 Conclusion

This paper presents a numerical approach to evaluate premixed flame properties of $CH_4 - H_2$-*diluent* mixtures by using complex chemistry. The proposed method is based on a priori simulations of 1D premixed flames to generate a wide chemical database. A benchmark of several available kinetic schemes of the literature was realized in order to evaluate and to choose the more adapted kinetic mechanism to generate the database. The GRI 3.0 scheme turned out to be the best compromise between robustness, precision and CPU-cost and was finally retained. Simulations were achieved considering thermodynamic conditions representative of those found in modern combustion systems to extend the domain of validity of experimental correlations to high hydrogen contents in the fuel, high residual burned gas mass ratios and high pressures and temperatures. A detailed study of the H_2 addition effect on the combustion process was also achieved to understand the known three regimes stepping in the hythane propagation and to explain the non-linear evolution of the laminar velocity. Laminar flame speeds and thicknesses correlations were then developed from the look-up tables. The new laminar flame speed correlation is in a very good agreement with Premix results and a modified Zel'dovitch correlation for the laminar flame thickness seems to be more appropriate to describe the thermal flame thickness than the Blint's one. Future work will be devoted to the use of a priori complex chemistry simulations for other types of fuels (natural gas, ethanol gasoline blends...).

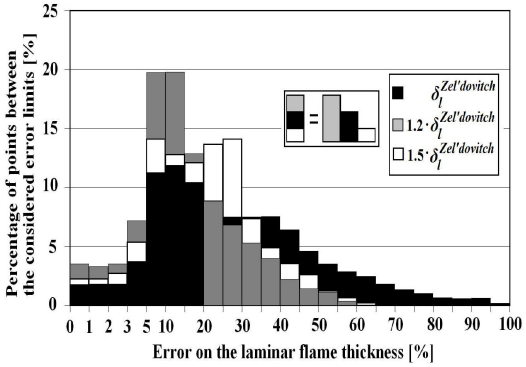

Figure 5.14: Improvement of results on the laminar flame thickness by slightly increasing the Zel'dovitch correlation by a factor c.

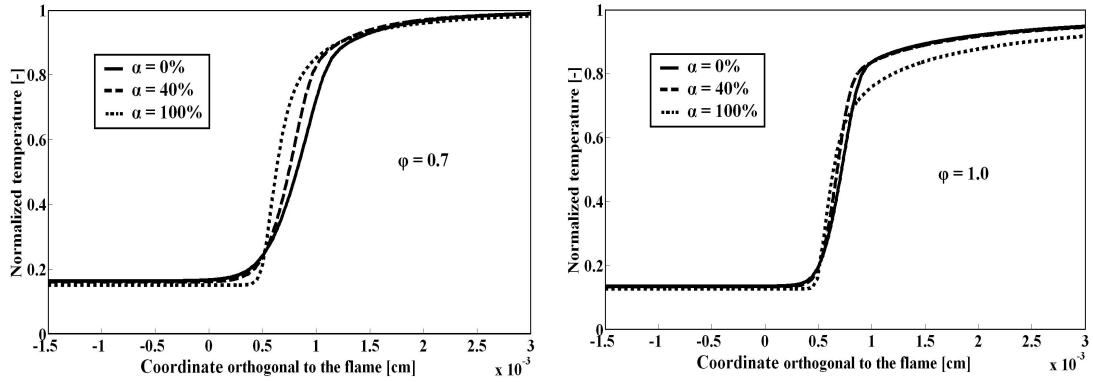

(a) (b)

Figure 5.15: Temperature profiles for different hydrogen rates in the fuel obtained using GRI 3.0 mechanism: (a) results for $\varphi = 0.7$, $Y^u_{res} = 0\%$, $P = 0.1MPa$ – (b) results for $\varphi = 1.0$, $Y^u_{res} = 0\%$, $P = 0.1MPa$.

5.2 Integration of complex chemistry to compute the species oxidation through the flame front source term

---

- **Title**: On the combination of complex chemistry with a 0-D coherent flame model to account for the fuel properties in spark ignition engines simulations: Application to methane-air-diluent mixtures
- **Authors**: S. Bougrine* **, S. Richard*, Denis Veynante**
  * IFP Energies nouvelles
  ** Laboratoire EM2C, CNRS Ecole Centrale Paris
- **Reference**: Thirty-third International Symposium on Combustion, Proc. Combust. Inst., 2011, 33:3123-30

5.2.1 Abstract

A promising way to reduce green house gases emissions of spark ignition (SI) engines is to burn alternative fuels like biomass-derived products, hydrogen or compressed natural gas. However, their use strongly impacts combustion processes in terms of burning velocities and emissions. Specific engine architectures as well as dedicated control strategies should then be optimized to take advantage of these fuels. Such developments are today increasingly performed using complete engine simulators running in times close to the real time and thus requiring very CPU efficient models. For this purpose, 0-dimensional models are commonly used to describe combustion processes in the cylinders. However, these models should reproduce the engine response for all possible fuels, which is not an obvious task regarding the evocated CPU constraints. This paper deals with the extension of a 0-dimensional coherent flame model (CFM), called CFM1D, to integrate chemical effects related to the fuel composition at low computational costs. Improvements have been carried out using an innovative approach based on *a priori* simulations of 1D premixed flames with a complex chemistry code. Databases of laminar flame speeds and thicknesses as well as burned gases compositions in engine-like conditions are generated from these simulations, all these information being required as inputs in CFM1D. The proposed approach is here applied to methane-air-diluent mixtures to simulate a large range of operating conditions of a spark-ignition (SI) engine. A new laminar flame speed correlation adapted to engine thermodynamic conditions is also developed to save CPU time. Comparisons are made with experiments and with simulations performed using the original version of CFM1D based on a simple chemistry. The achieved results evidence the advantage of this new approach to account for the fuel composition effects on the engine behavior.
Keywords: Laminar flame speed correlation; Methane; Engine cycle simulation; Complex chemistry; CFM

5.2.2 Introduction

Environmental regulations compel automotive engineers to develop new engine technologies to replace old power units by new eco-aware systems. An interesting way to reduce green house gases emissions in spark ignition (SI) engines is to burn alternative fuels like gasoline blended with bio-mass derived components, hydrogen or compressed natural gas (CNG). Nevertheless, such fuels modify combustion processes and then affect the engine behaviour in terms of burning velocities, emissions, cyclic variabilities, sensitivity to knock, ... Therefore, to take advantage of the potential of these fuels, specific engine architectures and control strategies have to be developed. Today, such developments are increasingly carried out using simulators integrating

all the engine components and running in times close to the real time. These simulators thus require very CPU efficient models and 0-dimensional approaches, based on simplified descriptions of chemical processes, are commonly used to represent combustion phenomena in the cylinders. Simple descriptions of chemistry are not sufficient to predict the response of engines burning different types of fuels. On the other hand, the implementation of detailed chemical schemes is not currently possible because of the evocated CPU constraints. To use strongly reduced mechanisms may lead to a significant lost of information. An interesting alternative to maintain low computational times while integrating complex chemical processes is to use *a priori* simulations of prototype flames in conditions representative of those found in the engine with a complex chemistry code. These simulations provide data, which can be incorporated in 0-dimensional models under the form of look-up tables or correlations. In this paper, this approach is applied to the combustion of methane-air-diluent mixtures in a SI engine, methane being the main component of CNG (Compressed Natural Gas) and implemented in a 0D version of the coherent flame model (CFM), called CFM1D (Richard et al. 2009), obtained by reduction of the 3D ECFM (Richard et al. 2007, Vermorel et al. 2007). This reduction process represents a very innovative approach compared to two-zones semi-empirical models previously proposed in the literature (Tabaczynski et al. 1977, Heywood 1988). The CFM1D model requires as inputs the evolution of the laminar flame speed and thickness during the engine cycle to describe the turbulent burning rate. The corresponding species consumption rate was originally based on a single step chemistry to describe fuel oxidation process in the turbulent flame as well as pollutant formation in burned gases. Laminar flame speeds and thicknesses can be obtained by experimental correlations, but such correlations not available for all fuel compositions and are generally based on low pressure and temperature measurements, which are not representative of conditions encountered in modern SI engines. In this work, simulations of 1D premixed flames with the GRI 3.0 mechanism (Smith et al. 2000) are then used to generate new correlations and to improve the description of chemical species through a tabulation method. The modified CFM1D model is finally validated by comparison with experimental data obtained at the engine bench for a wide range of operating conditions.

5.2.3 Combustion model - CFM1D

Principles and assumptions are presented in Chapter 4

The approach considered here is inspired from the PCM-CFM model developed by Lecocq et al. (Lecocq 2010, Lecocq et al. 2011). This model is based on the coupling of the CFM approach aiming at describing the flame surface and the PCM-FPI model describing the species evolution through the flame front. It results the following expression for the local reaction rate of a species i through the flame front :

$$\left.\frac{d\rho_u Y_i}{dt}\right|_{ff} = -\rho_u \left(Y_i^{eq} - Y_i^u\right) U_l \bar{\Sigma} \tag{5.16}$$

where ρ_u is the fresh gases density, U_l is the laminar flame speed, Y_i^u and Y_i^{eq} are the mean mass fractions of the ith species respectively in the fresh gases and in the products of the fuel oxidation reaction through the flame and $\bar{\Sigma}$ represents the filtered flame surface density. In such an approach the composition at equilibrium Y_i^{eq} is tabulated allowing thus the direct integration of complex chemistry to describe oxidation processes.

In the present work, this model is adapted by integrating the expression of Eq. 5.16 over a control volume V_c (corresponding to the combustion chamber volume) supposing that all properties (P, T^u, φ, etc.) are homogeneous throughout the flame front. It comes then the following expression for the mass variation of species i through the flame front (stepping in Eq. 4.2) :

$$\left.\frac{dm_i}{dt}\right|_{ff} = \int_{V_c} \left.\frac{d\rho_u Y_i}{dt}\right|_{ff} dV = -\rho_u \left(Y_i^{eq} - Y_i^u\right) U_l \int_{V_c} \bar{\Sigma} dV = -\rho_u \left(Y_i^{eq} - Y_i^u\right) U_l A_T \tag{5.17}$$

Y_i^u is initialized at intake valve closure (IVC) and accounts for gas exchanges phenomena between the intake, the exhaust and the combustion chamber. Then this composition can evolve if fuel

is injected during the compression stroke. *Details on the calculation of the fresh gas density and turbulent flame surface (A_T) are given in Chapter 4*

5.2.4 Complex chemistry integration in CFM1D

This section describes the determination of U_l, δ_l and Y_i^{eq} from complex chemistry computations.

Approach and assumptions

One-dimensional premixed flames are computed first using a complex chemistry code (Premix module of the CHEMKIN software (Kee et al. 1989)). Many chemical kinetics mechanisms are available and several of them (GRI 3.0 (Smith et al. 2000), Wang et al. (Wang et al.), Konnov et al. (Konnov 2011), Lecong et al. (Lecong and Dagaut 2009)) were tested in this work against a wide database of laminar flame speed measurements from the literature. The GRI 3.0, built-up with 53 species and 325 reactions and designed for the combustion of natural gas, was finally chosen. This mechanism indeed represents a good compromise between prediction and robustness, especially at high temperature and pressure conditions found in modern SI engines. One of the essential model assumptions is to consider that the pressure varies slowly compared to chemical time scales. Figure 5.16 shows that the pressure variations during a flame time $\tau_l = \delta_l/U_l$ are not significant. Indeed, for example, the relative variations are lower than 4% for an engine speed of 2000 rpm and for loads from idle to wide open throttle (4 to 30 bars of IMEP - Indicated Mean Effective Pressure). This assumption can thereby be considered as true authorising a priori premixed flames simulations at constant pressure to generate information for engine calculations. Simulations were then performed for a very wide range of thermodynamic conditions T^u and P and fresh mixture compositions (equivalence ratio ϕ and diluent mass fraction Y^u_{res}, diluent being approximated as additional N_2) (Table 5.5), representative of those encountered in engine applications, leading to the generation of a database containing more than 4100 points.

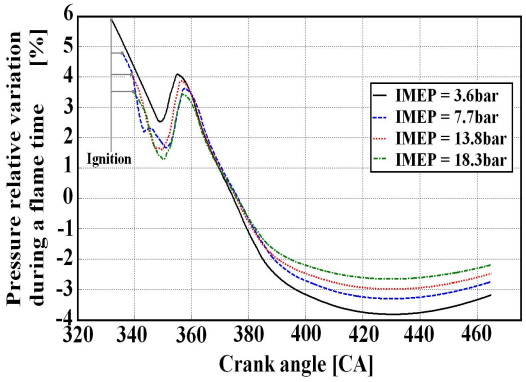

Figure 5.16: Relative pressure variation during a flame time $\tau_l = \delta_l/U_l$ at 2000 rpm and $\phi = 1$.

	Range of variation	Number of points
φ [-]	0.6 – 1.3	9
Y^u_{res} [m/m%]	0 – 25	7
T^u [K]	300 – 950	12
P [0.1MPa]	1 – 110	14

Table 5.5: Characteristics of the 1D-premixed flames database.

Species evolution through the flame

In the present model, reactants of composition Y_i^u are converted into products of composition Y_i^{eq} through the flame front (Eq. 5.17). The products composition was previously (see Chapter 4) inferred from a single step chemical (s.s.c) reaction producing CO_2, H_2O, CO and H_2 in proportions depending on the fuel composition and the equivalence ratio (Bougrine et al. 2009).

However, this simple chemistry does not account for the possible variation of Y_i^{eq} with the pressure, temperature and dilution and can then not provide correct compositions and enthalpy levels downstream of the flame, which may affect both the combustion heat release and post-flame chemical reactions. An alternative to s.s.c. consists in storing products compositions, obtained from the Premix calculations, as a function of the pressure, fresh gases temperature, equivalence ratio and residuals mass fractions (tabulated chemistry, t.c.). At each time step, this composition is obtained by interpolation in the look-up table using the current P, T^u, φ and Y_{res}^u values and is then injected in Eq. 5.17. In practice, only CH_4, CO_2, CO, H_2O mass fractions are stored while O_2, H_2, and UHC (here considered as CH_4) mass fractions are reconstructed from the atomic conservation of C, H and O through the flame.

Laminar flame speed and thickness

To limit redundancy this part of the paper will not be described. The laminar flame velocity correlation used has been presented in previous section (5.1) in Table 5.4. The laminar flame thickness correlation used here is the Zel'dovitch one presented in Eq. 5.14.

5.2.5 Engine application

The modified CFM1D has been implemented in the AMESim® simulation software (Albrecht et al. 2005) and tested in the case of a 4-cylinder turbocharged SI engine (Table 5.6). A wide experimental database of 59 operating points was available comprising results for 4 engine speeds (1000 to 5500 rpm) and loads from idle to Wide Open Throttle (Indicated Mean Effective Pressure, IMEP, from 3 to 25 bar). A unity equivalence ratio was retained for all operating conditions.

$Bore\ (mm)$	82.7
$Stroke\ (mm)$	93
$Compression\ ratio$	11
$Connecting-rod\ length(mm)$	143
$Displacement(cm^3)$	2000

Table 5.6: 4-cylinders engine characteristics

Simulator set-up

The simulator is constituted by several components representing the different parts of the engine. The combustion model is plugged in the cylinder component and heat transfer at the walls are accounted for with the widely used Woschni model (Woschni 1697). The calculation time for a whole engine cycle is today about 1s but can be further optimized. The boundary conditions (pressure and temperature) and engine settings (spark advance, injection timing and duration) are set from the experimental database.

Model validation

The complexity of SI engines geometries (air-path, combustion chamber, etc) requires first a calibration of the 0D turbulence model, which does not explicitly resolve the main flow motions on a computational mesh, contrary to 3D models. The calibration methodology was detailed in

(Richard et al. 2009) and mainly aims at describing the effect of the engine geometry on the aerodynamics of the combustion chamber by setting the tumble number of the flow at IVC. This tumble number can be seen as an initial condition of the simulation and is an image of the mean flow kinetic energy K at IVC. Results in terms of cylinder pressure trace and pollutant emissions are presented in the following.

Cylinder Pressure Trace An example of simulated cylinder pressure curves obtained at 2000 rpm and for several engine loads are displayed in Figure 5.17 and shows a very good agreement with experimental data for all operating conditions. Figure 5.18 gives an overview of the results for the 59 operating points: errors on the maximum cylinder pressure and indicated mean effective pressure do not exceed respectively 1% and 0.4 bars for 90% of the simulated points. All these results show that the evolution of the burning velocity – and then the heat release rate – is well predicted by the proposed correlations for the laminar flame speed and thickness, which are the main chemical ingredients to describe the turbulent flame propagation (Eqs. 5.17, 4.7 and 4.15).

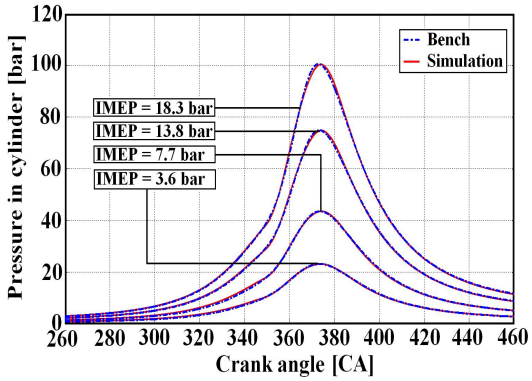

Figure 5.17: Comparisons between experimental and simulated cylinder pressure curves for different engine loads at 2000 rpm.

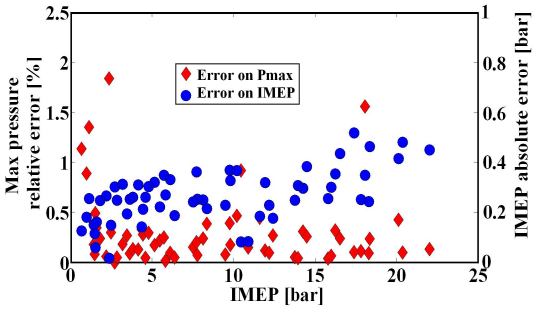

Figure 5.18: Errors on the maximum cylinder pressure and indicated mean pressure for the 59 operating points.

Pollutant Emissions Figure 5.19 shows an example of NO and CO levels at the exhaust for a fixed engine speed (2000 rpm) and different loads. Experimental data are compared with results obtained using tabulated (t.c.) and single step chemistry (s.s.c.) to describe the species evolution through the flame. For both cases, trends are respected but s.s.c. overestimates NO levels at low loads and underestimates them at high loads, while t.c. recovers experimental curve over all loads. The difference between the two models is more significant for CO emissions as s.s.c. predicts twice higher levels compared to experiments. Figures 5.20 and 5.21 give an overview of the results for

the 59 operating points reinforcing the previous observation. Indeed, t.c. CO errors are lower than 15% for 83% of the simulated points, which is satisfactory regarding the low handled CO concentrations. On the contrary, errors are larger than 30% for 90% of simulated points for s.s.c.. Similarly, t.c. leads to errors lower than 20% for 88% of the operating points for NO levels, while only 37% of these points are below this level with s.s.c. The differences between s.s.c. and t.c. may be explained by the fact that enthalpy levels and oxygen concentrations in combustion products strongly differs, affecting dissociation processes and NO formation in the burned gases zone of CFM1D.

5.2.6 Conclusion

This paper presents the integration of complex chemistry in the CFM1D combustion model (Richard et al. 2009). To respect the CPU constraints of full engine simulations, the proposed approach is based on a priori simulations of 1D premixed flames to generate a wide chemical database (composition, laminar flame speed and thickness), which can be directly plugged in the combustion model. In this work, methane-air-diluent mixtures are considered and the GRI 3.0 mechanism has been retained for complex chemistry calculations. A new description of the fuel oxidation chemistry of CFM1D has then been proposed, interpolating realistic compositions of the products of fuel oxidation from a look-up table. To maximize CPU-efficiency, laminar flame thicknesses and speeds were estimated respectively from the Blint correlation and a new correlation adapted to high pressure and temperature levels found in modern SI engines. The proposed model was then validated on a wide range of operating points from a 4 cylinder turbocharged SI engine. Simulations results were in very good agreement with experiments in terms of cylinder pressure traces, showing the validity of the proposed laminar flame speed and thickness correlations. To replace a single step chemical scheme by complex chemistry is found to have a huge impact on the prediction of pollutant emissions, giving better results and demonstrating the interest of tabulated complex chemistry in 0D simulations. It should be noticed that this approach could be extended to the 3D ECFM model for RANS or LES applications. Future work will be devoted to the use of a priori complex chemistry simulations for other types of fuels (hytane, ethanol gasoline blends...).

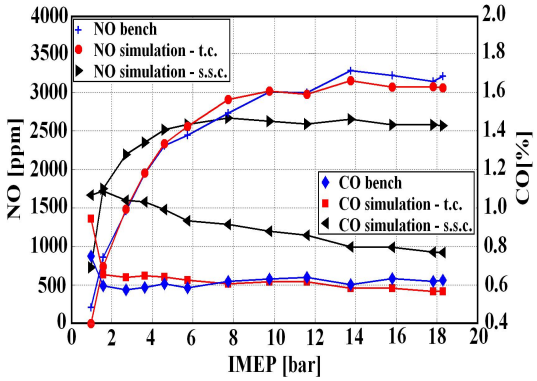

Figure 5.19: Comparison of experimental and simulated NO and CO concentrations at the exhaust at 2000 rpm and for different loads.

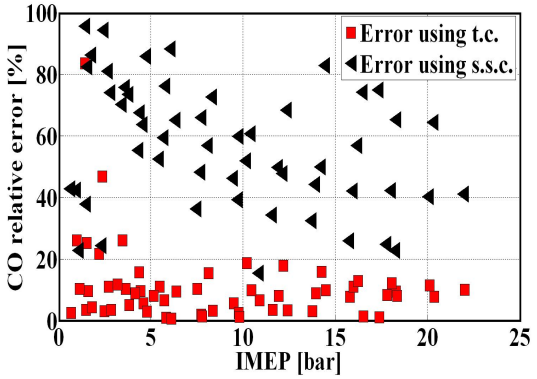

Figure 5.20: CO emissions relative errors, using a single step or a tabulated chemistry for the fuel oxidation in the flame, for the 59 operating points.

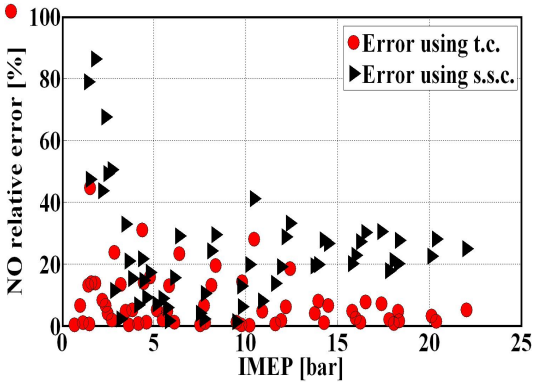

Figure 5.21: NO emissions relative errors, using a single step or a tabulated chemistry for the fuel oxidation in the flame, for the 59 operating points.

5.3 Complementary comments

Iso-octane-ethanol blends

The approach used to generate the laminar flame velocity correlation (Section 5.1, Figure 5.3) has been developed for methane-hydrogen-air-nitrogen mixtures and can be applied to the development of new laminar flame speed correlations for other fuel formulations as gasoline-ethanol mixtures. However, the treatment of octane-alcohol fuels can be a harder task and the failed cases (Figure 5.3) number generated using the tool presented in Section 5.1 can be higher than for methane-hydrogen case. Indeed, computing the first flame is not always easy and if the fields given initially for the temperature and for all species composition are too far from the solution, convergence can be hard to obtain. Therefore, when fuels requiring hundred of species and thousand of reactions (as gasoline) must be computed this initialization is even more complex. As previously mentioned (Figure 5.3), a solution can consist on using continuation run strategies but here also the important required species number often lead to unstable chemical models making here also flame initialization difficult. Despite of these constraints, a new correlation adapted to the combustion of gasoline-ethanol mixtures has been developed at IFPEn using the approach presented in this thesis and the IDETHANOL (Pires.da.Cruz et al. 2010) complex chemistry mechanism. This latter has been developed at IFPEn in collaboration with PSA, Renault and CORIA (CNRS) and is dedicated to injection, combustion, auto-ignition and pollutant formation problems in GDI engines burning ethanol-gasoline blends. The new developed correlation has been validated against a wide range of temperature ($300 < T^u < 800K$), pressure ($1 < T^u < 6MPa$) and composition ($0.6 < \varphi < 1.3$, $0 < Y^u_{res} < 30\%$, $0 < V < 100\%$ (where V is the proportion of ethanol in gasoline)) conditions. Figures 5.22 and 5.23 give some examples of validation results showing that IDETHANOL globally allows to recover experimental laminar flame speed levels. The new correlation is given here:

$$U_l\left(\varphi, T^u, P, V, Y^u_{res}\right) = U^0_l\left(\varphi, V\right) \cdot \left(\frac{T^u}{T^0}\right)^{(2.236)} \cdot \left(\frac{P}{P^0}\right)^{-0.2832} \cdot f(Y^u_{res}) \tag{5.18}$$

with $T^0 = 400K$, $P^0 = 1bar$ and

$$U^0_l\left(\varphi, V\right) = \left(1 + 0.14892\left(V\right)^{2.4698}\right) \cdot 0.90931\left(\varphi\right)^{2.4269} \exp\left(3.154 \cdot \left(\varphi - 0.68157\right)^2\right) \tag{5.19}$$

and

$$f(Y^u_{res}) \;=\; \left(1 - 2.4832 Y^u_{res} - 0,0020312 {Y^u_{res}}^2 - 0,0041743 {Y^u_{res}}^3\right) \tag{5.20}$$

Pollutants

According to conclusion of Section 5.2, the integration of the tabulation approach and of the new laminar flame speed function appears as a very good solution to improve results in terms of pollutants emissions, in particular for CO formation. Complementary results are displayed in Figure 5.24 which compares simulated and experimental NO and CO levels at two other engine speeds (3000 and 4000 rpm) for methane fuel. However, it should be noticed that this solution is not significantly efficient with regard to system simulation. Indeed, as mentioned in Section 4.3, an important parameter to optimize is the computational time. In fact, the most CPU expensive part of the combustion model is the pollutant sub-model ($\approx 90\%$ of the total CPU consumption) and more particular the post-oxidation sub-model ($\approx 80\%$ of the pollutant model CPU consumption) computing the second RHS term of Eq. 4.2 ($dm_i|_{pf}$) reminded here :

$$\frac{dQ_{comb}}{dt} = \sum_i h_{f_i} \left(\left.\frac{dm_i}{dt}\right|_{ff} + \left.\frac{dm_i}{dt}\right|_{pf} \right) \tag{5.21}$$

Indeed, the description of dissociation processes and NO_x formation in the burnt gases (Section 4.1) involves 10 reactions and 13 species which associated kinetics can be particularly low. Moreover, such a post-oxidation sub-model requires the calibration of several parameters (see Chapter

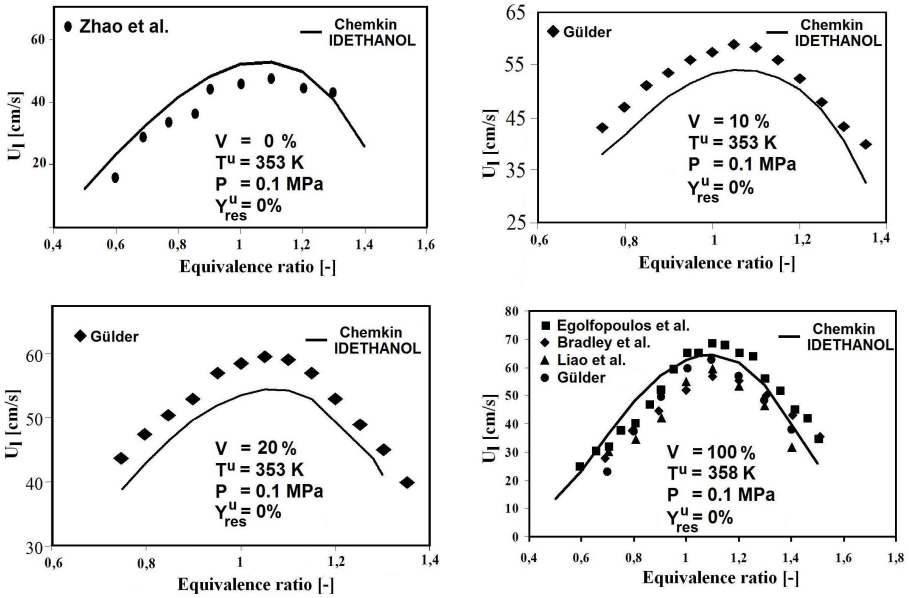

Figure 5.22: Comparison of experimental and simulated laminar fame speed variations as a function of the equivalence ratio and for different ethanol rate ($0 \leq V \leq 100\%$) in iso-octane. Operating conditions: $T^u = 353K$, $P = 1MPa$. Experimental results were obtained by Gülder (1982), Egolfopoulos et al. (1992), Bradley et al. (2009), Liao et al. (2007) and Zhao et al. (2003). Simulation results were obtained using the IDETHANOL kinetic scheme (Pires.da.Cruz et al. 2010).

6) allowing to catch phenomena not described by the reduced chemistries. A solution to complement the pollutant model development is therefore to integrate a similar tabulation approach to directly describe CO and NO formation in the burnt gases. A new approach called CORA for (CO Relaxation Approach) inspired from the NO approach for NO (Vervisch et al. 2011) is presented in Section 6. Such an approach has the advantage to be totally generic, requiring no parameter calibration.

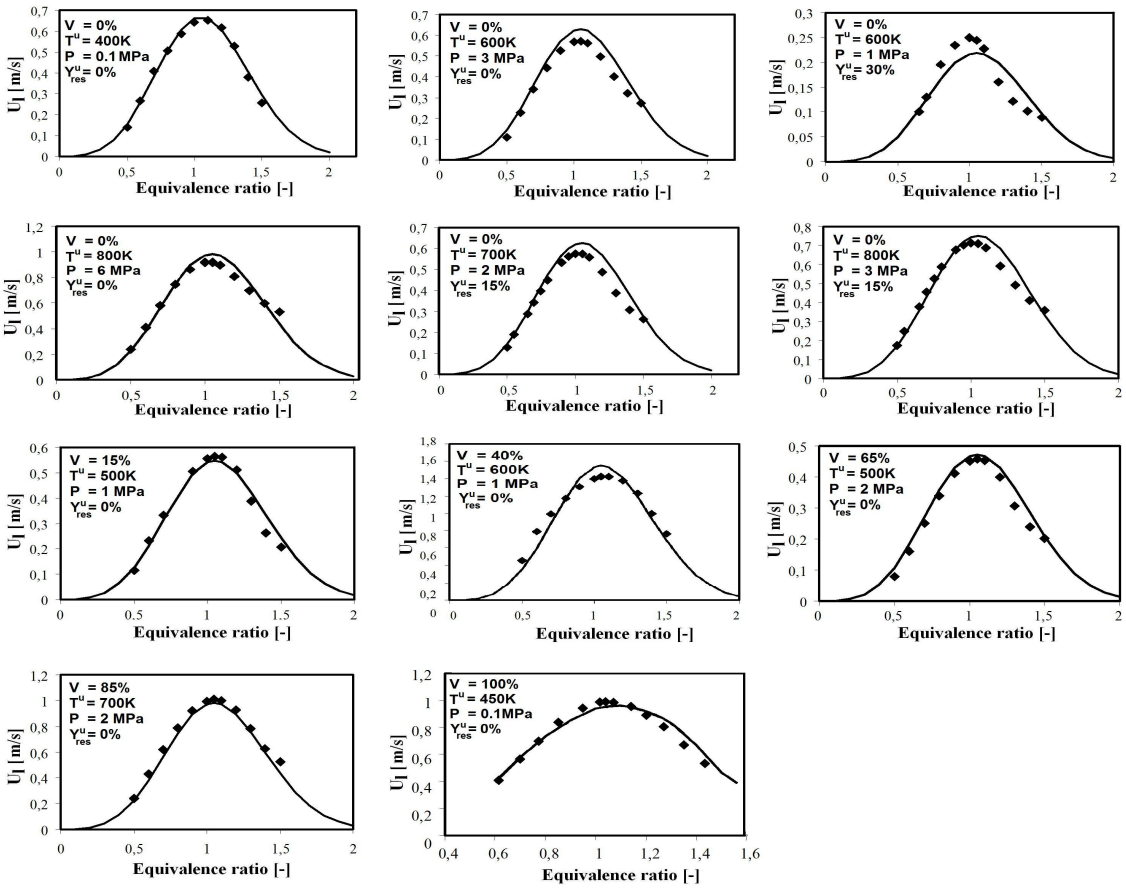

Figure 5.23: Laminar fame speed variations as a function of the equivalence ratio and for different conditions (ethanol rate V, unburnt temperature T^u, pressure P and residual mass fraction Y^u_{res}). Symbols: correlation 5.18. Line: Results from Chemkin (Kee et al. 1989) using the IDETHANOL kinetic scheme (Pires.da.Cruz et al. 2010).

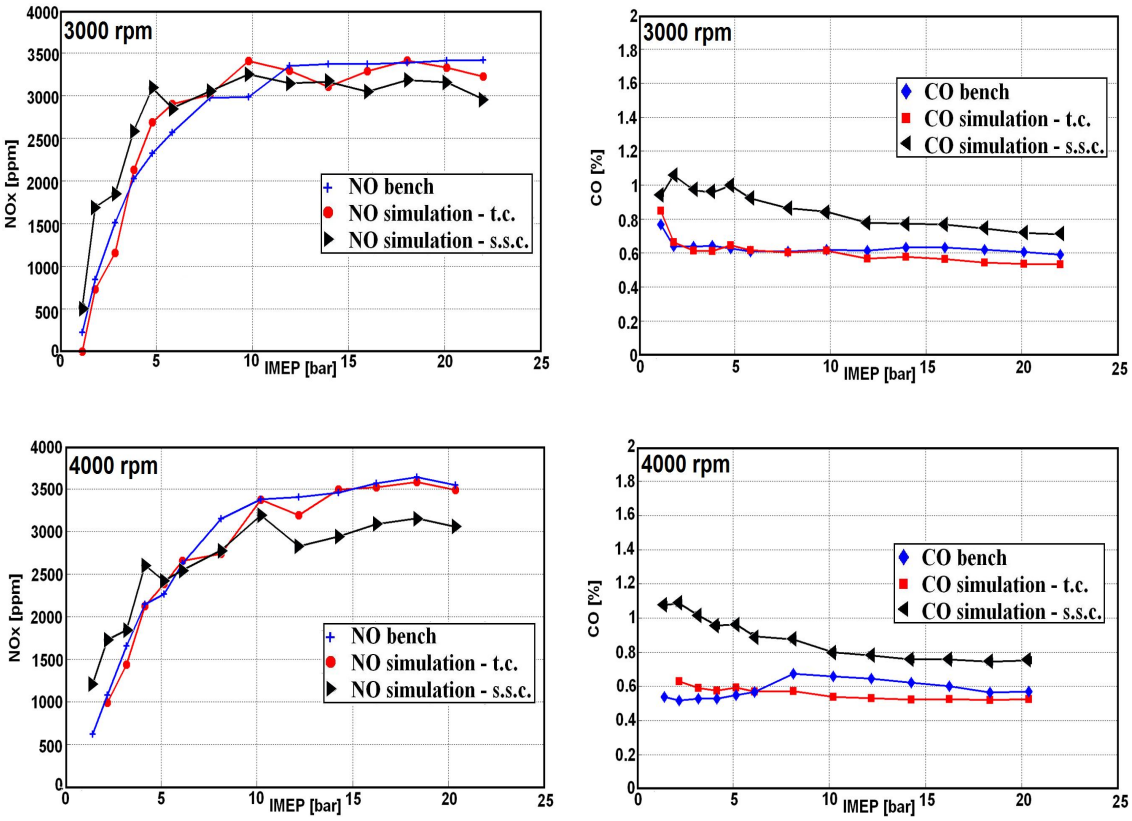

Figure 5.24: Comparison of experimental and simulated NO and CO concentrations at the exhaust at 3000 and 4000 rpm and for different engine loads. First column : NO evolutions – Second column : CO evolutions. Fuel = methane.

Chapter 6

Post-oxidation processes – The CORA and NORA approaches

This chapter presents the tabulation approach used to integrate complex chemistry in the CFM1D model to describe post-oxidation processes (Figure 6.1). This new approach named CORA (CO Relaxation Approach) is inspired from the NO Relaxation Approach (NORA) (Vervisch et al. 2011) and consists in the tabulation of compositions at equilibrium $Y_k^{b,eq}$ and characteristic relaxation times τ_k (where k stands for NO and CO (Figure 6.2)). In the following, after a description of the CORA approach, the final heat release and pollutant model named CFM1D-TC integrating developments presented in Chapter 5 and in the present one is validated against a wide range of operating conditions of an IFPEn SI engine burning methane. Works described in this Section were integrated in an article submitted to Combustion and Flame.

Remark: For the sake of clarity and for a better readability, some parts already described in previous Chapters are reminded in this Section.

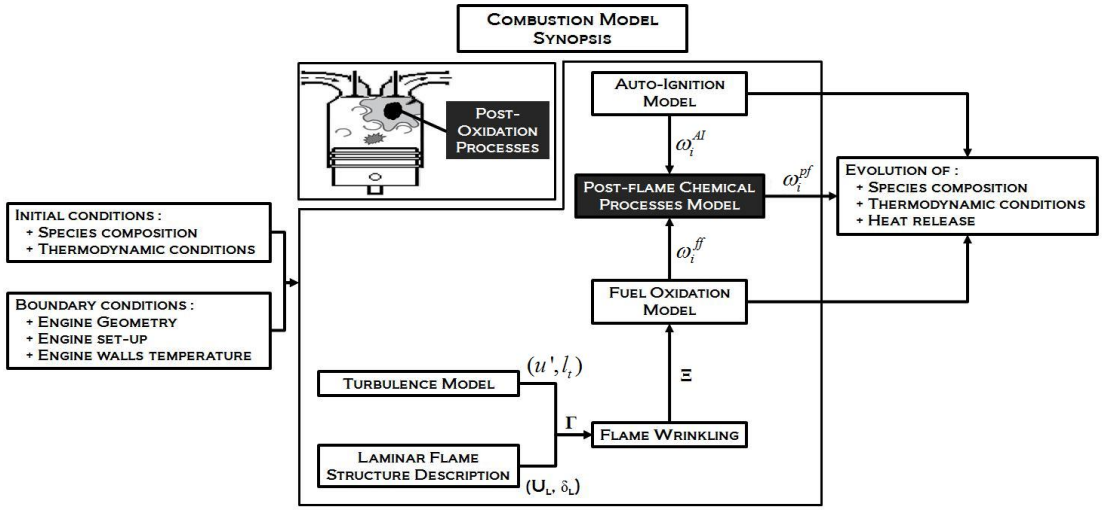

Figure 6.1: Combustion model global synopsis: **focus on the post-oxidation model**. ω_i^{ff},ω_i^{pf} and ω_i^{AI} refer to the rates of consumption/production of species i associated respectively to the combustion, post-oxidation and auto-ignition processes stepping in Figures 1.3 and 1.4.

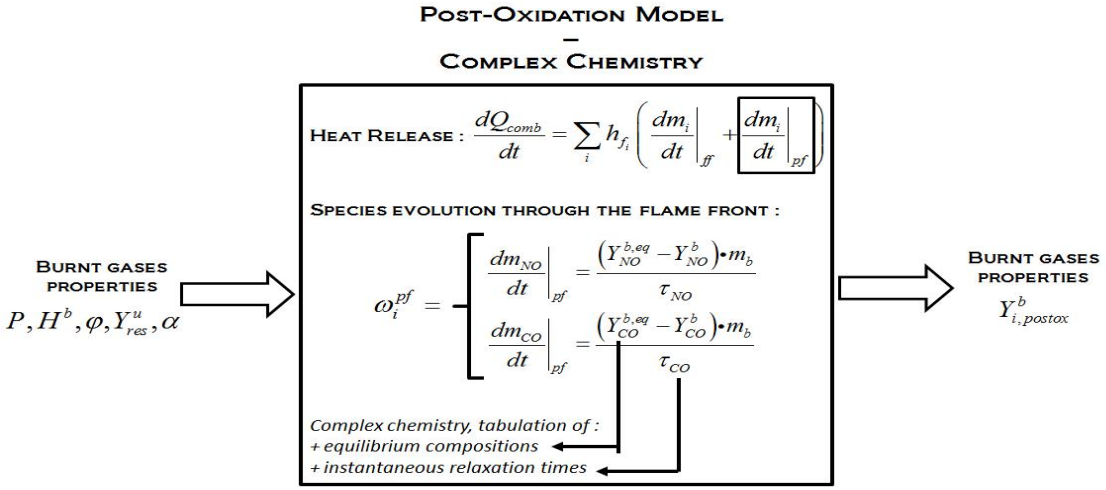

Figure 6.2: The new post-oxidation model global description (see Figure 4.1 for the old one) – All parameters will be defined in the following sections – ω_i^{pf} refers to the rate of consumption/production of species i stepping in Figure 1.3.

6.1 Integration of complex chemistry to compute the species post-oxidation source term using NORA and CORA approaches

---

- **Title**: Simulation of CO and NO Emissions in a SI Engine Using a 0D Coherent Flame Model Coupled with a Tabulated Chemistry Approach
- **Authors**: S. Bougrine* **, S. Richard*, Jean-Baptiste Michel*, Denis Veynante**
  * IFP Energies nouvelles
  ** Laboratoire EM2C, CNRS Ecole Centrale Paris
- **Reference**: submitted to Combustion and Flame

6.1.1 Abstract

Environmental issues stimulate the elaboration of new powertrain systems and fuels for transport as an essential priority to decrease air pollution and green house gases emissions. Developments ranging from architecture definition to engine control and calibration are today increasingly performed using complete vehicle simulators running close to real times. The challenge for engineers is therefore to develop models able to accurately reproduce the engine response without altering the CPU efficiency of the simulator. For this purpose, 0-dimensional models are commonly used to describe combustion processes in engine combustion chambers. This paper extends a 0-dimensional coherent flame model (CFM), called CFM1D, to incorporate chemical effects related to the fuel composition and thermodynamic conditions at low computational costs. Improvements are carried out integrating the NO relaxation approach (NORA) based on *a priori* homogeneous reactor computations and initially developed for 3D simulations to describe post-oxidation processes in the burnt gases. In this work, this method is extended to the modeling of CO production and oxidation leading to the CORA (CO Relaxation Approach) model. Both NO and CO reaction rates are therefore written as linear relaxations towards their equilibrium mass fraction values Y_k^{eq} (where k stands for NO or CO) within a characteristic time τ_k. In this approach, Y_k^{eq} and τ_k are tabulated as functions of equivalence ratio, fresh gases dilution rate by burnt gases, pressure and enthalpy. The resulting new model, called CFM1D-TC (CFM1D-Tabulated Chemistry), is then used to perform simulations on a large range of operating conditions of a spark-ignition engine burning methane-air-dilutent mixtures. Comparisons are made with experiments and with simulations performed using a classical reduced chemical scheme in the burnt gases. The achieved results evidence the interest in terms of accuracy and CPU-efficiency of this new approach to describe post-flame processes in spark ignition engines.
Keywords: NO, CO, SI engine, tabulation, 0D modeling.

6.1.2 Introduction

Because of climate change processes, the transport industry and more particularly the automotive sector are subject to environmental regulations prescribing to investigate low greenhouse gases emissions strategies. In this context, the development of new environmentally friendly engines becomes crucial. Due to the increasing cost and the duration of experimental campaigns, such systems combining many high technology components with new specific fuels, dedicated architectures and advanced control strategies are today more and more designed using numerical simulation tools. Among them, 0D/1D approaches are of special interest as they are very CPU efficient and associated simulators are today able to run in real time. However, such models, mainly based on

simple physical descriptions, can suffer from a lack of predictivity especially when dealing with complex fluid mechanics problems like combustion and pollutants formation in engine combustion chambers. Developing new models including more physics while remaining low CPU consuming is therefore a crucial issue for an extensive use at all stages of the engine development, from concepts definition to powertrain control development and calibration. First 0D models, like Wiebe model (Wiebe 1956), were based on simple empirical descriptions of the combustion heat release and were not able to account for complex physical phenomena like combustion/turbulence interactions. Phenomenological models have then been developed to describe the heat release through physical quantities such as flame speed or turbulence parameters, also estimated from phenomelogical laws. A non-exhaustive list of main works on such models comprises Tabaczynski et al. (1977), Poulos and Heywood (1983), Bozza et al. (2005), Nishiwaki (2008), for spark ignition (SI) engines or Chelma and Orthaber (1999) and Barba et al. (2000), for Diesel applications. Nevertheless, the description of fuel oxidation processes is generally not based on theoretical basis and cannot allow a precise description of combustion processes, like, for example, the evolution of the flame surface in SI applications, or the spray zone in Diesel ones. This motivated the development of refined physical laws for the heat release derived from the reduction of 3D combustion models (Mauviot et al. 2006, Dulbecco 2009, Lafossas et al. 2005, Richard et al. 2009, Kwon et al. 2011). In the Diesel context, developments concerned the integration of chemistry tabulation approaches deduced from formalisms like the Tabulated Kinetics for Ignition method (TKI) (Colin et al. 2005) for auto-ignition phenomena or the Flame Prolongated of ILDM method (FPI) (Gicquel et al. 2000, Ribert et al. 2006) for species evolutions. Developments were also achieved to account for spray inhomogeneities integrating probability density function (PDF) approaches. For SI applications, main works concerned the reduction of the Coherent Flame Model (CFM) adapted to premixed flames by Lafossas et al. (2005) and Richard et al. (2009) who derived the bases of the associated reduced combustion model CFM1D. In the latter, the heat release explicitly accounts for the turbulent flame surface under a flamelet assumption. To ensure a high computational efficiency, all these 0-dimensional models are generally based on simple descriptions of chemistry for post-flame processes (Barba et al. 2000, Lafossas et al. 2005, Richard et al. 2009, D'Errico and Onorati 2004, D'Errico and Lucchini 2005, D'Errico et al. 2006, Heywood et al. 1979). However, reduced chemical schemes still need significant computational resources with regard to system simulation and are not expected to be predictive for all thermodynamic conditions and for all fuel compositions currently found in actual engine applications (pressures up to 13 MPA, temperatures up to 3000 K, equivalence ratios between 0.6 and 1.3 and dilution rates by burnt gases up to 30%). This is particularly true for NOx formation which, on the one hand, occurs on large time scales compared to fuel oxidation processes and, on the other hand, is very sensitive to temperature and equivalence ratio. An interesting alternative to optimise computational times while accounting for complex chemical processes is to implement tabulation methods as performed in recent 3D CFD simulations (Colin et al. 2005, Gicquel et al. 2000, Ribert et al. 2006, Vervisch et al. 2011). This paper deals with the development of a new 0D pollutant emissions model to reduce computational times and to account for enthalpy, pressure and gas composition variations in SI engines. This new formalism is integrated in the last version of the CFM1D model considering an FPI tabulation approach to compute the heat released by the fuel oxidation (Bougrine et al. 2011). The description of nitrogen oxides formation mainly relies on the adaptation of a NO tabulation approach initially proposed by Michel (2008) and Colin et al. (2010). and is based on the assumption of an exponential relaxation of the NO concentration towards equilibrium. This assumption allows to directly write the NO reaction rate as a linear function of NO mass fraction with an instantaneous characteristic time required to reach this equilibrium state. Both quantities are extracted from look-up tables resulting from *a priori* homogeneous reactor simulations using the GRI 3.0 mechanism (Smith et al. 2000). This method, already validated by Vervisch et al. (2011) in engine configurations, naturally allows to retrieve the NO evolution during the expansion step in SI engines characterized by concentrations higher than equilibrium ones. This behavior has also been observed for the carbon monoxide (Heywood 1988) which evolutions are closely similar to those of NO. In this study, the same approach is therefore extended to CO prediction. The proposed developments are performed in the continuity of the last works of

Bougrine et al. (2011) who incorporated a tabulation model describing the fuel oxidation process in SI engines in CFM1D. This combustion model is presented in Section 6.1.3. The tabulation method and considered assumptions are thereafter described in Section 6.1.4. Finally, the modified CFM1D called here CFM1D-TC (for CFM1D-Tabulated Chemistry) model is implemented in an engine simulation software (Malbec et al. 2009). Validations are performed by comparison with experimental data obtained at the engine bench for a wide range of operating conditions and with simulations performed using the original version of CFM1D based on a reduced chemical scheme (Section 6.1.5).

6.1.3 Combustion modeling

Principle and assumptions

The developments proposed in this work are based on the CFM1D model obtained by reduction of the 3D CFD CFM model (Lafossas et al. 2005, Richard et al. 2009, Bougrine et al. 2011). The CFM formalism distinguishes two zones (Figure 6.3): fresh and burnt gases which are separated by a flame front propagating from the burnt gases towards the fresh mixture. Chemical reactions of fuel oxidation occur in a very thin layer (the flame front ff) compared to all scales of the turbulent flow and post-flame (pf) chemistry takes place in burnt gases. The heat released by the combustion processes, dQ_{comb}/dt, is then expressed as (Lafossas et al. 2005):

$$\frac{dQ_{comb}}{dt} = \sum_i h_{f_i} \left(\left.\frac{dm_i}{dt}\right|_{ff} + \left.\frac{dm_i}{dt}\right|_{pf} \right) \tag{6.1}$$

where h_{f_i} is the formation enthalpy of species i, $dm_i|_{ff}$ and $dm_i|_{pf}$ are the mass variations of this species respectively in the flame front and in the burnt gases due to post-flame chemistry reactions.

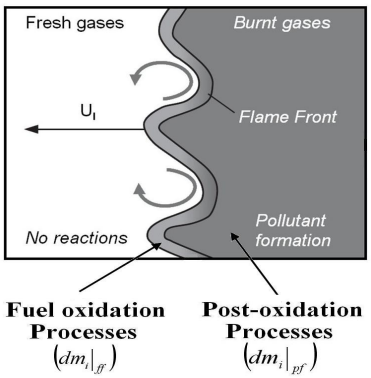

Figure 6.3: The coherent flame approach

Fuel oxidation model

In the CFM formalism, the fuel oxidation term $dm_i|_{ff}$ (Eq. 6.1, Figure 6.3) is modeled considering a conversion of reactants of composition Y_i^u into products of composition $Y_i^{u,eq}$ through the flame front (Bougrine et al. 2011):

$$\left.\frac{dm_{fuel}}{dt}\right|_{ff} = -\rho_u \left(Y_i^{u,eq} - Y_i^u\right) U_l A_T \tag{6.2}$$

where ρ_u is the fresh gases density, U_l is the laminar flame speed, Y_i^u and $Y_i^{u,eq}$ are the mass fractions of the i^{th} species respectively in the fresh gases and in the products of the fuel oxidation reaction just downstream the flame. Such a composition is close to equilibrium because

of the high temperature of this zone which still has not been subjected to losses through heat transfer or expansion. The quotation u, eq have been arbitrarily chosen to dissociate equilibriums reached through the oxidation processes to equilibrium reached through the post-oxidation processes (which will be quoted in the following b, eq). $A_T = \Xi \cdot A_m$ is the turbulent flame surface written as the product of a mean flame surface A_m and a flame wrinkling factor Ξ depending on specific speeds and scales for the turbulence and the flame (laminar flame speed U_l and thickness δ_l) as described in Bougrine et al. (2011). The original version of CFM1D (Lafossas et al. 2005) computed the products composition using a single step chemical reaction producing CO_2, H_2O, CO and H_2 in proportions depending on the fuel composition and the equivalence ratio φ. This simple chemistry was not able to accurately reproduce the possible variation of $Y_i^{u,eq}$ with the pressure (P), unburnt gas temperature (T^u) and dilution (Y_{res}^u), leading therefore to erroneous compositions and enthalpy levels downstream of the flame, affecting both the combustion heat release and post-flame chemical reactions. An alternative to this single step chemistry has therefore been proposed by Bougrine et al. (2011) and is used in the CFM1D-TC model presented in this paper. This approach consists in performing laminar one-dimensional premixed flames computations at constant pressure using a dedicated solver (in this work the PREMIX module from the CHEMKIN software (Kee et al. 1989)) and storing the resulting products compositions as functions of the pressure, fresh gases temperature, equivalence ratio and residuals mass fractions. At each time step, this composition is obtained by interpolation in look-up tables using the current P, T^u, φ and Y_{res}^u values and is then injected in Eq. 6.2. In practice, only $fuel$, CO_2, CO, H_2O mass fractions are stored while O_2, H_2, and UHC (unburnt hydrocarbons, here considered as CH_4) mass fractions are reconstructed from the atomic conservation of C, H and O through the flame. Finally, laminar flame speed U_l and thickness δ_l were also tabulated (Bougrine et al. 2011) to reproduce the effects of fuel composition and thermodynamic conditions on the turbulent flame surface A_T in Eq. 6.2.

Post-oxidation model

CFMD1D In CFM1D the post-flame chemistry term $dm_i|_{pf}$ (Eq. 6.1, Figure 6.3) was initially expressed using a reduced chemistry approach (Richard et al. 2009) combining dissociation processes with the effects of the NO kinetics:

$$\left.\frac{dm_i}{dt}\right|_{pf} = \left.\frac{dm_i}{dt}\right|_{diss} + \left.\frac{dm_i}{dt}\right|_{NOkin} \tag{6.3}$$

The first right hand side term, describing the dissociation processes of several species like CO and CO_2, was computed considering an equilibrium scheme (Meintjes and Morgan 1987) (see Chapter 4) based on a set of 10 species and 6 equations complemented by 4 conservation equations for C, O, H and N. As concentrations of these species are not reached instantaneously, a pseudo kinetics was used in the burnt gases:

$$\left.\frac{dm_i}{dt}\right|_{diss} = \frac{m_i^{eq} - m_i}{\tau} \tag{6.4}$$

where τ is a constant parameter representing the time needed to relax the current burnt gases composition towards the chemical equilibrium and is set to 1.10^{-3} s. In order to capture the freezing effect of CO generally observed when pressure and temperature quickly fall in the expansion stroke and which cannot be described by a simple constant value of τ, $dm_i|_{diss}$ is computed as long as the temperature of the burnt gases is such that $T^b > T_{CO}^{cut}$ where T_{CO}^{cut} is set to 1700 K (Heywood 1988). Below this temperature, $dm_i|_{diss}$ is set to 0 and the concentration of CO remains constant. The second term of Eq. 6.3 describing the formation of NO and its impact on the other species, was computed using an extended Zel'dovitch mechanism based on a set of 3 reversible equations and 7 species (Heywood 1988) (see Chapter 4). Likewise, it is computed as long as the temperature of the burnt gases satisfies $T^b > T_{NO}^{cut}$ where T_{NO}^{cut} is typically set to 2000 K (Heywood 1988). To summarize, 10 reaction equations and 13 species are required in

CFM1D model to compute the post-oxidation term $dm_i|_{pf}$ (Eq. 6.1, Figure 6.3) leading to high computational times. Moreover, the relative simplicity of reduced chemistry can not be sufficient to accurately describe the effects of thermodynamic variations on pollutants production in the burnt gases.

The CFM1D-Tabulated Chemistry model (CFMD1D-TC) A promising way to reduce the computational time and to improve the accuracy is to implement a model based on a tabulated complex chemistry. This approach has the advantage of decreasing the number of species transported in the code by tabulating only the needed species namely NO and CO. In addition, the model becomes able to account for the effects of mixture composition, pressure and temperature on post-flame processes. Developments brought here are inspired by previous works of Vervisch et al. (2011) concerning the NO prediction in Diesel engines. Based on the observation that the NO mass fraction evolution in a perturbed homogeneous reactor can be represented by an exponential relaxation (Vervisch et al. 2011, Ihme and Pitsch 2008), the NO reaction rate is directly written as:

$$\dot{\omega}_{NO} = \left.\frac{dm_{NO}}{dt}\right|_{pf} = \left.\frac{dY^b_{NO}\cdot m_b}{dt}\right|_{pf} = \frac{\left(Y^{b,eq}_{NO} - Y^b_{NO}\right)\cdot m_b}{\tau_{NO}} \tag{6.5}$$

where m_{NO} is the current mass of NO in the combustion chamber, m_b the mass of burnt gases, Y^b_{NO} the NO mass fraction in the burnt gases, $Y^{b,eq}_{NO}$ the NO mass fraction at equilibrium and τ_{NO} the current characteristic time necessary to reach equilibrium.

As presented in Section 6.1.4, this exponential relaxation assumption is also valid for the CO prediction and is thereby considered here to develop the CORA (CO Relaxation Approach) model. As a consequence, using the same framework than for NO, the CO reaction rate $\dot{\omega}_{CO}$ is written:

$$\dot{\omega}_{CO} = \left.\frac{dm_{CO}}{dt}\right|_{pf} = \left.\frac{dY^b_{CO}\cdot m_b}{dt}\right|_{pf} = \frac{\left(Y^{b,eq}_{CO} - Y^b_{CO}\right)\cdot m_b}{\tau_{CO}} \tag{6.6}$$

The approach used here finally consists in tabulating $Y^{b,eq}_{NO}$, $Y^{b,eq}_{CO}$, τ_{NO} and τ_{CO} according to the methodology described in Section 6.1.4. At each time step, these parameters are obtained by interpolation in the look-up table using the current φ, Y^u_{res}, P and burnt gases enthalpy H^b values as input parameters and are injected in Eqs. (6.5, 6.6) and thus in the post-flame chemistry term $dm_i|_{pf}$ in Eq. 6.1. In practice, H_2O mass fractions are also stored to reconstruct CO_2, O_2 and N_2 mass fractions from the atomic conservation of C, O, N and H in the burnt gases.

The methodology adopted to build tables for $Y^{b,eq}_k$, τ_{NO}, with $k = NO$ or CO is described in next Section.

6.1.4 Complex chemistry integration in CFM1D

This Section describes the tabulation approach and the process used to generate NO and CO mass fractions and characteristic time scale tables from detailed chemistry computations.

Methodology

The present approach is based on the tabulation of $Y^{b,eq}_{NO}$, $Y^{b,eq}_{CO}$, τ_{NO} and τ_{CO} stepping in Eqs. (6.5, 6.6). In a recent work, Vervisch et al. (2011) chose as input parameters for these quantities the equivalence ratio φ, the diluent mass fraction, Y^u_{res}, the pressure, P, and the burnt gases temperature reached at the equilibrium, $T^{b,eq}$. The fact is that a given burnt gases mixture need to be relaxed from an initial state (φ, Y^u_{res}, P and $T^{u,eq}$) towards the equilibrium state defined by an equilibrium composition, $Y^{b,eq}_k$, pressure, P, and temperature, $T^{b,eq}$. In practice, using an equilibrium temperature $T^{b,eq}$ to generate the table can lead to small errors since during a

combustion simulation the burnt gases mixture is currently not at equilibrium and therefore the only one available information during the computation is the current burnt gases temperature $T^b \neq T^{b,eq}$. A solution would be to generate the tables using as input parameter the temperature just downstream the flame, $T^{u,eq}$. Nevertheless, this temperature is here also generally not provided by the combustion model. Another solution to fix this problem, can be the use of the burnt gases enthalpy H^b (available during the computation) as table input parameter instead of $T^{b,eq}$. Indeed, according to the first law of thermodynamics, the burnt gases enthalpy is preserved when an adiabatic system at state A turns into state B at constant pressure. As a result, this table input parameter definition is here coherent with the variable provided by the combustion model during the computation. Moreover, this solution has the advantage of accounting for enthalpy losses due to heat losses and piston work. Thus, although the choice of $T^{b,eq}$ as input of tables did not show any identifiable limits in the past, in this work H^b is finally chosen instead.

A very wide range of thermodynamic conditions (burnt gases enthalpy and pressure) and fresh mixture compositions (equivalence ratio and diluent mass fraction) covers the operating conditions encountered in SI engines. For this purpose, an automatic procedure, described in Figure 6.4, is followed. Chemical equilibrium state computations are first performed using Equil (Kee et al. 1989) (Figure 6.4, step 1) to generate tables of NO and CO equilibrium mass fractions. Several parameters are set in the Equil input file for each mixture definition, like the initial reactant mass fractions Y_i^{init} depending on φ and Y_{res}^u, the pressure P or the input temperature T^{init}. Resulted mass fraction of NO and CO are finally stored (Figure 6.4, step 1'). Homogeneous reactors calculations are then performed using SENKIN (Kee et al. 1989) (Figure 6.4, step 2) by singly perturbing NO and CO mass fractions respectively by a quantity ΔY_{NO} and ΔY_{NO} as:

$$Y_k^{senkin}\left(t=0\right) = Y_k^{b,eq} + \Delta Y_k \tag{6.7}$$

After relaxation of these perturbed states toward equilibrium, time evolutions of NO and CO mass fractions are stored and the respective relaxation characteristic times defined in Eqs. (6.5, 6.6), are deduced (Figure 6.4, step 2') for a single value of ΔY_k. The choice of this value will be discussed in the following.

All parameters involved here are discussed in the next subsection.

Database construction

Equilibrium compositions Computations previously described are performed using the GRI 3.0 mechanism (Smith et al. 2000) built-up with 53 species and 325 reactions and initially designed for the combustion of natural gas. This kinetic scheme has already been the subject of several validation works in the past and has proved to be an adapted chemical kinetics mechanism in terms of relevance for methane-air-nitrogen mixtures combustion, accuracy, numerical consistence and CPU-cost (Bougrine et al. 2011, Dong et al. 2002, Kishore et al. 2008, Fairweather et al. 2009). Simulations have been performed in the conditions presented in Table 6.1, leading to the generation of a database containing 17712 points (a point corresponds to a set of parameters). For each point, several values are stored such as the NO and CO mass fractions.

To reduce computational times, pressure and burnt gases enthalpy have been chosen according to conditions currently encountered in SI engines and displayed in Figure 6.5. These ranges have been estimated from engine simulations using CFM1D and providing an evaluation of the burnt gases enthalpy levels accounting for heat losses during the combustion process in the chamber.

The EQUIL input temperature T^{init} (Figure 6.4) is then deduced from the considered input enthalpy H^b taken from Table 6.1 and the reactant initial mass fractions Y_i^{init} depending on φ and Y_{res}^u and determined from Eqs. (6.8–6.11):

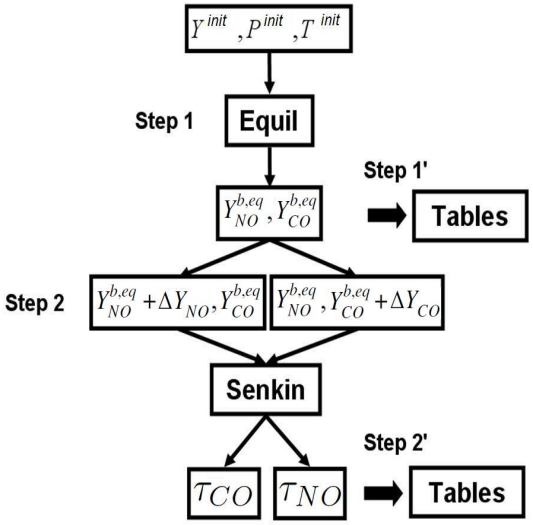

Figure 6.4: Global procedure for generating tables of NO and CO mass fractions at equilibrium and relaxation times scales.

	Range of variation	Number of points
φ [-]	$0.6 - 1.3$	9
Y_{res}^{u} [m/m%]	$0 - 25$	6
$\left(H^b \times P\right)$ [MJ/kg] $\times$ [0.1 MPa]	$(-1.1 - 1.1) \times (1 - -130)$	164 (see Figure 6.5)
$(\lvert\Delta Y_{NO}\rvert \times \lvert\Delta Y_{CO}\rvert)$ [-]	$(1.10^{-2}) \times (1.10^{-2})$	2
		Total = 17712

Table 6.1: Characteristics of homogeneous reactors database.

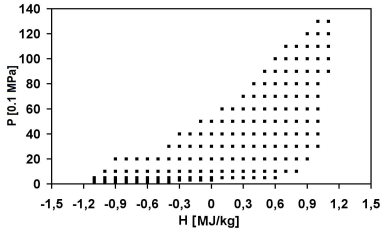

Figure 6.5: Map of pressure & burnt gases enthalpy used for the table generation.

$$C_xH_yO_z + \left(x + \frac{y}{4} - \frac{z}{2}\right) \cdot O_2 \rightarrow x \cdot CO_2 + \frac{y}{2} \cdot H_2O \tag{6.8}$$

$$n_m = 1 + (1+\lambda) \cdot \frac{(x+y/4)}{\varphi} + \frac{Y^u_{res}}{1 - Y^u_{res}} \cdot \frac{W_{N_2}}{W_{fuel} + \frac{1}{\varphi}\left(x + \frac{y}{4}\right) \cdot (W_{O_2} + \lambda W_{N_2})}$$

$$Y^{init}_{fuel}(t=0) = \frac{1}{n_m} \cdot \frac{W_{fuel}}{W_m} \tag{6.9}$$

$$Y^{init}_{O_2}(t=0) = \frac{1}{\varphi \cdot n_m}\left(x + \frac{y}{4}\right) \cdot \frac{W_{O_2}}{W_m} \tag{6.10}$$

$$Y^{init}_{N_2}(t=0) = 1 - Y_{fuel} - Y_{O_2} \tag{6.11}$$

where λ is the mole ratio between O_2 and N_2 in pure air, n_m the normalized mixture mole number (corresponding to the total mole number of the initial mixture for one mole of fuel), W_i the molar weight of species i and W_m the mean mixture molar weight. Y^u_{res} (Table 6.1) is here a mass fraction of diluent considered as additional N_2 only. Within the framework of engine simulation, this assumption could lead to small differences with experimental data since it does not account for the presence of combustion products (CO_2, H_2O, N_2) as well as residual reactants (fuel, O_2, N_2) in non-stoichiometric cases. Nevertheless, in practice diluent can be approximated at the first order as N_2 representing the majority species in mass as shown by Bougrine et al. (Bougrine et al. 2011).

Perturbed state As previously noticed the equilibrium state obtained is then perturbed and relaxed. However, these perturbations, simply defined in Eq. 6.7, change the atomic balance and then the equivalence ratio, the diluent mass fraction and the mixture enthalpy. Consequently, the initial compositions for SENKIN computations (Figure 6.4) need to be rewritten. In the case of the NO perturbation, a solution to this problem is to modify the initial oxygen and nitrogen balances by modifying the equivalence ratio and dilution fraction leading respectively to ϕ' and $Y^{u'}_{res}$:

$$\varphi^{'} = \frac{\varphi}{1 - \frac{\Delta Y_{NO} \cdot W_{O_2}}{Y^{init}_{O_2} \cdot 2W_{NO}}} \tag{6.12}$$

$$Y^{u\ '}_{res} = Y^u_{res} - \frac{W_{N_2}}{2W_{NO}} \Delta Y_{NO} \tag{6.13}$$

As noticed by Vervisch et al. (2011), this modification is not the unique way to conserve the atomic budget but has the advantage to be easy to set. In contrast, to use the same initialization approach for CO species is not possible because the carbon and oxygen balances cannot be both driven only by the equivalence and dilution ratios. A solution to this problem is to assume that the perturbation of CO only affects the CO_2 and O_2 concentrations. This assumption allows to conserve the atomic balance of C and O by perturbing the equilibrium states of the CO, CO_2 and O_2 species as:

$$Y^{senkin}_{CO}(t=0) = Y^{b,eq}_{CO} + \Delta Y_{CO} \tag{6.14}$$

$$Y^{senkin}_{CO_2}(t=0) = Y^{b,eq}_{CO_2} - \Delta Y_{CO} \frac{W_{CO_2}}{W_{CO}} \tag{6.15}$$

$$Y_{O_2}^{senkin}(t=0) = Y_{O_2}^{b,eq} + \Delta Y_{CO}\frac{W_{O_2}}{2 \cdot W_{CO}} \tag{6.16}$$

Finally, to ensure $\sum Y_i^{senkin}(t=0) = 1$, mass fractions $Y_i^{senkin}(t=0) = 1$ of all species i have to be normalized by coefficients α_{NO} and α_{CO}, respectively for NO and CO perturbations. These coefficients are defined by:

$$\alpha_{NO} = 1 + \Delta Y_{NO} \tag{6.17}$$

$$\alpha_{CO} = 1 + \Delta Y_{CO} \cdot \frac{W_{CO}}{2 \cdot W_m} \tag{6.18}$$

Moreover, this normalization leads to a change of the effective perturbations amplitudes read in Table 6.1. As a consequence, ΔY_{NO} and ΔY_{CO} (as defined in Eqs. (6.12–6.16), are turned up into $\Delta Y_{NO}^{'}$ and $\Delta Y_{CO}^{'}$:

$$\Delta Y_{NO}^{'} = \frac{\Delta Y_{NO}}{1 - \Delta Y_{NO}\frac{W_m}{W_{NO}}} \tag{6.19}$$

$$\Delta Y_{CO}^{'} = \frac{\Delta Y_{CO}}{1 - \Delta Y_{CO}\frac{W_m}{2W_{CO}}} \tag{6.20}$$

Figure 6.6 displays homogeneous reactor calculations starting from equilibrium state at different equivalence ratios. The evolutions of NO and CO are weakly sensitive to the sign of the corresponding perturbations. This observation, already noticed by Vervisch et al. (2011) for NO relaxation is thus also verified here for CO. The post-oxidation model implemented in the CFM1D-TC model presented in Section 6.1.3 will therefore consider the same τ_k indifferently from the sign of $\left(Y_{NO}^{b,eq} - Y_{NO}^{b}\right)$ (Eqs. 6.5, 6.6).

Figure 6.6 shows that NO and CO mass fractions seem to evolve in an exponential way corresponding to the linear form of the respective reactions rates $\dot{\omega}_{NO}$ and $\dot{\omega}_{CO}$ given in Eqs. (6.5, 6.6). This feature was already observed for the NO in previous works (Vervisch et al. 2011, Ihme and Pitsch 2008). It is thus interesting to recover this trend for the CO evolution, avoiding here a direct tabulation of $\dot{\omega}_{CO}$. Figures 6.7 and 6.8 display the evolutions of NO and CO relaxations for different pressures and temperatures. Figures 6.7.b,d and 6.b,d verify that the linearity of $\log\left(Y_k - Y_k^{b,eq}\right)$ with time for all pressure and temperature conditions. This linearity should indeed be theoretically observed for an exponential relaxation, for which time integrated solutions are given by:

$$Y_k^b(t) = Y_k^{b,eq} + \Delta Y_k \cdot e^{-t/\tau_k} \tag{6.21}$$

Solutions are here obtained for given perturbations ΔY_k when relaxation times τ_k are assumed to be constant. These figures also show that equilibrium values $Y_k^{b,eq}$ depend on pressure and temperature. Moreover the relaxation speed increases with pressure and temperature. The equilibrium state is quickly reached for $T^{b,eq} = 2500$ K for almost all pressures (Figure 6.7). On the other hand, for lower temperatures, although this state seems to be reached (Figures 6.8.a,c), NO and CO still relax at larger time scales. Finally, with regards to these figures, the assumption of an exponential relaxation of NO and CO is verified. Characteristic relaxation times τ_{NO} and τ_{CO} stepping in Eqs. (6.5, 6.6) can then be deduced from Eq. 6.21 and from the perturbation "mean life-time" defined by $Y_k^b(t_m) = Y_k^{b,eq} + \Delta Y_k/2$ leading to the final expression for τ_k:

$$\tau_k = \frac{-t_m}{\ln\left(\frac{Y_k^b(t_m) - Y_k^{b,eq}}{Y_k^b(t=0) - Y_k^b}\right)} = \frac{t_m}{\ln(2)} \tag{6.22}$$

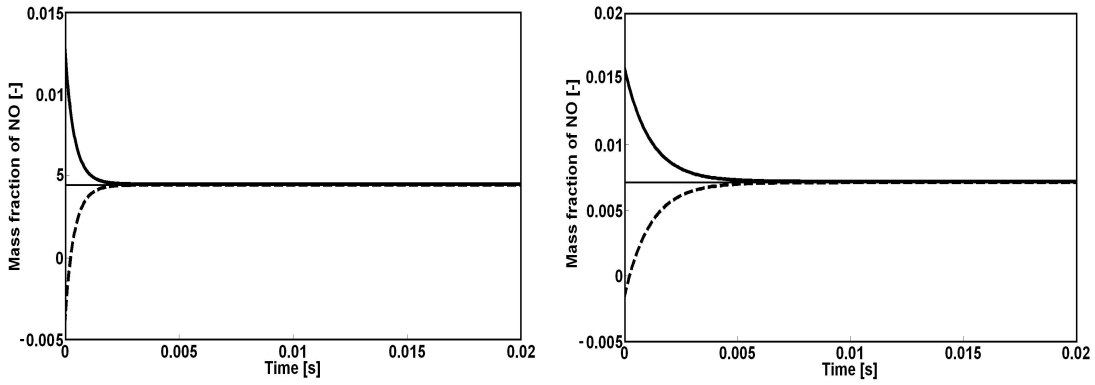

(a)

(b)

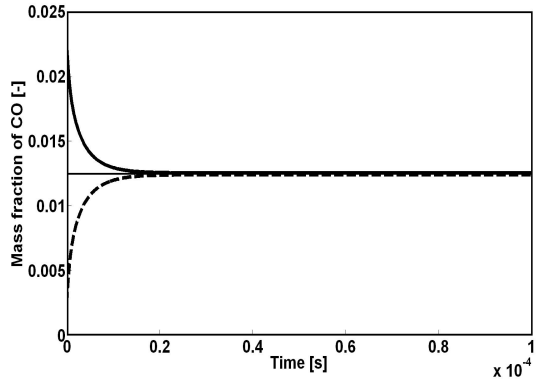

(c)

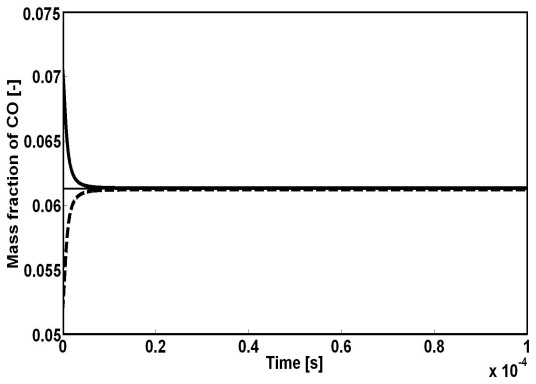

(d)

Figure 6.6: NO and CO mass fractions evolutions after perturbations with positive (-) and negative (- - -) values of $\Delta_{NO} = \Delta_{CO} = 10^{-2}$. Conditions: $Y^u_{res} = 0\%$, $P = 4MPa$ and $T^b_{eq} = 2500$ K – (a) NO, $\varphi = 1.0$, – (b) NO, $\varphi = 0.9$, – (c) CO, $\varphi = 1.0$, – (d) CO, $\varphi = 1.2$.

τ_k is then stored in the same way than $Y_k^{b,eq}$ as function of φ, Y_{res}^u, P and H^b. In the case of the CO relaxation, note that a short initialization step can be needed before $\dot{\omega}_{CO}$ begins to relax linearly. This behavior showed in Figure 6.9 for different perturbation appears at the first stages of simulation and could be partially justified by the approach used to initialize the perturbed state (Eqs. 6.14–6.16). It could indeed initiate or inhibit at the very beginning reactions which are not supposed to be. In these cases, the slope $-1/\tau_{CO}$ of the linear function $\log\left(Y_{CO} - Y^b_{CO_{eq}}\right)$ have therefore to be computed after this initialization step.

Figure 6.9 also shows the impact of the perturbation on the relaxation dynamics. Vervisch et al. (2011) used ΔY_k as a fifth input parameter in their look-up table with amplitudes from 10^{-5} to 10^{-2}. They observed that this range was sufficient in most cases to represent the NO relaxation. In this work, only one perturbation $\Delta Y_{NO} = \Delta Y_{CO} = 10^{-2}$ was considered. Indeed, the following assumption was retained: for a given perturbation, if this latter is high enough, the considered species should rise all perturbed states between the initial perturbed state and the equilibrium. This observation is verified in the test case of Figure 6.9 showing that, after the short initialization step, the slope $(-1/\tau_{CO})$ of function $\log\left(Y_{CO} - Y^b_{CO_{eq}}\right)$ remains the same regardless the perturbation level. In other words, in addition to the asset of using only positive amplitudes of the considered perturbations ΔY_{NO} and ΔY_{CO} (Figure 6.6), the approach used here (Eqs. 6.5, 6.6) also allows to deduce relaxation times for all perturbed states from a single one. It thus represents a considerable time and memory savings compared to approaches in which ΔY_{NO} and ΔY_{CO} are considered as input parameters as for example, direct tabulation of $\dot{\omega}_k$ requiring about 50 discrete values of each parameter for positive as well as negative amplitudes Vervisch et al. (2011). A summary of the database construction methodology is proposed in Figure 6.10.

Finally, examples of evolutions of tabulated variables $Y_{NO}^{b,eq}$, $Y_{CO}^{b,eq}$, τ_{NO} and τ_{CO} as functions of table input parameters φ, Y_{res}^u, P and H^b are displayed in Figures 6.11, 6.12. Figure 6.11 shows that the equilibrium mass fractions of both species NO and CO increase when the burnt gases enthalpy (which is the image of burnt gases temperature) increases and decrease when pressure increases. Moreover, values of $Y_{CO}^{b,eq}$ are very low for equivalence ratio under $\varphi = 0.9$ and a maximum value of $Y_{NO}^{b,eq}$ is found around $\varphi = 0.9$. Finally the inhibiting effect of diluent addition is recovered for both species when Y_{res}^u increases. On the other hand, Figure 6.12 shows that τ_{NO} and τ_{CO} naturally decrease when H^b increases but also when P increases. In addition, NO relaxation time scales increase when the equivalence ratio decreases. On the contrary, the inhibiting effect of diluent addition is here also recovered for relaxation times which increase when Y_{res}^u increases. Figures 6.11, 6.12 show that equilibrium states and relaxation times are highly dependent on composition and thermodynamic conditions. A summary of Y_k^{eq} and τ_k variations as function of composition and thermodynamic conditions is given in Table 6.2. It will be shown in the next Section that the study of pollutant formation requires to integrate both equilibrium and kinetics aspects and to be able to evaluate which one take over under a given composition and thermodynamic condition which is not an obvious task with regards to Table 6.2.

$H^b \nearrow$	$Y_k^{eq} \nearrow$	$\tau_k \searrow$
$P \nearrow$	$Y_k^{eq} \searrow$	$\tau_k \searrow$
$Y_{res}^u \nearrow$	$Y_k^{eq} \searrow$	$\tau_k \nearrow$
$\phi \nearrow$	$Y_{CO}^{eq} \nearrow$	$\tau_{CO} \searrow$
$\phi < 0.9 \nearrow$	$Y_{NO}^{eq} \nearrow$	$\tau_{NO} \searrow$
$\phi > 0.9 \nearrow$	$Y_{NO}^{eq} \searrow$	$\tau_{NO} \searrow$

Table 6.2: Summary of Y_k^{eq} and τ_k variations as function of composition and thermodynamic conditions.

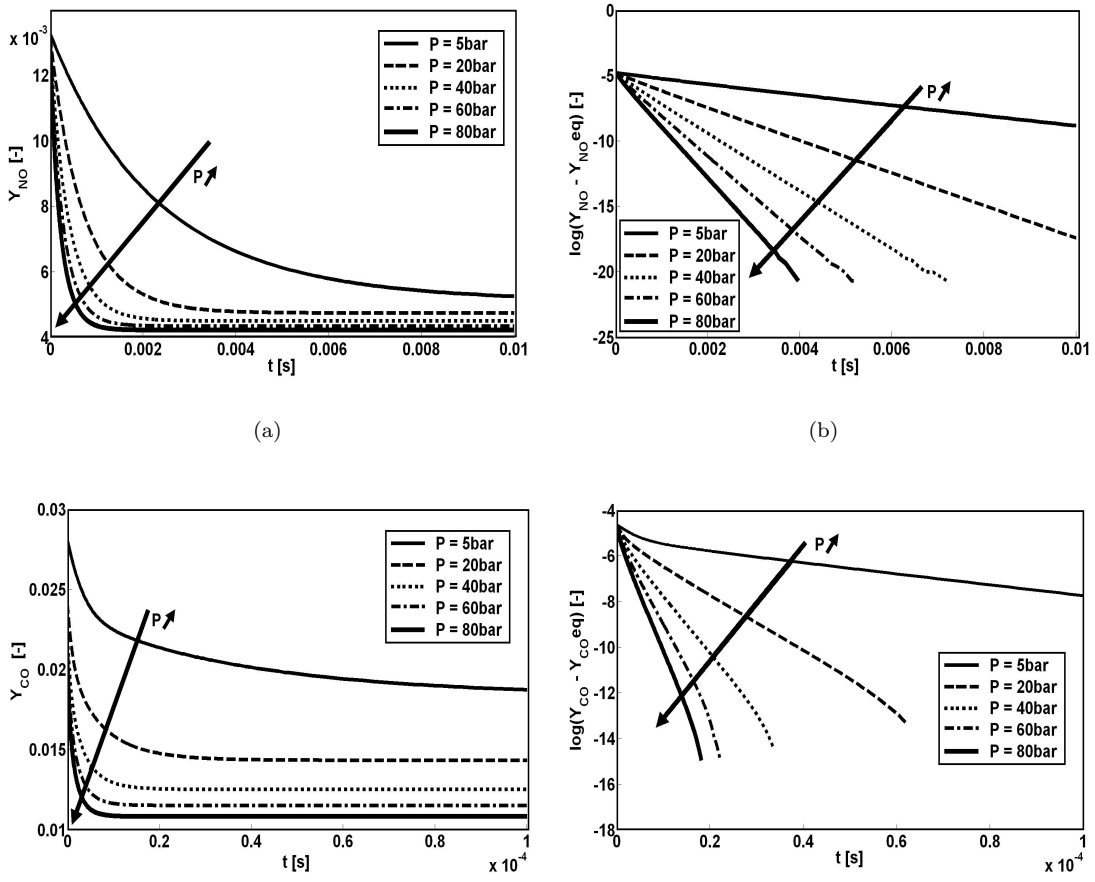

(a) (b)

(c) (d)

Figure 6.7: NO and CO evolutions at different pressures for $\Delta_{NO} = \Delta_{CO} = 10^{-2}$, $\varphi = 1.0$, $Y^u_{res} = 0\%$ and $T^b_{eq} = 2500$ K – (a) Y_{NO}, – (b) $\log\left(Y_{NO} - Y^b_{NO_{eq}}\right)$, – (c) Y_{CO}, – (d) $\log\left(Y_{CO} - Y^b_{CO_{eq}}\right)$.

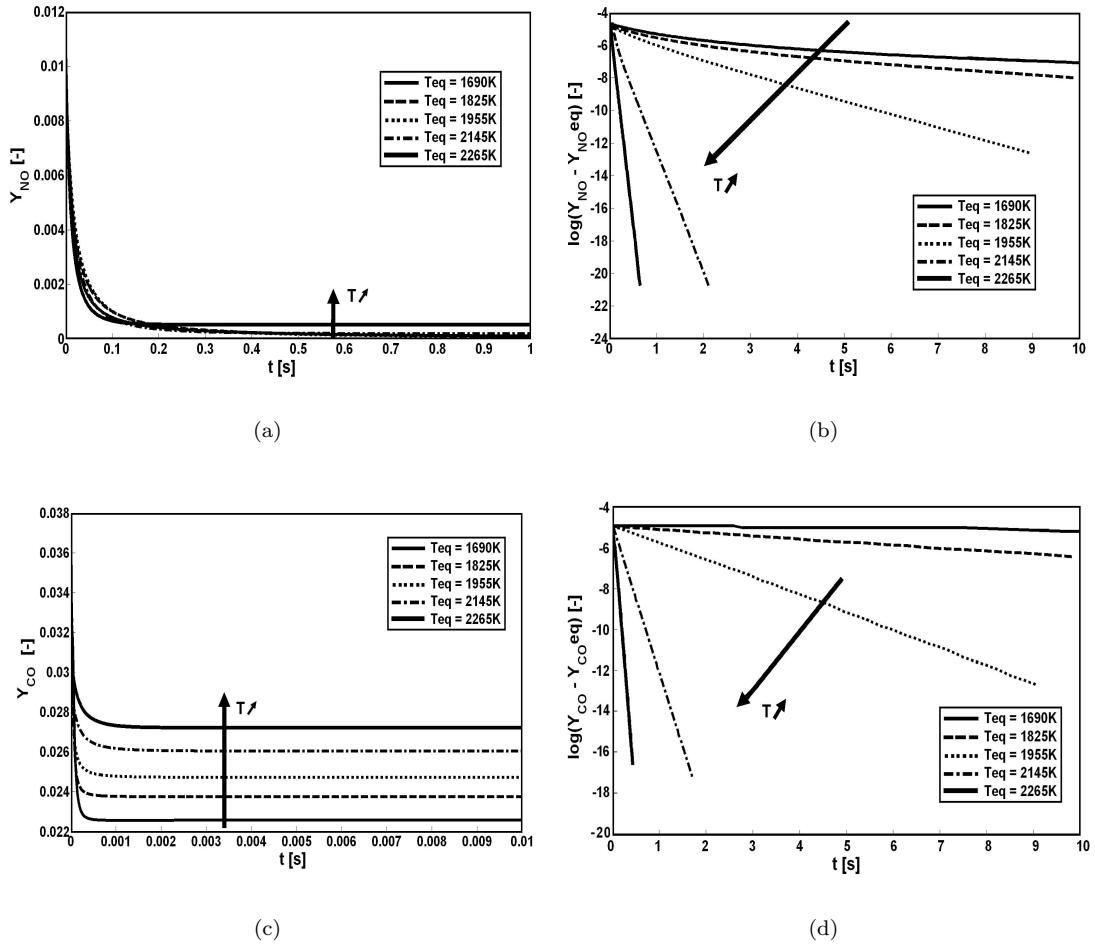

(a) (b)

(c) (d)

Figure 6.8: NO and CO evolutions at different temperatures for $\Delta_{NO} = \Delta_{CO} = 10^{-2}$, $\varphi = 1.0$, $Y^u_{res} = 0\%$ and $P = 0.3MPa$ – (a) Y_{NO}, – (b) $\log\left(Y_{NO} - Y^b_{NO_{eq}}\right)$, – (c) Y_{CO}, – (d) $\log\left(Y_{CO} - Y^b_{CO_{eq}}\right)$.

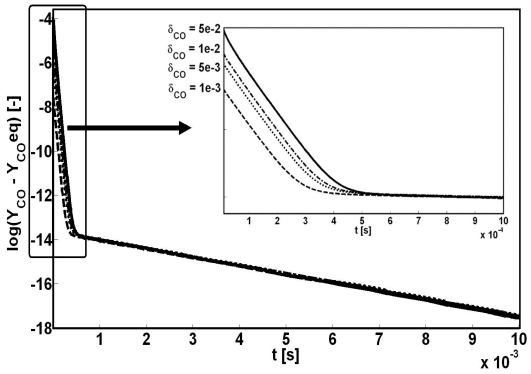

Figure 6.9: CO evolution at different perturbations $\Delta_{CO} = 5.10^{-2}, 1.10^{-2}, 5.10^{-3}, 1.10^{-3}$ for $\varphi = 1.0$, $Y^u_{res} = 0\%$ and $P = 0.1MPa$ and $T^b = 2500$ K.

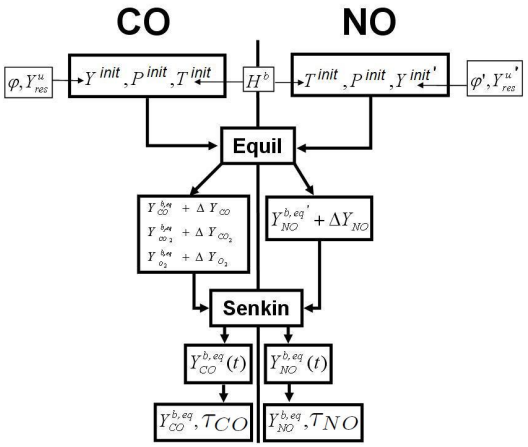

Figure 6.10: Summary of the database construction methodology for NO and CO relaxation.

6.1.5 Engine simulations

Experimental database

The CFM1D-TC model presented in Section 6.1.3 has been implemented in the AMESim® engine simulation software (Malbec et al. 2009) and tested on a wide range of steady state operating conditions of an IFP Energies nouvelles (IFPEn) 4-cylinder turbocharged SI prototype engine burning methane. An extended experimental database of 59 operating points has been used. It comprises results for four engine speeds from 1000 to 5500 rpm and loads from idle to Wide Open Throttle (Indicated Mean Effective Pressure (IMEP) from 0.3 to 3 MPa). An unity equivalence ratio was retained for all operating conditions. The engine main characteristics are presented in Table 6.3 and a summary of experimental operating conditions is given in Table 6.4.

Bore [mm]	82.7
Stroke [mm]	93
Compression ratio	11
Connecting − rod length [mm]	143
Displacement [cm^3]	2000

Table 6.3: 4-cylinders engine characteristics

Engine Speed [rpm]	IMEP [MPa]	Plenum Pressure [MPa]	Plenum Temperature [K]	Exhaust Pressure [MPa]	Exhaust Temperature [K]	Spark Advance [CAD]
1000	0.07 - 0.109	0.0241 - 0.1138	312.9 - 296.2	0.107 - 0.119	601 - 841	32 - 17
2000	0.10 - 0.183	0.0234 - 0.1720	303.6 - 310.4	0.099 - 0.178	728 - 1014	38 - 20
3000	0.11 - 0.220	0.0239 - 0.2009	299.9 - 309.9	0.099 - 0.255	867 - 1119	39 - 22
4000	0.14 - 0.204	0.0278 - 0.1090	301.4 - 311.0	0.111 - 0.288	961 - 1167	37 - 25
5000	0.15 - 0.174	0.0296 - 0.1715	398.7 - 316.0	0.110 - 0.299	1007 - 1204	38 - 27

Table 6.4: Experimental operating conditions. Ranges are given from low to high loads.

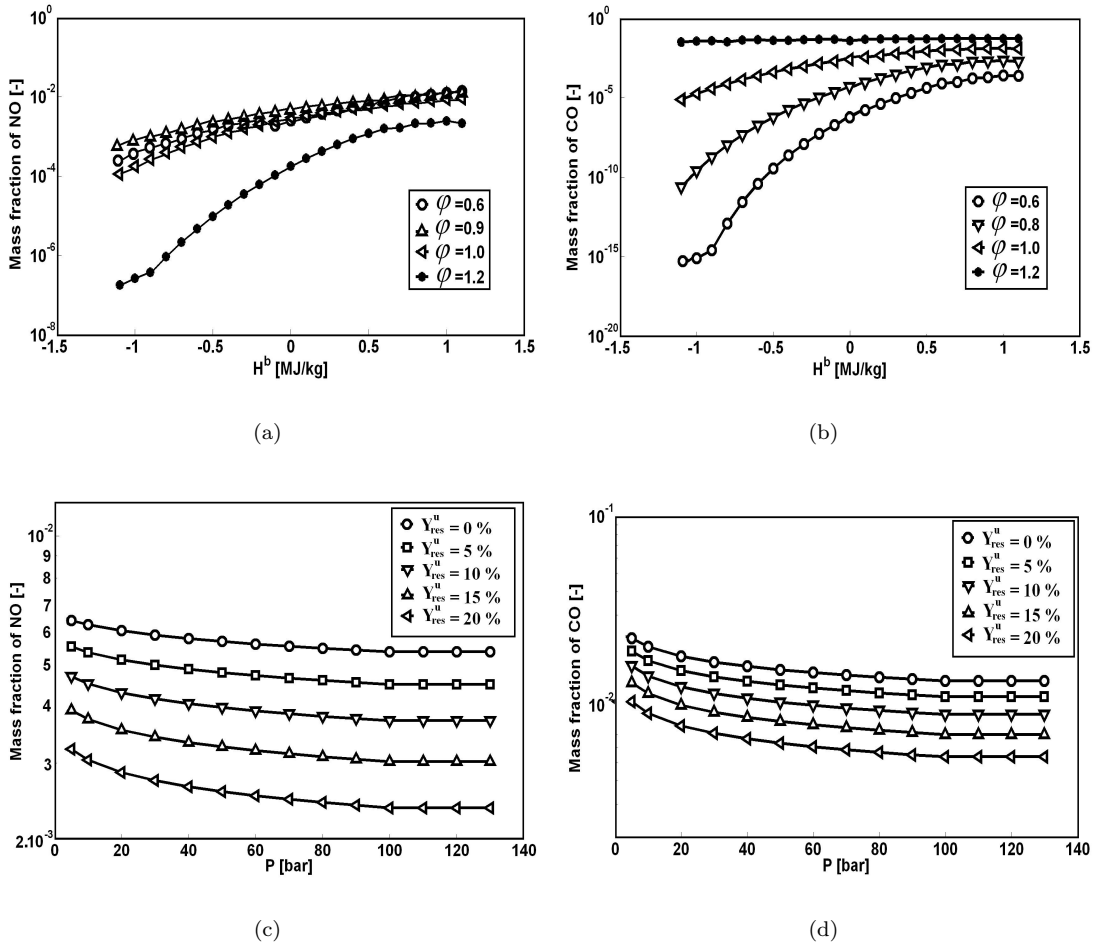

Figure 6.11: Evolutions of tabulated equilibrium mass fraction of NO and CO as function of table input parameters φ, Y^u_{res}, P and H^b. First column: evolution of $Y^{b,eq}_{NO}$ – Second column: evolution of $Y^{b,eq}_{CO}$ – First raw: Evolution of mass fractions as function of the burnt gases enthalpy and equivalence ratio at $P = 0.5MPa$ and $Y^u_{res} = 0\%$ – Second raw: Evolution of mass fractions as function of the pressure and diluent mass fraction at $H^b = 0.6MJ/kg$ and $\varphi = 1$.

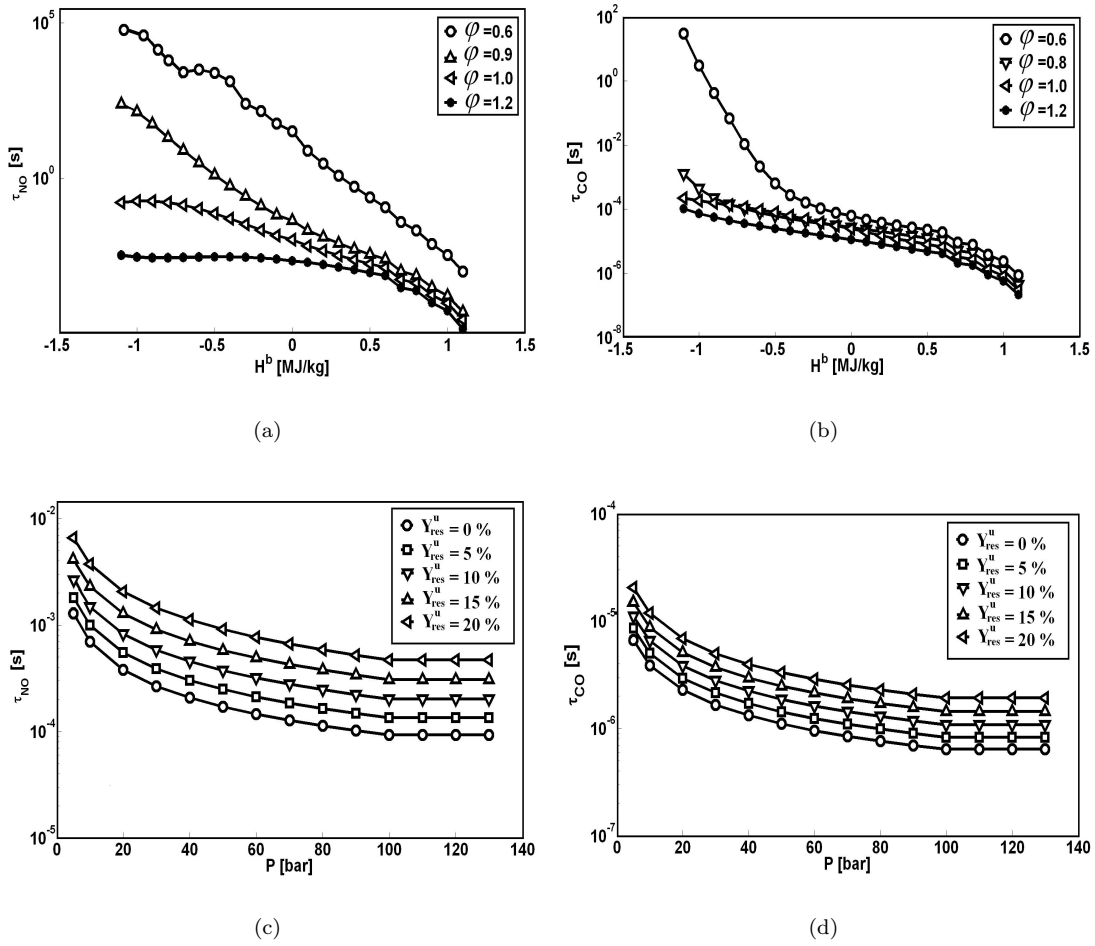

Figure 6.12: Evolutions of tabulated equilibrium mass fraction of NO and CO as function of table input parameters φ, Y^u_{res}, P and H^b. First column: evolution of τ_{NO} – Second column: evolution of τ_{CO} – First raw: Evolution of mass fractions as function of the burnt gases enthalpy and equivalence ratio at $P = 0.5MPa$ and $Y^u_{res} = 0\%$ – Second raw: Evolution of mass fractions as function of the pressure and diluent mass fraction at $H^b = 0.6MJ/kg$ and $\varphi = 1$.

Simulator set-up

A simplified scheme of the engine simulator used in this study is presented in Figure 6.13. The combustion model is embedded in the cylinder component and heat transfer at the walls are represented by the classical Woschni model (Woschni 1697) (see Chapter 4). The boundary conditions (pressure and temperature) and engine settings (spark advance, injection timing and duration) are set from the experimental database (Table 6.4).

Simulation results

The heat released by the combustion as defined in Eq. 6.1 is computed considering the species evolution in the chamber and the flame development through U_l and A_T (Eq. 6.2). A_T is dependent on flame properties (laminar flame velocity, U_l, and thickness, δ_l given by correlations (Bougrine et al. 2011)) and turbulence characteristics (turbulent velocity fluctuation, u', and integral length scale, l_t) which are very sensitive to the domain geometry (chamber, airpaths, etc.). The turbulence integral length scale l_t is assumed to be close to the piston-cylinder head distance at spark timing and is assumed constant during the whole combustion process. The turbulence intensity $u' = \sqrt{2/3 \cdot k}$ is obtained from a phenomenological turbulent model based on a 0-D equation for the turbulent kinetic energy k (Lafossas et al. 2005, Richard et al. 2009):

$$\frac{dk}{dt} = T_{K \to k} - C_{diss} \cdot k \tag{6.23}$$

where $T_{K \to k}$ is a transfer term from the mean flow kinetic energy K to the turbulent one and $C_{diss} = 150$ s-1 is a modeling constant. The complexity of SI engines geometries (airpath, combustion chamber, etc...) requires first an adjustment of this 0-D turbulence model parameters, which does not explicitly resolve the main flow motions on a computational mesh, contrary to 3D models. The calibration methodology is detailed in (Bougrine et al. 2009) and mainly aims at describing the effect of the engine geometry on the aerodynamics of the combustion chamber by setting the tumble number of the flow at IVC (Inlet Valve Closure). This tumble number can be seen as an initial condition of the simulation and is an image of the mean flow kinetic energy K at IVC. An example of simulated cylinder pressure curves obtained at 3000 rpm and for several engine loads are displayed in Figure 6.14 and shows a very good agreement with experimental data for all operating conditions. Turbulence parameters were here adjusted fore each operating point.

The present CFM1D-TC model using a detailed description of the chemistry through the CORA tabulation approach is here compared to the original version of CFM1D based on simple and reduced chemistries as detailed in Section 6.1.3. Figure 6.15 compares at 3000 rpm and for different loads (Table 6.4) experimental measurements of NO and CO concentrations at EVO (Exhaust Valve Opening) with simulated ones obtained with that two models. The new model and the original one lead to different results for both NO and CO. Indeed, Figure 6.15 shows that CFM1D-TC significantly changes the global evolutions of NO and CO mass in the burnt gases compared to the ones obtained with CFM1D. It can also be observed that the freezing effect is naturally described by the present model (Figure 6.15.b,d) while it is imposed with ad hoc constraints in CFM1D. In contrast, basic (simple and reduced) chemistries do not allow to reach high enough levels of NO and CO during the engine cycle and do not oxidize them enough during the expansion stroke which leads in the end to low values at the exhaust. Finally, even if the new CFM1D-TC model seems to overestimate the experimental NO and CO level at low loads and to underestimate it at higher ones for the considered engine speed (3000 rpm), it globally leads to better exhaust levels for both species with acceptable relative errors compared to experiments.

Indeed, as shown in Figure 6.16, for CFM1D-TC, as the chemical equilibrium is not reached instantaneously, the mass of both species naturally evolves towards a kinetic equilibrium controlled by the tabulated instantaneous time scale τ_k. When the temperature decreases (from ≈2700 K for NO and ≈2200 K for CO), τ_k increases and the corresponding mass of species k (m_k) begin

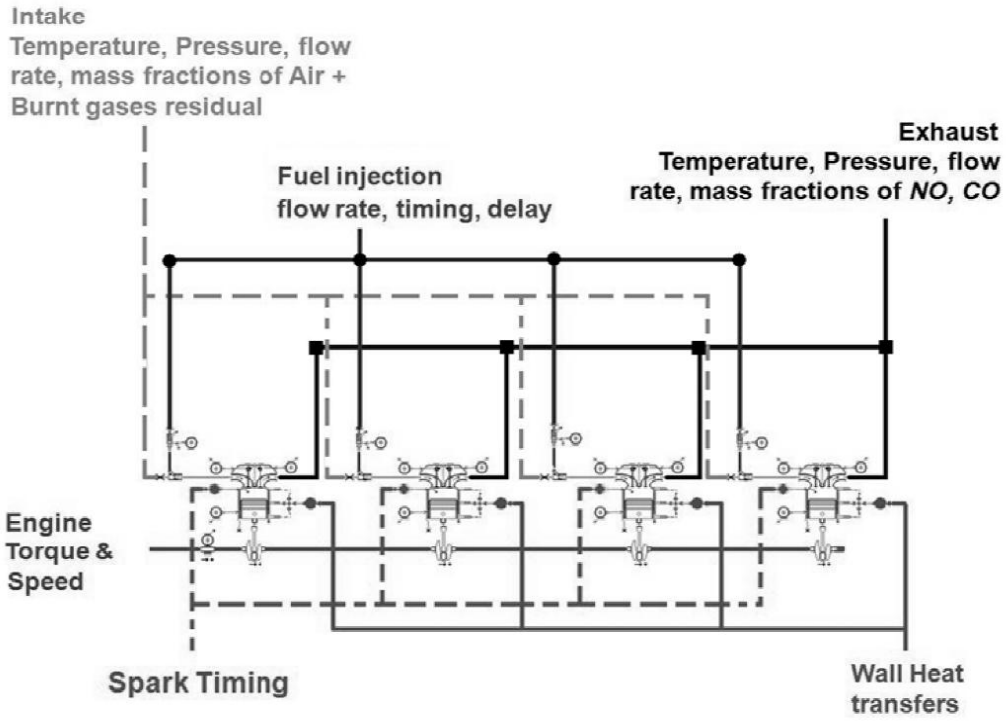

Figure 6.13: Presentation of the AMESim® sketch used to simulate operations of the IFPEn 4-cylinder turbocharged SI engine. The combustion sub-model is represented by the engine chamber icons.

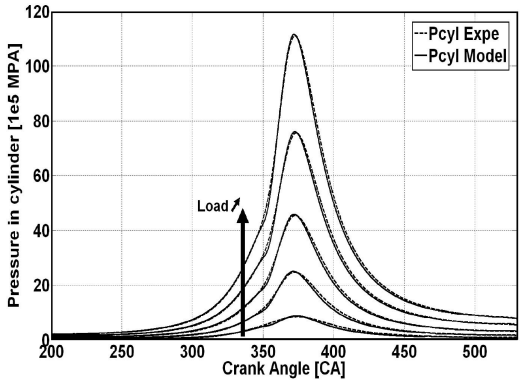

Figure 6.14: Comparisons between experimental and simulated cylinder pressure curves for different engine loads at 3500 rpm.

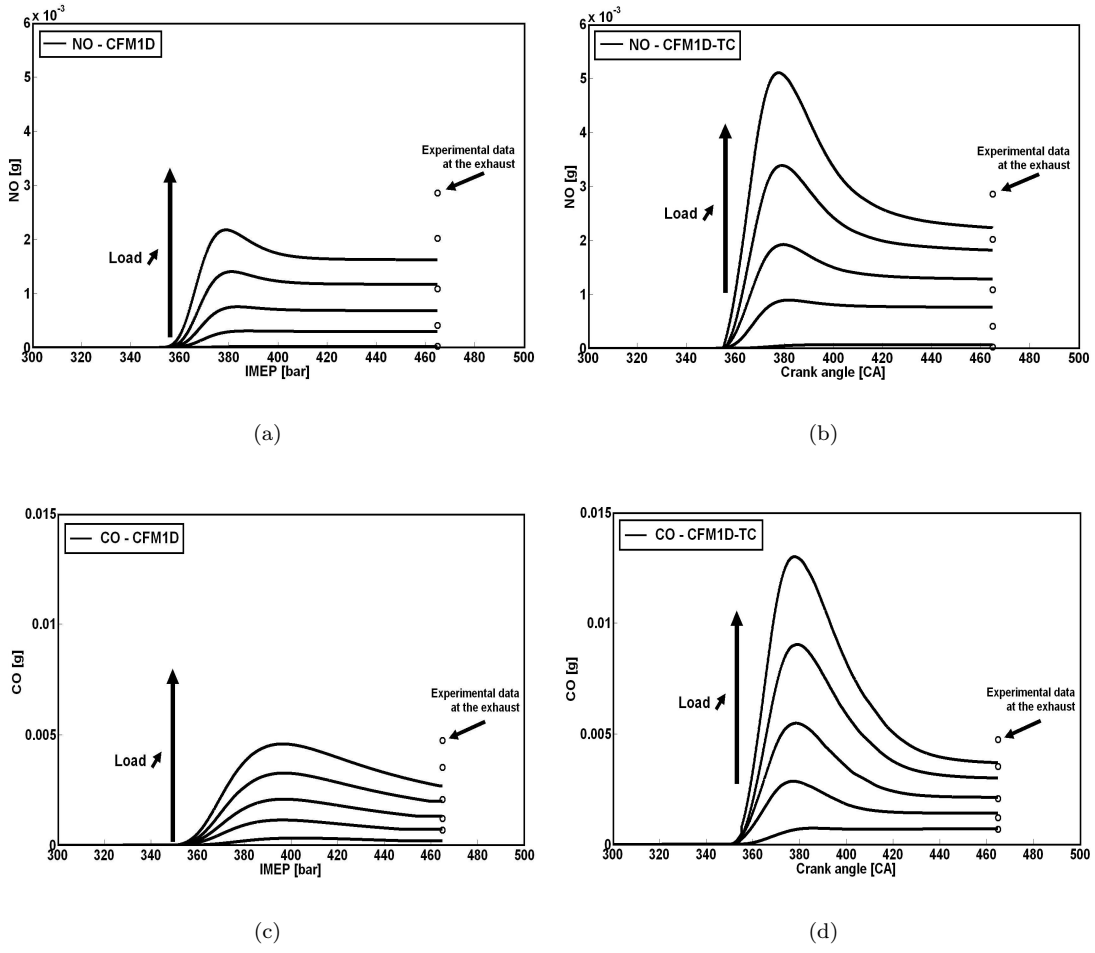

Figure 6.15: Mass of NO and CO evolutions as functions of the crank angle for different loads at 3000 rpm and for the different chemistry approaches: Fist row: NO evolutions – Second row: CO evolutions – First column: Original version of CFM1D – Second column: CFM1D-TC.

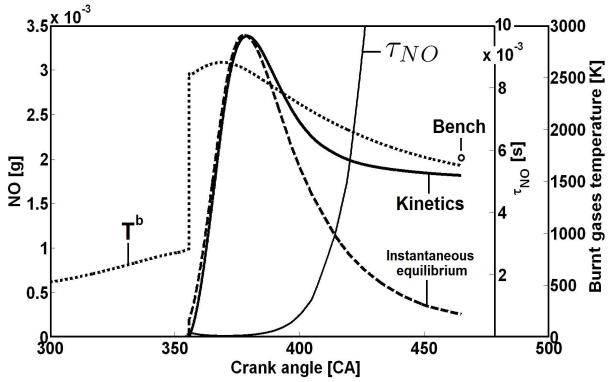

(a)

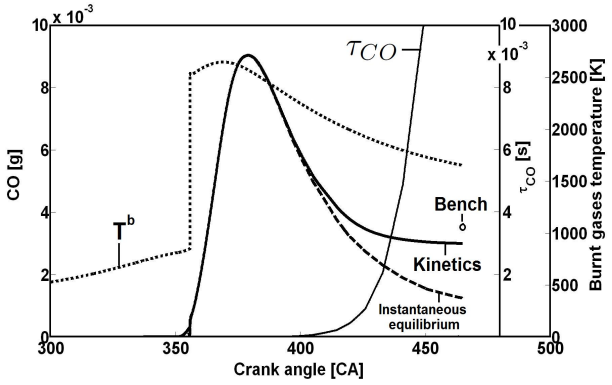

(b)

Figure 6.16: Evolutions of mass of NO and CO and corresponding burnt gases temperature (T^b) and instantaneous time scale (τ_k) as function of the crank angle (CFM1D-TC): Top: mass of NO – Bottom: mass of CO. The curve "Kinetics" corresponds to the values obtained using the CFM1D-TC model accounting for kinetics processes. The curve "Instantaneous equilibrium" corresponds to the values obtained considering that the equilibrium state is instantaneously reached. Operating conditions: IMEP = 1.5 MPa; engine speed = 3000 rpm; engine cycle delay = 0.04s.

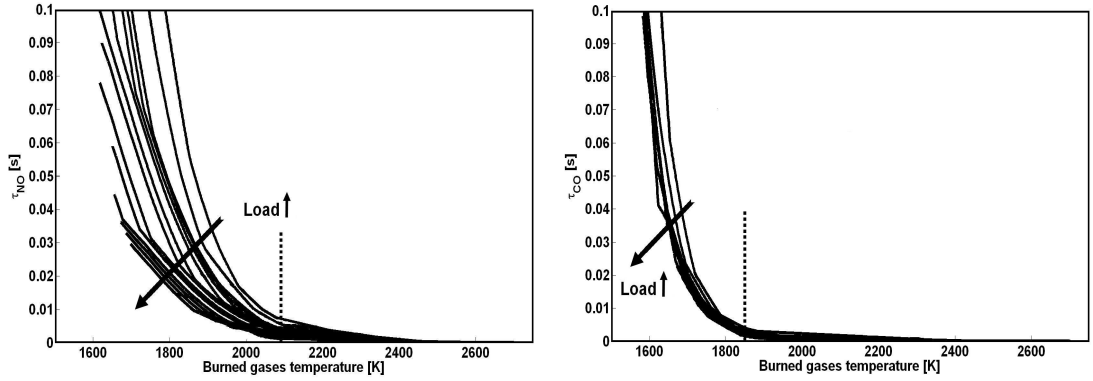

(a) (b)

Figure 6.17: Evolution of NO and CO instantaneous tabulated time scale as function of the burnt gases temperature (CFM1D-TC): (a) NO - (b) CO. Operating conditions: engine speed = 3000 rpm; engine cycle delay = 0.04s.

to deviate from the equilibrium path. Thereafter, when the temperature reach specific values (≈2100 K for NO and ≈1800 K for CO) , τ_k significantly increases until reaching values of the order of the engine cycle delay (here equal to 0.04 s), the reaction rates $\dot{\omega}_k$ strongly decrease and species k finally freeze. In contrast, as explained in Section 6.1.3, this freezing effect is arbitrarily imposed in CFM1D where both RHS terms of Eq. 6.3 are computed as long as the temperature of the burnt gases $T^b > T^{cut}_{NO}$ for the first one and $T^b > T^{cut}_{CO}$ for the second one. In CFM1D, T^{cut}_{NO} and T^{cut}_{CO} are set to 1700 K and 2000 K. It is then interesting to note that CFM1D-TC naturally allows to retrieve these typical levels from the literature (Heywood 1988). Indeed, as shown on Figure 6.17, when the burnt gases temperature decreases below $T^b \approx 2100$ K for NO and below $T^b \approx 1900$ K for CO, the respective instantaneous tabulated relaxation time scales soar. Contrary to τ_{CO}, τ_{NO} seems to be highly sensitive to the load and decreases when this load increases. Figure 6.18 compares at different loads and for the five engine speeds of the database experimental data with NO and CO mass at the exhaust obtained using CFM1D or CFM1D-TC. It confirms previous observations on Figure 6.16 where, in particular, experimental NO and CO levels are underestimated at low loads and overestimated at higher ones when the new model is used. It shows also that the CFM1D leads to very low values of both species mass.

Discrepancies between experimental and simulated NO levels obtained with CFM1D-TC can first be explained by the fact that experimental data provided results for NOx levels while here only NO is considered. Moreover, scavenging and backflow processes in the combustion chamber which are complex phenomena may not be precisely accounted for and can then lead to uncertainties on the dilution ratio Y^u_{res} representing the residual mass fraction from the previous thermodynamic cycle. These uncertainties have been estimated at an absolute maximum level of $+/-$ 5% by Bougrine et al. (2009) who finally showed that the dilution ratio can have a major effect on the final NO level. However, the most likely source of error on NO prediction can be the non-consideration of burnt gas temperature inhomogeneities. Indeed, NO is known to be very sensitive to the local temperature and a single mean temperature is probably not a sufficient information to correctly describe the evolution of the mean NO mass in the chamber, especially if the standard deviation of burnt gas temperature is high. As noted by Heywood (1988) in SI engines, a natural temperature stratification forms in the burnt gases because of the burning of fresh gases elements at different times. The first fresh gas pockets which are compressed before burning will then lead to higher temperatures than late-burning elements which are compressed after combustion. This last observation is of high importance since the earlier burning fractions of the charge are the most

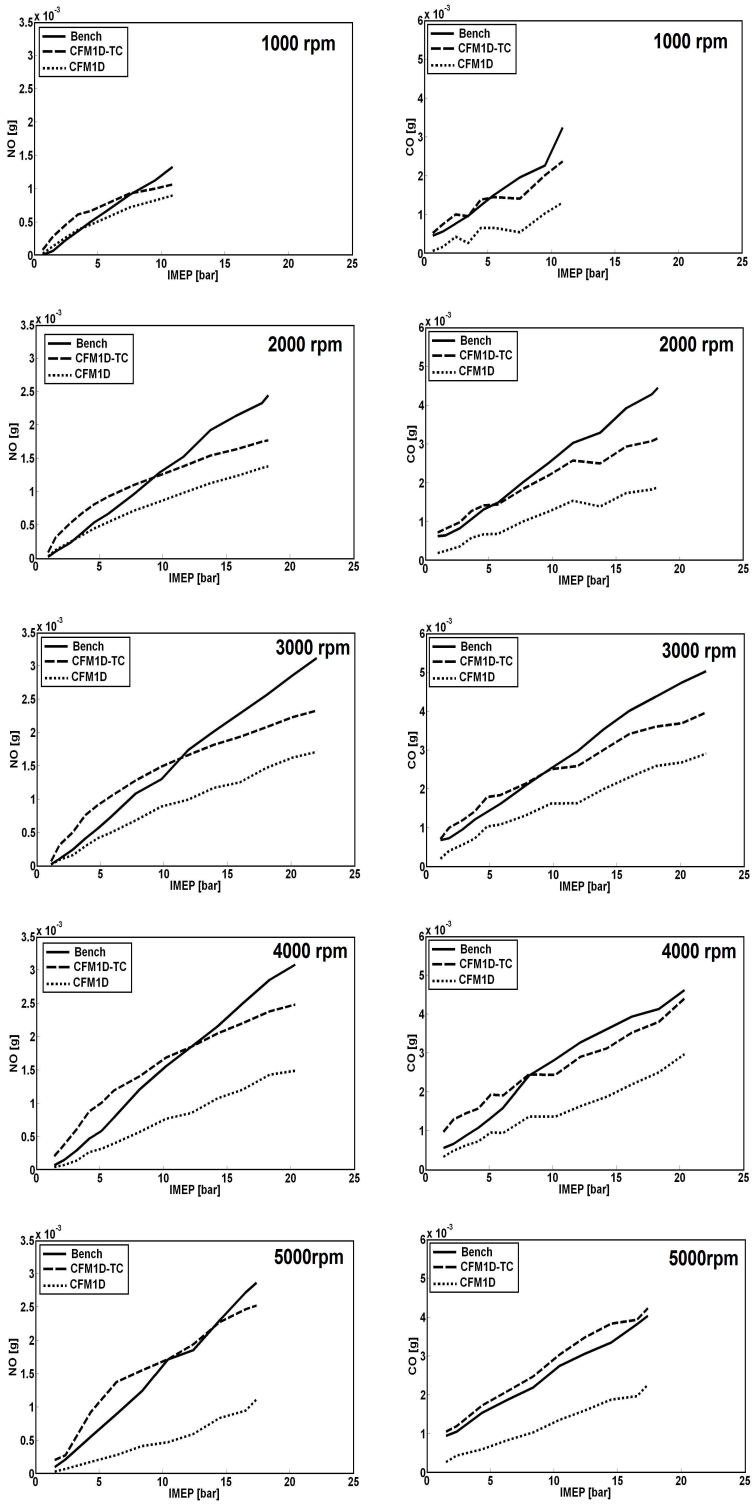

Figure 6.18: *NO* and *CO* evolutions as functions of engine load for the different chemistry approaches and for the 59 operating points: (first column) *NO* evolutions - (second column) *CO* evolutions.

contributors to the exhausted NO (Heywood 1988). This can produce exhaust levels an order of magnitude higher than concentration in late burning elements. The mean burnt gas temperature being lower than the one of early burning elements, the mass of NO is logically underestimated for high loads despite low values of time scales (Figure 6.17.a) since the corresponding equilibrium mass fractions would be too low. On the other hand, for low loads, the mean temperature is closer to the temperature of the earlier burning fractions of the charge. As a consequence, tabulated equilibrium mass fractions can be supposed to be coherent and the overestimation of NO at low loads could then mainly be explained by too high values of tabulated time scales (Figure 6.17.a). The same comments can explain the discrepancies between experimental and simulated CO levels obtained from CFM1D-TC. Indeed, although the effect of temperature inhomogeneities on the CO evolution is not supposed to have the same influence as for NO, it still can be the main reason of the underestimation of CO levels at high loads.

To evaluate the amplitude of the temperature stratification in SI engines, 3D RANS (Reynolds Averaged Navier Stokes) calculations have been performed using IFP-C3D (Bohbot et al. 2009) to simulate two engine operating conditions at 2000 rpm (IMEP = 9 and 24 bar). The engine configuration used here is the same than the one previously presented in Table 6.3. Figure 6.19 shows the corresponding burnt gas temperature fields at three moments in the engine cycle for two loads. The burnt gas temperature discrepancy previously involved is here clearly evidenced. From these calculations an estimation of the temperature mass distribution is performed. Figure 6.20 presents the probability density function of T^b at same times than Figure 6.19 for both operating conditions. It shows that whatever the position in the combustion process, the temperature distribution is large leading to a high deviation between mean and maximum burnt gases temperatures which confirms previous guesses.

Different solutions can be proposed to address the problems of temperature inhomogeneities. First 0-dimensional models developed for Diesel applications describe the combustion chamber through a small number of zones allowing to improve the monitoring of fuel droplets, mixture inhomogeneities or temperature distribution (Kwon et al. 2011, Hiroyashu et al. 1983, Asay et al. 2004). However, these models require to resolve all conservations equations for all zones and to control interface exchanges. Such models have therefore the disadvantage of being very expensive in term of computational time (Ho and Kuo 1997). Another solution to approximate the temperature variations in the chamber consists of using statistical methods commonly used in RANS or in large eddy simulations (LES): the distribution of a variable Q can be described by a presumed probability density function $P(Q)$ (for example a Gaussian or a β-function) as function of the mean value of Q, $\widetilde{Q}$ and its variance $\widetilde{Q''^2}$ (Bilger 1993, Klimenko 1995, Bradley et al. 1990, Peters 2000). These approaches have the advantage of being easy to couple with the present model since the mean temperature is known. Nevertheless, modeling efforts are needed to estimate the temperature variance, which represents one of the major challenges for future 0D premixed combustion models.

Despite all these limitations, the present model CFM1D-TC is able to globally recover the experimental curves (Figure 6.18), which corresponds to the initial objective of this work, that was, to develop a generic and efficient model and to reduce the CPU cost. Table 6.5 confirms that results for the 59 operating points are improved for NO and CO. Moreover this new CFM1D-TC model based on the CORA model allows to significantly reduce the CPU time globally by half.

	CFM1D	CFM1D-TC
Mean error on mass of NO [%]	43.1	34.3
Mean error on mass of CO [%]	46.9	19.6

Table 6.5: Mean errors on NO and CO for the 59 operating points. $\epsilon = \sum \frac{|k_{expe} - k_{simu}|}{k_{expe}} / 59$, where k_{expe} and k_{simu} are respectively the experimental and simulated mass of NO or CO.

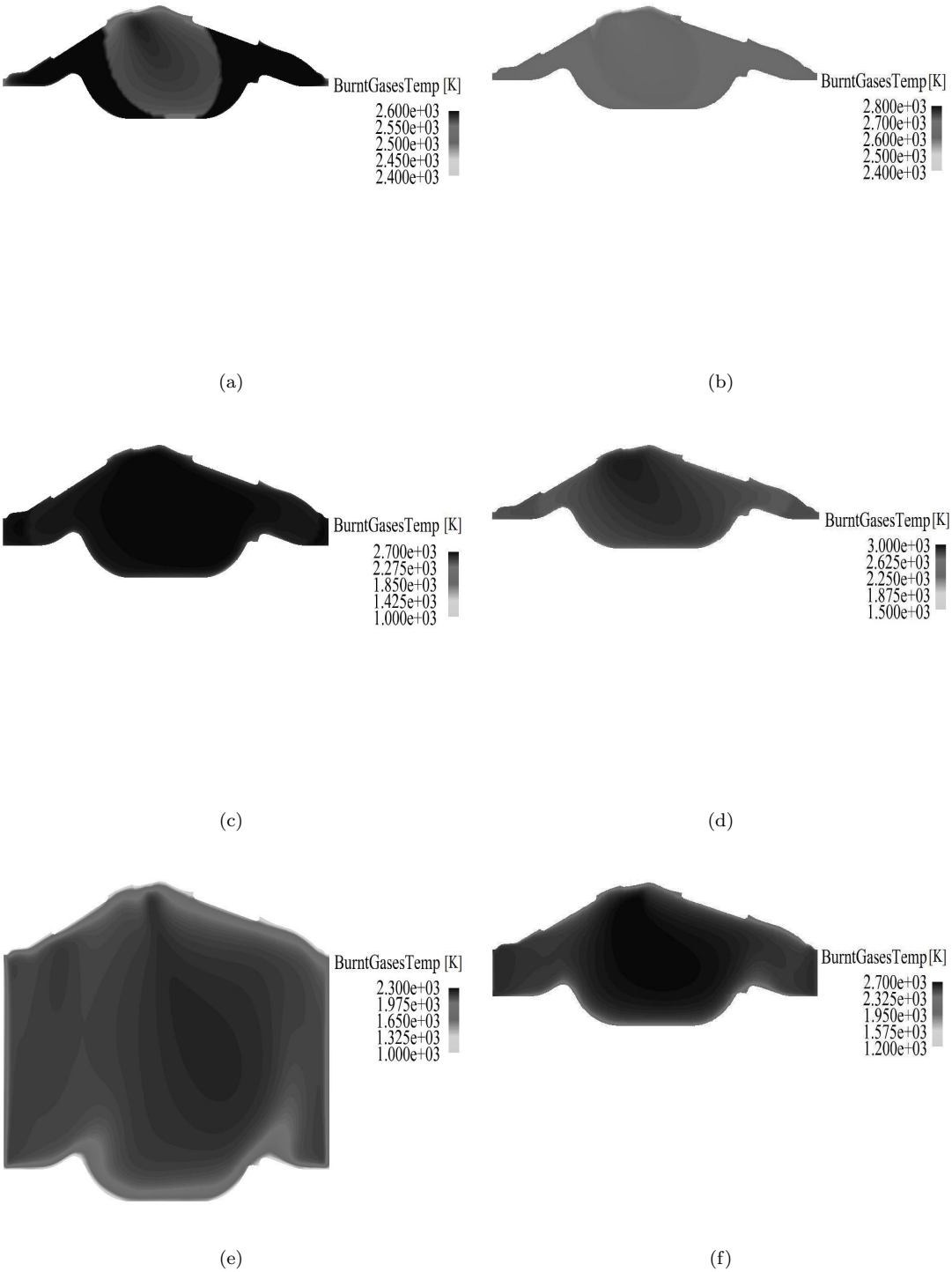

Figure 6.19: Visualization of simulated burnt gas temperature distribution in an IFPEn SI engine prototype at 2000 rpm for 2 loads (First column: IMEP = 9 bar, Second column: IMEP = 24 bar) and at three different times in the engine cycle (First raw: $Y_{fuel} = 0.95 \cdot Y^0_{fuel}$, Second raw: $Y_{fuel} = 0.5 \cdot Y^0_{fuel}$, Third raw: $Y_{fuel} = 0.1 \cdot Y^0_{fuel}$).

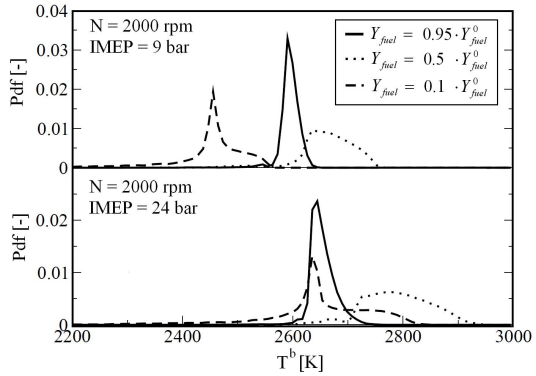

Figure 6.20: Burnt gases temperature distribution in the cylinder for three progress variable values at 2000 rpm and at two engine loads (IMEP =9 bar ; 24 bar).

6.1.6 Conclusion

This paper proposes of a new 0-dimensional combustion model, CFM1D-TC, based on the integration of complex chemistry in the CFM1D model. The aim of this new model, CFM1D-TC, is to simulate at low CPU-cost pollutant emissions in spark-ignition engines using a tabulation method initially developed for 3D simulations of NO emissions. This model called NORA was here extended and developed to the prediction of CO emissions leading to the CORA model (CO Relaxation Approach). The proposed approach consists in *a priori* calculations of 1D premixed flames and homogeneous reactors to generate a chemical database covering a wide range of parameters (equilibrium compositions and characteristic time scales), and directly accessed by the combustion model to determine pollutant concentrations. In this work, methane-air-diluent mixtures were considered and the GRI 3.0 mechanism was retained for complex chemistry calculations. A new description of the post-flame chemistry of the CFM1D was proposed, writing NO and CO reaction rates as linear functions of the respective mass fractions including a characteristic relaxation response time necessary to reach the equilibrium state. Mass fractions and times scales are interpolated from look-up tables using the current values of pressure, burnt gases enthalpy, equivalence ratio and diluent mass fraction. Characteristic time scales are computed using species evolution from a perturbed state to the equilibrium in homogeneous reactors. In this paper, a methodology for the initialization of the perturbed states of NO and CO was presented. It was shown that chemical relaxations for a given perturbation and its opposite follow the same trends and lead to the same equilibrium. Moreover, in this work, only one perturbation $\Delta_{NO} = \Delta_{CO} = 10^{-2}$ was considered. The proposed model was then validated on a wide range of operating points from a 4-cylinder turbocharged SI engine. Simulations results were globally in good agreement with experiments in terms of NO and CO mass evolutions (as function of engine load). It was shown that both species relax until freezing when the burnt gases temperature reaches the characteristic values 2000 K for NO and 1800 K for CO. Replacing direct solving of simple and reduced chemistries by tabulating complex has a huge impact on computational times improving at the same time the prediction level of pollutant emissions and demonstrating the interest of tabulated complex chemistry in 0-D simulations. This approach could be extended to 3D models for RANS or LES applications. Future work will be devoted to the use of *a priori* complex chemistry simulations for other types of fuels (hydrogen, ethanol gasoline blends...) and to the development of statistical methods to improve the temperature inhomogeneities description in SI engines combustion chambers.

6.2 Complementary comments

According to previous conclusion, the new CFM1D-TC model appears as an interesting tool to predict at low computational cost NO and CO formation in SI engines. However, with regards to the very well-fitted results obtained in Section 5.2 (Figures 5.19-5.21) the agreement of the present results does not seem so good. This observation has been explained in the previous Section by the strong dependence of pollutant kinetics to the local thermodynamic conditions. Regarding 0D modeling where only mean values are considered, the challenge is therefore to develop approaches able to describe the inhomogeneities in engine combustion chambers. The parameters calibration (T_{CO}^{cut} and T_{NO}^{cut}) required by the initial version of CFM1D implicitly allows to globalized these heterogeneities effects (and potential others 3D effects). On the contrary, the new model has the crucial advantage of requiring no parameter calibration making it theoretically more robust and sensitive to fuel composition variations.

Chapter 7

Auto-ignition modeling

This Chapter presents a new auto-ignition (AI) model for the prediction of controlled and uncontrolled AI phenomena in SI engines (see Figure 7.1). The previous model presented in Chapter 4 dedicated to the prediction of knock was based on simple phenomenological approaches to estimate a characteristic AI delay and knock intensity (Eqs. 4.26 – 4.31 and 4.41). The main drawback of such a model is to require a specific parameters calibration and to be totally independent from the combustion model. Indeed, no specific AI consumption rate is computed which would have a direct impact on the global species evolution and heat release. Regarding knock occurrence, this last point is not so important since this phenomenon is not expected to appear. However, regarding the development of downsizing technologies coupled with the increasing use of alternative fuels such as hydrogen such phenomenological approaches can be limited and the development of more physical model appears crucial. Moreover, in the case of CAI technology (Chapter 1) the species evolution is mainly driven by the AI species consumption rate and a simple phenomenological model is here also not sufficient. To fix this problem, a similar approach to the one presented in Chapter 5 integrating complex chemistry in the CFM1D to improve the pollutants prediction, is used and presented here. The idea here is to rewrite Eq. 5.17 describing the heat release by combustion as proposed by Lecocq et al. (Lecocq 2010, Lecocq et al. 2011) in LES. It results into (see Figure 7.2):

$$\frac{dQ_{comb}}{dt} = \sum_i h_{f_i} \left(\left.\frac{dm_i}{dt}\right|_{ff} + \left.\frac{dm_i}{dt}\right|_{pf} + \left.\frac{dm_i}{dt}\right|_{AI} \right) \tag{7.1}$$

where $dm_i|_{AI}$ represents the mass variations of species i due to AI processes. The approach presented in this Chapter consist in adapting and coupling classical tabulation methods dedicated to AI modeling with the CFM1D-TC model detailed in Chapter 6.

7.1 Tabulation approach

Recent tabulation methods were proposed to describe auto-ignition processes in IC engines. A non-exhaustive list of main works on such methods comprises the models FPI (Flame Prolongation of Intrinsic Low-Dimensional Manifolds) (Gicquel et al. 2000), FGM (Flamelet-Generated Manifold) (van Oijen et al. 2001) and TKI (Tabulated Kinetics for Ignition) (Colin et al. 2005). The two first methods are very similar and consist in representing the chemical path through an unique parameter for given thermodynamic conditions, the progress variable, which goes from 0 in fresh gases to 1 in fully burned gases. FPI was initially based on the tabulation of unstrained laminar premixed flames but was extended to AI cases (Michel et al. 2009). It was successfully applied to the simulation of combustion in a Diesel engine (Pera et al. 2009). In this work, the TKI approach, which showed also good results in such an application (Knop and Jay 2006), was finally chosen.

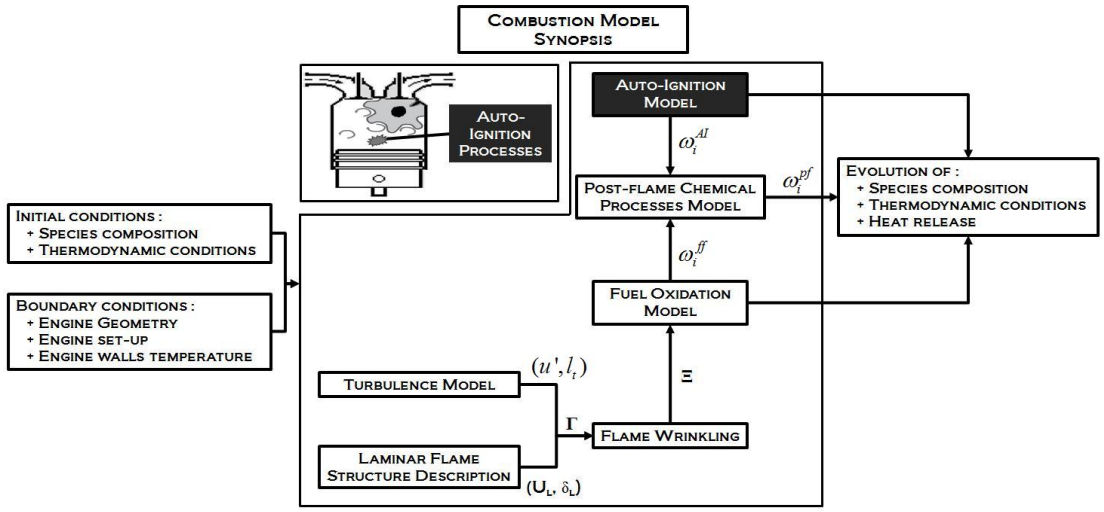

Figure 7.1: Combustion model global synopsis: **focus on the auto-ignition model**. ω_i^{ff},ω_i^{pf} and ω_i^{AI} refer to the rates of consumption/production of species i associated respectively to the combustion, post-oxidation and auto-ignition processes stepping in Figures 1.3 and 1.4.

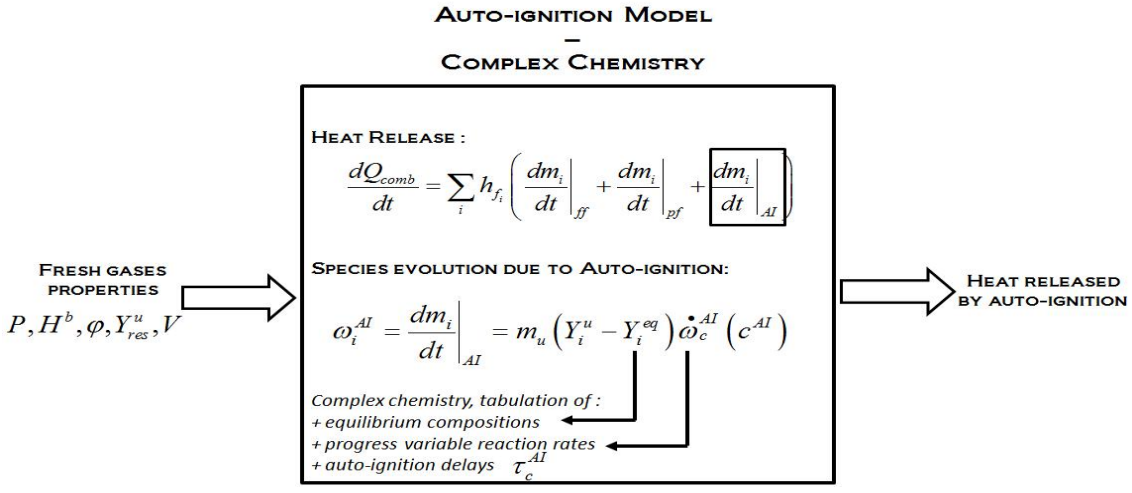

Figure 7.2: The new auto-ignition model global description (see Fig. 4.1 for the old one) – All parameters will be defined in the following sections – ω_i^{AI} refers to the rate of consumption/production of species i stepping in Fig. 1.3.

Actually, it would also have been possible to use the FPI approach considering only one species describing the progress variable. However, TKI having already been coupled to the CFM-PCM-I 3D combustion model and validated thereafter (Lecocq 2010, Lecocq et al. 2011), it appeared therefore more suitable to adapt it in the present CFM1D-TC model.

Approach Similarly to both methods presented in Chapters 5 and 6, preliminary calculations of homogeneous reactors at constant pressure are carried out covering the whole range of thermodynamic conditions encountered in the engine using the Senkin code (Kee et al. 1989). In this work, the complex chemistry calculations were performed considering gasoline-ethanol-air-diluent blends under conditions presented in Table 7.1.

	Range of variation	Number of points
V [v/v%]	0.0 – 100	6
φ [-]	0.3 – 3.0	6
Y^u_{res} [m/m%]	0 – 80	4
T^u [K]	300 – 1450	14
P [0.1MPa]	1 – 180	13

Table 7.1: Characteristics of homogeneous reactors database. V is the ethanol volume fraction in gasoline, φ the fuel/air equivalence ratio, Y^u_{res} the diluent mass fraction, T^u the fresh gases temperature and P the pressure.

The kinetic scheme considered here is the IDETHANOL (Pires.da.Cruz et al. 2010) complex chemistry mechanism already used to develop the laminar flame correlation for gasoline-ethanol blends combustion (see Chapter 5). This latter has been developed in collaboration between DCPR (CNRS) and IFPEn and is dedicated to combustion problems in GDI engines. It has been validated against a wide range of experimental measurements of auto-ignition delays at different composition and thermodynamic conditions and for many ethanol-n-heptane-iso-octane-toluene blends. Examples of validation results are given in Figure 7.3 where auto-ignition delays obtained with IDETHANOL mechanism are compared with experimental data. These experimental results were obtained from different previous works (Natarajan and Bhaskaran 1982, Ciezki and Adomeit 1993, Minetti et al. 1995, Herzler et al. 2007, Fieweger et al. 1997, Shen et al. 2008, Davidson et al. 2005, Fikri et al. 2008) measuring auto-ignition delays for different composition and thermodynamic conditions using shock wave tubes (SWT) or rapid compression machines (RCM). A good agreement is found between experiments and simulation for a wide range of temperature, pressure, equivalence ratio and fuel composition.

Two look-up tables are generated from previous calculations containing:

- The physical time τ_c^{AI} required to reach a given value c^* of the progress variable (here $c^* = 10^{-6}$);
- The chemical progress rates $\dot{\omega}_c^{AI}$ stored for discrete values of the progress variable.

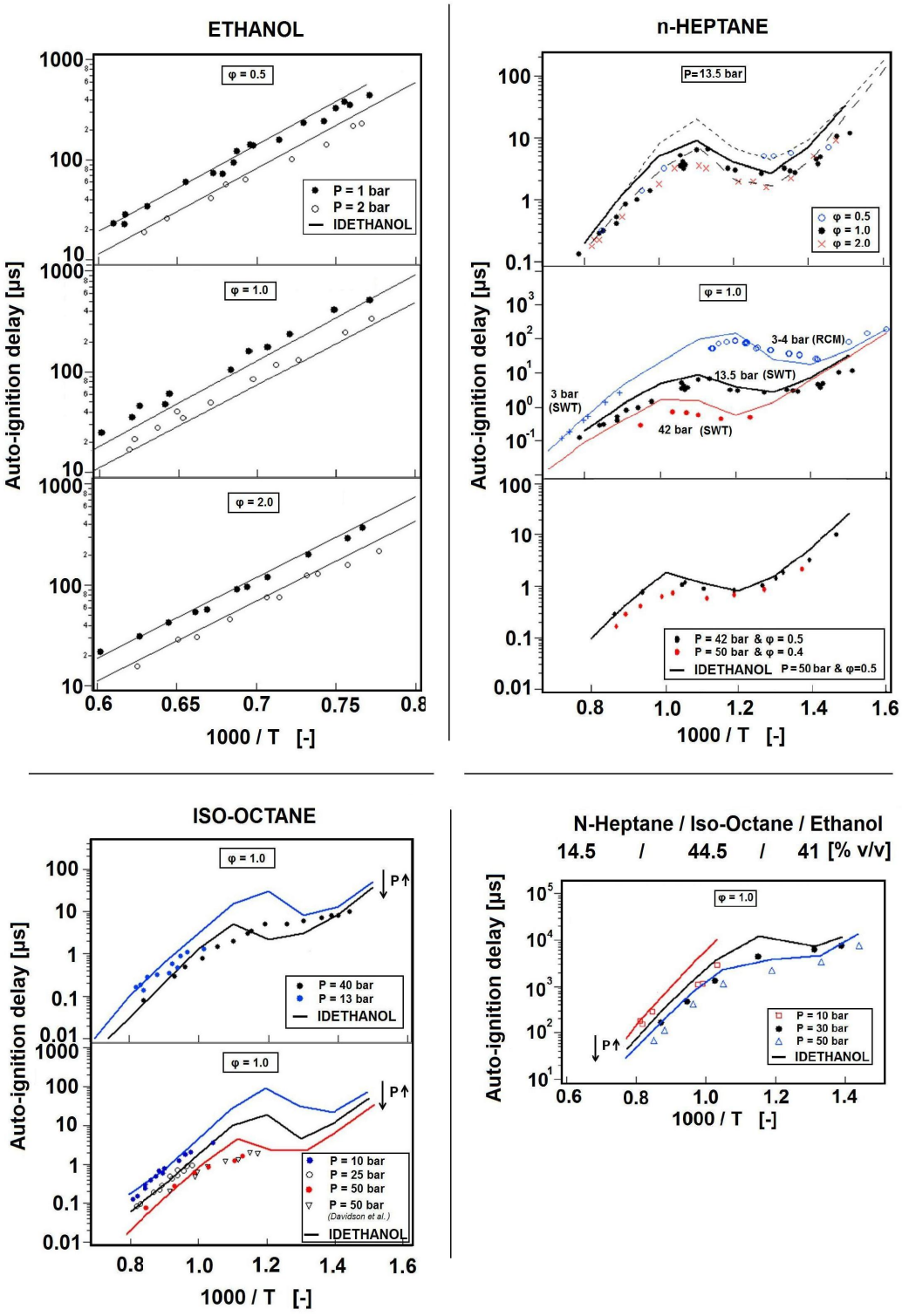

Figure 7.3: Comparison between simulated (lines) and experimental (symbols) auto-ignition delays for different temperatures, pressures, equivalence ratii and fuel formulations. Simulation results were obtained using the IDETHANOL kinetic mechanism. Experimental levels were obtained by: Ethanol – Natarajan and Bhaskaran (1982) (shock wave tube (SWT)) ; n-Heptane – Ciezki and Adomeit (1993) (SWT), Minetti et al. (1995)(rapid compression machines (RCM)) and Herzler et al. (2007) (SWT) ; Iso-octane – Fieweger et al. (1997) (SWT), Shen et al. (2008) and Davidson et al. (2005) (SWT) ; n-Heptane/Iso-Octane/Ethanol – Fikri et al. (2008) (SWT). Source of these figures: IDETHANOL internal report (Pires.da.Cruz et al. 2010).

7.2 Coupling CFM1D and TKI

The PCM-CFM-TKI model

The approach considered here is inspired from the PCM-CFM-I 3D model developed by Lecocq et al. (Lecocq 2010, Lecocq et al. 2011) in a LES framework. This model is based on the coupling of the CFM approach describing combustion processes with the TKI model. In such a model, a bimodal distribution of the progress variable is presumed: each cell contains fresh and burnt gases, their respective mean mass fraction being $(1-\tilde{c})$ and $\tilde{c}$, where $\tilde{c}$ is the progress variable which writes:

$$\tilde{c} = 1 - \widetilde{Y}_{fuel}/\widetilde{Y}_{Tfuel} \tag{7.2}$$

where $\widetilde{Y}_{fuel}$ is the mean mass fraction of fuel and $\widetilde{Y}_{Tfuel} = m^u_{fuel}/m_u$ is the fuel tracer present in the fresh gases (m^u_{fuel} is the mass of fuel in the fresh gases and m_u is the fresh gases mass).

A reaction rate for the progress variable integrating simultaneously AI and flame propagation can be written (Colin et al. 2005):

$$\bar{\rho}\widetilde{\dot{\omega}}_c = \rho_u U_l \overline{\Sigma}_{\tilde{c}} + (1-\tilde{c})\bar{\rho}\widetilde{\dot{\omega}^{AI}_c} \tag{7.3}$$

where $\overline{\Sigma}_{\tilde{c}}$ is the flame surface density (FSD), $\bar{\rho}$ is the mean gas density and ρ_u the local fresh gas density.

The factor $(1-\tilde{c})$ weights the auto-ignition contribution with the remaining fresh gases mass fraction. Values of $\tilde{\dot{\omega}}^{AI}_c$ [1] are interpolated in the TKI table as function of the fresh gases temperature T^u, the pressure P, the equivalence ratio φ, the diluent mass fraction Y^u_{res}, the ethanol volume fraction V and a specific progress variable for auto-ignition c^{AI}. Indeed, recent works (Michel et al. 2009) showed that the total heat release Q_{comb} (eq 7.1) can be overestimated when $\tilde{c}$ is used as table input. In fact, this interpolation is expected to begin only when the AI delay is reached. But at this moment, a flame front can be already established and $\tilde{c} \neq 0$. As a result, in such a case initial AI reaction rates are interpolated from a non-zero progress variable which can finally lead to too high values of $\tilde{\dot{\omega}}^{AI}_c$. To fix this problem, the solution adopted by Lecocq et al. (Lecocq 2010, Lecocq et al. 2011) therefore consisted on decoupling the progress dedicated to the premixed flame propagation and the one corresponding to auto-ignition of fresh gases. This solution was inspired by Michel et al. (2009) works who integrated two new variables, the mass fraction of fuel consumed by AI, Y^{AI}_{fuel}, and by flame propagation, Y^{ff}_{fuel}. The fuel mass fraction in the fresh gases writes:

$$\widetilde{Y}^u_{fuel} = \widetilde{Y}_{Tfuel} - \widetilde{Y}^{ff}_{fuel} - \widetilde{Y}^{AI}_{fuel} \tag{7.4}$$

Deducing $\tilde{Y}^{AI}_{fuel}$ from Eq. 7.4, a new progress variable dedicated to auto-ignition can be defined as:

$$c^{AI} = \frac{\widetilde{Y}^{AI}_{fuel}}{\widetilde{Y}_{Tfuel} - \widetilde{Y}^{ff}_{fuel}} \tag{7.5}$$

$$= \frac{\widetilde{Y}^{AI}_{fuel}}{\widetilde{Y}^{AI}_{fuel} + \widetilde{Y}^{u}_{fuel}} \tag{7.6}$$

Quantity $\widetilde{Y}_{Tfuel} - \widetilde{Y}^{ff}_{fuel}$ represents the remaining mass fraction of fuel which can potentially be consumed by auto-ignition.

[1] Actually the table contains values of $\dot{\omega}^{AI}_c$ which is assumed to be homogeneous in the fresh gases since the fresh gases are here assumed to be homogeneous in term of composition, pressure and temperature (in a given cell). As a result it is assumed that $\overline{(\rho\dot{\omega}^{AI}_c)} = \bar{\rho}\widetilde{\dot{\omega}^{AI}_c} = \bar{\rho}\dot{\omega}^{AI}_c$.

The mass fraction of the fuel consumed by AI, $\widetilde{Y}_{fuel}^{AI}$, comes from the resolution of:

$$\frac{\partial \bar{\rho}\widetilde{Y}_{fuel}^{AI}}{\partial t} + \nabla \cdot \left(\bar{\rho}\tilde{u}\widetilde{Y}_{fuel}^{AI}\right) = \nabla \cdot \left(\bar{\rho}\left(\frac{\nu}{S_c} + \frac{\nu_t}{S_{ct}}\right)\nabla \widetilde{Y}_{fuel}^{AI}\right) + (1-\tilde{c})\bar{\rho}\widetilde{\dot{\omega}_c^{AI}}\left(c^{AI}\right)\widetilde{Y}_{Tfuel} \tag{7.7}$$

where ν and S_c are respectively the laminar viscosity and Schmidt number and ν_t and S_{c_t} are respectively the turbulent viscosity and the turbulent Schmidt number.

The reaction rates of the chemical species were chosen to take a formulation similar to the one used in the PCM-CFM-I model given in Eq. 5.16 leading to:

$$\bar{\rho}\widetilde{\dot{\omega}_{Y_i}^{AI}} = (1-\tilde{c})\bar{\rho}\widetilde{\dot{\omega}_c^{AI}}\left(c^{AI}\right)\left(\tilde{Y}_i^{eq} - \widetilde{Y}_i^u\right) \tag{7.8}$$

where $\widetilde{Y}_u$ and $\widetilde{Y}_i^{eq}$ are respectively the mass fractions of the i-th species in the fresh and burnt gases.

In practice, the interpolation of $\widetilde{\omega_c^{AI}}$ is not directly activated at the beginning of the computation. Three steps are actually considered as shown in Figure 7.4:

- **Step 1:** The value of the AI delay τ_c^{AI} is interpolated in the table at the current composition, φ, Y_{res}^u, and thermodynamic conditions T^u, P. As already mentioned, τ_c^{AI} is computed by measuring the time required to reach a value c* of the progress variable c^{AI}. However, considering the strong variations of thermodynamic condition during compression and combustion strokes, the AI delay τ_c^{AI} can not be directly used and a model describing the evolution of an AI precursor $\widetilde{Y}_{IR}$ has to be defined. In the PCM-CFM-TKI model, $\widetilde{Y}_{IR}$ is described as:

$$\frac{\partial \bar{\rho}\widetilde{Y}_{IR}}{\partial t} + \nabla \cdot \left(\bar{\rho}\tilde{u}\widetilde{Y}_{IR}\right) = \nabla \cdot \left(\bar{\rho}\left(\frac{\nu}{S_c} + \frac{\nu_t}{S_{ct}}\right)\nabla \widetilde{Y}_{IR}\right) + \bar{\rho}\tilde{Y}_{Tfuel}F(\tau_c^{AI}) \tag{7.9}$$

  where F is a function accounting for the non-linear production of precursor during AI processes (Richard et al. 2009).
  At this step, the AI delay is not reached yet ($\widetilde{Y}_{IR} < \widetilde{Y}_{Tfuel}$) and the progress variable reaction rate $\widetilde{\dot{\omega}_c^{AI}} = 0$ and the progress variable c^{AI} (Eq. 7.6) remains equal to zero.

- **Step 2:** As soon as the AI precursor $\widetilde{Y}_{IR}$ reaches the mass fraction of fuel tracer $\widetilde{Y}_{Tfuel}$, $\widetilde{\dot{\omega}_c^{AI}}$ is computed as:

$$\widetilde{\dot{\omega}_c^{AI}} = -\frac{c^{start}}{\tau^*} \tag{7.10}$$

  where τ^* is a parameter about a few time steps allowing to quickly tend towards the progress $c^{start} \approx c^*$ as display in the scheme of Figure 7.4. After this step, the progress variable c^{AI} is not equal to zero anymore.

- **Step 3:** When $c^{AI} = c^{start}$, $\widetilde{\dot{\omega}_c^{AI}}$ is directly interpolated into the TKI table allowing to describe the real evolution of c^{AI}.

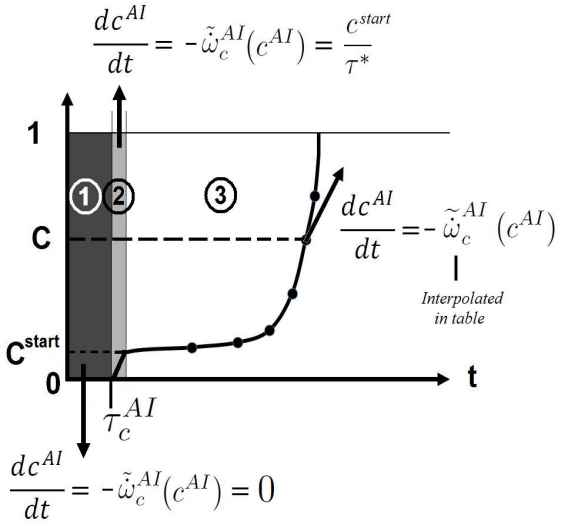

Figure 7.4: TKI model principle. Step 1: the AI delay is not reached yet and the progress variable reaction rate $\widetilde{\dot{\omega}_c^{AI}} = 0$. Step 2: the AI delay is reached and $\widetilde{\dot{\omega}_c^{AI}} = -c^*/\tau^*$. Step 3: The progress variable reaches the value c^* and $\widetilde{\dot{\omega}_c^{AI}}$ is interpolated in the table.

The CFM1D-TC-TKI model

A new 0D model is developed to compute the third RHS term of Eq. 7.1 from the PCM-CFM-TKI model presented in the previous section. The principle consists here in integrating previous equations over a control volume V_c (corresponding to the combustion chamber volume). Assuming that the AI progress variable, the pressure, the fresh gases temperature, dilution and equivalence ratio are homogeneously distributed in the cylinder, and Eq. 7.7 thus becomes:

$$\left.\frac{dm_{fuel}}{dt}\right|_{AI} = \int_\Omega \frac{\bar{\rho}\widetilde{Y}_{fuel}^{AI}}{dt} dV = (1-c) m \widetilde{\dot{\omega}_c^{AI}}\left(c^{AI}\right) Y_{fuel}^0 = m_u \widetilde{\dot{\omega}_c^{AI}}\left(c^{AI}\right) Y_{fuel}^0 \tag{7.11}$$

where c is the progress variable defined in Eq. 4.12, m the total mass of gas, m_u the total mass of fresh gases, $\dot{\omega}_c^{AI}$ is the total AI chemical progress rate and $Y_{fuel}^0 = \widetilde{Y}_{T_{fuel}}$ is the initial mass fraction of fuel in the combustion chamber.

The mass variation of species due to AI process can then be computed as:

$$\left.\frac{dm_i}{dt}\right|_{AI} = \upsilon_i \frac{W_i}{W_f} \left.\frac{dm_{fuel}}{dt}\right|_{AI} \tag{7.12}$$

where W_i denotes the molecular weight of a species i and υ_i is the stoichiometric coefficient of specie i associated to the simple chemistry described in Chapter 4, Eq. 4.19.

However, regarding the present goal of integrating complex chemistry description, the same approach than the one considered in the 3D PCM-CFM-TKI model was in fact used. From the integration of Eq. 7.8 over the combustion chamber volume, it results the following expression for the reaction rate $dm_i|_{AI}$ of a species i due to the AI processes:

$$\left.\frac{dm_i}{dt}\right|_{AI} = m_u \left(\widetilde{Y}_i^{eq} - \widetilde{Y}_i^u\right) \widetilde{\dot{\omega}_c^{AI}}\left(c^{AI}\right) \tag{7.13}$$

Such a model is equivalent to the oxidation model presented in Chapter 5 (Eq. 5.17) where fresh gases are converted into burnt gases through specific kinetics.

Eq. 5.17 is recalled here:

$$\left.\frac{dm_i}{dt}\right|_{ff} = -\rho_u \left(\widetilde{Y}_i^{eq} - \widetilde{Y}_i^{u}\right) U_l A_T \tag{7.14}$$

where ρ_u the fresh gases density, U_l the laminar flame speed, A_T the turbulent flame surface and Y_i^u and Y_i^{eq} the mass fractions of the ith species respectively in the fresh gases and in the products of the fuel oxidation reaction through the flame.

The assumption made here is that high temperature levels encountered allow to reach the chemical equilibrium directly after the AI. This approach has the advantage of allowing the use of the same table for $\widetilde{Y}_i^{eq}$ than the one used in the oxidation model (Eq. 7.14).

The progress variable c^{AI} is given here as function of the different mass and similarly writes:

$$c^{AI} = \frac{m_{fuel}^{AI}}{m_{fuel}^{AI} + m_{fuel}^{u}} \tag{7.15}$$

$$\tag{7.16}$$

where m_{fuel}^{u} is the mass of fuel in the fresh gases and $m_{fuel}^{AI} = \int_0^t \left.\frac{dm_{fuel}}{d\tau}\right|_{AI} d\tau$ is the mass of fuel burnt by AI.

The model describing the evolution of the AI precursor (Eq. 7.9) becomes:

$$\frac{dY_{IR}}{dt} = Y_{fuel}^0 F(\tau_c^{AI}) \tag{7.17}$$

The function F is the same than the one used in the phenomenological knock model presented in Chapter 4 (Eq. 4.28) recalled here:

$$F(\tau_c^{AI}) = \frac{\sqrt{\alpha^2 \tau_c^{AI2} + 4\left(1 - \alpha\tau_c^{AI}\right)\frac{\widetilde{Y}_{IR}}{Y_{fuel}^0}}}{\tau_c^{AI}} \tag{7.18}$$

where $\alpha = 1s^1$ is a constant. When $\widetilde{Y}_{IR} = Y_{fuel}^0$, auto-ignition occurs and the corresponding heat released is computed.

First results

The new CFM1D-TC-TKI model presented in the previous section has been finally implemented in the AMESim® simulation software (Malbec et al. 2009) and validation tests are still ongoing at IFPEn. As a consequence, no conclusions are provided in this work but some perspectives and development propositions can be cited here.

To this end some steady state operating conditions of an IFP Energies nouvelles (IFPEn) single-cylinder SI prototype engine burning ethanol-gasoline blends have been performed using the new model. The engine and sub-models set-ups have been already presented in Section 4.2. An example of achieved results is presented in Figure 7.5 which displays comparison between experimental and simulated in-cylinder pressures at 2000 rpm (IMEP = 20 bars) and for three ignition timings (spark advance SA):

- $SA = SA_{ref}$ spark advance provided by the engine bench at the optimal setting (also called reference setting or best setting).
- $SA = SA_{ref} - 5CAD$

- $SA = SA_{ref} + 5CAD$

These spark advance variations around the optimal point have been performed to evaluate the model response with regards to knock prediction. The first observation is that a pressure peak appears during the expansion stroke for the optimal case (Figure 7.5.a) while no particular heat release is expected to occur since SA is supposed to have been calibrated to prevent knock occurrence. On the other hand, the relative effect of SA variations are well-described. Indeed, when SA is decreased (Figure 7.5.a), i.e. when the fuel mixture is initiated latter, the pressure (and temperature) level is lower and no particular heat release is observed in the pressure curve. On the other hand, when SA is increased (Figure 7.5.c), i.e. when the fuel mixture is initiated earlier, the pressure (and temperature) level is higher and a pressure peak is clearly observed, higher than the one occurring at the optimal setting.

Despite the low number of information provided by previous observations some development propositions can be proposed here:

- **An experimental data post-processing methodology need to be developed.** The use of post-processed experimental data is generally quite difficult since the achieved information are not of the same nature than the model outputs. Indeed, the pressure signal provided by the bench is filtered by the engine and the sensor itself and locally measured for each cycle by an accelerometer through a transfer function which is generally unknown. By contrast, the auto-ignition model provides a mean pressure trace resulting from the main combustion and auto-ignition process which can only be compared to the average of local experimental pressures data measured over several engine cycles.

- **An adequate intensity indicator has then to be specified.** In TKI models Colin et al. (2005) evaluated this intensity by defining a ratio between the heat release by the main combustion and the one by auto-ignition (Noda et al. 2004, Laget et al. 2010).

- **Accounting for cycle-to-cycle variations.** In a recent work, Pera et al. (2012) developed a 1D model able to account for these variations by exploiting multi-cycle engine LES. Nevertheless, their approach were based on an adjustment of the turbulence model parameters and therefore, specific developments have to be achieved to adapt this approach to the present problem of AI heat release variations.

- **Accounting for temperature stratification in the combustion chamber.** As for pollutant emissions (see Chapter 6), the auto-ignition processes are known to be very sensitive to the local temperature (more precisely the fresh gases temperature). Considering the natural temperature stratification formed in the fresh gases due to heat diffusion processes (from the flame and walls), the present model which considers as input the mean fresh gases temperature could potentially present significant errors. In order to evaluate the amplitude of the temperature stratification in SI engines, results from the 3D RANS (Reynolds Averaged Navier Stokes) calculations performed using IFP-C3D (Bohbot et al. 2009) to simulate two engine operating conditions at 2000 rpm (IMEP = 9 and 24 bars) and presented in Chapter 6 are used here again. Figure 7.6 shows the corresponding fresh gas temperature fields at three moments in the engine cycle. The fresh gas temperature discrepancy previously evoked is here clearly evidenced. From these calculations an estimation of the temperature distribution is performed. Figure 7.7 presents the probability density function of T^u at same times than Figure 7.6 for both operating conditions. It shows that whatever the position in the combustion process, the temperature distribution is large leading to a high deviation between mean and maximum burnt gases temperatures which confirms previous guesses. A solution to approximate the temperature variations in the chamber consists in using statistical methods commonly used in RANS or in large eddy simulations (LES): the distribution of a variable Q can be described by a presumed probability density function $P(Q)$ (for example a Gaussian or a β-function) as function of the mean value of Q , $\tilde{Q}$ and its variance $\tilde{Q}''^2$ (Bilger 1993, Klimenko 1995, Bradley et al. 1990, Peters 2000). These approaches have

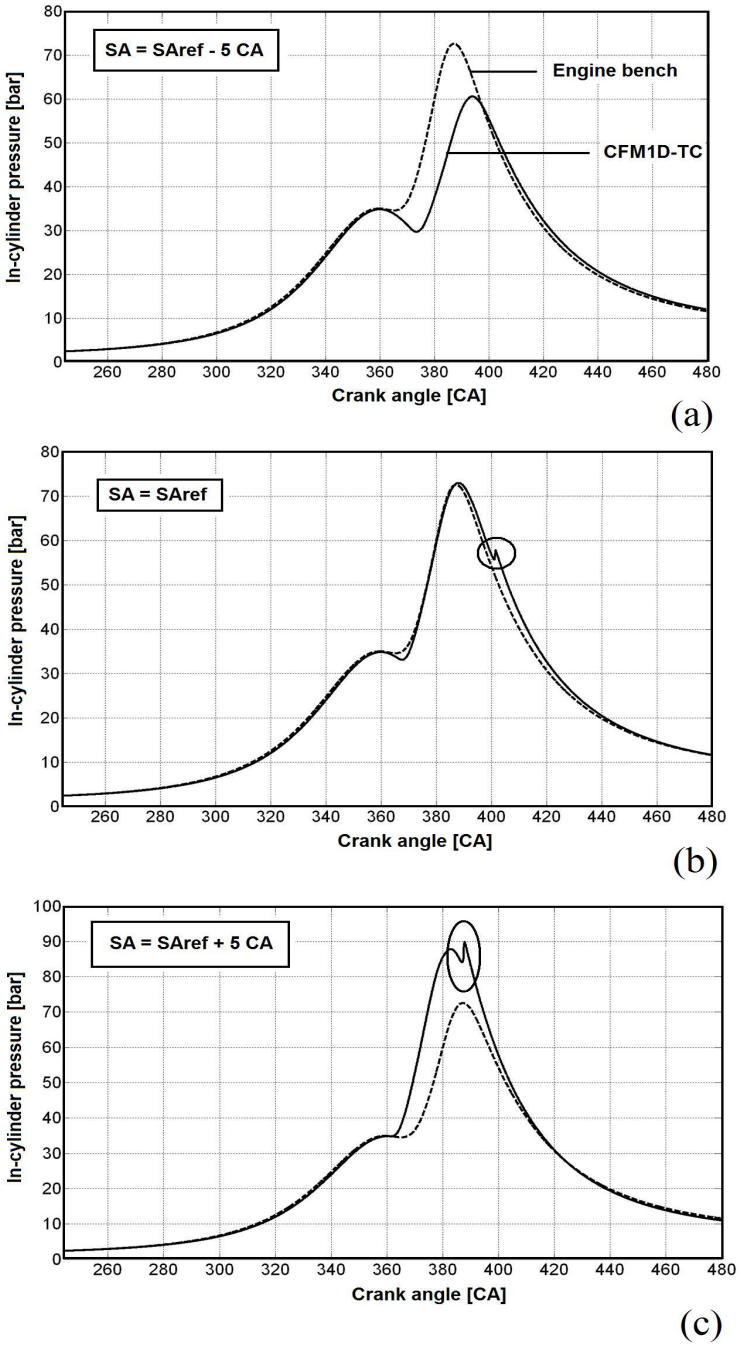

Figure 7.5: Effects of SA variations on the simulated in-cylinder pressure using the CFM1D-TC model for a given operating condition at 2000 rpm and IMEP=20 bar. SA_{ref} corresponds to the optimal setting provided by the bench. The reference experimental pressure trace obtained at the optimal setting, $SA_{ref} = -1$ CAD, is also plotted. Fuel=gasoline.

the advantage of being easy to couple with the present model since the mean temperature is known. Nevertheless, modeling efforts are needed to estimate the temperature variance, which represents one of the major challenges for future 0D premixed combustion models.

- **Integrating effects of turbulence.** The present model provides levels of laminar burning rate due to the auto-ignition processes. In the case of knock prediction, this information is enough to evaluate its potential occurrence and its intensity. However, in the case of CAI strategies developments, the total combustion rate is not mainly driven by the classical oxidation process any more. Indeed, auto-ignition processes take over and the turbulence effects which will promote species mixing and tend to increase the total combustion reaction rate have thus to be modeled.

7.3 Conclusion

In this Chapter a new 0D auto-ignition model has been presented. It has been inspired from the PCM-CFM-TKI model developed by Lecocq et al. (Lecocq 2010, Lecocq et al. 2011) and is based on the tabulation of AI delays and progress variable reaction rates. These tables have been obtained from a priori calculations of homogeneous reactors at constant pressure using the IDETHANOL (Pires.da.Cruz et al. 2010) complex kinetic scheme and consider as inputs the pressure, the fresh gases temperature, the fuel/air equivalence ratio, the dilution rate, the volume fraction of ethanol in fuel and a specific auto-ignition progress variable. This latter differs from the progress variable associated to the flame propagation to ensure auto-ignition to begin at a progress variable equal to zero. The new model has been integrated as a new part of the CFM1D-TC model and was built to predict knock occurrence and to allow the simulation of CAI configurations. It has been implemented in the AMESim® engine simulation software (Malbec et al. 2009) but validation tests are still ongoing at IFPEn. Therefore, no conclusions have been provided in this work. Nevertheless, some perspectives and development suggestions have been proposed. It concerns the need to define adequate indicators common to both experimental and simulation data to allow comparisons and developing approaches to account for cycle-to-cycle variations, fresh gases temperature stratification and turbulence effects on AI processes.

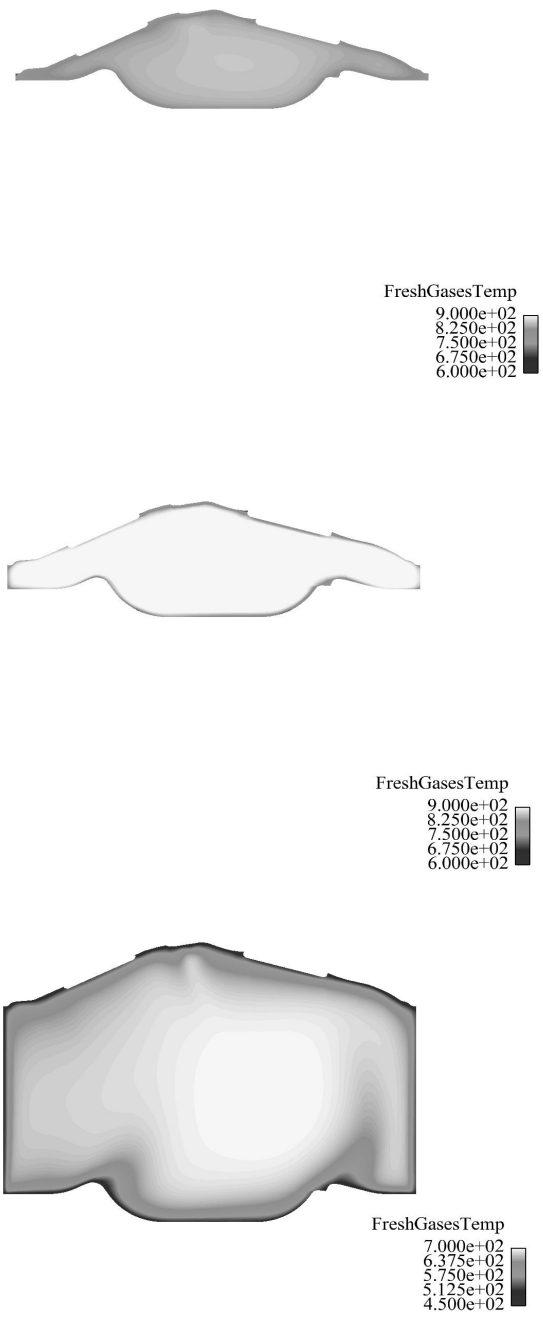

Figure 7.6: Visualization of simulated fresh gas temperature distribution in an IFPEn SI engine prototype at 2000 rpm, IMEP = 9 bar and at three different times in the engine cycle (First raw: $Y_{fuel} = 0.95 \cdot Y^0_{fuel}$, Second raw: $Y_{fuel} = 0.5 \cdot Y^0_{fuel}$, Third raw: $Y_{fuel} = 0.1 \cdot Y^0_{fuel}$). These 3D RANS calculations were performed at IFPEn by J.-B. Michel using IFP-C3D (Bohbot et al. 2009).

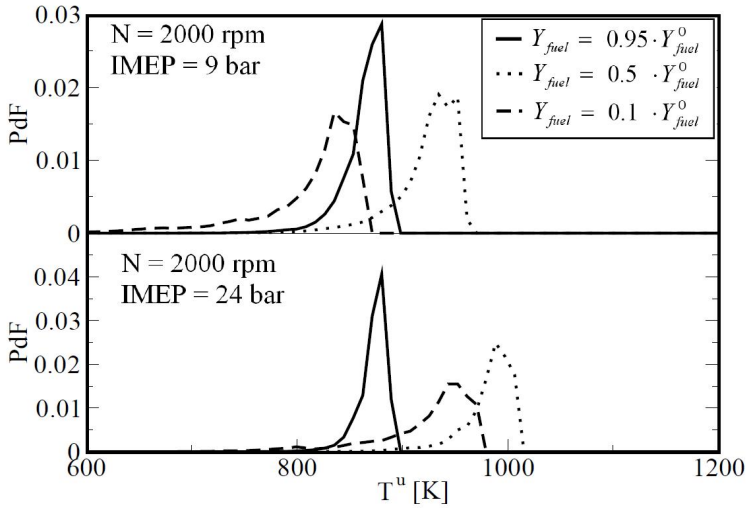

Figure 7.7: Burnt gases temperature distribution in the cylinder for three progress variable values at 2000 rpm and at two engine loads (IMEP =9 bar ; 24 bar).

Chapter 8

Turbulent flame propagation modeling - Effect of fuel composition

8.1 Chapter purpose

This chapter investigates the effects of fuel composition on flame/turbulence interaction processes (Figures 8.2 and 8.3).

As shown in section 4.3, differences between experimental and simulated pressures can be observed when using the CFM1D model. These differences which are small when dealing with ethanol-gasoline blends, can be more significant when burning hydrogen-methane mixtures. In the present model, the heat release is mainly controlled by the first RHS term in Eq. 4.2 recalled here:

$$\left.\frac{dm_{fuel}}{dt}\right|_{ff} = -\rho_u \left(Y_i^{eq} - Y_i^u\right) U_l \Xi A_m \tag{8.1}$$

Considering that the mean surface A_m, the equilibrium compositions Y_i^{eq} and the laminar flame velocity U_l are well defined (see Chapter 5), the error on the heat release rate may come from the turbulent flame velocity through the flame wrinkling factor Ξ. As previously mentioned, Ξ is computed solving a 0-D equation (Eq. 4.15) derived from the 3D CFM transport equation for the filtered surface density $\overline{\Sigma}$ (measuring the flame surface per unit volume, $\bar{}$ stands here for the spatial filter) which writes (Veynante and Poinsot 1997):

$$\frac{\partial \overline{\Sigma}}{\partial t} + \nabla \cdot \left(\langle u \rangle_s \overline{\Sigma}\right) = \langle \nabla \cdot u - nn : \nabla u \rangle_s \overline{\Sigma} - \nabla \cdot \left(\langle U_d n \rangle_s \overline{\Sigma}\right) + \langle U_d \nabla \cdot n \rangle_s \overline{\Sigma} \tag{8.2}$$

where $n = -\nabla c / |\nabla c|$ is the local normal vector to the flame front pointing towards the fresh gases, $\langle \phi \rangle_s$ is the conditioned averaged value of $\langle \phi \rangle_s = \overline{\phi \Xi} / \overline{\Xi}$ along the flame surface, u is the local flow velocity vector and U_d is the displacement speed of an iso-surface of the progress variable c relatively to the flow. Ξ can be defined here as:

$$\Xi = \frac{\overline{\Sigma}}{|\nabla \overline{c}|} \tag{8.3}$$

Reducing Eq. 8.2 therefore consists to apply a spatial filter larger than the turbulent integral length scale l_t considering that all the flame wrinkling lies at the non-resolved scale level. Assuming an homogeneous and isotropic turbulence (HIT), the wrinkling is homogeneously distributed along

the flame front, leading to:

$$\underbrace{\int_{\Omega} \overline{\Sigma} \delta V}_{A_{tot}} = \int_{\Omega} \Xi \left| \nabla \overline{c} \right| \delta V = \Xi \underbrace{\int_{\Omega} \left| \nabla \overline{c} \right| \delta V}_{A_{res}} \tag{8.4}$$

where A_{tot} represents the total flame surface, A_{res} is the resolved flame surface and Ω is the integration domain (here the combustion chamber). Hence, writing $\Xi = A_{tot}/A_{res}$, it comes:

$$\frac{1}{\Xi}\frac{d\Xi}{dt} = \underbrace{-\frac{1}{A_{res}}\frac{dA_{res}}{dt}}_{\kappa_{res}} + \underbrace{\frac{1}{A_{tot}}\frac{dA_{tot}}{dt}}_{\kappa_{tot}} \tag{8.5}$$

where κ_{res} defines the resolved flame surface strain rate and κ_{tot} corresponds to the total flame surface strain rate. The closure of both previous terms has been closed by Richard and Veynante (2007) and lead to the final 0-D equation for the flame wrinkling factor Ξ previously presented and recalled here:

$$\frac{1}{\Xi}\frac{d\Xi}{dt} = \underbrace{\Gamma\left(u'_{\lambda_{max}}/U_l, \lambda_{max}/\delta_l\right)\frac{u'_{\lambda_{max}}}{\lambda_{max}}\left(\frac{\Xi_{equ}-\Xi}{\Xi_{equ}-1}\right)}_{Str_{turb}} - \underbrace{\frac{2}{r_b}\left(1+\tau\right)\left(\Xi-1\right)U_l}_{Str_{mean}} \tag{8.6}$$

where r_b is a burnt gases radius defined considering the burnt gases volume $V^b = 4\pi r_b^3/3$, λ_{max} is the size of the biggest eddy able to wrinkled the flame, $u'_{\lambda_{max}}$ the turbulent velocity of this eddy and:

- Str_{turb} corresponds to the strain rate of the flame front induced by the different eddies of the flow. This strain rate does not account for the whole turbulence spectrum but only the effects of the eddies able to wrinkle the flame front *i.e.* of size lower than λ_{max}. In practice, λ_{max} is taken as: $\lambda_{max} = \min(2r_b, l_t)$. However, a more precise expression for λ_{max} can be written considering that an eddy able to wrinkle the flame satisfies: $\tau_\lambda \leq \tau_l$, where τ_λ is turnover time of a given eddy and τ_l a characteristic time for the flame growth (Richard and Veynante 2007). Then:

$$\lambda_{max} = \left(\frac{u'}{(1+\tau)U_l l_t^{1/3}}\, r_b\right)^{\frac{3}{2}} \tag{8.7}$$

  where $1+\tau = \rho_u/\rho_b$ is the thermal expansion rate (ρ_u and ρ_b are respectively the fresh and burnt gases densities).

- Str_{mean} stands for the impact of the mean strain rate due to thermal expansion and curvature. Indeed, the burnt gases dilatation tends to impose a positive curvature and to limit the flame wrinkling (Richard and Veynante 2007).

Finally, considering that Eq. 8.6 is representative of the flame wrinkling evolution (cf. validations by Richard and Veynante (2007)), results displayed on Figure 4.48 (displayed here again on Figure 8.1) can lead to some questions about the flame stretch ($\Gamma \cdot (u'max/\lambda_{max})$) definition especially for the stretch efficiency function Γ. Indeed, as it will be discussed in Section 8.2, commonly used efficiency functions are generally validated only on a single chemistry. Thus, the effect of fuel composition on some physical phenomena – as thermo-diffusive instabilities occurring in combustion of hydrogen blended fuels – might not be well described by these functions. The new stretch efficiency function proposed here has been developed to account for fuel composition variations. Moreover, as already mentioned in Chapter 2, with regards to Figure 2.10 future engines with high downsizing levels are expected to run in operating zones not considered yet by current modeling functions describing U_T as Γ. Developments have therefore to be performed to describe

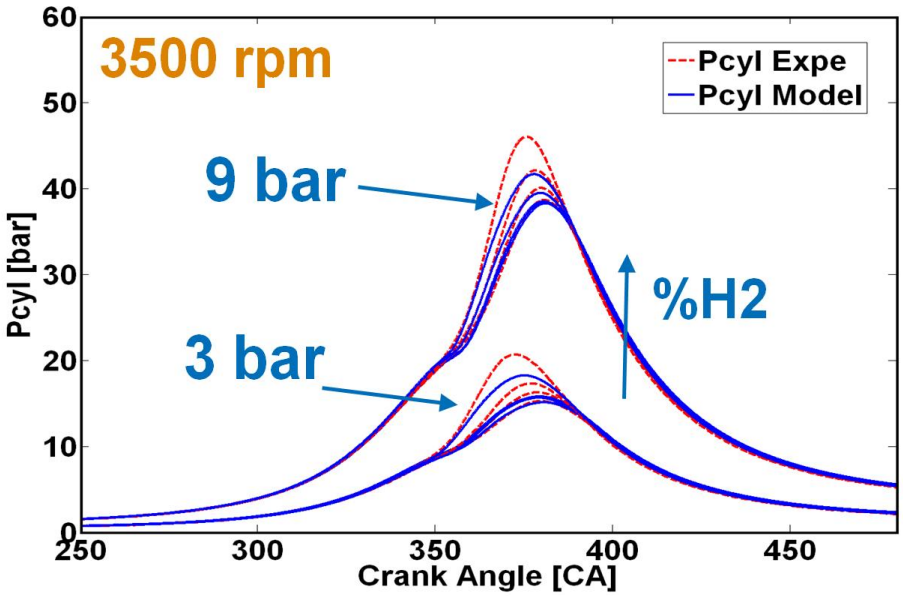

Figure 8.1: Comparisons between experimental and simulated cylinder pressure curves for different engine loads (IMEP = 3bar and 9bar) at 3500 rpm and for different hydrogen ratii (α) in methane ($\alpha = 0\%; 10\%; 20\%; 40\%$).

the flame/turbulence interaction at high turbulence levels ($D_a \approx 1$). The new function proposed here improves the description of the turbulent flame stretch at high u'/U_l ratii.

Works presented in this chapter are organized as follow:

- **Section 8.2 : Development of a new efficiency function for the flame stretch accounting for fuel composition** – DNS of flame/vortex interaction are performed for several fuel compositions and results about the stretch efficiency function are compared with common functions. Works described in this section have been submitted to **Combustion and Flame**.
- **Section 8.3 : Complementary comments** – The new efficiency function is integrated in the CFM1D-TC model (in the flame surface density balance equation (Eq. 4.15 and Figure 8.3) and validated by comparison with experimental data obtained at the engine bench for a wide range of operating conditions.

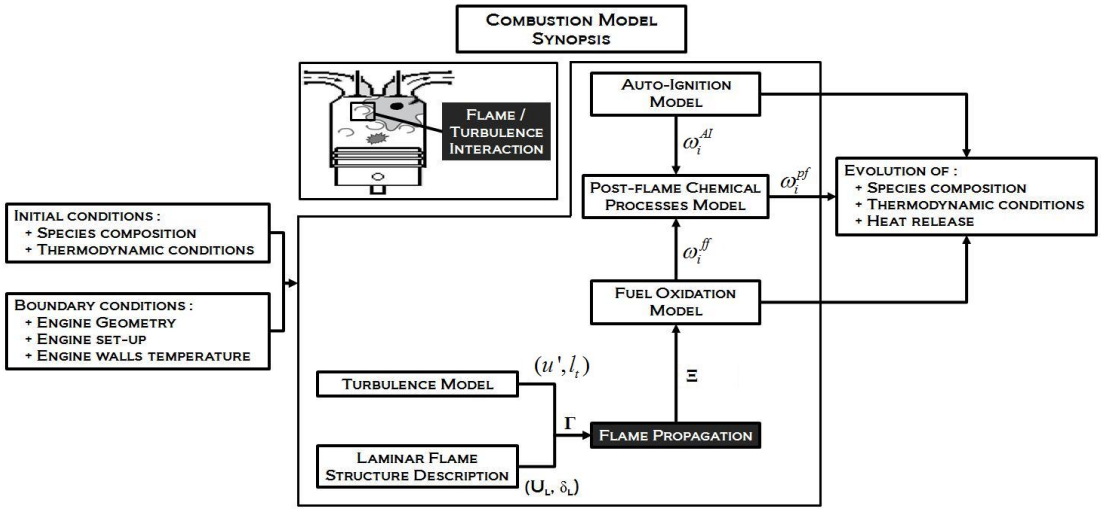

Figure 8.2: Combustion model global synopsis: **focus on the flame/turbulence interaction modeling**. ω_i^{ff},ω_i^{pf} and ω_i^{AI} refer to the rates of consumption/production of species i associated respectively to the combustion, post-oxidation and auto-ignition processes stepping in Figures 1.3 and 1.4.

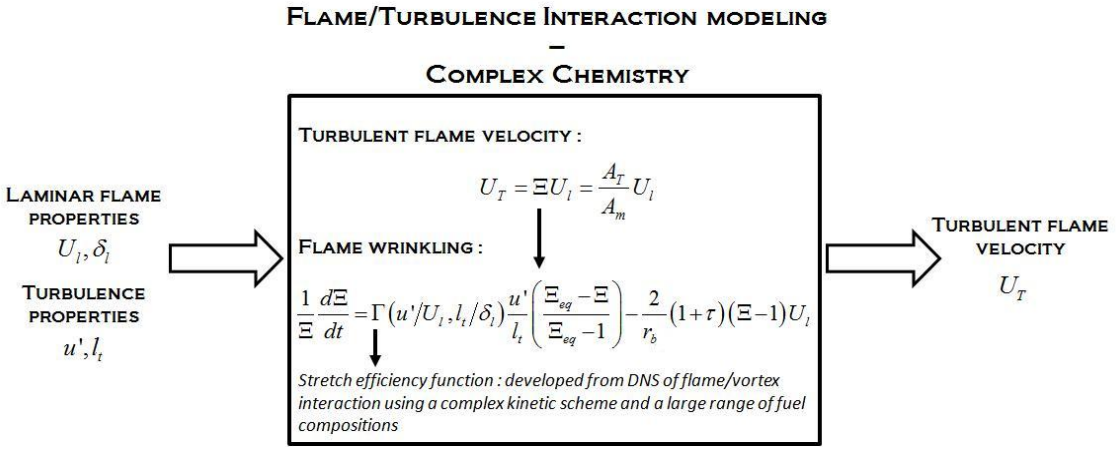

Figure 8.3: The new wrinkling model global description (see Fig. 4.1 for the old one) – All parameters will be defined in the following sections

8.2 Development of a new efficiency function for the flame stretch

---

- **Title**: Fuel composition effects on flame stretch in turbulent premixed combustion: DNS analysis of flame-vortex interaction and formulation of a new efficiency function
- **Authors**: S. Bougrine* **, S. Richard*, Olivier Colin*, Denis Veynante**
  * IFP Energies nouvelles
  ** Laboratoire EM2C, CNRS Ecole Centrale Paris
- **Reference**: submitted to Combustion and Flame

8.2.1 Abstract

Direct numerical simulations (DNS) of flame-vortex interaction are performed to study the effect of fuel composition on premixed flames wrinkling. Flame stretches are deduced from the DNS and compared with phenomenological functions from the literature for a range of vortex characteristics. Such functions, which are used as an input in most flamelet models for premixed combustion, depend on the turbulent scale parameters and the laminar flame properties. Therefore, all mixture related effects are supposed to be described by these latter quantities. However, such an assumption can be restrictive when considering various fuels and especially low Lewis number mixtures. In these conditions, thermo-diffusive instabilities can occur, leading to an increase of the flame wrinkling, which is not correctly described by common stretch models. To overcome this issue, DNS performed in this work integrate a description of chemistry processes through a new 4-steps kinetic scheme dedicated to the combustion of CH_4-H_2 and C_3H_8-H_2 blends. It is shown that fuel composition effects can at first order be described through the mixture Lewis number, but also that the asymptotic behavior of current stretch functions are not relevant at large turbulent length scales. A new efficiency function for the flame stretch is thus finally proposed.
Keywords: Flame/vortex interaction, efficiency function, premixed combustion modeling, stretch, DNS, Lewis number.

8.2.2 Introduction

Turbulence flame interactions are complex phenomena generally characterized by a strong coupling between the heat release rate and flow motions. In the premixed combustion framework, recent reviews from Lipatnikov and Chomiak (Lipatnikov and Chomiak 2010) and Driscoll (Driscoll 2008) discussed about the flame effects on turbulence and turbulent scalar transport as well as wrinkling and quenching due to flame stretching by the flow. This latter phenomenon results of strain, curvature and propagation mechanisms, which depend on flame and turbulent structures properties (Peters 2000). Eddies larger than the flame front thickness δ_l mainly lead to a distortion of the interface between fresh and burnt gases, while small scales can enter the preheated or reaction zones, then promoting mixing processes and modifying the flame structure and its local properties. The papers of Lipatnikov and Chomiak (Lipatnikov and Chomiak 2010) and Driscoll (Driscoll 2008) also reviewed out current modeling approaches and issues in premixed combustion. Regarding flame stretch and wrinkling, the flamelet concept is dominantly adopted and proposes to gather all these phenomena in a single quantity: the turbulent flame velocity U_T. Considering that this velocity is mainly linked to the enhancement of the flame surface A_T under the action of the flow, Damköhler (Damköhler 1940) defined the flame wrinkling Ξ as:

$$\Xi = \frac{U_T}{U_l} = \frac{A_T}{A_l} \tag{8.8}$$

where U_l and A_l are respectively the laminar flame velocity and unwrinkled flame surface. The measurement of the turbulent flame surface being a difficult task, the turbulent velocity notion is generally preferred (Gülder et al. 2000, Chen and Bilger 2002, Filatyev et al. 2005, Kobayashi et al. 2005, Wu et al. 1990, Driscoll and Gulati 1988, Cheng 1995, Cho et al. 1986, Lawn and Schefer 2006, Smith and Gouldin 1979, Bradley et al. 2003, Kido et al. 2002, Shepherd and Cheng 2001, Bradley et al. 1992, Kobayashi et al. 1997, Ziegler 1998). Many authors provided experimental correlations for U_T as function of the turbulent flow and flame properties. Damköhler (Damköhler 1940) was the first to propose a simple expression for the turbulent burning velocity, depending only on the velocity fluctuation u' and laminar flame speed:

$$\frac{U_T}{U_l} \approx 1 + C\frac{u'}{U_l} \tag{8.9}$$

where C is a model parameter. Zimont (Zimont 2000), Peters (Peters 2000) or Gülder (Gülder 1990), proposed to introduce the effect of turbulent length scales in their models, to account for the various combustion regimes (Peters 1999). For this purpose, the two latter directly implemented the Damköhler number Da in the U_T expression:

$$\frac{U_T}{U_l} \approx 1 + Da^{0.25}\frac{u'}{U_l} \tag{8.10}$$

However, these expressions only depend on the turbulent flow and laminar flame properties although several experimental works (Lee et al. 1993, Wu et al. 1991, Goix and Shepherd 1993) suggest that flame stretch and differential diffusion have important effects on the local response and overall burning velocity of premixed flames. Lipatnikov and Chomiak (Lipatnikov and Chomiak 2010) discussed in their review the importance of molecular transport effects associated to highly turbulent flames. Integrating these phenomena in turbulent velocity models is therefore of crucial importance in particular when dealing with the impact of fuel composition on combustion. To this end, Bradley (Bradley et al. 1992) or Driscoll (Driscoll 2008) proposed new expressions based on experimental data (Gülder et al. 2000, Chen and Bilger 2002, Filatyev et al. 2005, Kobayashi et al. 2005, Wu et al. 1990, Driscoll and Gulati 1988, Cheng 1995, Cho et al. 1986, Lawn and Schefer 2006, Smith and Gouldin 1979, Bradley et al. 2003, Kido et al. 2002, Shepherd and Cheng 2001, Bradley et al. 1992) for different fuels, especially CH_4, C_3H_8, H_2), written:

$$\frac{U_T}{U_l} \approx 1 + (KaLe)^{-\epsilon}\frac{u'}{U_l}^{\beta} \tag{8.11}$$

where Ka is the Karlovitz number, Le the Lewis number, allowing to account for diffusion effects, and α and β are fitting coefficients. In the same way, Eickhoff (2002) or Lee et al. (1995), Lee et al. (1993) observed that the U_T/U_l ratio decreases with the Lewis number in a nearly linear way. The development of CFD combustion models describing the turbulent propagation of premixed flames has also generating numerous works in numerical simulation. Most models were developed to simulate flames under combustion regimes satisfying the flamelet assumption. Applications of such models range from RANS (Baritaud et al. 1996, Colin et al. 2003, Dahms et al. 2011) to LES (Hawkes and Cant 2000, Richard et al. 2007, Fiorina et al. 2010, Weller et al. 1998, Colin et al. 2002) or even quasi-dimensional (0D) simulations (Richard et al. 2009, Bougrine et al. 2011). All these approaches are implicitly or explicitly based on the turbulent flame surface concept, which evolution is related to the flame stretch due to all scales of the flow through (Candel and Poinsot 1990, Matalon 1983):

$$K = \frac{1}{A_T}\frac{dA_T}{dt} \tag{8.12}$$

In turbulent premixed combustion modeling, the flow is often treated as a set of eddies of different scales. The complex problem is therefore reduced to the study of interactions between the flame and single turbulent structures, the overall flame stretch being considered as a superposition

of the stretches induced by all the scales of the flow. The flame stretch associated to a single eddy of velocity u'_r and size r is generally linked to its strain rate defined by u'_r/r. Poinsot et al. (1990) showed that this relation between the strain rate and the induced stretch is not always obvious in particular for small turbulence structures. Indeed, if the eddy size is small compared to the flame thickness, δ_l, no effect on the flame is observed. Moreover, for eddies larger than δ_l, if they are close enough to the Kolmogorov scale, their lifetime is short due to viscous effects and therefore, while they exhibit large theoretical strain rates, they cannot act during a sufficiently long time to affect the flame structure. This observation led Meneveau and Poinsot (1991) to introduce a correction through an efficiency function which limits the stretch induced by small scales, a phenomena difficult to study properly using experimental data. This function further developed in Meneveau and Poinsot (1991), Colin et al. (2002), Charlette et al. (2002), deduced from a spectral diagram obtained using direct numerical simulations (DNS). These simulations aimed at describing the interactions between a laminar flame and a vortex pair for a number of velocity and length ratii (u'_r/U_l, r/δ_l). However all these studies were carried out for a single chemical configuration (Lewis number = 1.2) using a simple one-step chemistry with an Arrhenius law to describe combustion processes. The assumption was therefore made that all chemical effects, including equivalence ratio or fuel composition variations, are entirely accounted for through the laminar flame velocity and thickness. In addition, the reaction zone thickness to the total flame diffusion thickness ratio δ_r/δ_l was maintained at a constant value while it should be considered (see section 8.2.4) as another parameter of the turbulence/flame interaction problem (Peters 2000). These last assumptions can be restrictive when considering fuel variations with very different chemistries. Moreover, in the cas of low Lewis number mixtures, thermo-diffusive instabilities may occur and the associated flame wrinkling can finally be different from the one predicted by current efficiency functions.
An important question is thus to know if experimental results showing important effects of chemical composition on the turbulent burning velocity (Gülder et al. 2000, Chen and Bilger 2002, Filatyev et al. 2005, Kobayashi et al. 2005, Wu et al. 1990, Driscoll and Gulati 1988, Cheng 1995, Cho et al. 1986, Lawn and Schefer 2006, Smith and Gouldin 1979, Bradley et al. 2003, Kido et al. 2002, Shepherd and Cheng 2001, Bradley et al. 1992, Kobayashi et al. 1997, Ziegler 1998) could be correctly described by efficiency functions from the literature. Otherwise, which improvements can be brought on the base of previous experimental works (Driscoll 2008, Gülder 1990, Peters 1999, Lee et al. 1993, Wu et al. 1991, Goix and Shepherd 1993, Bradley et al. 1992, Eickhoff 2002, Lee et al. 1995, Lee et al. 1993, Aluri et al. 2006)? Especially, is the Lewis number parameter sufficient to account for all mixture composition variations? The first objective of this work is therefore to perform direct simulations of flame-vortex interactions varying the nature of the fuel, the equivalence ratio and the Lewis number to evaluate existing efficiency functions. The DNS are conducted following exactly the methodology proposed in previous studies (Meneveau and Poinsot 1991, Colin et al. 2002). A 4-steps kinetic scheme dedicated to the combustion of CH_4-H_2-air and C_3H_8-H_2-air mixtures, specially developed for this study is first presented. The mixture composition effect on the flame stretch is then analyzed through DNS results. The behavior of different efficiency functions from the literature is also evaluated against DNS data. Finally, a new model is proposed to correctly describe flame stretches for a variety of fuels and for asymptotic behaviors observed at large velocity and scale ratii.

8.2.3 Range of fuel characteristics definition and chemistry modeling

The study of fuel composition effects on flame/turbulence interactions requires to cover a wide range of composition (fuel/air equivalence ratio, fuel formulation) and corresponding chemical parameters (flame velocity and thickness, Lewis number). This latter condition is only possible if the considered fuels are well defined and if the flame chemistry and physical processes are well described. In the two following sections, the range of fuel characteristics considered in this study is presented as well as a new reduced kinetic scheme especially developed for this work.

Fuel formulation and Lewis number evaluation

The different fuels considered in this work are summarized in Table 8.1.

Fuel	CH_4	C_3H_8	H_2	Equ. Ratio φ	Lewis number
Fuel 1	100%	0%	0%	0.7 ; 1,0	0,98 ; 0,97
Fuel 2	60%	0%	40%	0.7 ; 1,0	0,75 ; 0,76
Fuel 3	0%	100%	0%	0.7 ; 1,0	1,91 ; 1,88
Fuel 4	0%	65%	35%	0.7 ; 1,0	0,94 ; 0,95
Fuel 5	0%	7%	93%	0.7 ; 1,0	0,52 ; 0,54
Fuel 6	0%	0%	100%	0,4 ; 1,0	0,41 ; 0,44

Table 8.1: Range of fuel compositions considered. Operating conditions: $T^u = 300$ K and $P = 0.1$ MPa, where T^u is the fresh gases temperature and P the pressure.

These compositions have been chosen to explore a wide range of fuel Lewis numbers, but also to compare different mixtures at nearly constant Le. This approach allows to separate heat and species differential diffusion effects from those more related to chemistry and linked to the laminar flame structure and properties. Lewis numbers can be easily computed for pure fuels considering the ratio between the thermal and species diffusivities. However, to define an effective Lewis number (Le_{bifuel}) for binary fuels mixtures is not as simple. A number of works have been dedicated to the formulation of this parameter (Law et al. 2005, Muppala et al. 2009, Dinkelacker et al. 2011). In this paper, the simple expression from Muppala et al. (2009), which is easy to implement in CFD codes, is retained:

$$Le_{bifuel} = (1 - \alpha) \cdot Le_{fuelA} + \alpha Le_{fuelB} \tag{8.13}$$

where α is the volume fraction of fuel B in fuel A. Figure 8.4 displays the evolution of Le_{bifuel} as a function of the equivalence ratio φ. The effective Lewis number weakly depends on φ. Moreover, Fuels 1 and 4 have a different chemical composition but approximately the same effective Lewis number, allowing to separate chemistry effects from thermo-diffusive ones. Finally, the chosen fuels allow to cover a wide range of Lewis numbers, from 0.37 to 2.

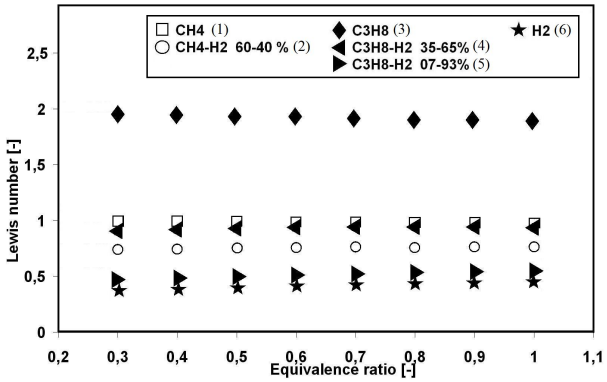

Figure 8.4: Effective Lewis numbers of two-fuel mixtures as function of equivalence ratio following the formulation from Muppala et al. (2009) (Eq. 8.13).

Reduced kinetic scheme

Each flame of Table 8.1 is characterized by its laminar velocity and thickness but also by its adiabatic temperature and species distribution through the front. With regards to the present study which aims at describing flame stretch evolutions for a number of mixture compositions and

vortex characteristics, a correct description of diffusion and reaction processes is required. For this purpose, direct numerical simulations are performed using reduced kinetic schemes dedicated to premixed flames. Many schemes extracted from detailed kinetic mechanisms and generally developed for 3D applications have been proposed for hydrocarbon combustion (Poinsot and Veynante 2001, Jones and Lindset 1988). However, such mechanisms suffer from a lack of predictivity and genericity when dealing with fuel composition variations. As a consequence, a 4-steps global scheme (Eqs. 8.14-8.15) devoted to the combustion of CH_4-H_2-air and C_3H_8-H_2-air mixtures has been specially developed for this study to finely describe flames of Table 8.1 under atmospheric conditions. Arrhenius constants for reaction rates are given in Table 8.2.

For methane/hydrogen/air mixtures:

$$\left\{\begin{array}{ll} (I) & CH_4 + 3/2O_2 \Rightarrow CO + 2H_2O \\ (II) & CO + 1/2O_2 \Leftrightarrow CO_2 \\ (III) & H_2 + O_2 \Leftrightarrow 2OH \\ (IV) & H_2 + 2OH \Leftrightarrow 2H_2O \end{array}\right. \tag{8.14}$$

For propane/hydrogen/air mixtures, reactions (I) and (II) are replaced respectively by:

$$\left\{\begin{array}{ll} (I') & C_3H_8 + 7/2O_2 \Rightarrow 3CO + 4H_2O \\ (II') & CO + 1/2O_2 \Leftrightarrow CO_2 \end{array}\right. \tag{8.15}$$

These coefficients were fitted to retrieve laminar flame velocities U_l and thicknesses δ_l from 1D detailed kinetics flame calculations. The proposed scheme was validated on the GRI 3.0 mechanism (Smith et al. 2000) for methane-hydrogen blends, on the Delaware mechanism (Qin et al. 2000) for propane-hydrogen blends and on the Conaire scheme (Conaire et al. 2004) for pure hydrogen. Table 8.3 compares detailed schemes with the 4-steps scheme for the different conditions of Table 8.1. The flame thickness, δ_l, is here estimated from the temperature gradients between fresh and burnt gases $(T^b - T^u)/\max(dT/dx)$, where T^b is the burnt gases temperature. A very good agreement with the detailed scheme results is obtained for both U_l and δ_l and all considered fuels and equivalence ratii (the mean relative error is about 5% for both U_l and δ_l).

Complementary validations were performed comparing temperature and species profiles as presented in Figure 8.5 for methane-hydrogen mixtures and in Figure 8.6 for propane-hydrogen mixtures. The amplitudes of observed deviations are of the same order of magnitude for all fuels and most important differences are observed for the evolution of minor species (CO and OH). Moreover, it can finally be noticed that the temperature growth seems to be faster with the proposed scheme. Nevertheless, burnt gases temperatures are reasonably retrieved for all conditions as well as fuel consumption evolutions and equilibrium values of minor species like CO or OH.

8.2.4 Parameters characterizing flame/turbulence interactions

Following Meneveau and Poinsot, the effective flame stretch K is computed applying a correction function Γ to the theoretical strain defined as the ratio between the vortex velocity u'_r and its length scale r:

$$K = \frac{1}{A_T}\frac{dA_T}{dt} = \Gamma\left(\frac{r}{\delta_l}, \frac{u'_r}{U_l}\right)\frac{u'_r}{r} \tag{8.16}$$

As mentioned in introduction, many formulations for Γ were proposed in the past (Meneveau and Poinsot 1991, Colin et al. 2002, Charlette et al. 2002) and were derived from direct numerical simulations (DNS) of flame-vortex interactions for a wide range of vortex characteristics. In the early work of these authors (Meneveau and Poinsot 1991), the efficiency function depended only on the length scale ratio r/δ_r. Further developments were then performed to account for the

Reaction	Reaction Rate	Reaction rate constant		
		A	b	E
I	$k_I(T)\,[CH_4]^{0.65}\,[O_2]^{0.70}$	1.3 10^{11}	0	35000
II	$k_{II}(T)\,[CO]\cdot[O_2]^{0.5}\cdot[CO_2]^{-1}$	-2.0 10^{9}	0	12000
III	$k_{III}(T)\,[H_2]\cdot[O_2]\cdot[OH]^{-2}$	-5.3 10^{15}	0	30000
IV	$k_{IV}(T)\,[H_2]\cdot[OH]\cdot[H_2O]^{-2}$	-7.0 10^{21}	0	5000
I'	$k_{I'}(T)\,[C_3H_8]^{0.55}\,[CH_4]^{0.90}$	2.1 10^{12}	0	41500
II'	$k_{II'}(T)\,[CO]\cdot[O_2]^{0.5}\cdot[CO_2]^{-1}$	-4.5 10^{10}	0	20000

Table 8.2: Proposed reduced scheme (Eqs. 8.14,8.15) for CH_4-H_2 and C_3H_8-H_2 fuels premixed combustion. Reaction rates are expressed as $k_i = AT^b \exp(-E/RT)$. Units are mol, cm, s, K, cal.

	U_l **[m/s] detailed scheme**		U_l **[m/s] 4-steps scheme**		δ_l **[mm] detailed scheme**		δ_l **[mm] 4-steps scheme**	
	$\varphi = 0.7$	$\varphi = 1.0$	$\varphi = 0.7$	$\varphi = 1.0$	$\varphi = 0.7$	$\varphi = 1.0$	$\varphi = 0.7$	$\varphi = 1.0$
$\mathbf{CH_4}$	0.194	0.382	0.209	0.385	0.666	0.444	0.689	0.446
$\mathbf{CH_4}$-$\mathbf{H_2}$	0.268	0.53	0.266	0.502	0.535	0.371	0.53	0.379
$\mathbf{C_3H_8}$	0.206	0.418	0.214	0.40	0.585	0.382	0.579	0.375
$\mathbf{C_3H_8}$-$\mathbf{H_2}$	0.287	0.56	0.289	0.518	0.476	0.326	0.484	0.325
$\mathbf{C_3H_8}$-$\mathbf{H_2}$	0.543	1.14	0.578	1.028	0.359	0.262	0.345	0.276
$\mathbf{H_2}$	1.222	2.357	1.197	2.165	0.342	0.239	0.332	0.242
$\mathbf{H_2}, \varphi = 0.4$	0.142		0.138		0.848		0.835	

Table 8.3: Comparison between laminar flame velocities and thicknesses obtained from detailed chemistry and from the present 4-steps scheme. Detailed schemes used were: GRI 3.0 (Smith et al. 2000) for methane-hydrogen blends, Delaware (Qin et al. 2000) for propane-hydrogen blends and Conaire (Conaire et al. 2004) for pure hydrogen. Operating conditions: $T^u = 300$ K and $P = 0.1$ MPa. Values presented in this table were estimated with the AVBP code (Moureau et al. 2005).

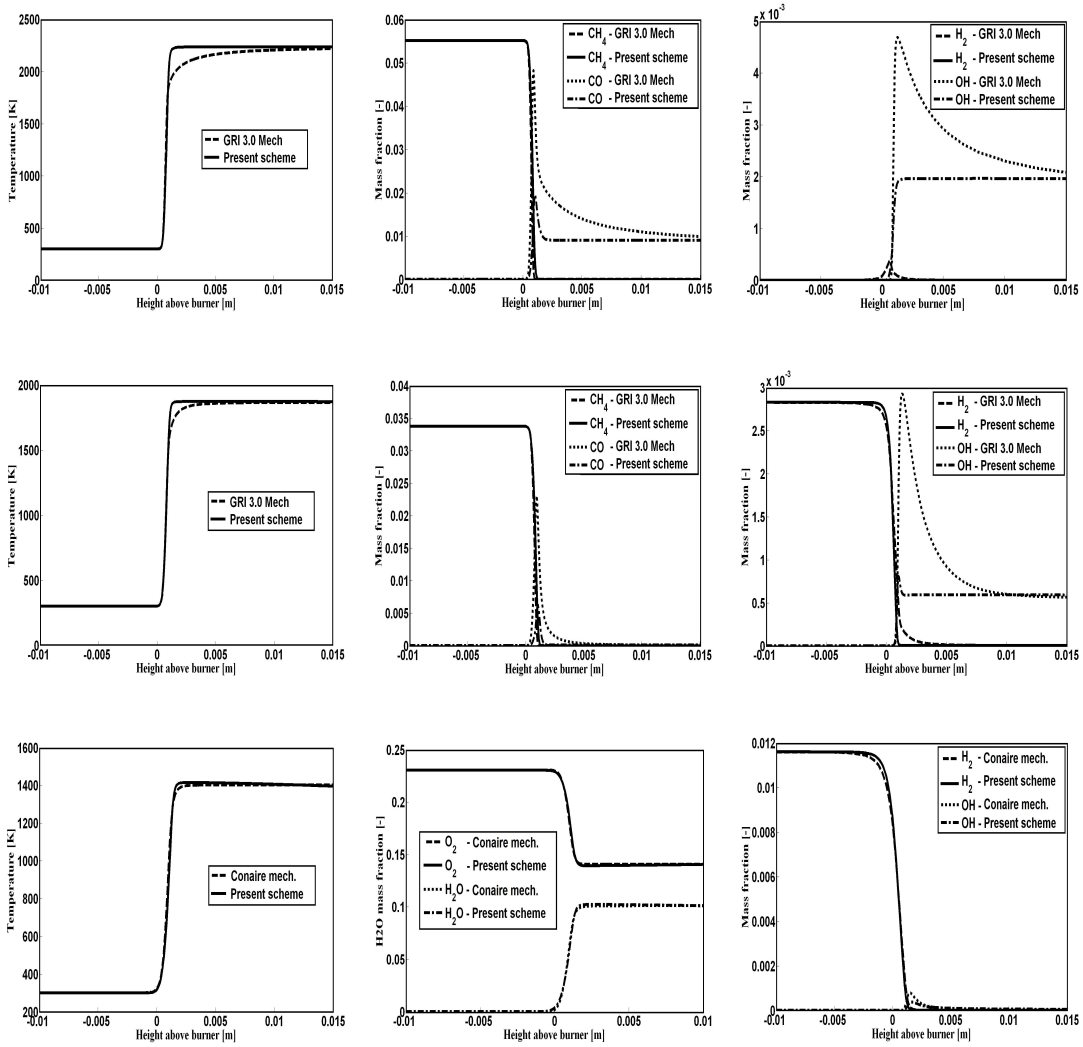

Figure 8.5: Temperature and species evolutions using the present scheme for methane-hydrogen mixtures: First raw: CH_4, $\varphi = 1.0$ - Second raw: CH_4-H_2 (60%-40% v/v), $\varphi = 0.7$ - Third raw: H_2, $\varphi = 0.4$

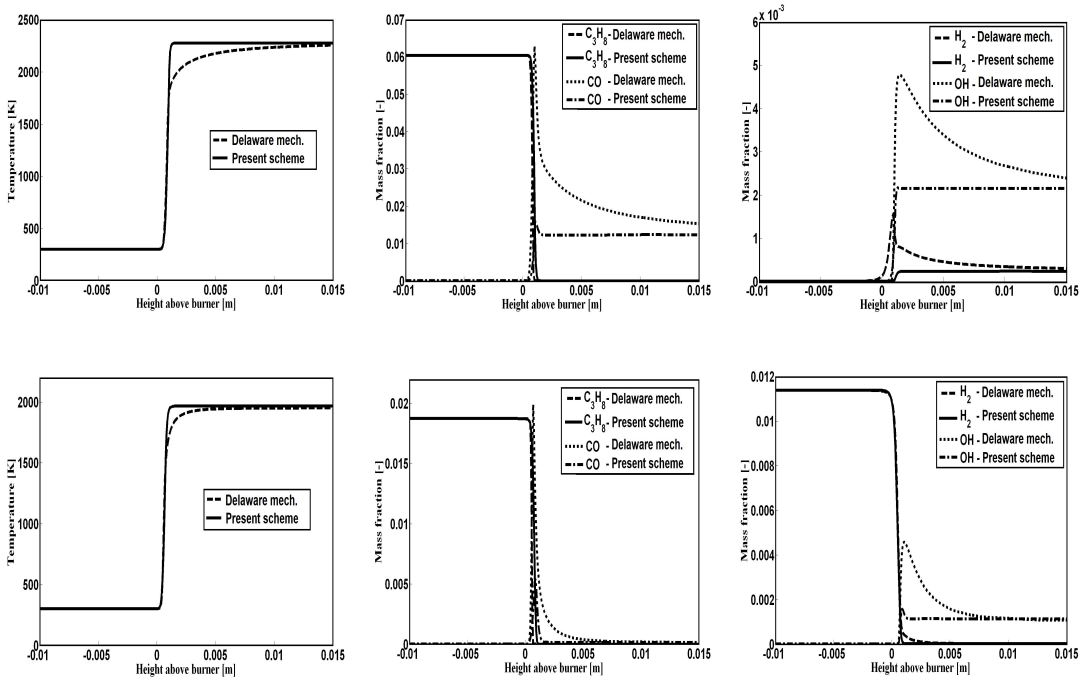

Figure 8.6: Temperature and species evolutions using the present scheme for propane-hydrogen mixtures , First raw: C_3H_8, $\varphi = 1.0$ - Second raw: C_3H_8-H_2 (7%-93% v/v), $\varphi = 0.7$.

velocity ratio u'_r/U_l (Colin et al. 2002, Charlette et al. 2002). However, these two ratios may not be sufficient to fully characterize flame/vortex interactions. Moreover, the question might be asked whether if the classical input parameter δ_l is appropriate to describe the combustion chemistry and if a reaction thickness δ_r for example would not be more suitable. In fact, it can be shown that the flame/vortex interaction is expected to be also governed by the length scale ratio δ_l/δ_r. Indeed, starting from the progress variable c balance equation for a steady one-dimensional premixed flame:

$$\rho_u U_l \frac{\partial c}{\partial x} = \frac{\partial}{\partial x}\left(\rho D \frac{\partial c}{\partial x}\right) + \dot{\omega}_c \tag{8.17}$$

where D is the molecular diffusion coefficient, ρ the gas density, and $\dot{\omega}_c$ the progress variable reaction rate,

and using the transformation of Howarth-Dorodnitzyn (Williams 1985, Poinsot and Veynante 2001):

$$x^+ = \int_0^x \frac{\rho_u U_l}{\rho D} dx \quad ; \quad dx^+ = \frac{\rho_u U_l}{\rho D} dx \tag{8.18}$$

it comes:

$$\frac{\partial c}{\partial x^+} = \frac{\partial^2 c}{\partial {x^+}^2} + \dot{\omega}_c^+ \tag{8.19}$$

where

$$\dot{\omega}_c^+ = \frac{\rho D}{(\rho U_l)^2} \dot{\omega}_c^+ \tag{8.20}$$

is a reduced reaction rate (Ribert et al. 2006). A reaction zone thickness δ_r may be introduced and defined as:

$$\delta_r = \frac{1}{\dot{\omega}_c^{max}} \int_{-\infty}^{+\infty} \dot{\omega}_c dx \tag{8.21}$$

where $\dot{\omega}_c^{max}$ denotes the maximal value of the reaction rate $\dot{\omega}_c$ across the flame front. In the particular case of a Gaussian evolution :

$$\dot{\omega}_c = \dot{\omega}_c^{max} \exp\left(-\left(\frac{x}{\delta}\right)^2\right) \tag{8.22}$$

with δ the Gaussian thickness. Equation 8.21 then gives :

$$\delta_r = \int_{-\infty}^{+\infty} \exp\left(-\left(\frac{x}{\delta}\right)^2\right) dx \tag{8.23}$$

$$= 2\delta \int_{0}^{+\infty} \exp\left(-\left(\frac{x'}{\delta}\right)^2\right) dx' = \delta\sqrt{\pi} \tag{8.24}$$

while the half-weight thickness of the heat release is :

$$\delta_{1/2} = 2\delta\sqrt{\ln(2)} \tag{8.25}$$

This finally leads to :

$$\delta_r = \frac{\sqrt{\pi}}{2\sqrt{\ln(2)}} \approx \delta_{1/2} \tag{8.26}$$

showing that Eq. 8.21 provides a relevant definition of the reaction zone thickness.

Under the assumption that $\rho D = \rho_0 D_0$ is constant (D_0 and ρ_0 are respectively the fresh gases molecular diffusion coefficient and density) and defining a diffusive flame thickness as $\delta_l = D_0/U_l$ (corresponding to $Re_f = U_l\delta_l/D_0 = 1$, with Re_f the flame Reynolds number), the reduced reaction rate $\dot{\omega}_c^+$ (Eq. 8.20) may be rewritten as:

$$\dot{\omega}_c^+ = \frac{\rho D}{(\rho U_l)^2}\dot{\omega}_c^+ = \frac{D_0}{U_l}\frac{\omega_c^{\dot{m}ax}}{\rho_u U_l}\frac{\dot{\omega}_c}{\omega_c^{\dot{m}ax}} = \frac{\delta_l}{\delta_r}\frac{\dot{\omega}_c}{\omega_c^{\dot{m}ax}} \tag{8.27}$$

Equation 8.19 can then be rewritten:

$$\frac{\partial c}{\partial x^+} = \frac{\partial^2 c}{\partial {x^+}^2} + \frac{\delta_l}{\delta_r}\frac{\dot{\omega}_c}{\omega_c^{\dot{m}ax}} \tag{8.28}$$

Note that the occurrence of the length scale ratio δ_l/δ_r may be explained roughly as follows: spatial coordinates are made non-dimensional using the diffuse flame thickness δ_l while the reaction zone thickness δ_r is more relevant for the reaction rate.

To conclude, by keeping constant the flame characteristics (U_l, δ_l and δ_r), the reaction rate ${\dot{\omega}_c}^+$ is therefore also kept constant. According to Eq. 8.28 and the subsequent derivations of previous equations (Eqs. 8.17-8.28), the flame/vortices interaction is expected to be governed by:

- the length scale ratio r/δ_l
- the velocity ratio u'_r/U_l
- the reduced reaction rate $\dot{\omega_c^+}$, or the length scale ratio δ_l/δ_r.

	δ_l [mm]		δ_r [mm]		ratio δ_l/δ_r [-]	
	$\varphi = 0,7$	$\varphi = 1$	$\varphi = 0,7$	$\varphi = 1$	$\varphi = 0,7$	$\varphi = 1$
CH_4	0.689	0.446	0.307	0.221	2.24	2.09
$CH_4 - H_2$	0.53	0.379	0.30	0.23	1.77	1.63
C_3H_8	0.579	0.375	0.294	0.218	1.95	1.71
$C_3H_8 - H_2$	0.484	0.325	0.279	0.195	1.73	1.67
$C_3H_8 - H_2$	0.345	0.276	0.204	0.171	1.69	1.61
H_2	0.332	0.242	0.2	0.16	1.65	1.51
H_2 $\varphi = 0,4$	0,835		0,377		2,23	

Table 8.4: Ratii (δ_l/δ_r) of flame studied in this work.

In their DNS, previous authors (Meneveau and Poinsot 1991, Colin et al. 2002, Charlette et al. 2002) varied the vortex characteristics (size r and velocity $u'(r)$) keeping constant the flame characteristics U_l, δ_l and therefore δ_r too. Thus, using δ_r instead of δ_l in the corresponding functions is not expected to change their behavior since the ratio δ_l/δ_r was also kept constant. However, in the case of fuel formulation variations, this ratio can evolve and these functions could not be appropriate any more. In the case of present developments, this ratio indeed changes from one flame to another one as presented in Table 8.4. Values of δ_l and δ_r were obtained respectively from the temperature gradients between fresh and burnt gases, $(T^b - T^u)/\max(dT/dx)$, and from the definition of Eq. 8.26 measuring the half-weight thickness of the total heat release. As shown, δ_l/δ_r ratii associated to the flames considered in this work (see Table 8.1) exhibit close values ($1.5 < \delta_l/\delta_r < 2.2$). Thus, the differences observed in Table 8.4 were finally assumed to be negligible. As a result, only the ratii u'_r/U_l and r/δ_l are accounted for in this work.

8.2.5 Simulations of flame-vortex interaction

This section describes the estimation of the flame stretch and investigates how flame-turbulence interactions are affected by the mixture composition.

Principle

The same approach used in previous studies (Meneveau and Poinsot 1991, Colin et al. 2002, Charlette et al. 2002) is followed in this work: as shown in Figure 8.7, the flame stretch $1/A_T dA_T/dt$ is approximated by $\frac{1}{Q}dQ/dt$ where Q is the total reaction rate. It should be noticed that the local flame speed is assumed to not change under the effect of stretch which can be strongly wrong especially when non-unity Lewis number ($Le << 1$ or $Le >> 1$) mixtures are burnt. These last assumption can therefore lead to significant errors in the evaluation of the stretched flame surface. Nevertheless, the approach developed here is coherent with almost CFD codes where the heat released by combustion is usually written as the product between the unstretched laminar flame speed U_l and the turbulent flame surface A_T defined for example as $A_T = \int_\Omega \Sigma dV$ (Richard et al. 2007) (where Σ is the flame surface density and Ω the considered integration volume). Following this procedure, the effect of flame stretch of the local flame velocity are directly integrated in the efficiency function Γ. Finally, the heat release ($dQ/dt \approx U_l A_T$) can be accurately computed even if local flame speed and surface are not well estimated. Moreover, the present approach allows to account for heat and species differential diffusion effects by directly integrating these latter in the stretch efficiency function Γ (Eq. 8.16). Contrary to previous works (Meneveau and Poinsot 1991, Colin et al. 2002, Charlette et al. 2002), Γ is therefore not only a function describing turbulence effects on the flame stretch any more but represents the combination of both turbulence and Lewis number effects on the reaction rate.

As presented by Meneveau and Poinsot (Meneveau and Poinsot 1991), the evolution of Q can be described by three phases. The first one corresponds to the induction phase where vortices

move and enter in the influence area of the flame. These vortices start stretching the flame in the second phase and the reaction rate grows exponentially ($K = constant$). The third phase is characterized by an interaction between the flame fronts leading to flame surface destruction due to mutual annihilation[1]. This last phase will not be discussed in this work. In practice the stretch K is deduced by estimating the maximum slope of the curve $(1/Q \cdot dQ/dt)_{max}$ in the second phase.

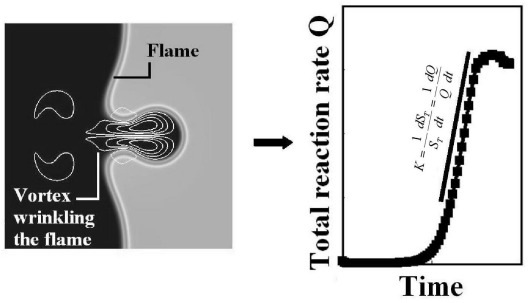

Figure 8.7: Approach used to estimate the flame stretch

An efficiency function Γ can then be deduced from Eq. 8.16 analyzing the two first phases of the interaction. Several expressions for Γ were previously proposed, especially by the functions of Meneveau and Poinsot (1991), Γ_{MP}, Colin et al. (2002), Γ_{CDVP}, and Charlette et al. (2002), Γ_{CMV}:

$$\Gamma_{MP} = 10^{-\frac{0.545}{(\log 10(r/\delta_l) + 0.364)}} \tag{8.29}$$

$$\Gamma_{CDVP} = 1/2 \left(1 + erf\left(0.6 \log\left(\frac{r}{\delta_l}\right) - 0.6 \Big/ \sqrt{\frac{u'_r}{U_l}}\right)\right) \tag{8.30}$$

$$\Gamma_{CMV} = \Gamma_{CDVP} \cdot \frac{1}{2}\left(1 + erf\left(3 \log\left(2\frac{u'_r}{U_l}\right)\right)\right) \tag{8.31}$$

All these functions were built using a single step chemistry and a fixed Lewis number ($Le = 1.2$), therefore neglecting mixture composition effects. The aim of this study being to investigate the fuel composition impact on the flame stretch and efficiency function formulation, different flames are here considered, corresponding to different fuels including methane, propane, hydrogen and blends at different equivalence ratii and Lewis numbers.

DNS set-up

The new 4-steps scheme was implemented in the AVBP code (Moureau et al. 2005) and was firstly used to simulate 2D steady planar laminar flames in a square domain as shown in Figure 8.8, to generate initial conditions for the DNS. The size $L_x \times L_x/2$ of this domain is defined as function of the laminar flame thickness δ_l and size r of the pair of counter-rotating vortices (as shown in

[1] Actually, during a simulation, after the vortex transit, the flame comes back to its initial position without necessarily any interaction between neighbor fronts. If it occurs, annihilation leads to the creation of fresh gases pockets.

Table 8.5 $L_x = 6 \cdot r = 6 \cdot r_L \cdot \delta_l$ where $r_L = r/\delta_l$ is a an input of the problem as well as the velocity ratio $r_V = u'_r/U_l$). These vortices defined through the stream function Ψ (Eq. 8.32) are then convected until interaction with the flame.

$$\Psi(x,y) = \Theta \exp - \frac{(x-x_c)^2 + (y-y_c)^2}{2r^2} \tag{8.32}$$

where Θ represents the vortex strength and $(x-x_c)^2 + (y-y_c)^2$ the distance to the vortex center. In practice, $x_c = L_x/4$ (the flame is centered in the domain) and $y_c = \pm r/2$. The velocity flow field is initialized using as input r and the characteristic turbulent velocity u'_r corresponding here to the maximum velocity induced by the vortex defined as $u'_r = \Theta/(r \cdot \sqrt{e})$. Following Meneveau and Poinsot (Meneveau and Poinsot 1991), each turbulence configuration is defined by one length scale ratio $r_L = r/\delta_l$ and one velocity ratio $r_V = u'_r/U_l$, which correspond to the main parameters of the problem when chemistry is fixed. Each flame of Table 8.3 is therefore defined by its own velocity fluctuation and length scale and finally by its own maximal stretch K as defined in Eq. 8.16. Two values of r_L and r_V are considered leading to four cases for each flame of Table 8.1. A total of 48 flame/vortex interactions have been computed. Four additional cases are used to allow a more detailed evaluation of existing efficiency functions at intermediate length scale ratii. Numerical parameters are summarized in Table 8.5.

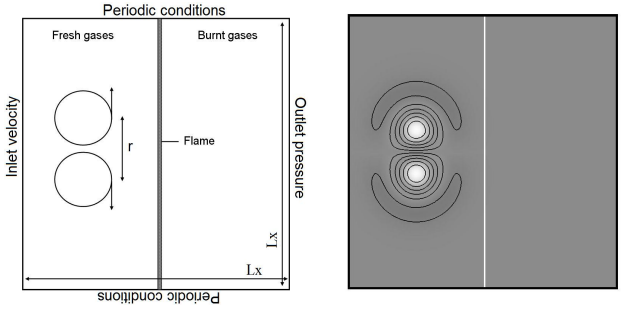

Figure 8.8: DNS configuration of flame-vortex interactions. A pair of counter-rotating vortices (size r) interacts with an initially planar premixed flame. a) Schematic configuration - b) Visualization of initial vorticity and flame temperature fields.

Considering the symmetrical nature of the problem, all simulations were performed considering only half of the computational domain which allowed to significantly reduced the computational time. Figure 8.9 displays a snapshot comparison between two computations considering on the one hand the whole domain (Figure 8.9.a) and on the other hand an half of the domain (Figure 8.9.b). The flame temperature and vorticity fields remain the same which finally leads to identical total reaction rate evolutions (Figure 8.9.c).

Results and analysis

Four DNS visualizations at different length scale and velocity ratii for a methane flame at $\varphi = 1$ are displayed in Figure 8.10 to illustrate the effect of the vortex size and velocity on the flame. Vorticity and reaction rate fields are superposed at different instants of the flame-vortex interaction corresponding to cases (Ak12, $k = 1-4$). As already observed by Colin et al. (2002), the flame is mainly stretched at high velocity ratii r_V. This is confirmed by Figure 8.11 where the temporal evolutions of the total reaction rates Q are plotted for two equivalence ratii ($\phi = 0.7$ and 1.0) showing that the slopes are higher at high r_V values. Times are reduced using the flame time $t^+ = t \cdot U_l/\delta_l$ and reaction rates are normalized as well, giving a direct image of the effective

CASE	$\boldsymbol{L_x}$ **/** $\boldsymbol{r}$	$r_L = r/\delta_l$	$r_V = u'_r/U_l$	$\boldsymbol{N_x}$
A1ij	6	30	0.8	1786
A2ij	6	5	0.8	300
A3ij	6	5	8.0	300
A4ij	6	30	8.0	1786
B1	6	15	0.8	894
B2	6	3	8.0	180
B3	6	3	8.0	180
B4	6	15	0.8	894

Table 8.5: DNS set-up of flame-vortex interactions. For each fuel i = (1,2,3,4,5,6) = (CH_4 / CH_4 -H_2 (40/60%) / C_3H_8 / C_3H_8 -H_2(35/65%) / C_3H_8 -H_2(07/93%) / H_2) and both equivalence ratio j = (1,2) = ($\varphi = 0.7, \varphi = 1.0$). In the H_2 combustion cases, $j = (\varphi = 0.7, \varphi = 0.4)$. Operating conditions: $T^u = 300K$ and $P = 0.1$ MPa. Complementary cases B_k ($k = 1, 4$) are also performed and only concern methane flame at $\varphi = 1.0$. Considering the symmetrical nature of the problem, all simulations were performed considering only half of the computational domain which is sized as $L_x \times L_x/2$. The grid mesh contains $N_x \times N_x/2$ points.

stretch (Eq. 8.16). A first result is that the equivalence ratio has an effect on the reduced reaction rate leading to different values of $(1/Q \cdot dQ/dt^+)_{max}$) and therefore of the efficiency function Γ. Table 8.6 gives theoretical strains $K_{ref} = u'_r/r$ and efficiency relative differences between the two equivalence ratii for the different cases of Figure 8.11. Highest discrepancies are observed at low velocity ratii, which correspond to relatively low stretches. Considering that associated vortices have a limited contribution to the total flame stretch in a turbulent flow, this effect could be neglected at first order. In other terms, the laminar flame characteristics (U_l and δ_l) could be enough to describe the chemical effect of equivalence ratio on the flame stretch using current efficiency functions presented in Eqs. 8.29, 8.30 and 8.31.

	$\varphi = 0.7$			$\varphi = 1.0$			
	K_{ref} [s^{-1}]	K_{dns} [s^{-1}]	Γ [-]	K_{ref} [s^{-1}]	K_{dns} [s^{-1}]	Γ [-]	ε [%]
$r_V = 0.8$; $r_L = 5$	48.5	13.192	0.272	138.1	47.3683	0.343	26.1
$r_V = 0.8$; $r_L = 30$	8.1	7.9704	0.984	23	27.807	1.209	22.8
$r_V = 8.0$; $r_L = 5$	485	99.425	0.205	1381	303.82	0.22	7.1
$r_V = 8.0$; $r_L = 30$	81	24.543	0.303	230	74.06	0.322	6.3

Table 8.6: Theoretical strain $K_{ref} = u'_r/r$, strain K_{dns} obtained from DNS, corresponding value of Γ and efficiency Γ relative difference $\varepsilon = abs\left(1 - \frac{\Gamma(i)}{\Gamma(j)}\right)$ between cases $i(\varphi = 0.7)$ and $j(\varphi = 1.0)$ for methane.

An other effect of mixture composition is observed when varying the nature of the fuel at constant equivalence ratio (0.7) as shown in Figure 8.12, where snapshots of DNS are compared at the same flame time for given velocity and length scale ratii. An impact on the flame wrinkling is clearly observed and is more significant when introducing hydrogen in the fuel as displayed for example in Figure 8.12 (a,c,f), which shows that methane and propane flames are less affected than pure hydrogen flames. These last observations could be linked to heat and species differential diffusion phenomena depending on the mixture composition and which can lead to the occurrence of thermo-diffusive instabilities. These latter may generate an additional flame wrinkling. In other words, with regards to Figure 8.12, the flame wrinkling could be related to the fuel mixture Lewis number. Methane and propane flames corresponding to $Le \geq 1$ are thus more resistant to the turbulent flow than hydrogen flames corresponding to $Le \approx 0.4$ (Figure 8.4). Actually, turbulence and thermo-diffusive instabilities are independent phenomena and it is not obvious

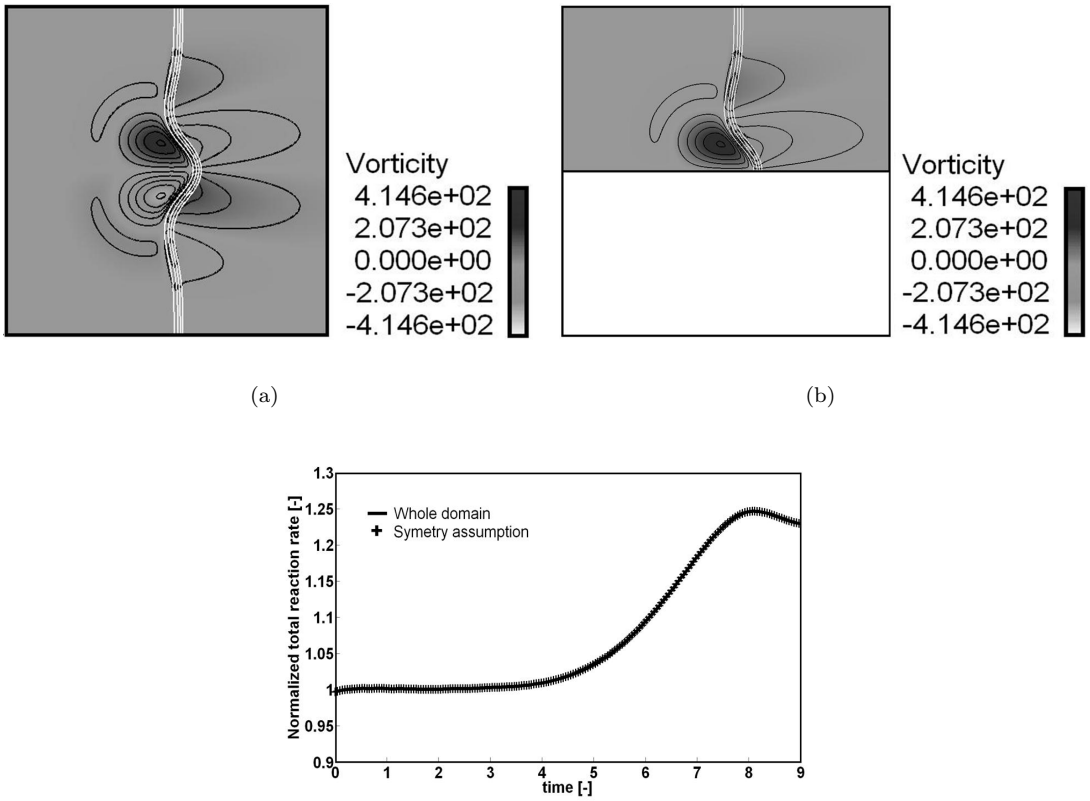

Figure 8.9: Snapshot comparison between two direct numerical simulations of flame-vortex interactions considering on the one hand the whole domain (a) and on the other hand an half of the domain (b). Both computations lead to the same flame temperature and vorticity fields shapes (a,b) and total reaction rate evolution (c).

in fact to distinguish the wrinkling due to turbulence processes to thermo-diffusive phenomena. Paul and Bray (Paul and Bray 1996) for example dissociated both aspects in their stretch model. Nevertheless, in the present work the choice has been done to directly integrate thermo-diffusive effects in the turbulence term through Γ. As a result, the question was therefore to understand if the effect of the flame chemistry can be described solely by the laminar flame velocity and thickness in the definition of the efficiency function Γ or if a new function is required to account for heat and species differential diffusion effects through the fuel Lewis number Le.

Figure 8.13 displays the evolution of Γ as a function of r_L for both values of r_V and for all fuels at $\varphi = 0.7$. As already observed by Meneveau and Poinsot (Meneveau and Poinsot 1991) for a single chemistry, the efficiency decreases with decreasing values of the length scale ratio r/δ_l and for mixtures with $Le \geq 1$, the maximum value of Γ is around unity. However, for other mixtures, this value can be higher than unity and can reach $\Gamma_{max} \approx 2$ for pure hydrogen flames. Previous observations on the effect of the effective Lewis number on the flame wrinkling (Figure 8.12) are thus recovered for the efficiency. On the contrary, the impact of fuel composition on the stretch efficiency at constant Lewis number (fuels 1 and 4) is not significant (Figure 8.13). All these results comfort the assumption that the efficiency dependency to the mixture composition is mainly driven by its effective Lewis number. Following these statements, a new function for the flame stretch by a pair of vortices is proposed in the following accounting for length scale and

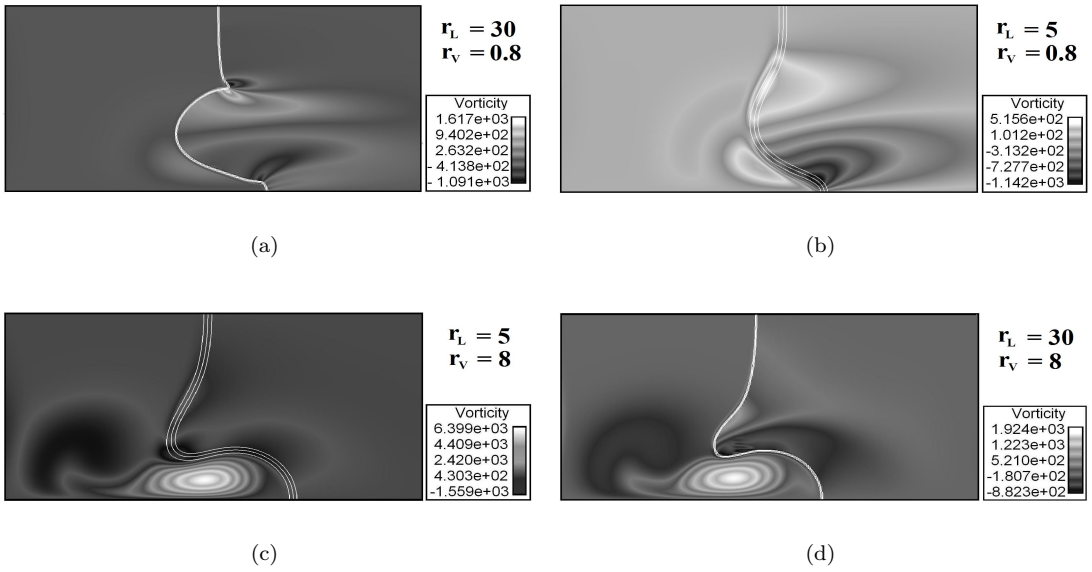

Figure 8.10: Snapshots of direct numerical simulations of flame-vortex interactions for methane and $\varphi = 1.0$. Reaction rate and vorticity fields are superimposed for different flame times $t^+ = t \cdot U_l/\delta_l$. (a) Case A112, $t^+ = 28$ – (b) Case A212, $t^+ = 6$ – (c) Case A312, $t^+ = 2$ – (d) Case A412, $t^+ = 9$. Results are shown for a half domain. (Vorticity fields are given in rad.s-1).

velocity ratii, as well as fuel Lewis dependencies.

8.2.6 New efficiency function formulation

The efficiency function proposed in this work is inspired from previous attempts (Eqs. 8.29–8.31) and writes for a unity Lewis number mixture:

$$\Gamma = \frac{1 + \Gamma_r\left(r/\delta_l\right)}{1 + 0.3 \cdot \left(u'_r/U_l\right)\Gamma_r\left(r/\delta_l\right)} \tag{8.33}$$

with

$$\Gamma_r = 1 + erf\left(0.9 \cdot \ln\left(r/\delta_l\right) - 2\right) \tag{8.34}$$

The function Γ_r corresponds to an asymptotic efficiency function when u'_r tends toward zero and therefore only depends on r_L. The final function Γ in Eq. 8.33 introduces a correction factor to the velocity ratio r_V. Figure 8.14 compares this new function with the expressions of Meneveau and Poinsot (1991), Colin et al. (2002) and Charlette et al. (2002) and with the new DNS results. As expected Meneveau and Poinsot function does not depend on the velocity ratio and therefore does not fit present DNS. It is then evidenced that Colin et al. function only considers the effect of the velocity ratio at low length scale ratii, then leading to significant errors in the large length scale ratii region when r_V increases. Charlette et al. added a new term in the Colin et al. function (Eq. 8.31) to account for this last effect. Nevertheless their function exhibits also important differences compared to present results. On the contrary, the formulation of Eq. 8.33 shows a very good agreement with the DNS, even if it does not allow to describe the trend observed at low length scale ratii ($r/\delta_l < 4$), characterized by an efficiency increase with the velocity ratio. This phenomenon was also observed by Colin et al. (2002), but as it corresponds to low stretch values it may not be of importance in the total turbulent stretch evaluation.

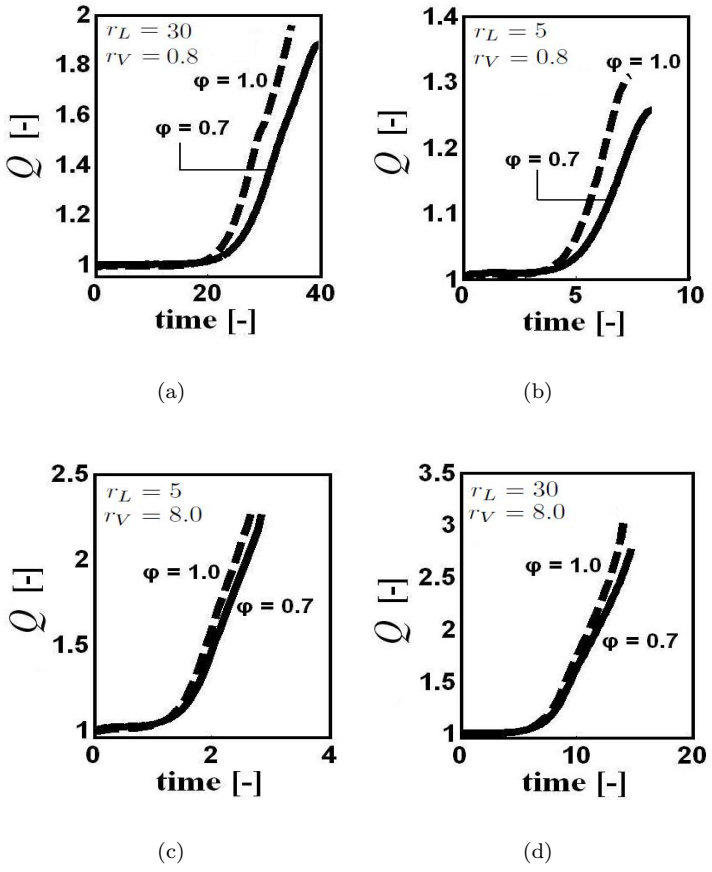

Figure 8.11: Total reaction rate versus time during flame-vortex interaction for methane and for both equivalence ratii $\varphi = 0.7$ and $\varphi = 1.0$. (a) Case A11k – (b) Case A21k – (c) Case A31k – (d) Case A41k (k=1,2). Reaction rate values Q are made non-dimensional using the corresponding planar laminar flame quantities $Q(t = 0)$. Times are reduced using the flame time $t^+ = t \cdot U_l/\delta_l$.

Finally, assuming that fuel composition effects are mainly related to the mixture effective Lewis number, a correction of the efficiency function is proposed here, retaining a formulation similar to experimental correlations proposed for turbulent flame velocities (Gülder et al. 2000, Chen and Bilger 2002, Filatyev et al. 2005, Kobayashi et al. 2005, Wu et al. 1990, Driscoll and Gulati 1988, Cheng 1995, Cho et al. 1986, Lawn and Schefer 2006, Smith and Gouldin 1979, Bradley et al. 2003, Kido et al. 2002, Shepherd and Cheng 2001, Bradley et al. 1992, Kobayashi et al. 1997, Ziegler 1998):

$$\Gamma(Le) = \Gamma(Le = 1) \cdot \left(\frac{1}{Le} \cdot (1.76 + \tanh(Le - 2)) \right) \tag{8.35}$$

This correction is written as function of Le^{-1}, but is multiplied by a second term to straighten the efficiency for $Le > 1$ as observed in Figure 8.15, which compares this new function with a function only considering a correction by Le^{-1} ($f = \Gamma(Le = 1) \cdot 1/Le$) and DNS results.

The final efficiency function is then:

$$\Gamma = \frac{1 + erf(0.9 \cdot \ln(r/\delta_l) - 2)}{1 + 0.3 \cdot (u'_r/U_l) \cdot (1 + erf(0.9 \cdot \ln(r/\delta_l) - 2))} \bullet \left(\frac{1}{Le} \cdot (1.76 + \tanh(Le - 2)) \right) \tag{8.36}$$

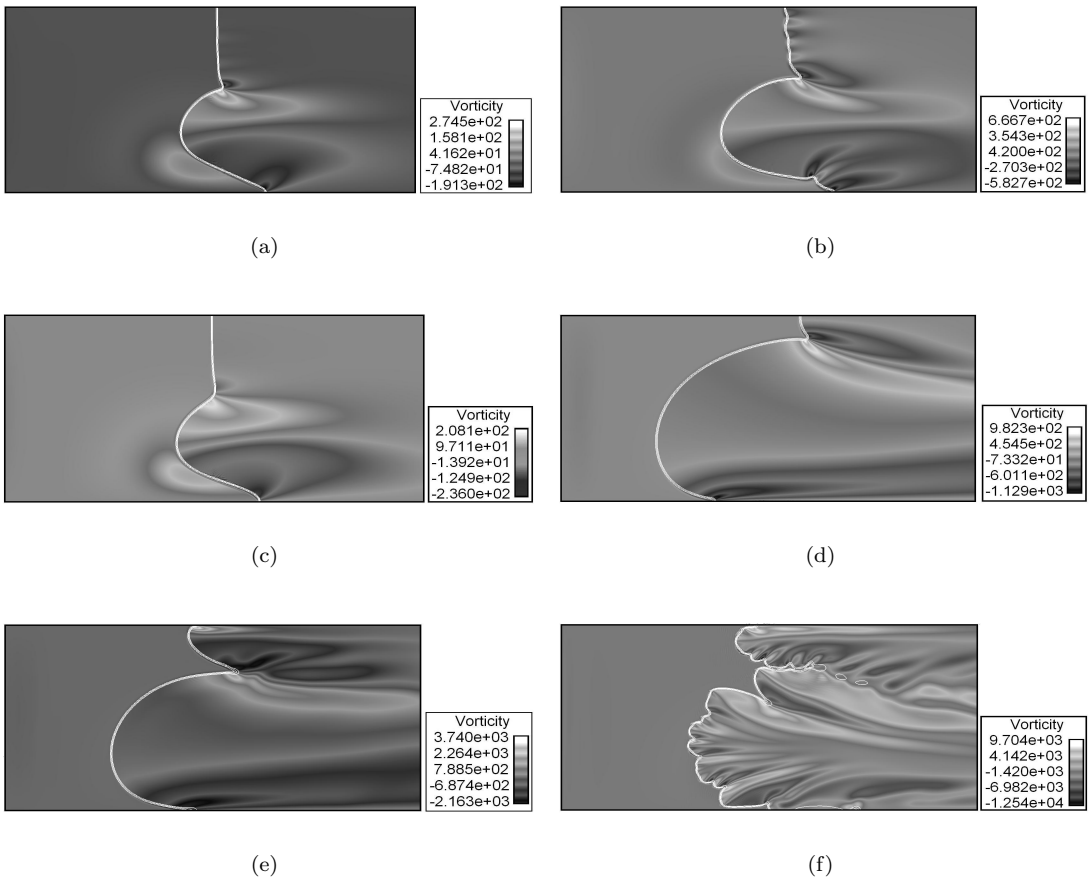

Figure 8.12: Snapshots of direct numerical simulations of flame-vortex interactions for different fuels and $\varphi = 0.7$. Reaction rate and vorticity fields are superposed for the same flame times $t^+ = t \cdot U_l/\delta_l = 30$. $r_L = 30$ and $r_V = 0.8$. (a) Case A111 (methane) – (b) Case A121 (methane-hydrogen) – (c) Case A131 (propane) – (d) Case A141 (propane hydrogen) – (e) Case A151 (propane hydrogen) – (f) Case A161 (hydrogen). Results are shown for a half domain. (Vorticity fields are given in rad.s-1).

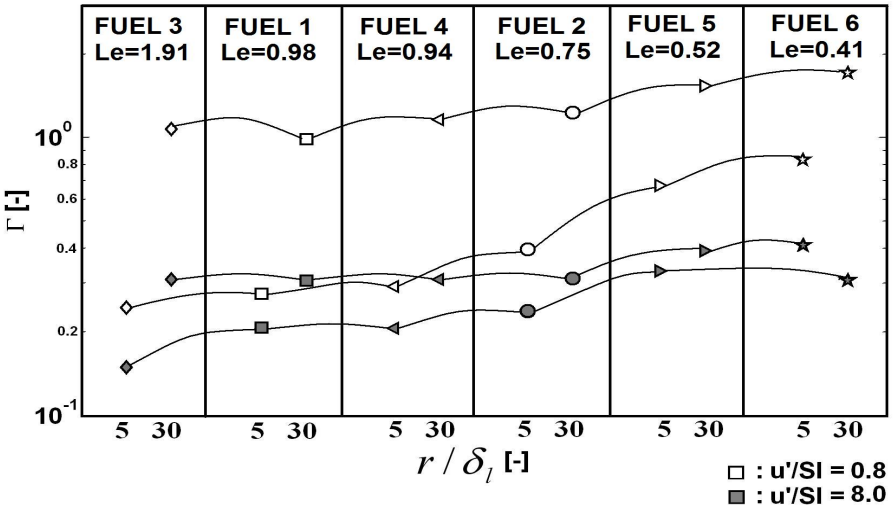

Figure 8.13: Evolution of the stretch efficiency function Γ deduced from DNS as function of the length scale ratio r/δ_l for different fuels at $\varphi = 0.7$ and for two values of r_V.

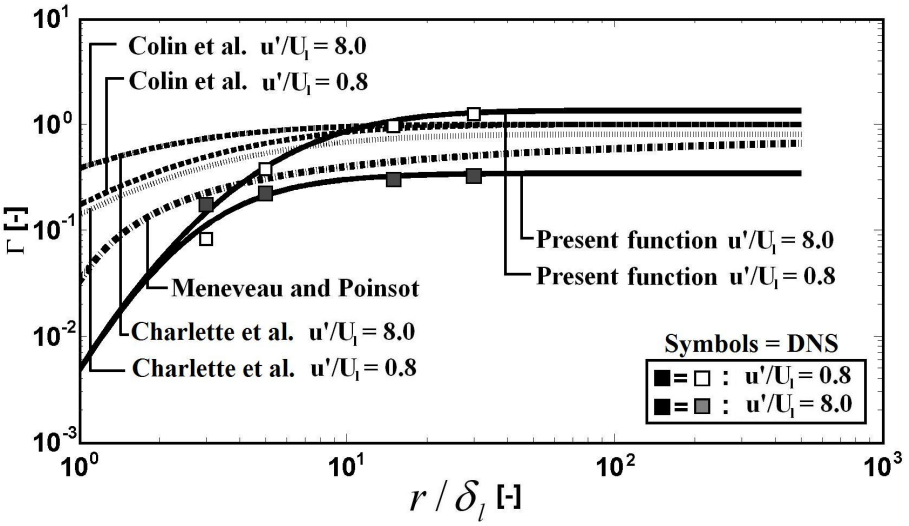

Figure 8.14: Comparison of the efficiency factor Γ deduced from DNS (cases Ak12 and Bk, $k = 1 - 4$, corresponding to methane fuel at $\varphi = 1$) with three common functions (Meneveau and Poinsot (1991), Colin et al. (2002) and Charlette et al. (2002)) and the present proposition (Eq. 8.33).

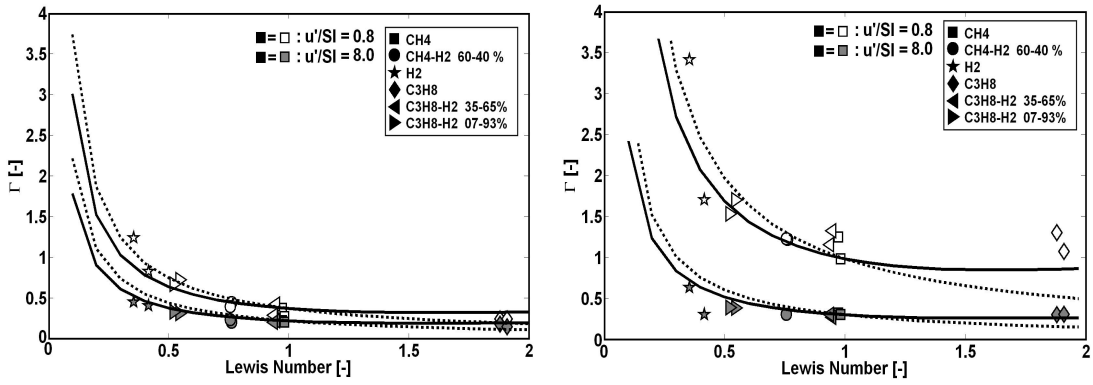

(a) (b)

Figure 8.15: Stretch efficiency as a function of the Lewis number at several equivalence ratii. (a) $r/\delta_l = 5$; (b) $r/\delta_l = 30$. The corrected function of Eq. 8.35 (Solid line) is compared with the expression ($f = \Gamma(Le = 1) \cdot 1/Le$) (Dashed line).

A comparison between DNS data and different efficiency formulations over the 52 simulated cases of Table 8.5 is displayed in Figure 8.16. The proposed correlation fits very well present DNS and clearly improves results compared to previous functions. Table 8.7 confirms this global observation showing that this new function reduces by a factor 2.5 the error induced by the function of Meneveau and Poinsot and by 7.5 the error induced by the function of Colin et al. or Charlette et al.. As already mentioned, errors exhibited by the three previous functions can be mainly explained by the use of a single-step chemistry which is not able to reproduce fuel composition effects. Moreover, these function consider as inputs describing the flame only the laminar flame velocity and thickness while the present function integrates a Lewis number. Note that Lewis number effects could be incorporated in common efficiency functions by multiplying these functions by the Lewis number term defined in Eq. 8.36. Potential improvements were not estimated in this work. Finally, it should by noticed that DNS and functions of previous authors were calibrated considering the diffusion thickness $\delta_l = D_u/U_l$ which may be different from the present laminar flame thickness defined from the maximum gradient between fresh and burnt gases $(T^{eq} - T^u)/\max(dT/dx)$. Differences between both definitions could here also explain a part of the errors presented in Table 8.7.

Stretch efficiency functions	**Relative Error [%]** $\varepsilon = \frac{\sqrt{\sum \lvert K_{DNS} - K_\Gamma \rvert^2}}{\sum K_{DNS}}$
Meneveau and Poinsot (1991)	9.2
Colin et al. (2002)	47.3
Charlette et al. (2002)	47.4
Present function	5.2

Table 8.7: Mean error on the effective flame stretch for all the 52 cases of Table 8.5. $K_{DNS} = (1/QdQ/dt)_{max}$ is the stretch deduced from present DNS and $K_\Gamma = \Gamma u'_r/r$ the stretch computed using the considered efficiency function.

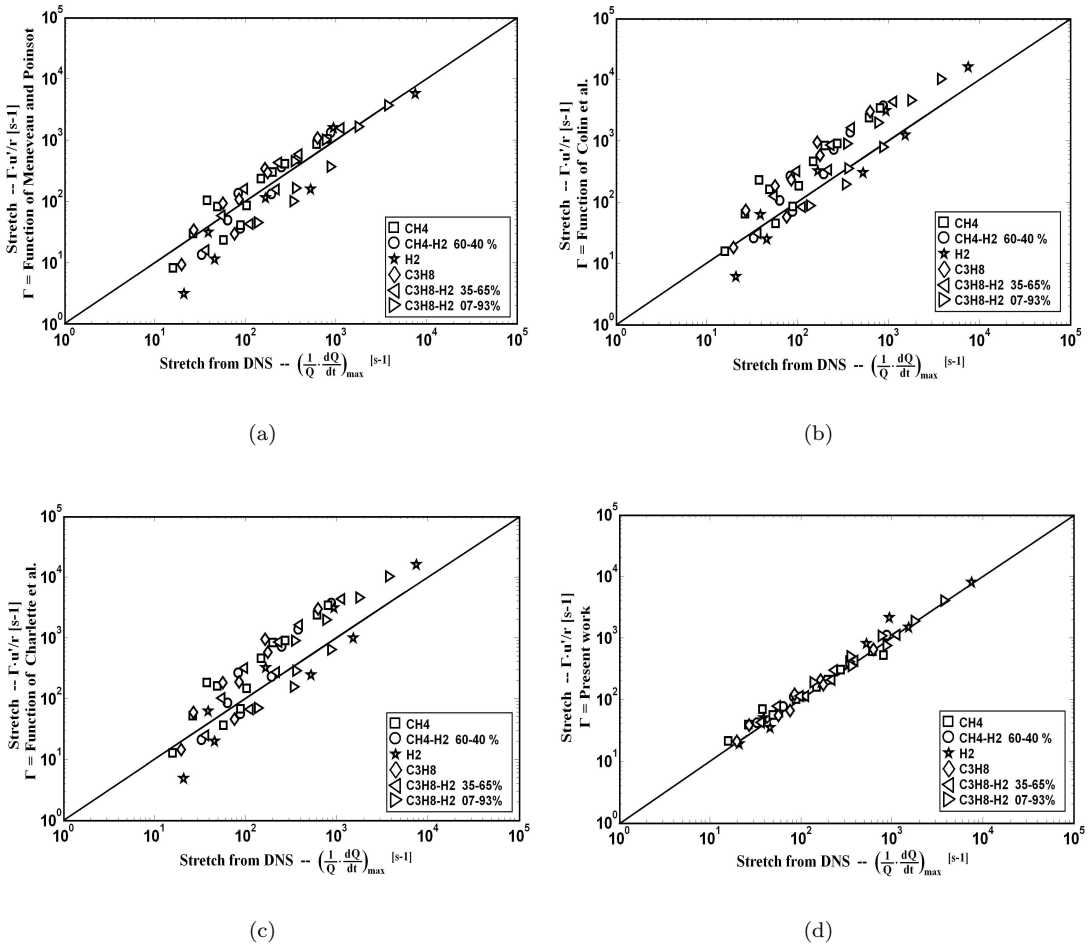

Figure 8.16: Errors on the effective flame stretch for the 52 cases of Table 8.5. Comparison between effective stretches from DNS and from several Γ functions: (a)-Meneveau and Poinsot (1991) function ; (b) Colin et al. (2002) function ; (c) Charlette et al. (2002) function. ; (d) Present work (Eq. 8.36).

8.2.7 Conclusion

In most combustion models based on the flamelet assumption, the flame stretch induced by a single eddy of velocity u'_r and size r is generally linked to its strain defined by u'_r/r . However, as shown by Meneveau and Poinsot (Meneveau and Poinsot 1991), this relation is not always obvious and needs to be corrected in particular at small scales where the theoretical strain is high. Several works (Meneveau and Poinsot 1991, Colin et al. 2002, Charlette et al. 2002) introduce efficiency functions to limit this stretch were performed in the past. However, these studies based on direct numerical simulations (DNS) of flame-vortex interaction were carried out only for a single chemical configuration using a simple one-step chemistry with an Arrhenius law to describe combustion processes. The assumption was therefore made that all chemical effects, including equivalence ratio or fuel composition variations, are entirely accounted for through the laminar flame velocity and thickness. This last assumption can be restrictive in particular when low Lewis number mixtures are burnt. Indeed, thermo-diffusive instabilities may occur and the associated flame wrinkling can finally be different from the one predicted by current efficiency functions (in the case where these phenomena are expected to be described only by this function). In this work, DNS of flame-

vortex interaction are performed varying the nature of the fuel, the equivalence ratio and the Lewis number to study the effect of chemical composition on premixed flames wrinkling. Flame stretches are deduced from the DNS following the methodology proposed in previous works (Meneveau and Poinsot 1991, Colin et al. 2002, Charlette et al. 2002) and compared with phenomenological functions from the literature for a number of vortex characteristics. To account for chemical effects, DNS performed in this work integrate a description of chemistry processes through a new 4-steps kinetic scheme dedicated to the combustion of CH_4-H_2 and C_3H_8-H_2 blends and validated using detailed kinetic mechanisms. It results first from this work that existing efficiency functions do not take into account the strong influence of the velocity ratio at large length scales. As a consequence a new formulation inspired from previous attempts is proposed and shows a very good agreement with the DNS, even if it does not allow to describe the trend observed at low length scale ratii. However, these scales correspond to relatively low stretch values and may not be of importance in the total turbulent flow stretch evaluation. A second conclusion resulting from this work is that the fuel composition has a strong effect on the flame stretch in particular when varying the fuel Lewis number. Indeed, the sensitivity of the efficiency function to the equivalence ratio observed on DNS results is significant only at low velocity ratii corresponding to relatively low stretches which can be considered to have only a limited contribution to the total flame stretch in a turbulent flow. On the other hand, DNS show also that for a given Lewis number, the effect of the fuel chemistry is almost negligible. Finally, only Lewis number effects, which are related to the diffusion mechanism, are considered and a correction of the new efficiency function developed here is proposed. The final function is compared with DNS over the 52 simulated cases and shows significant improvements of results in comparison with previous functions. Further studies will be dedicated to the integration of this function over the turbulence spectrum following the same approach considered in previous works (Colin et al. 2002, Charlette et al. 2002) and to its implementation in CFD codes to evaluate its performance in real physical configurations.

8.3 Complementary comments

The two previous studies pointed out the effects of fuel composition on the flame propagation. These effects are well-known and already seen in many experimental measurement campaigns. However, with regards to premixed combustion modeling and especially to flamelet approaches, the chemical impact of the fuel composition is often only described by the laminar flame properties (U_l and δ_l) which appears to be not sufficient to accurately account for some physical phenomena such as thermo-diffusive instabilities. The solution chosen here was to incorporate a Lewis number parameter to account for these diffusion phenomena and the Muppala et al. (2009)formulation for Le_{bifuel} has been chosen among other presented below.

Lewis number formulation

The new stretch efficiency function developed here aims at accounting at first order for diffusion effects through the Lewis number. The Muppala et al. (2009) formulation of the effective Lewis number Le_{bifuel} (8.13) was chosen in this work to develop the present efficiency function. However, it should be noticed that several other formulations for binary fuels mixtures are available and two of them are presented below (8.37–8.39). Law et al. (2005) proposed to compute Le_{bifuel} pondering the Lewis numbers of both fuels Le_{fuel1} and Le_{fuel2} by their respective fuel heating values (LHV) (8.37–8.38):

$$Le_{bifuel} = 1 + \frac{q_{fuel1} \cdot (Le_{fuel1} - 1) + q_{fuel2} \cdot (Le_{fuel2} - 1)}{q_{fuel1} + q_{fuel2}} \tag{8.37}$$

with

$$q_{fuelk} = \frac{Y_{fuelk} \cdot LHV_{fuelk}}{Y_{fuel1} \cdot LHV_{fuel1} + Y_{fuel2} \cdot LHV_{fuel2}} \qquad k = 1, 2 \tag{8.38}$$

Dinkelacker et al. (2011) studied the Lewis number effect of methane-hydrogen mixtures on the turbulent flame velocity U_T and concluded that both formulations 8.13 ($Le_{bifuel} = (1-\alpha) \cdot Le_{fuelA} + \alpha Le_{fuelB}$) and 8.37 are globally equivalent for hydrogen ratio in fuel up to 20% and proposed a new formulation based on diffusivity considerations:

$$\frac{1}{Le_{bifuel}} = \frac{(1-\alpha)}{Le_{fuel1}} + \frac{\alpha}{Le_{fuel2}} \tag{8.39}$$

Figure 8.17 displays the evolution of Le_{bifuel} as function of equivalence ratio φ for poor cases and shows first that globally Le_{bifuel} does not depend on the equivalence ratio and an the other hand that the three formulations lead to totally different values. As a consequence, the use of another formulation than the one used to develop the present efficiency function (8.13) should be done with care.

Diffusive and reactive flame thickness ratio

It has been assumed in Section 8.2 that the differences observed in Table 8.4 between values of δ_l/δ_r – associated to the flames considered in this work (see Table 8.1) – could be negligible. These ratii are indeed globally close but actually more DNS should be performed to evaluate the impact of these differences on the efficiency function. In this regard, 8 additional DNS have been performed for a CH_4 flame and for 2 equivalence ratii ($\varphi = 0.7; 1.0$) corresponding to the same cases Ak1j ($k = 1, 2, 3, 4$ and $j = 1, 2$) of Table 8.5. For these 8 additional DNS, the domain, vortex and mesh sizing (10 nodes in the reaction thickness) were set as function of the reaction thickness δ_r instead of the diffusion thickness δ_l. Comparing results of Figure 8.18 with those of Figure 8.11 (recalled here in Figure 8.18) it can be seen that the effects of the equivalence ratio

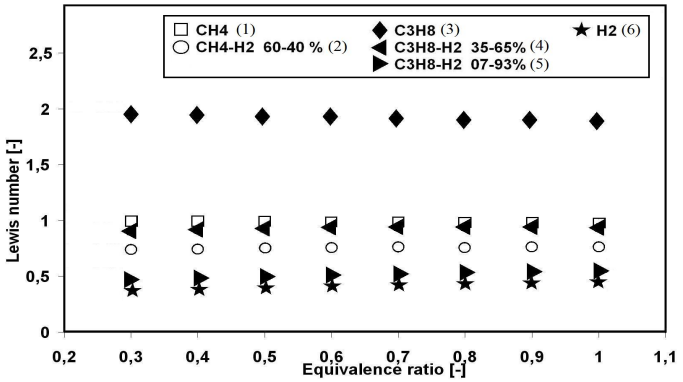

(a)

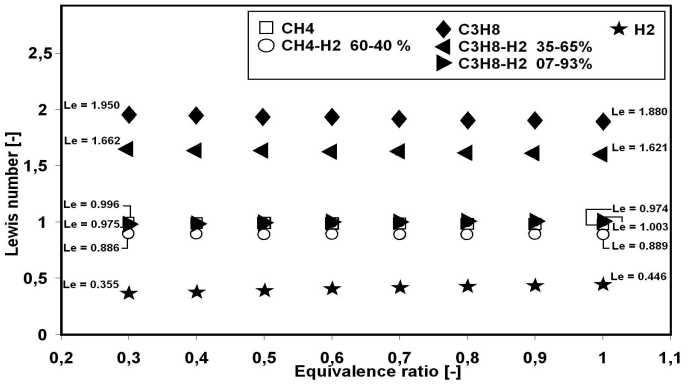

(b)

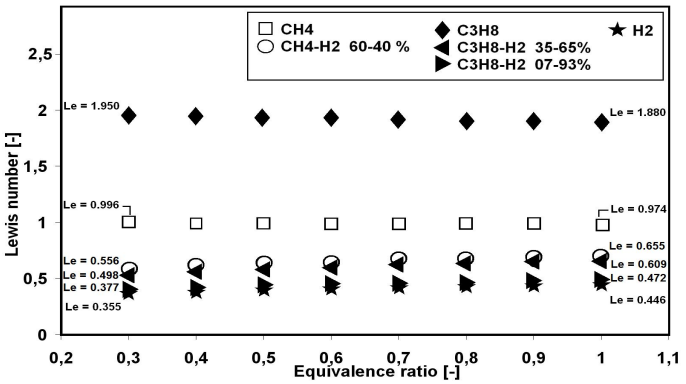

(c)

Figure 8.17: Effective Lewis numbers of two-fuel mixtures as function of equivalence ratio following the formulation from: (a) **Recalled Figure 8.4:** Muppala et al. (2009), Eq. 8.13; (b) Law et al. (2005), Eqs. 8.37,8.38; (c) Dinkelacker et al. (2011), Eq. 8.39.

on the unidimensional strain are globally similar showing that the difference between both ratii $\delta_{l(CH_4,\varphi=0.7)}/\delta_{r(CH_4,\varphi=0.7)} = 2.24$ and $\delta_{l(CH_4,\varphi=1.0)}/\delta_{r(CH_4,\varphi=1.0)} = 2.09$ can be neglected here.

However, in the case where this difference would be significant, additional DNS should be performed considering a large range of ratii δ_l/δ_r. If important effects are observed, a reflexion should then be initiated about:

- the integration in the efficiency function, Γ, of a new parameter, δ_r, and more particularly the ratio δ_l/δ_r. Indeed, as previously demonstrated (see Section 8.2.4), the flame/vortex interaction is theoretically expected to be also governed by this latter.
- the definition of δ_r. Indeed, contrary to the diffusion flame thickness δ_l, no phenomenological correlation easy to implement in CFD codes is currently available.

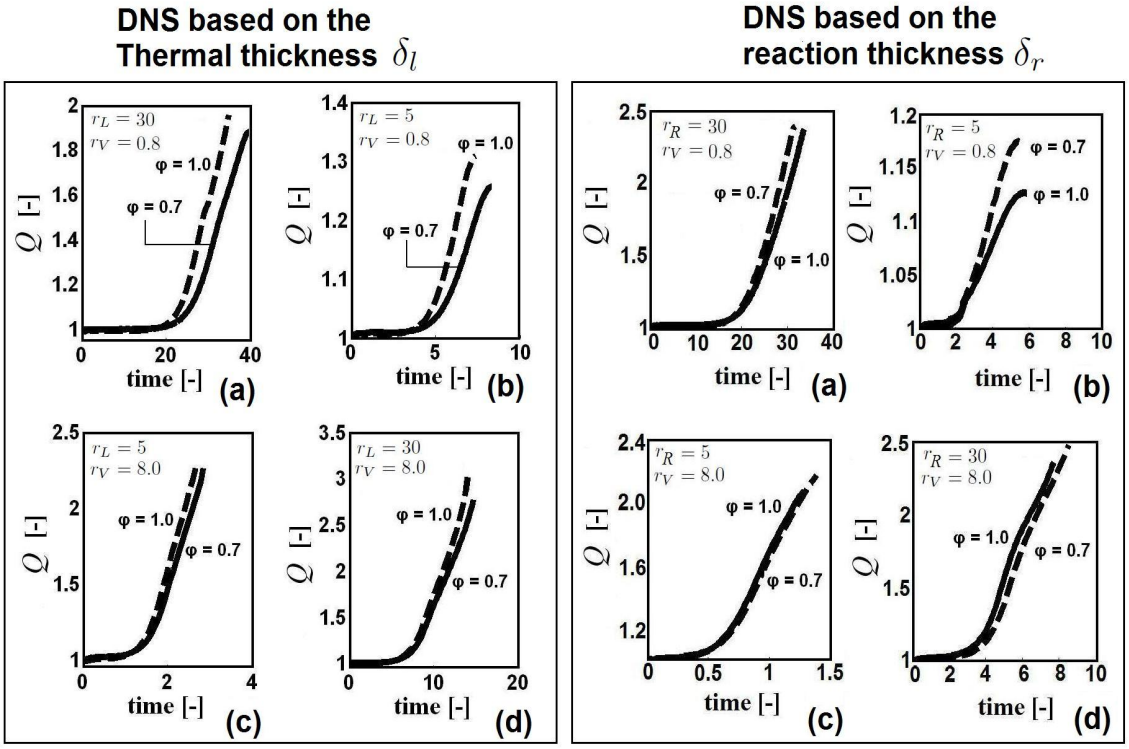

Figure 8.18: Total reaction rate versus time during flame-vortex interaction for methane and for both equivalence ratii $\varphi = 0.7$ and $\varphi = 1.0$. (a) Case A112 – (b) Case A212 – (c) Case A312 – (d) Case A412. Reaction rate values Q are made non-dimensional using the corresponding planar laminar flame quantities $Q(t = 0)$. Times are reduced using the flame time: left: $t^+ = t \cdot U_l/\delta_l$; right: $t^+ = t \cdot U_l/\delta_r$. The length scale ratio r_R is defined as $r_R = r/\delta_r$.

Validation of the new efficiency function

0D simulation The new efficiency function has been implemented[2] in the AMESim® simulation software (Malbec et al. 2009) and tested in the case of the single-cylinder turbocharged SI engine used in this thesis and already presented in previous sections (Table 4.2). A dedicated experimental campaign was performed at IFPEn to study the effect of hydrogen addition in

[2]The new function is integrated over the turbulence spectrum following the same approach considered in previous works (Colin et al. 2002, Charlette et al. 2002).

methane. It resulted in the generation of a wide experimental database of 72 operating points for fuels formulations (0, 10, 20 and 40% of hydrogen in methane), 3 engine speeds (1500/2000/3500 rpm) and loads from idle to partial open throttle (Indicated Mean Effective Pressure, IMEP, from 2 to 9 bar). An unity equivalence ratio was retained for all operating conditions. The simulator used in this study is the same than the one presented in Chapter 4. The correlation of Bougrine et al. (2011) was chosen to describe the laminar flame velocity U_l and the Zel'dovitch definition 2.8 for the laminar flame thickness δ_l was retained. The turbulence parameters u' and l_t were estimated using the methodolgy presented in Section 4.1.4.
Examples of simulated cylinder pressure curves are presented in Figure 8.20 for different rates of hydrogen in fuel. Results obtained using function of Charlette et al. (2002), Eq. 8.33 (Bougrine et al. (I)) and Eq. 8.36 (Bougrine et al. (II)) are compared against experimental data for 4 operating conditions. As already observed (see Figure 4.48) Charlette et al. function does not allow to retrieve exactly the experimental pressure levels. It is interesting also to see that the present function without the Lewis number factor (Bougrine et al. (I)) improves results showing that the effects of the velocity ratio r_V at high length scale ratii r_L (see Section 8.2, Figure 8.13) have an impact on the final heat release and thus on the global flame turbulent velocity. However, it should be noticed that these improvements remain limited compared to the results obtained using the full present efficiency function (Bougrine et al. (II)). Indeed as shown in Figure 8.20, the experimental pressure curves are globally recovered for all hydrogen ratii in methane (at least until 40%) conforting the initial assumption of a Lewis effect linked to H_2 addition in fuel. These observations are confirmed by Figure 8.19 which displays errors on the maximum cylinder pressure as function of the hydrogen ratio. For the sake of clarity, are displayed only 16/72 (x3) operating points corresponding to the results presented in Figure 8.20. As expected, for both Charlette et al. and Bougrine et al. (I) functions, error increases when the hydrogen ratio increases and is constant when Bougrine et al. (II) is used. Moreover, observations in Figure 8.20 are confirmed here with mean errors (curves) lower when Bougrine et al. functions are used. Nevertheless present comparison concern error levels which not exceed 10% for almost points. However, if higher hydrogen rates are expected to be used and if curves of Figure 8.19 are extrapoled, it can be imagined that the use of Charlette et al. (2002) function could lead to more significant error levels. The proposed function therefore appears as a good solution to develop engine burning high hydrogen blended fuels.

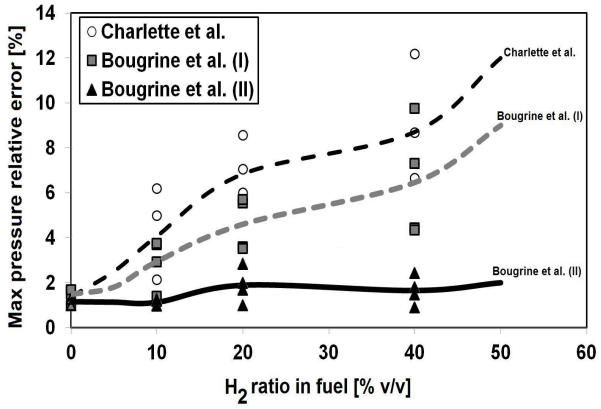

Figure 8.19: Relative errors on the maximum cylinder pressure levels from the simulation as function of the hydrogen ratio in methane and for the 16 operating points of Figure 8.20. Simulation results were obtained using functions of Charlette et al. (2002), Bougrine et al. (I) and Bougrine et al. (II). Curves representing the mean relative error are also plotted as function of the hydrogen ratio.

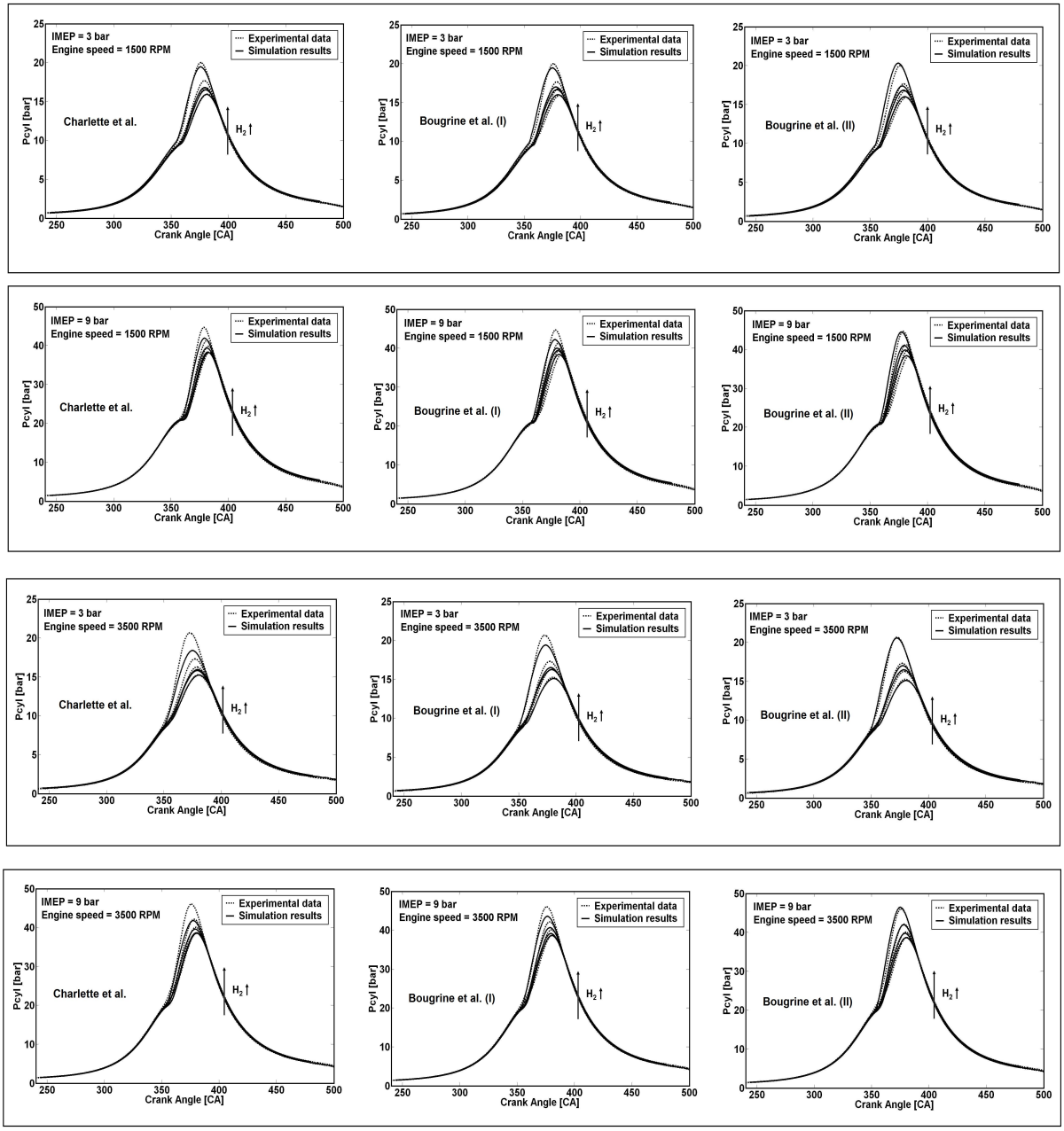

Figure 8.20: Comparisons between experimental and simulated cylinder pressure curves for different engine operating conditions and fuels. Simulation results are obtained using: (first column) function of Charlette et al. (2002) – (Second column) Eq. 8.33 (Bougrine et al. (I)), (Third column) Eq. 8.36 (Bougrine et al. (II)).

Part IV

Conclusion & Outlooks

Conclusions & Outlooks

Conclusions

With regards to the current environmental and economical context, the development of new eco-aware and more efficient engine concepts has become in the last few years one of the main priorities for car manufacturers. Because of the high complexity of engine operations, the high number of parameters (engine technologies and strategies, fuel composition, etc.) to be calibrated and the increasing cost of experimental campaigns, it seems crucial to develop accurate simulation tools able to support the engine development from design to control strategies development and calibration. In such a prospect, the system simulation approach appears today as an essential solution.

This thesis aimed at proposing a combustion chamber system simulation model able to accurately represent the different phenomena associated to all common technologies (GDI, EGR, downsizing, VCR, CAI, etc.) and to the use of alternative fuels (CNG, H2, Gasoline, ethanol and liquid or gaseous hydrocarbon mixtures). It has resulted in a new 0D combustion model, CFM1D-TC which integrates several new approaches developed in this work:

- A new fuel oxidation model based on a tabulation approach,
- A new post-oxidation model based on a tabulation approach (CORA, NORA),
- Two new laminar flame speed correlations adapted to the combustion of methane-hydrogen and iso-octane-ethanol blends,
- A new 0D auto-ignition model based on a tabulation approach,
- A new stretch efficiency function formulation accounting for fuel composition effects.

All these developments were presented in this manuscript following a three-part framework.

In a first part, after an overview of the current environmental, economical and technical contexts, basic concepts used in this thesis were defined. A review of main 0-dimensional approaches for system simulation tools with regards to IC engines developments was then proposed. A description of existing models for heat release prediction has been presented distinguishing empirical from phenomenological and reduced models. A presentation of typical 0D turbulence, pollutant and auto-ignition models has been developed. As a first result, it has been concluded that only few works studied in the past the description of fuel composition effects on combustion processes through 0D models. Moreover, it has been discussed that current 0D models were generally developed to optimize one or some criteria such as precision, ability for extrapolation, ease of calibration or CPU-cost.

This last observation motivated the development of the CFM1D and CFM1D-TC models presented in this work which have been built upon predictive physical approaches able to precisely describe complex phenomena occurring during the combustion process ensuring at the same time accuracy and low CPU times.

The CFM1D model has been presented in a second part. It aims at solving the physical phenomena occurring in SI engines. It follows from the reduction of the 3D CFD ECFM combustion model and is based on reduced descriptions of chemistry in the flame front and in the burnt gases and on phenomenological approaches to solve the turbulent flame propagation and auto-ignition phenomena. An equilibrium scheme (Meintjes and Morgan 1987) was adopted to describe the production of CO in the burnt gases while an extended Zeldovitch mechanism (Heywood 1988) was used for NO. A physical equation for the temporal evolution of the flame wrinkling was considered. This equation was obtained by reduction of the 3D CFD equation for the flame surface density (Richard et al. 2007, Richard and Veynante 2007) and includes an efficiency function Γ of the turbulent flow on the flame strain (Charlette et al. 2002) limiting the stretch induced by small turbulent structure. The laminar flame speed was estimated using dedicated experimental correlations adapted to the combustion of iso-octane-ethanol (Metghalchi and Keck 1982) and methane (Rahim et al. 2002). The combustion model was then coupled to a simple phenomenological 0D turbulence K-k model based on a set of two equations for the mean and turbulent kinetic energy densities. The study of such a model was out of this thesis scope. Finally, a knock model based on the description of the evolution of an auto-ignition precursor in the fresh gases coupled with an estimation of the knock intensity was proposed.

The CFM1D model was then implemented in the AMESim® simulation software and used to simulate on the one hand, a wide range of steady state operating conditions of a spark ignition (SI) engine burning iso-octane-ethanol and methane-hydrogen blends and, on the other hand, variations of the spark advance and fuel air equivalence ratio around optimal engine settings. A correct description of the engine performances (IMEP, cylinder pressure curve) was obtained in terms of trends and levels for all the points of the engine map. The optimal spark advance was also correctly predicted in the no knock zone. An overall good estimation of pollutant emissions was also achieved and variations of the equivalence ratio showed a correct evolution of simulated CO and NOx. Finally, the knock limited zone frontiers such as the border-line spark advances in this zone were correctly delineated and a good agreement was obtained with experiments, with errors close to experimental uncertainties. In particular, the effect of ethanol addition in fuel on knock was well described. The CFM1D model finally appeared as a good tool to describe physical phenomena occurring in SI engines as well as combustion, post-oxidation and knock and to account for fuel composition variation effects on these last phenomena. Nevertheless, three limitations made this model insufficient:

- Regarding emissions restrictions, the precision on pollutants prediction is more and more severe and observed differences between experimental data and simulations using CFM1D finally remain significant, notably in term of CO prediction. Moreover, the chemistries solved to account for species evolution require significant computational resources with regards to system simulation. Indeed, the calculation time for a whole engine cycle using CFM1D is about 1s. This order of magnitude is satisfying regarding engine development and evaluation of the potential of new strategies. It is also low enough to allow an use in the learning process of neural network based models to build real-time combustion models for engine control applications. Nevertheless, a computational time of 1s still too high to allow direct real-time calculation. Considering that the most consuming part of the model is the solving of chemistry, it appeared essential to provide solutions to describe species evolutions when varying the fuel composition simultaneously decreasing the computational time.
- Knock is the most efficiency limiting phenomena in SI engines. In this regard, its prediction is a crucial issue in the context of SI engine developments and the simple phenomenological model integrated in the CFM1D model appears as a promising tool to predict with a correct precision occurrence of knock in particular when varying the fuel composition. However, such a model requires a specific parameters calibration and above all is totally independent from the combustion model. Indeed, this model does not allow to compute an auto-ignition specific consumption rate which would have a direct impact on the global species evolution

and heat release. Regarding knock occurrence, this last point is not really important since this phenomena is not expected to appear. However, regarding the development of downsizing technologies coupled with the increasing use of alternative fuels like hydrogen such phenomenological approaches can be limited and the development of a more physical model appears crucial. Moreover, in the case of CAI technology the species evolution is mainly driven by the AI species consumption rate and a simple phenomenological model is here also not sufficient anymore.

- Results on mean in-cylinder pressures prediction using CFM1D are quite satisfying showing that the evolution of the heat release rate - and therefore the turbulent flame speed - is well-described. However, small deviations have been found when increasing the ethanol ratio in fuel mixture. The error levels which were relatively low in the case of gasoline-ethanol blends, were more significant when dealing with methane-hydrogen fuels. Indeed, simulations on the same engine basis confirmed this last point showing that cylinder pressure levels are more and more underestimated when increasing the hydrogen ratio in methane. From this last observation, a reflexion about the description of fuel composition effect on the turbulence/flame interaction processes has been initiated.

Finally, in a third part, the new CFM1D-TC model has been presented. It integrates first a new tabulation approach used to incorporate complex chemistry in the CFM1D model to precisely describe the oxidation process and to respect the CPU constraints of full engine simulations. As a first part of the new pollutant model development, this approach consisted in interpolating realistic compositions of the products of fuel oxidation from a look-up table and writing the mass variation of a species i as function of the equilibrium compositions Y_i^{eq} and of the turbulent flame velocity $U_T = U_l \cdot \Xi$. Y_i^{eq} were deduced from *a priori* calculation of 1D premixed flames using a detailed kinetic scheme. A benchmark of several available kinetic schemes of the literature was realized in order to evaluate and choose the more adapted kinetic mechanism to generate the database. The GRI 3.0 scheme turned out to be the best compromise between robustness, precision and CPU-cost and was finally retained. A database of laminar flame velocity was also generated and two new expressions for the laminar flame velocity U_l was developed to complement and improve common experimental correlations which are generally restricted to low pressures and temperatures levels and often defined for a single fuel. These new correlation are adapted to the combustion of methane-hydrogen-air-diluent and iso-octane-ethanol-air-diluent blends. Simulations were achieved considering thermodynamic conditions representative of those found in modern combustion systems to extend the domain of validity of experimental correlations to high hydrogen contents in the fuel, high residual burned gas mass ratios and high pressures and temperatures. The proposed model was then validated on a wide range of operating points from a 4 cylinder turbocharged SI engine. Simulations results were in very good agreement with experiments in terms of cylinder pressure traces, showing the validity of the proposed laminar flame speed and thickness correlations. To replace a single step chemical scheme by complex chemistry is found to have a huge impact on the prediction of pollutant emissions, giving better results and demonstrating the interest of tabulated complex chemistry in 0D simulations. However, this solution did not appear significantly efficient with regard to system simulation. Indeed, an important parameter to optimize is the computational time. In fact, the most CPU expensive part of the CFM1D model is the pollutant sub-model and more particular the post-oxidation sub-model. Indeed, the description of dissociation processes and NO_x formation in the burnt gases involves 10 reactions and 13 species which associated kinetics can be particularly low. Moreover, such a post-oxidation sub-model requires the calibration of several parameters allowing to catch phenomena not described by the reduced chemistries. A solution to complement the pollutant model development in the CFM1D-TC model was therefore to integrate a similar tabulation approach to directly describe CO and NO formation in the burnt gases.

A new approach called CORA for (CO Relaxation Approach) inspired from the NO approach for NO (Vervisch et al. 2011) was then developed to integrate complex chemistry in the CFM1D

model to describe post-oxidation processes. Such an approach has the advantage to be totally generic, requiring no parameter calibration. It consisted in calculations of homogeneous reactors to generate a chemical database covering a wide range of parameters (equilibrium compositions and characteristic time scales) directly accessed by the combustion model to determine pollutant concentrations at low CPU-cost. Methane-air-diluent mixtures were considered and the GRI 3.0 mechanism was here also retained for complex chemistry calculations. A new description of the post-flame chemistry of the CFM1D was proposed, writing NO and CO reaction rates as linear functions of the respective mass fractions including a characteristic relaxation response time necessary to reach the equilibrium state. Mass fractions and times scales were interpolated from look-up tables using the current values of pressure, burnt gases enthalpy, equivalence ratio and diluent mass fraction. Characteristic time scales were computed using species evolution from a perturbed state to the equilibrium in homogeneous reactors. A methodology for the initialization of the perturbed states of NO and CO was also presented. It was shown that chemical relaxations for a given perturbation and its opposite follow the same trends and lead to the same equilibrium. Moreover, only one perturbation $\Delta_{NO} = \Delta_{CO} = 10^{-2}$ was considered. The proposed model was then validated on a wide range of operating points from a 4-cylinder turbocharged SI engine. Simulations results were globally in good agreement with experiments in terms of NO and CO mass evolutions (as function of engine load). It was shown that both species relax until freezing when the burnt gases temperature reaches the characteristic values 2000 K for NO and 1800 K for CO. Replacing direct solving of simple and reduced chemistries by tabulating complex chemistry has a huge impact on computational times improving at the same time the prediction level of pollutant emissions and demonstrating the interest of tabulated complex chemistry in 0D simulations. However, with regards to the very well-fitted results obtained with the CFM1D model, the simulations performed using the new CFM1D-TC model lead to results which don't seem so good. This observation has been explained by the strong dependence of pollutant kinetics to the local thermodynamic conditions. Regarding 0D modeling where only mean values are considered, the challenge is therefore to develop approaches able to describe the inhomogeneities in engine combustion chambers. In the CFM1D model, two calibration parameters implicitly allowed to globalized these heterogeneities effects (and potential others 3D effects). On the contrary, the new CFM1D-TC model has the crucial advantage of no requiring parameter calibration making it theoretically more robust and sensitive to fuel composition variations.

The impact of tabulated approaches use is summarized in Table 8.8 which compares mean computational performances estimations of the CFM1D and CFM1D-TC models. In particular, results obtained using a 3 gases version of the CFM1D (CFM1D-3g) is also presented. This version considers only 3 species (air, fuel and products) under an assumption of a stoichiometric combustion and is restricted to the prediction of heat release and knock (no pollutant model is solved). Estimations of Table 8.8 were obtained from all simulations performed during this thesis on both single-cylinder and four-cylinder basis. Single-cylinder computations were performed on the same computer with a single processor while four-cylinders ones were performed on an hexa-core computer. For this last case, one core was dedicated to the air-path, one for the engine control and four for the combustion chambers. Simulations were performed considering both fixed and variable time steps. However, for the four-cylinders case, as the the engine control unit is incompatible with the use of a variable time step, only the fixed time step case is presented. Regarding the single-cylinder results, the computational time increases with increasing values of the engine speed when a fixed time step is considered while it is unchanged for the variable time step cases. Indeed, in this last case, the solver adapts the time step to the phenomena dynamics which evolve with the engine speed. Table 8.8 also demonstrates the positive impact of tabulated chemistry on the computational efficiency showing that CFM1D-TC performances tend towards the CFM1D-3g. In particular, the CPU times are divided by 2.5 compared to the CFM1D (15 gases) with a variable time step and by 5 with a fixed time step. Finally, it is important to note that these first results are still estimations and that the CPU times levels given here will be made clearer by tests currently performed at IFPEn.

Engine speed [rpm]	CFM1D-3g (3 gases)	CFM1D (15 gases)	CFM1D-TC (8 gases)
	Single-cylinder basis – Variable time step – Single core		
1000	2.5 RT	20 RT	7.5 RT
3000	2.5 RT	20 RT	7.5 RT
6000	2.5 RT	20 RT	7.5 RT
	Single cylinder basis – Fixed time step =25μs – Single core		
1000	0.12 RT	1.37 RT	0.25 RT
3000	0.37 RT	4.12 RT	0.75 RT
6000	0.75 RT	8.25 RT	1.5 RT
	Four-cylinders basis – Fixed time step =25μs – Hexa-core		
1000	0.13 RT	1.5 RT	0.31 RT
3000	0.39 RT	4.5 RT	0.93 RT
6000	0.78 RT	9 RT	1.8 RT

Table 8.8: Estimations of mean computational performances of the CFM1D and CFM1D-TC models. These estimations were obtained from all simulations performed during this thesis on both single-cylinder and four-cylinder basis. Single-cylinder computations were performed on the same computer with a single processor. Four-cylinders computations were performed on an hexa-core computer. For this last case, one core was dedicated to the air-path, one for the engine control and four for the combustion chambers. Moreover, as the the engine control unit is incompatible with the use of a variable time step, only the fixed time step case is presented. CPU times are given as function of the real time (RT).

To answer the issue of phenomenological models for auto-ignition (AI) prediction previously mentioned, a new 0D AI model for the prediction of controlled and uncontrolled AI phenomena in SI engines was developed. A similar approach to the one integrating complex chemistry in the CFM1D to improve the pollutants prediction, was used and presented. It has been inspired from the PCM-CFM-TKI model developed by Lecocq et al. (Lecocq 2010, Lecocq et al. 2011) and is based on the tabulation of AI delays and progress variable reaction rates. These tables have been obtained from a priori calculations of homogeneous reactors at constant pressure using the IDE-THANOL (Pires.da.Cruz et al. 2010) complex kinetic scheme and consider as inputs the pressure, the fresh gases temperature, the fuel/air equivalence ratio, the dilution rate, the volume fraction of ethanol in fuel and a specific auto-ignition progress variable. This latter differs from the progress variable associated to the flame propagation to ensure auto-ignition to begin at a progress variable equal to zero. The new model has been integrated as a new part of the CFM1D-TC model and was built to predict knock occurrence and to allow the simulation of CAI configurations. It has been implemented in AMESim® but validation tests are still ongoing at IFPEn. Therefore, no conclusions have been provided in this work. Nevertheless, some perspectives and development suggestions have been proposed. It concerned the need to define adequate indicators common to both experimental and simulation data to allow comparisons and developing approaches to account for cycle-to-cycle variations, fresh gases temperature stratification and turbulence effects on AI processes.

In a last chapter, effects of fuel composition on flame/turbulence interaction processes have been investigated to explained differences between experimental and simulated pressures observed when using the CFM1D model. These differences which were small when dealing with ethanol-gasoline blends, were more significant when burning hydrogen-methane mixtures. Starting from the assumption that the laminar flame velocity and surface were well-defined, this investigation led to some questions about the flame wrinkling description and more particularly about the flame stretch definition.
In most combustion models based on the flamelet assumption, the flame stretch induced by a

single eddy of velocity u'_r and size r is generally linked to its strain defined by u'_r/r . However, as shown by Meneveau and Poinsot (Meneveau and Poinsot 1991), this relation is not always obvious and needs to be corrected in particular at small scales where the theoretical strain is high. Several works (Meneveau and Poinsot 1991, Colin et al. 2002, Charlette et al. 2002) introducing efficiency functions to limit this stretch were performed in the past. However, these studies based on direct numerical simulations (DNS) of flame-vortex interaction were carried out only for a single chemical configuration using a simple one-step chemistry with an Arrhenius law to describe combustion processes. The assumption was therefore made that all chemical effects, including equivalence ratio or fuel composition variations, are entirely accounted for through the laminar flame velocity and thickness. This last assumption can be restrictive in particular when low Lewis number mixtures are burnt. Indeed, thermo-diffusive instabilities may occur and the associated flame wrinkling can finally be different from the one predicted by current efficiency functions (in the case where these phenomena are expected to be described only by this function). DNS of flame-vortex interaction were performed varying the nature of the fuel, the equivalence ratio and the Lewis number to study the effect of chemical composition on premixed flames wrinkling. Flame stretches were deduced from the DNS following the methodology proposed in previous works (Meneveau and Poinsot 1991, Colin et al. 2002, Charlette et al. 2002) and compared with phenomenological functions from the literature for a number of vortex characteristics. To account for chemical effects, DNS performed in this work integrate a description of chemical processes through a new 4-steps kinetic scheme dedicated to the combustion of CH_4-H_2 and C_3H_8-H_2 blends and validated using detailed kinetic mechanisms. It resulted first that existing efficiency functions do not take into account the strong influence of the velocity ratio at large length scales. As a consequence a new formulation inspired from previous attempts was proposed and showed a very good agreement with the DNS, even if it did not allow to describe the trend observed at low length scale ratii. However, these scales correspond to relatively low stretch values and may not be of importance in the total turbulent flow stretch evaluation. A second conclusion was that the fuel composition has a strong effect on the flame stretch in particular when varying the fuel Lewis number. Indeed, the sensitivity of the efficiency function to the equivalence ratio observed on DNS results is significant only at low velocity ratii corresponding to relatively low stretches which can be considered to have only a limited contribution to the total flame stretch in a turbulent flow. On the other hand, DNS showed also that for a given Lewis number, the effect of the fuel chemistry is almost negligible. Finally, only Lewis number effects, which are related to the diffusion mechanism, are considered and a correction of the new efficiency function developed here is proposed. The final function is compared with DNS over the 52 simulated cases and showed significant improvements of results in comparison with previous functions.

The new efficiency function has been implemented in AMESim® and tested in the case of the single-cylinder turbocharged SI engine used in this thesis. A dedicated experimental campaign was performed at IFPEn to study the effect of hydrogen addition in methane. It resulted in the generation of a wide experimental database of 72 operating points for fuels formulations (0, 10, 20 and 40% of hydrogen in methane), 3 engine speeds (1500/2000/3500 rpm) and loads from idle to partial open throttle (Indicated Mean Effective Pressure, IMEP, from 2 to 9 bar). An unity equivalence ratio was retained for all operating conditions. The correlation developed in this thesis (Bougrine et al. 2011) was chosen to describe the laminar flame velocity U_l and the Zel'dovitch definition 2.8 for the laminar flame thickness δ_l was retained. Examples of simulated cylinder pressure curves were presented showing the impact of the choice a given efficiency function formulation when varying hydrogen ratio in methane. Results obtained using function of Charlette et al. (Charlette et al. 2002) and present one were compared against experimental data for 4 operating conditions. As already observed Charlette et al. function did not allow to retrieve exactly the experimental pressure levels. On the contrary, the present function allowed to globally recover experimental pressure traces for all hydrogen ratii in methane (at least until 40%) conforting the initial assumption of a Lewis effect linked to H_2 addition in fuel.

The new CFM1D-TC model has been validated against a wide range of experimental measurements and is adapted to the combustion of methane-hydrogen and iso-octane-ethanol blends. It allows especially to describe at low CPU cost the effects of these fuels on the flame propagation, pollutants emissions and auto-ignition processes. Finally, it is important to note that this model has been built to accept tables for any fuel blends provided that the complex kinetic scheme used to generate these tables is predictive.
All the CFM1D and CFM1D-TC submodels presented in the previous chapters are summarized in the following table.

Outlooks

The new CFM1D-TC model exhibited very satisfying results in terms of precision and computational performances and fulfills therefore the initial thesis intentions. Nevertheless, some developments are still required to account for:

- Stratified conditions – Tabulation methods developed in this work for pollutant and auto-ignition prediction are highly dependent on the tables inputs as the local temperature, pressure or composition. During the the combustion simulation several variables such as the equilibrium mass fractions, times scales or AI delays are interpolated in the look-up tables using the current mean values of pressure, temperature (or enthalpy), equivalence ratio and diluent mass fraction. As shown in this thesis, in realistic configurations, despite of an homogeneous assumption, a natural temperature stratification forms in the fresh and burnt gases leading to strong deviations between the mean and local temperature values. This last observation is even more true in stratified combustion systems where heterogeneities are high. Developments need therefore to be initiated to account for these inhomogeneities in combustion chambers integrating statistical methods initially developed for RANS or LES. These latter allow indeed to refine the representation of a physical variable Q describing its distribution by a presumed probability density function (PDF) $P(Q)$ (for example a Gaussian or a β-function (Lecocq 2010)) as function of the mean values of Q, $\tilde{Q}$, and its variance, $\tilde{Q}''^2$ (Bilger 1993, Klimenko 1995, Bradley et al. 1990, Peters 2000). These approach could have the advantage to be easy to couple with a 0D model since the mean values of variables such as temperature, pressure or composition are known. Nevertheless, modeling efforts are also required to estimate the variances of these parameters, which represent one of major challenges for future 0D combustion models.
- Knock occurrence – Adequate indicators common to both experimental and simulation data need to be defined to allow comparisons.
- Turbulence effects on AI – The 0D AI model proposed in this thesis provides levels of laminar burning rate velocities due to the auto-ignition processes. In the case of knock prediction, this information is enough to evaluate its potential occurrence and its intensity. However, in the case of CAI strategies developments, the total combustion rate is not mainly driven by the classical oxidation process any more. Indeed, auto-ignition processes take over and the turbulence effects which will promote species mixing and tend to increase the total combustion reaction rate have thus to be modeled.
- Reaction thickness contribution – Common stretch efficiency functions Γ are generally formulated as function of ratii between flame and turbulence characteristic velocities and lenght scales. However, it has been shown in this thesis that Γ is actually expected to be also dependent on the laminar flame diffusion thickness to the reaction one ratio. This assumption could not be verified in this thesis since the differences between values of this ratio associated to the flames considered in this work were negligible. As a result, in the case where

this difference would be significant, additional DNS should be performed considering a large range of ratii δ_l/δ_r. If important effects are observed, a reflexion should then be initiated about the integration of this new parameter in Γ.

- Turbulence – The K-k turbulence model used in this thesis is based on a simplified approach presented in the first part. The main drawback of such a model is to require experimental data to calibrated several model parameter. As a consequence, without experiments, this model coupled to the combustion model can lead to erroneous results. Therefore, a future work have to be devoted to the reduction of a 3D turbulence model.

- HC and soots emissions – In the present work, only NO and CO were considered to describe pollutants emissions. However, with the development of stratified combustion technologies (Gasoline Direct Injection, etc.), specific models should be developed to account for HC and soots emissions which regulation standards are more and more restrictive. These models can be inspired from tabulation approaches presented in this thesis and from previous works devoted to the emissions prediction in Diesel engines (Vervisch 2012).

Over the short-term, the approaches developed in this thesis ($CORA$, laminar flame correlations, efficiency function, etc.) will be extended to the 3D ECFM model for RANS or LES applications. Complementary validation steps will thus be required to evaluate performances of these approaches in real physical configurations.

Moreover, a specific work will be realized to integrate the new CFM1D-TC model in an Engine Control Unit to control and optimize in real time the engine operations.

More generally, a specific work will be devoted to the adaptation and development of new system simulation tools adapted to aeronautic propulsion systems. This new challenge follows the new aeronautic environmental and economical contexts which tend to be more and more restrictive. Works performed in this thesis are thus expected to be used as a basis for future developments.

Summary Table

<table>
<tr><th>CFM1D</th><th>CFM1D-TC</th></tr>
<tr><td colspan="2">Enthalpy balance for the combustion chamber</td></tr>
<tr><td colspan="2">$$\frac{dmh}{dt} = V\frac{dP}{dt} + \frac{dQ_{comb}}{dt} - \frac{dQ_{wall}}{dt} + \sum_{in,out} h_j \frac{dm_j}{dt}$$</td></tr>
<tr><td colspan="2">Heat released by combustion</td></tr>
<tr><td>$$\frac{dQ_{comb}}{dt} = \sum_i h_{f_i}\left(\left.\frac{dm_i}{dt}\right|_{ff} + \left.\frac{dm_i}{dt}\right|_{pf}\right)$$</td><td>$$\frac{dQ_{comb}}{dt} = \sum_i h_{f_i}\left(\left.\frac{dm_i}{dt}\right|_{ff} + \left.\frac{dm_i}{dt}\right|_{pf} + \left.\frac{dm_i}{dt}\right|_{AI}\right)$$</td></tr>
<tr><td colspan="2">Oxidation</td></tr>
<tr><td>$$\left.\frac{dm_i}{dt}\right|_{ff} = \upsilon_i \frac{W_i}{W_f}\left.\frac{dm_{fuel}}{dt}\right|_{ff} = -\upsilon_i \frac{W_i}{W_f}\rho_u Y_{fuel}^u U_l A_T$$</td><td>$$\left.\frac{dm_i}{dt}\right|_{ff} = \rho_u\left(Y_{fuel}^{eq} - Y_{fuel}^u\right)U_l A_T$$</td></tr>
<tr><td colspan="2">Laminar flame velocity</td></tr>
<tr><td colspan="2">$$U_l(\alpha, Y_{res}^u, T^u, P, \varphi) = U_l^0 \cdot \left(\frac{T^u}{T^\circ}\right)^{\alpha_T} \cdot \left(\frac{P}{P^\circ}\right)^{\alpha_P} \cdot \left(1 - \alpha_{res} \cdot f(Y_{res}^u)\right)$$</td></tr>
<tr><td>Parameters calibration based on experimental measurements</td><td>Parameters calibration based on complex chemistry simulation</td></tr>
<tr><td colspan="2">Laminar flame thickness</td></tr>
<tr><td>$$\delta_l^0 = 2 * \frac{\lambda_u}{\rho_u C_p U_l} * \left(\frac{T_b}{T_u}\right)^{0,7}$$
Blint correlation</td><td>$$\delta_l^0 = \left(\frac{\lambda}{\rho \cdot c_p}\right)_u \frac{1}{U_l}$$
Zel'dovitch correlation</td></tr>
<tr><td colspan="2">Turbulent flame surface</td></tr>
<tr><td colspan="2">$$A_T = \Xi \cdot A_m$$
A_m is a priori tabulated as function of the burned gases volume and the piston position considering a spherical propagation of the mean flame</td></tr>
<tr><td colspan="2">Flame wrinkling factor</td></tr>
<tr><td colspan="2">$$\frac{d\Xi}{dt} = \Gamma\left(\frac{u'}{U_l}, \frac{l_t}{\delta_l}\right)\frac{u'}{r}\left(\frac{\Xi_{eq} - \Xi}{\Xi_{eq} - 1}\right) - \frac{2}{r_{bg}}(1+\tau)(\Xi - 1)U_l$$
Deduced from the reduction of the 3D flame surface density balance equation</td></tr>
</table>

Stretch efficiency function	
$\Gamma\left(\frac{r}{\delta_l},\frac{u_r'}{U_l}\right)=\Gamma_{Colin\_et\_al.}\cdot\frac{1}{2}\left[1+erf\left(3\log\left(2\frac{u_r'}{U_l}\right)\right)\right]$ Parameters calibration based on DNS with a single flame and a fictive chemistry	$\Gamma\left(\frac{r}{\delta_l},\frac{u_r'}{U_l}\right)=\frac{1+erf\left(0.9\cdot\ln(r/\delta_l)-2\right)}{1+0.3\cdot(u_r'/U_l)\cdot\left(1+erf\left(0.9\cdot\ln(r/\delta_l)-2\right)\right)}\bullet f_{Lewis}$ $f_{Lewis}=\frac{1}{Le}\cdot\left(1.76+\tanh(Le-2)\right)$ Parameters calibration based on DNS with many flames and a realistic chemistry
Post-oxidation	
$\left.\frac{dm_i}{dt}\right\vert_{pf}=\left.\frac{dm_i}{dt}\right\vert_{equil}+\left.\frac{dm_i}{dt}\right\vert_{Zel'dov}$ Based on reduced chemistries + 2 calibration parameters: the freezing temperatures of CO and NO	$\begin{cases}\frac{dY_{NO}(t)}{dt}=\frac{Y_{NOeq}-Y_{NO}(t)}{\tau_{NO}}\\ \frac{dY_{CO}(t)}{dt}=\frac{Y_{COeq}-Y_{CO}(t)}{\tau_{CO}}\end{cases}$ Based on a tabulation approach of equilibrium compositions and characteristic time scales
Auto-ignition	
$\theta=A\left(\frac{RON_{eff}}{100}\right)^{3.402}P_{eff}^{\ -n}e^{\left(\frac{B}{T^u}\right)}$ $K_n=K_1\left(1-bmf.\max(1,\varphi)\right)(\Pi-1).\sqrt{1-\frac{\theta_{knock}}{K_2}}.N_{eng}.\frac{LHV}{LHV_{ref}}$ Phenomenological model computing knock delay and intensity, no computation of any heat release due to AI	$\left.\frac{dm_i}{dt}\right\vert_{AI}=m_u\left(Y_i^{eq}-Y_i^u\right)\dot{\omega}_c^{AI}\left(c^{AI}\right)$ $c^{AI}=\frac{m_{fuel}^{AI}}{m_{fuel}^{AI}+m_{fuel}^u}$ Based on a tabulation approach of equilibrium compositions and AI progress variable reaction rates

Summary table: contains all the CFM1D and CFM1D-TC submodels presented in the previous chapters.

List of publications

Published:

• S. Richard, S. Bougrine, G. Font, F-A. Lafossas, and F. Le Berr. On the reduction of a 3d cfd combustion model to build a physical 0D model for simulating heat release and knock and pollutants in SI engines. *Oil Gas Sci. Technol.*, 64:223–242, 2009.

• S. Bougrine, S. Richard, and D. Veynante. Modelling and simulation of the combustion of ethanol blended fuels in a SI engine using a 0D coherent flame model. *SAE paper* 2009-24-0016, 2009.

• S. Richard, S. Bougrine, G. Font, F. Le Berr. Pollutant emissions and fuel efficiency prediction for a downsized spark ignition engine using a 0-dimensional combustion model. *SIA International Conference on "The Spark Ignition Engine of the Future: Facing the CO2 and electrification challenges"*, 2009 (Conference paper).

• S. Bougrine, S. Richard, A. Nicolle, and D. Veynante. Numerical study of laminar fame properties of diluted methane-hydrogen-air flames at high pressure and temperature using detailed chemistry. *Int. J. Hydrogen Energy*, 36(18):12035–47, 2011.

• S. Bougrine, S. Richard, and D. Veynante. On the combination of complex chemistry with a 0D coherent flame model to account for the fuel properties in spark ignition engines simulations: Application to methane-air-diluents mixtures. Thirty-third Int. Symp. Comb., *Proc. Combust. Inst.*, 33:3123–30, 2011.

• S. Bougrine, G. Bernard, R. Lebas and S. Richard. A unified detailed tabulated chemistry approach to predict pollutant emissions for both compression-ignition and spark-ignition engines. *COnference on MOdeling and DIAgnostics for Advanced Engine Systems, COMODIA*, 2012.

Submitted:

• S. Bougrine, S. Richard, J.-B. Michel, and D. Veynante. Simulation of CO and NO emissions in a SI Engine using a 0D coherent flame model coupled with a tabulated chemistry approach. *Applied Energy*, 2012.

• S. Bougrine, S. Richard, O. Colin, and D. Veynante. Fuel composition effects on flame stretch in turbulent premixed combustion: DNS analysis of flame-vortex interaction and formulation of a new efficiency function. *Combust. Flame*, 2012.

In addition:

• S. Bougrine, S. Richard, D. Veynante. Reduction of a 3D CFD combustion model to build a physical 0D model : An essential way for future engine's development. *General Assembly of the French Combustion Group*, 2010 (Poster).

In preparation:

• S. Bougrine, S. Richard, G. Wang, and D. Veynante. Experimental and numerical investigation of stoichiometric and lean burn operation in spark ignited systems running with hydrogen enriched methane and propane. *Int. J. Hydrogen Energy*, 2012.

References

Albrecht, A., G. Corde, V. Knop, H. Boie, and M. Castagne (2005). 1d simulation of turbocharged gasoline direct injection engine for transient strategy optimization. *SAE paper 01-0693*.

Ali, Y. (1995). *Ph.D. dissertation*. Ph. D. thesis, The University of Leeds and Department of Mechanical Engineering.

Aluri, N. K., S. Muppala, and F. Dinkelacker (2006). Substantiating a fractal-based algebraic reaction closure of premixed turbulent combustion for high pressure and the lewis number effects. *Combust. Flame 145*, 663–674.

Arregle, J., J. Lopez, J. Martin, and E. M. Mocholi (2006). Development of a mixing and combustion zero-dimensional model for engines. *SAE Technical Paper 2006-01-1382*.

Arsie, I., F. D. Genova, C. Pianese, G. Rizzo, A. Caraceni, P. Cioffi, and G. Flauti (2005). Development of a mixing and combustion zerodimensional model for engines. *SAE Technical Paper 2005-01-1121*.

Asay, R., K. Svensson, and D. Tree (2004). An empirical, mixing limited, zero-dimensional model for diesel combustion. *SAE Technical Paper*.

Assanis, D. and J. Heywood (1986). Development and use of a computer simulation of the turbocompounded diesel system for engine performance and component heat transfer studies. *SAE Technical Paper 860329*.

Attar, A. and G. Karim (1998). An analytical approach for the optimization of a si engine performance including the consideration of knock. *SAE International (981463)*.

Aung, K., L.K., Tseng, M. Ismail, and G. Faeth (1995). Effects of pressure and nitrogen dilution on flame/stretch interactions of laminar premixed h2/02/n2 flames. *Combust. Flame 102*, 52630.

Babkin, V. and L. Kozachenko (1966). Study of normal burning velocity in methane-air mixtures at high pressures. *Combust. Explos. Shock Waves 2*, 46–52.

Bakali, A. E., P. Dagaut, L. Pillier, P. Desgroux, J.-F. Pauwels, A. Rida, and P. Meunier (2004). Experimental and modeling study of the oxidation of natural gas in a premixed flame, shock tube, and jet-stirred reactor. *Combust. Flame 137*, 109–28.

Barassin, A., R. Lisbet, J. Combourieu, and P. Laffitte (1967). Etude de linfluence de la temperature initiale sur la vitesse normale de deflagration de melanges methaneair en fonction de la concentration. *Bull. Soc. Chim. France 104*, 2521–26.

Barba, C., C. Burkhardt, K. Boulouchos, and M. Bargende (2000). A phenomenlogical combustion model for heat release rate prediction in high-speed diesel engines with common rail injection. *SAE Technical Paper 2000-01-2933*.

Baritaud, T. (1989). Combustion and fluid dynamic measurements in a spark ignition engine effect of thermochemistry and velocity field and turbulent flame speed. *SAE paper 892098*.

Baritaud, T., J.-M. Duclos, and A. Fusco (1996). Modelling turbulent combustion and pollutant formation in stratified charge si engine. *In 26th Symp. Int. On Combustion*, 2627–35.

Barratta, M., A. Catania, E. Spessa, and A. Vassallo (2005). Flame propagation speed in si engines: Modeling and experimental assessment. *ASME Paper (ICEF2005-1216)*.

Bayraktar, H. (2005). Experimental and theoretical investigation of using gasoline-ethanol blends in spark-ignition engines. *J. Renewable Energy 30:1733-1747*.

Benson, S. (1981). The kinetics and thermochemistry of chemical oxidation with application to combustion and flames. *Prog. Energy Combust. Sci. 7*, 125–34.

Bilger, R. (1993). Conditional moment closure for reacting flow. *Physics of fluids 5*.

Blint, R. (1986). The relationship of the laminar flame width to flame speed. *Combust. Sci. And Tech. 49*, 79–92.

Boger, M., D. Veynante, H. Boughanem, and A. Trouv (1998). Dns analysis of fsd concept for les of turbulent premixed combustion. *Proceedings of the 27th Symposium (Int.) on Combustion and The Combustion Institute*, 917–25.

Bohbot, J., N. Gillet, and A. Benkenida (2009). Ifp-c3d: an unstructured parallel solver for reactive compressible gas flow with spray. *Oil Gas Sci. Technol. 64(3)*, 309–336.

Borghi., R. (1985). On the structure and morphology of turbulent premixed flames. *Rec. Adv. Aerosp. Sci.*, 117–138.

Bosschaart, K. and L. de Goey (2004). The laminar burning velocity of flames propagating in mixtures of hydrocarbons and air measured with the heat flux method. *Combust. Flame 136*, 261–9.

Bougrine, S., S. Richard, A. Nicolle, and D. Veynante (2011). Numerical study of laminar flame properties of diluted methane-hydrogen-air flames at high pressure and temperature using detailed chemistry. *Int. J. Hydrogen Energy 36:18*, 12035–47.

Bougrine, S., S. Richard, and D. Veynante (2009). Modelling and simulation of the combustion of ethanol blended fuels in a si engine using a 0d coherent flame model. *SAE paper 2009-24-0016*.

Bougrine, S., S. Richard, and D. Veynante (2011). On the combination of complex chemistry with a 0-d coherent flame model to account for the fuel properties in spark ignition engines simulations: Application to methane-air-diluents mixtures. *Thirty-third International Symposium on Combustion, Proc. Combust. Inst. 33*, 3123–30.

Bounaceur, R., F. Battin-Leclerc, V. Conraud, R. Fournet, and P.-A. Glaude (2004). Modelisation de loxydation du toluene pur et en melange avec un alcane. *DCPR laboratory (Nancy and France) and Research Contract CT 0308/PROG 357/IFP*.

Bowman, C. T. (1975). Kinetics of pollutant formation and destruction in combustion. *Prog. Energ. Combust. Sci. 1*, 33–45.

Bozza, F. and A. Gimelli (2004). A comprehensive 1d model for the simulation of a small-size and two-stroke si engine. *SAE paper 2004-01-0999*.

Bozza, F., A. Gimelli, S. Merola, and B. Vaglieco (2005). Validation of a fractal combustion model through flame imaging. *SAE paper 2005-01-1120*.

Bozza, F., A. Gimelli, S. Merola, and B. Vaglieco (2006). Validation of a fractal combustion model through flame imaging. *SAE Trans., J. engines 114-3*, 973–87.

Bozza, F., A. Gimelli, A. Senatore, and A. Caraceni (2001). A theoretical comparison of various vva systems for performance and emission improvements of si engines. *SAE paper 2001-01-0670*.

Bozza, F., A. Gimelli, L. Strazzullo, E. Torella, and C. Cascone (2007). Steady-state and transient operation simulation of a downsized turbocharged si engine. *SAE Technical Paper 2007-01-0381*.

Bradley, D., P. Gaskell, and A. Lau (1990). A mixedness-reactedness flamelet model for turbulent diffusion flames. *Proc. Combust. Inst. 23*, 685.

Bradley, D., M. Haq, R. Hicks, T. Kitagawa, M. Lawes, and C. Sheppard (2003). Turbulent burning velocity, burned gas distribution, and associated flame surface definition. *Combust. Flame 133*, 415–30.

Bradley, D., A. Lau, and M. Lawes (1992). Flame stretch rate as a determinant of turbulent burning velocity. *Philos. Trans. R. Soc. Lond.*, 338–359.

Bradley, D., M. Lawes, and M. Mansour (2009). Explosion bomb measurements of ethanolair laminar gaseous flame characteristics at pressures up to 1.4 mpa. *Combust. Flame 156*, 1462–70.

Brinkman, N. D. (1981). Ethanol fuel : a single-cylinder engine study of efficiency and exhaust emissions. *SAE paper 810345*.

Buckmaster, J. and A. Crowley (1982). Theory of laminar flames. *Cambridge University Press*.

Burwell, W. and D. Olson (1965). The spontaneous ignition of isooctane air mixtures under steady flow conditions. *SAE Paper 650510*, 839–49.

Bush, W. and F. Fendell (1970). Asymptotic analysis of laminar flame propagation for general lewis numbers. *Combust. Sci. Tech. 1*, 421.

Candel, S. and T. Poinsot (1990). Flame stretch and the balance equation for the flame surface area. *Combust. Sci. Tech. 70*, 1–15.

Castagne, M., J.-P. Dumas, S. Henriot, and F.-A. Lafossas (2003). New knock localization methodology for si engines. *SAE transaction 112*, 1587–94.

Castro, A., C. Koster, and E. Franieck (1994). Flexible ethanol otto engine management system. *SAE paper 942400*.

Cavalcante.Cordeiro.de.Melo, T., G. B. Machado, R. M. Jr, C. P. Belchior, and P. Pereira (2007). Thermodynamic modelling of compression, combustion and expansion processes of gasoline, ethanol and natural gas with experimental validation on a flexible fuel engine. *SAE technical paper 2007-24-0035*.

Charlette, F., C. Meneveau, and D. Veynante (2002). A power-law flame wrinkling model for les of premixed turbulent combustion. *Combust. Flame 131*, 159–180.

Chelma, F. and G. Orthaber (1999). Rate of heat release prediction for direct injection diesel engines based on purely mixing controlled combustion. *SAE Technical Paper 1999-01-0186*.

Chen, Y. and R. Bilger (2002). Experimental investigation of three dimensional flame front structure in premixed turbulent combustion-i: hydrocarbon air bunsen flames. *Combust. Flame 131*, 400–35.

Cheng, R. (1995). Velocity and scalar characteristics of premixed turbulent flames stabilized by weak swirl. *Combust. Flame 101*, 1–14.

Cho, P., C. Law, J. Hertzberg, and R. Cheng (1986). Structure and propagation of turbulent premixed flames stabilized in a stagnation flow. *Proc. Combust. Inst. 21*, 1493–9.

Ciezki, H. and G. Adomeit (1993). *Combust. Flame 93*, 421–33.

Clarke, A., R. Stone, and P. Beckwith (1995). Measuring the laminar burning velocity of methane/diluent/air mixtures within a constant-volume combustion bomb in a micro-gravity environment. *J. Inst. Energy 68*, 13036.

Clavin, P. (1985). Dynamic behavior of premixed flame fronts in laminar and turbulent flows. *Prog. Energ. Combusy. Sci. 11*.

Clavin, P. and F. Williams (1982). Effects of molecular diffusion and of thermal expansion on the structure and dynamics of premixed flames in turbulent flows of large scales and low intensity. *J. Fluid Mech. 116*, 251–82.

Coble, A. R., A. Smallbone, A. Bhave, S. Mosbach, M. Kraft, P. Niven, and S. Amphlett (2011). Implementing detailed chemistry and in-cylinder stratification into 0/1-d ic engine cycle simulation tools. *SAE International, 2011-01-0849*.

Colin, O., A. Benkenida, and C. Angelberger (2003). A 3d modeling of mixing and ignition and combustion phenomena in highly stratified gasoline engines. *Oil and Gas Science and Technology*, 47–62.

Colin, O., A. P. da Cruz, and S. Jay (2005). Detailed chemistry-based auto-ignition model including low temperature phenomena applied to 3-d engine calculations. *Proc. Combust. Inst. 30*, 2649–56.

Colin, O., F. Ducros, D. Veynante, and T. Poinsot (2002). A thickened flame model for large eddy simulations of turbulent premixed combustion. *Phys. Fluids 12(7)*, 1843–1863.

Colin, O., J.-B. Michel, and L. Vervisch (2010). New tabulated approaches for prediction auto-ignition and pollutant emissions of non-premixed turbulent flames. *ETMM8*.

Conaire, M., H. Curran, J. Simmie, W. Pitz, and C. Westbrook (2004). A comprehensive modeling study of hydrogen oxidation. *Int. J. Chem. Kin. 36(11)*, 603–622.

Coppens, F., J. D. Ruyck, and A. Konnov (2007a). The effects of composition on burning velocity and nitric oxide formation in laminar premixed flames of ch4 + h2 + o2 + n2. *Combust. Flame 149*, 409–17.

Coppens, F., J. D. Ruyck, and A. Konnov (2007b). Effects of hydrogen enrichment on adiabatic burning velocity and no formation in methane + air flames. *Therm. Fluid Sci. 31*, 437–44.

Cordiner, S. and V. Rocco (1997). Modeling of unburned hydrocarbons emissions in s.i. engines. *SAE Naples ICE Conference*.

Cowart, J. and W. Boruta (1995). Powertrain development of the 1996 ford flexible fuel taurus. *SAE paper 952751*.

Cowell, L. and A. Lefebre (1987). Influence of pressure on autoignition characteristics of gaseous hydrocarbonair mixtures. *SAE Paper 6*, 1–11.

Dahms, R., M. Drake, T. D. Fansler, T.-W. Kuo, and N. Peters (2011). Understanding ignition processes in spray-guided gasoline engines using high-speed imaging and the extended spark-ignition model sparkcimm. part b: Importance of molecular fuel properties in early flame front propagation. *Combust. Flame 158(11)*, 2245–60.

Damköhler, G. (1940). Der einfluder turbulenz auf die flammengeschwindigkeit in gasgemischen. *Z. Elektrochem 46*, 601–52.

Davidson, D., B. Gauthier, and R. Hanson (2005). Shock tube ignition measurements of iso-octane/air and toluene/air at high pressures. *Proceedings of the Combustion Institute 30*, 1175–82.

de.Ferrires, S., A. E. Bakali, B. Lefort, M. Montero, and J. Pauwels (2007). Investigation of laminar low pressure stoichiometric ch4/c2h6/c3h8/o2/n2 and ch4/c2h6/c3h8/h2/o2/n2 flames. *Third European Combustion Meeting*.

Delichatsios, M. (1972). The kinetics of co formation emissions from an internal combustion engine. *S.M. Thesis, Department of mechanical engineering, MIT*.

D'Errico, G., T. Cerri, and T. Lucchini (2006). Development and application of s.i. combustion models for emissions prediction. *SAE Technical Paper 2006-01-1108*.

D'Errico, G., G. Ferrari, A. Onorati, and T. Cerri (1996). Combustion modeling in si engines with a peninsula-fractal combustion model. *SAE paper 960072*.

D'Errico, G., G. Ferrari, A. Onorati, and T. Cerri (2002). Modelling the pollutant emissions from a si engine. *SAE Paper*, 01–0006.

D'Errico, G. and T. Lucchini (2005). A combustion model with reduced kinetic schemes for s.i. engines fuelled with compressed natural gas. *SAE Technical Paper 2005-01-1123*.

D'Errico, G., T. Lucchini, A. Onorati, M. Mehl, T. Faravelli, E. Ranzi, S. Merola, and B. Vaglieco (2007). Development and experimental validation of a combustion model with detailed chemistry for knock predictions. *SAE paper 2007-01-0938*.

D'Errico, G. and A. Onorati (2004). An integrated simulation model for the prediction of gdi engine cylinder emissions and echaus after-treatment system performance. *SAE Technical Paper 2004-01-0043*.

Dinkelacker, F., B. Manickam, and S. Muppala (2011). Modelling and simulation of lean premixed turbulent methane/hydrogen/air flames with an effective lewis number approach. *Combust. Flame 158*, 1742–49.

Dong, Y., C. Vagelopoulos, G. Spedding., and F. Egolfopoulos (2002). Measurement of laminar flame speeds through digital particle image velocimetry: mixtures of methane and ethane with hydrogen, oxygen, nitrogen, and helium. *Proc. Comb. Inst. 29*, 1419–26.

Dowdy, D., D. Smith, S. Taylor, and A. Williams (1991). The use of expanding spherical flames to determine burning velocities and stretch effects in hydrogen/air mixtures. *Proc. Combust. Inst. 23*, 325–32.

Drake, M. and D. Haworth (2008). Advanced gasoline engine development using optical diagnostic and numerical modeling. *Proc. Comb. Inst. 34*, 91–134.

Driscoll, J. (2008). Turbulent premixed combustion: Flamelet structure and its effect on turbulent burning velocities,. *Prog. Energy Combust. Sc. 34(1)*, 91–134.

Driscoll, J. and A. Gulati (1988). Measurement of various terms in the turbulent kinetic energy balance within a flame and comparison with theory. *Combust. Flame 72*, 131–52.

Ducourneau, F. (1974). Inflammation spontané de mé langes riches airké rosè ne. *Entropie 59*, 11–18.

Dugger, G. (1952). Effect of initial mixture temperature on flame speed of methaneair, propaneair and ethyleneair mixtures. *NACA Report of Investigations 1061 and Lewis Flight Propulsion Laboratory*.

Dulbecco, A. (2009). *Modeling of diesel HCCI combustion and its impact on pollutant emissions applied to global engine system simulation*. Ph. D. thesis, University of Toulouse, INPT.

Dyakov, I., A. Konnov, J. de Ruyck, K. Bosschaart, E. Brock, and L. de Goey (2001). Measurement of adiabatic burning velocity in methane-oxygen-nitrogen mixtures. *Combust. Sci. Technol. 172*, 81–96.

Egnell, R. (1998). Combustion diagnostics by means of multizone heat release analysis and no calculation. *SAE Technical Paper 981424*.

Egolfopoulos, F., P. Cho, and C. Law (1989). Laminar flame speeds of methane-air mixtures under reduced and elevated pressures. *Combust. Flame 76*, 375–91.

Egolfopoulos, F., D. Du, and C. Law (1992). A study on ethanol oxidation kinetics in laminar premixed flames, flow reactors, and shock tubes. *Proc. Combust. Inst. 24*, 833–41.

Eickhoff, H. (2002). Analysis of the turbulent burning velocity. *Combust. Flame 128*, 347–350.

Elia, M., M. Ulinski, and M. Metghalchi (2001). Laminar burning velocity of methane-air-diluent mixtures. *J. Eng. Gas Turbines Power and Trans. ASME 123*, 190–6.

Emery, P., F. Maroteaux, and M. Sorine (2003). Modeling of combustion in gasoline direct injection engines for the optimization of engine management system trough reduction of three-dimensional models to (nxone-dimensional) models. *Journ. Fluids Engineering 125*, 520–32.

Ern, A. and V. Giovangigli (1998). Thermal diffusion effects in hydrogen-air and methane-air flames. *Combust. Theory Model. 2*, 34972.

Fairweather, M., M. Ormsby, C. Sheppard, and R. Woolley (2009). Turbulent burning rates of methane and methanehydrogen mixtures. *Combust. Flame 156*, 780–790.

Farrell, J., R. Johnson, and I. Androulakis (2004). Molecular structure effects on laminar burning velocities at elevated pressure and temperature. *SAE paper 2004-01-2936*.

Fieweger, K., R. Blumenthal, and G. Adomeit (1997). *Combust. Flame 109*, 599–619.

Fikri, M., J. Herzler, R. Starke, C. Schulz, P. Roth, and G. Kalghatgi (2008). Autoignition of gasoline surrogate mixtures at intermediate temperatures and high pressures. *Combust. Flame 152*, 276–81.

Filatyev, S., J. Driscoll, C. Carter, and J. Donbar (2005). Measured properties of turbulent premixed flames for model assessment, including burning velocities, stretch rates and surface densities. *Combust. Flame 141*, 1–21.

Fiorina, B., R. Vicquelin, P. Auzillon, N. Darabiha, O. Gicquel, and D. Veynante (2010). A filtered tabulated chemistry model for les of premixed combustion. *Combust. Flame 157*, 465–75.

Gerke, U., K. Steurs, P. Rebecchi, and K. Boulouchos (2010). Derivation of burning velocities of premixed hydrogen/air flames at engine-relevant conditions using a single-cylinder compression machine with optical access. *Int. J. Hydrogen Energy 35*, 256677.

Gicquel, O., N. Darabiha, and D. Thvenin (2000). Laminar premixed hydrogen/air counterflow flame simulations using flame prolongation of ildm with differential diffusion. *Proc. Combust. Inst. 28*, 1901–8.

Goix, P. and I. Shepherd (1993). Lewis number effects in turbulent premixed flame structure. *Combust. Sci. Technol. 91*, 191–206.

Greenberg, J. (1980). On the prediction of thermal diffusion effects in laminar one-dimensional flames. *Combust. Sci. Technol. 24*, 838.

Griffiths, J. and S. Scott (1987). Thermokinetic intercations: fundamentals of spontaneous ignition and cool flames. *Prog. Energy Combust. Sci. 13*, 161–197.

Gu, X., Z. Haq, M. Lawes, and R. Woolley (2000). Laminar burning velocity and markstein lengths of methaneair mixtures. *Combust. Flame 121*, 41–58.

Guibet, J. and E. Fautre-Birchem (1996). Fuels and engines : Technology, energy, environment. *Technip Edition 1*.

Gülder, O. (1982). Laminar burning velocities of methanol and ethanol and isooctane-air mixtures. *Proc. Combust. Inst. 19:276-281*.

Gülder, O. (1984). Correlations of laminar combustion data for alternative si engine fuels. *SAE paper 841000*.

Gülder, O. (1990). Turbulent premixed flame propagation models for different combustion regimes,. *Twenty-third Symposium (International) on Combustion, The Combustion Institute*, 743–750.

Gülder, O., G. Smallwood, R. Wong, D. Snelling, R. Smith, and B. Deschamps (2000). Flame front surface characteristics in turbulent premixed propane/air combustion. *Combust. Flame 120*, 407–16.

Halpern, C. (1958). Measurement of flame speed by a nozzle burner method. *J. Res. Nat. Bureau Standards 60*, 535–46.

Halstead, M., L. Kirsch, and C. Quinn (1977). The auto-ignition of hydrocarbon fuels at high temperatures and pressures – fitting of a mathematical model. *Combust. Flame 30*, 45–60.

Halter, F., C. Chauveau, N. Djebali-Chaumeix, and I. Gkalp (2005). Characterization of the effects of pressure and hydrogen concentration on laminar burning velocities of methane-hydrogen-air mixtures. *Proceedings of the Combustion Institute 30*, 201–8.

Han, P., M. Checkel, B. F. BA, and N. Nowicki (2007). Burning velocity of methane/diluent mixture with reformer gas addition. *Fuel 86*, 585–96.

Hara, T. and K. Tanoue (2006). Laminar flame speeds of ethanol and n-heptane and isooctane air mixtures. *Fisita and F2006SC40*.

Hassan, M., K. Aung, , and G. Faeth (1998). Measured and predicted properties of laminar premixed methane/air flames at various pressures. *Combust. Flame 115*, 539–50.

Hawkes, E. and R. Cant (2000). A flame surface density approach to large-eddy simulation of premixed turbulent combustion. *Proc Combust Inst, 28,:5158 (2000) 28*, 51–58.

Hawkes, E. and J. Chen (2004). Direct numerical simulation of hydrogen-enriched lean premixed methane–air flames. *Combust. Flame 138*, 24258.

Hermanns, R. (2007). *Laminar burning velocities of methane–hydrogen–air mixtures, PhD Thesis*. Ph. D. thesis, Universiteit Eindhoven.

Hermanns, R., A. Konnov, R. Bastians, L. de Goey, K. Lucka, and H. Kohne (2010). Effects of temperature and composition on the laminar burning 3 velocity of ch4 + h2 + o2 + n2 flames. *Fuel 89*, 114–21.

Herzler, J., M. Fikri, K. Hitzbleck, R. Starke, C. Schulz, P. Roth, and G. Kalghatgi (2007). Shock tuble study of the autoignition of n-heptane/toluene/air mixtures at intermediates temperatures and high pressures. *Combust. Flame 149*, 25–31.

Heywood, J. (1988). *Internal Combustion Engine Fundamentals*. McGraw–Hill.

Heywood, J., J. Higgins, P. Watts, and R. Tabaczynski (1979). Development and use of a cycle simulation to predict si engine efficiency and nox emissions. *SAE paper 790291*.

Hiroyashu, H., T. Kadota, and M. Arai (1983). Development and use of a spray combustion modelling to predict diesel engine efficiency and pollutant emissions. *Bulletin of the JSME 26*.

Ho, S. Y. and T.-W. Kuo (1997). A hydrocarbon auto-ignition model for knocking combustion in si engines. *SAE paper 971672*.

Hountalas, D., D. Kouremenos, E. Patriotis, Schwarz, and Binder (2002). Using a phenomenological multi-zone model to investigate the effect of injection rate shaping on performance and pollutants of a di heavy duty diesel engine. *SAE Technical Paper 2002-01-0074*.

Hu, E., Z. Huang, J. He, C. Jin, and J. Zheng (2009). Experimental and numerical study on laminar burning characteristics of premixed methane–hydrogen–air flames. *Int. J. Hydrogen Energy 34*, 4876–88.

Huang, B., E. Hu, Z. Huang, J. Zheng, B. Liu, and D. Jiang (2009). Cycle-by-cycle variations in a spark ignition engine fueled with natural gas-hydrogen blends combined with egr. *Int J Hydrogen Energy 34*, 8405–14.

Huang, Z., Y. Zhang, A. Zeng, Q. Wang, and D. Jiang (206). Measurements of laminar burning velocities for natural gas–hydrogen–air mixtures. *Combust. Flame 146*, 302–311.

Ihme, M. and H. Pitsch (2008). Modeling of radiation and no formation in turbulent nonpremixed flames using a flamelet/progress variable formulation. *Phys. Fluids, 20*, 055110.

Ilbas, M., A. Crayford, I. Ylmaz, P. Bowen, and N. Syred (2006). Laminar-burning velocities of hydrogen–air and hydrogen–methane–air mixtures: An experimental study. *Int. J. hydrogen energy 31*, 1768–79.

Johnston, W. (1947). W.c. johnston measures flame velocity of fuels at low pressures. *Soc. Automot. Eng. J. 55*, 62–5.

Jones, W. and R. Lindset (1988). Global reaction schemes for hydrocarbon combustion. *Combust. Flame 73*, 233–49.

Jung, D. and D. Assanis (2001). Multi-zone di diesel spray combustion model for cycle simulation studies of engine performance and emissions. *SAE Technical Paper 2001-01-1246*.

Kapus, P., A. Fuerhapter, H. Fuchs, and G. Fraidl (2007). Ethanol direct injection on turbocharged si engines-potential and challenges. *SAE paper 2007-01-1408*.

Karim, G. (2004). A dimensionless criterion for predicting the onset of knock in spark ignition engines. *SAE paper 2004-01-1992*.

Karpov, V., G. Politenkova, and E. Severin (1986). Turbulent combustion of alcohols. *Comb. expl. and shock waves 22*, 397–9.

Keck, J. and D. Gillespie (1971). Rate-controlled partial-equilibrium method for treating reacting gas mixtures. *Combust. Flame 17*, 237–41.

Kee, R., F. Rupley, and J. Miller (1989). Chemkin-ii : a fortran chemical kinetics package for the analysis of gas phase chemical kinetics. Technical report, Tech. Rep. SAND89-8009B and Sandia National Laboratories.

Kido, H., M. Nakahar, K. Nakashima, and J. Hashimoto (2002). Influence of local flame displacement velocity on turbulent burning velocity. *Proc. Combust. Inst. 29*, 1855–61.

Kishore, R., N. Duhan, M. Ravi, and A. Ray (2008). Measurement of adiabatic burning velocity in natural gas-like mixtures. *Exp. Therm. and Fluid Science 33*, 10–16.

Klimenko, A. (1995). Note on the conditional moment closure in turbulent shear flows. *Phy. Fluids 7*, 446.

Knop, V. and S. Jay (2006). Latest developments in gasoline auto-ignition modelling applied to an optical cai engine. *Oil Gas Sci. Technol. 61*, 121–37.

Kobayashi, H., T. Nakashima, T. Tamura, K. Maruta, and T. Niioka (1997). Turbulence measurements and observations of turbulent premixed flames at elevated pressures up to 3.0 mpa. *Combust. Flame 108*, 104–117.

Kobayashi, H., K. Seyama, H. Hagiwara, and Y. Ogami (2005). Burning velocity correlation of methane/air turbulent premixed flames at high pressure and high temperature. *Proc Combust Inst 30*, 82734.

Kolmogorov, A. (1941). The local structure of turbulence in incompressible viscous fluid for very large reynolds numbers. *C.R. Acad. Sci. USSR 30*, 301.

Konnov, A. (2011). http://homepages.vub.ac.be/ akonnov/.

Kwon, J., J. Seo, D. Lee, and K. Y. Huh (2011). Zero-dimensional simulation of diesel engine combustion and emission based on cmc model and skeletal reaction mechanism. *SAE Technical Paper 2011-01-0845*.

Lafay, Y., B. Renou, G. Cabot, and M. Boukhalfa (2008). Experimental and numerical investigation of the effect of h2 enrichment on laminar methane–air flame thickness. *Combust. Flame 153*, 54061.

Lafossas, F.-A., O. Colin, F. L. Berr, and P. Menegazzi (2005). Application of a new 1d combustion model to gasoline transient engine operation. *SAE paper 2005-01-2107*.

Lafossas, F.-A., M.Castagne, J.-P. Dumas, and S. Henriot (2002). Development and validation of a knock model in spark ignition engines using a cfd-code. *SAE paper 2002-01-2701*.

Laget, O., B. Reveille, L. Martinez, K. Truffin, C. Habchi, and C. Angelberger (2011). Les calculations of a four cylinder engine. doi :10.4271/2011-01-0832. *SAE International 69*.

Laget, O., J. Zaccardi, X. Gautrot, T. Mansion, and E. Cotte (2010). Establishing new correlations between in-cylinder charge motion and combustion process in gasoline engines through a numerical doe. *SAE Int. J. Engines 3(1)*, 183–201.

Lavoie, G. A., J. B. Heywood, and J. Keck (1970). Experimental and theoretical investigation of nitric oxide formation in internal combustion engine. *Combust. Sci. And Tech. 1*, 313–26.

Law, C., G. Jomaas, and J. Bechtold (2005). Cellular instabilities of expanding hydrogen/propane spherical flames at elevated pressure: theory and experiment. *Proc. Combust. Inst. 30*, 159–67.

Lawn, C. and R. Schefer (2006). Scaling of premixed turbulent flames in the corrugated regime. *Combust. Flame 146*, 180–99.

LeBerr, F., M. Miche, G. L. Solliec, and F.-A. Lafossas (2006). Modelling of a turbocharged si engine with variable camshaft timing for engine control purposes. *SAE paper 2006-01-3264*.

Lecocq, G. (2010). *Approches hybrides combinant chimie complexe, description, statistique et densité de surface de flamme pour la simulation aux grandes échelles de láuto-inflammation, lállumage par bougie et la flamme de pr-mélange dans les moteurs á allumage commandé*. Institut National des Sciences Appliquees de Rouen.

Lecocq, G., S. Richard, J.-B. Michel, and L. Vervisch (2011). A new les model coupling flame surface density and tabulated kinetics approaches to investigate knock and pre-ignition in piston engines. *Proc. Comb. Inst. 33*, 3105–14.

Lecong, T. and P. Dagaut (2009). *Proc. Comb. Inst. 32*, 427–35.

Lee, J. G., T.-W. Lee, D. A. Nyet, and D. A. Santavicca (1995). Lewis number effects on premixed flames interacting with turbulent karman vortex streets. *Combust. Flame 100*, 161–168.

Lee, T., G. North, and D. Santavicca (1993). Surface properties of turbulent premixed propane/air flames at various lewis numbers. *Combust. Flame 93*, 445–456.

Li, J., Z. Zhao, A. Kazakov, and F. Dryer (2011). http://www.princeton.edu/ combust/database/files/other/.

Liao, S., D. Jiang, and Q. Cheng (2004). Determination of laminar burning velocities for natural gas. *Fuel 83*, 1247–50.

Liao, S., D. Jiang, Z. Huang, K. Zeng, and Q. Cheng (2007). Determination of the laminar burning velocities for mixtures of ethanol and air at elevated temperatures. *App. Therm. Eng 27*, 374–80.

Lipatnikov, A. and J. Chomiak (2010). Effects of premixed flames on turbulence and turbulent scalar transport. *Prog. Energy Combust.Sci. 36*, 1–102.

Livengood, J. and Wu (1955). Correlation of auto-ignition phenomenon in internal combustion engines and rapid compression machines. *Proc. of Fifth Int. Symp. Comb.*, 347.

Maaren, A. V., D. Thung, and L. D. Goey (1994). Measurement of flame temperature and adiabatic burning velocity of methane/air mixtures. *Combust. Sci. Technol. 96*, 32744.

Maji, S., M. G. Babu, and N. Gupta (2001). A single cylinder engine study of power and fuel and consumption and exhaust emissions with ethanol. *SAE paper 2001-28-0029*.

Malbec, L.-M., F. L. Berr, S. Richard, G. Font, and A. Albrecht (2009). Modelling turbocharged spark-ignition engines: towards predictive real time simulators. *SAE Technical Paper 2009-01-0675*.

Mansouri, S. H., J. Heywood, and K. Radhakrishnan (1982). Divided-chamber diesel engine, part1 : A cycle-simulation which predicts performance and emissions. *SAE Paper 820273*.

Marriot, S., M. Wiles, J. Gwidt, and S. Parrish (2002). Development of a naturally aspirated spark ignition direct-injection flex-fuel engine. *SAE paper 2002-01-0839*.

Matalon, M. (1983). On flame stretch. *Combust. Sci. Technol. 31*, 169–181.

Matalon, M. and J. Matkowsky (1982). Flames as gasdynamic discontinuities. *J. Fluid Mech.*, 124–239.

Matlab. The language of technical computing and info at: ¡http://www.mathworks.com/¿.

Matthews, R. and Y. Chin (1991). A fractal-based si engine model: Comparisons of predictions with experimental data. *SAE Paper 910075*.

Matthews, R. and M. Hall (1996). Combustion modeling in si engines with a peninsula-fractal combustion model. *SAE paper 960072*.

Mauviot, G., A. Albrecht, and T. Poinsot (2006). A new 0d approach for diesel combustion modeling coupling probability density function with complex chemistry. *SAE Technical Paper 2006-01-3332*.

McKay, G. (1977). The gas-phase oxidations of hydrocarbons. *Prog. Energy Combust. Sci. 3*, 105–26.

Meintjes, K. and A. Morgan (1987). Element variables and the solution of complex chemical equilibrium problems. *General Motors research publications 5827*.

Meneveau, C. and T. Poinsot (1991). Stretching and quenching of flamelets in premixed turbulent combustion. *Combustion and Flame*, 311–32.

Metghalchi, M. and J. Keck (1980). Laminar burning velocity of propane-air mixtures at high temperature and pressure. *Combust. Flame 38*, 143–54.

Metghalchi, M. and J. Keck (1982). Burning velocities of mixtures of air with methanol and iso-octane and indolene at high pressure and temperature. *Combust. Flame 48*, 191–210.

Miao, H., M. Ji, Q. Jiao, Q. Huang, and Z. Huang (2009). Laminar burning velocity and markstein length of nitrogen diluted natural gas/hydrogen/air mixtures at normal, reduced and elevated pressures. *Int. J. Hydrogen Energy 34*, 3145–55.

Miao, H., Q. Jiao, Z. Huang, and D. Jiang (2008). Effect of initial pressure on laminar combustion characteristics of hydrogen enriched natural gas. *Int. J. Hydrogen Energy 33*, 3876–85.

Michel, J., O. Colin, and D. Veynante (2009). *Flow Turb. Combust. 83*, 33–60.

Michel, J., S. Richard, and O. Colin (2009). Differenciation des avancements ai/pf. *Technical report E2.3, GSM–IFP*.

Michel, J.-B. (2008). *Modelisation de la combustion turbulente d'un melange heterogene en auto-inflammation en vue de l'application a la simulation de moteurs Diesel*. Ph. D. thesis, Ecole Centrale Paris.

Minetti, R., M. Carlier, M. Ribaucour, E. Thersen, and L. Sochet (1995). *Combust. Flame 102*, 298–309.

Mizutani, Y. and T. Takada (1999). Effects of velocity, turbulence and wall impingement on the ignition of fuel sprays perpendicularly injected into a heated air stream. *In 17th ICDERS*.

Moureau, V., G. Lartigue, Y. Sommerer, C. Angelberger, O. Colin, and T. Poinsot (2005). Numerical methods for unsteady compressible multi-component reacting flows on fixed and moving grids. *J. Comput. Phys. 202(2)*, 710–736.

Muppala, S., M. Nakahara, N. Aluri, H. Kido, J. Wena, and M. Papalexandris (2009). Experimental and analytical investigation of the turbulent burning velocity of two-component fuel mixtures of hydrogen, methane and propane. *Int. J. Hydrogen Energy 34*, 9258–65.

Nakama, K., J. Kusaka, and Y. Daisho (2008). Effect of ethanol on knock in spark ignition gasoline engines. *JSAE 20084720-SAE paper 2008-32-0020*.

Nakata, K., S. Utsumi, A. Ota, K. Kawatake, T. Kawai, and T. Tsunooka (2006). The effect of ethanol fuel on a spark ignition engine. *SAE paper 2006-01-3380*.

Natarajan, K. and K. Bhaskaran (1982). *Thirteenth International Shock Tube Symposium*, 934.

Nishiwaki, K. (2008). A hybrid fractal flame model for si engine combustion comprising turbulent dissipation and laminar flamelets. *The 7th Int. Conf. on Modeling and Diagnostic for Advanced Engine Systems, COMODIA, JSME 8*, 202.

Noda, T., K. Hasegawa, M. Kubo, and T. Itoh (2004). Development of transient knock prediction technique by using a zero-dimensional knocking simulation with chemical kinetics. *SAE paper 2004-01-0618*.

Onorati, A., G. Ferrari, G. Montenegro, A. Caraceni, and P. Pallotti (2004). Prediction of si engine emissions during an ece driving cycle via integrated thermo-fluid dynamic simulation. *SAE paper 2004-01-1001*.

Patriotis, E., D. Hountalas, and C. Rakopoulos (2006). Sensivity analysis of multi-zone modeling for combustion and emissions formation in diesel engines. *SAE Technical Paper 2006-01-1383*.

Paul, R. and K. Bray (1996). Study of premixed turbulent combustion including landau-darrieus instability effects. *Symposium (International) on Combustion 26(1)*, 259–266.

Pelce, P. and P. Clavin (1982). Influence of hydrodynamics and diffusion upon stability limits of premixed flames. *J. Fluid Mech. 124*, 219.

Pera, C., O. Colin, and S. Jay (2009). *Oil Gas Sci. Technol. 64*, 243–58.

Pera, C., S. Richard, and C. Angelberger (2012). Exploitation of multi-cycle engine les to introduce physical perturbations in 1d engine models. *SAE Technical paper 2012-01-0127*.

Peters, N. (1986). Laminar flamelet concepts in turbulent combustion. *Proceedings of the 21st Symposium (International) on Combustion, The Combustion Institute*, 1231–1250.

Peters, N. (1999). The turbulent burning velocity for large-scale and small-scale turbulence. *J. Fluid. Mech. 384*, 107–132.

Peters, N. (2000). *Turbulent combustion*. Cambridge University Press.

Pires.da.Cruz, A., K. Truffin, J. Michel, C. Lacour, D. Maligne, V. Ricordeau, L. de Francqueville, S. Doreau, M. Yahyaoui, C. Tournebize, A. Cessou, B. Lecordier, R. Bounaceur, F. Battin-Leclerc, R. Fournet, O. Herbinet, and P. Glaude (2010). Idethanol. *Rapport interne IFPEn, DCPR(CNRS), PSA, Renault, CORIA, ADEME*.

Poinsot, T. and D. Veynante (2001). *Theoretical and Numerical Combustion*. Edwards.

Poinsot, T., D. Veynante, and S. Candel (1990). Diagram of premixed turbulent combustion based on direct simulation. *Proceedings of the 23rd Symposium (International) on Combustion, The Combustion Institute*, 561–606.

Poinsot, T., D. Veynante, and S. Candel (1991). Quenching processes and premixed turbulent combustion diagrams. *J. Fluid Mech. 228*, 561–606.

Poulos, S. and J. Heywood (1983). The effect of chamber geometry on spark ignition engine combustion. *SAE paper 830334*.

Qin, Z., V. Lissianski, H. Yang, W. Gardiner, S. Davis, and H. Wang (2000). Combustion chemistry of propane: a case study of detailed reaction mechanism optimization. *Proc. Comb. Inst. 28*, 1663–69.

Rahim, F., M., Elia, M., Ulinski, M., and Metghalchi (2002). Burning velocity measurements of methane-oxygen-argon mixtures and an application to extend methane-air burning velocity measurements. *Int. J. Eng. Res. 3*, 8192.

Rakopoulos, C. and D. Hountalas (2000). Development of new 3-d multizone combustion model for indirect injection diesel engines with a swirl type prechamber. *SAE Technical Paper 2000-01-0587*.

Ribert, G., O. Gicquel, N. Darabiha, and D. Veynante (2006). Tabulation of complex chemistry based on self-similar behaviour of laminar premixed flames,. *Combust. Flame 146(4)*, 649–64.

Richard, S., S. Bougrine, G. Font, F.-A. Lafossas, and F. L. Berr (2009). On the reduction of a 3d cfd combustion model to build a physical 0d model for simulating heat release and knock and pollutants in si engines. *Oil Gas Sci. Technol. 64*, 223–242.

Richard, S., O. Colin, O. Vermorel, A. Benkenida, C. Angelberger, and D. Veynante (2007). Towards large eddy simulation of combustion in spark ignition engines. *Proceedings of the Combustion Institute 31*, 3059–66.

Richard, S. and D. Veynante (2007). A 0-d flame wrinkling equation to describe the turbulent flame surface evolution in si engines. *IFPEn internal technical note*.

Rozenchan, G., D. Zhu, C. Law, and S. Tse (2003). Outward propagation, burning velocities, and chemical effects of methane flames up to 60 atm. *Proceedings of the Combustion Institute 29*, 1461–9.

Sabia, P., M. de Joannon, and E. R. A. Cavaliere (2007). Hydrogen-enriched methane mild combustion in a well stirred reactor. *Proc Eur Combust Meeting*.

Salih, F. and G. Andrews (1992). The influence of gasoline/ethanol blends on emissions and fuel economy. *SAE paper 922378*.

Sankaran, R. and H. Im (2006). Effect of hydrogenaddition on the flammability limit of stretched methane/air premixed flames. *Combust. Sci. Technol. 178*, 1585611.

Sarli, V. D. and A. D. Benedetto (2007). Laminar burning velocity of hydrogen–methane/air premixed flames. *Int J Hydrogen Energy 32*, 63746.

Schefer, R. (2003). Hydrogen enrichment for improved lean flame stability. *Int. J. Hydrogen Energy 28*, 113141.

Schramm, J. and S. Sorenson (1990). A model for hydrocarbon emissions from s.i. engines. *SAE paper 902169*.

Semenov, N. (1940). Thermal theory of combustion and explosion. *Prog. Phys. Sci. (U.S.R.R.) 24:4*, 433–486.

Shen, H., J. Vanderover, and M. Oehlschlaeger (2008). A shock tube study of iso-octane ignition at elevated pressures: The influence of diluent gases. *Combust. Flame 155*, 739–55.

Shepherd, I. and R. Cheng (2001). The burning rate of premixed flames in moderate and intense turbulence. *Combust. Flame 127*, 2066–75.

Simmie, J. (2003). Detailed chemical knetic models for the combustion of hydrocarbon fuels. *Prog. Energy Combust. Sci. 29*, 599634.

Smith, G., D. Golden, M. Frenklach, N. Moriarty, B. Eiteneer, M. Goldenberg, C. Bowman, R. Hanson, S. Song, W. Gardiner, V. Lissianski, and Z. Qin (2000). Gri mech. *http://www.me.berkeley.edu/gri mech*.

Smith, K. and F. Gouldin (1979). Turbulence effects on flame speed and flame structure. *AIAA J 11(5)*, 1243–50.

Spadaccini, L. (1977). Autoignition characteristics of hydrocarbon fuels at elevated temperatures and pressures. *J. Eng. Power, Trans. ASME*, 83–87.

Starkman, E., H. Newhall, , and R. Sutton (1964). Comparative performance of alcohol and hydrocarbon fuels. *SAE paper 640649*.

Stodart, A., J. Maher, J. Greger, and J. Carlsson (1998). Fuel system development to improve cold start performance of a flexible fuel vehicle. *SAE paper 982532*.

Stone, R., A. Clarke, and P. Beckwith (1998). Correlations for the laminar-burning velocity of methane/ diluent/air mixtures obtained in free-fall experiments. *Combust. Flame 114*, 546–55.

Stringer, F., A. Clarke, and J. Clarke (1969). The spontaneous ignition of hydrocarbon fuels in a flowing system. *Proc. Instn. Mech. Engrs. 184*, 212–225.

Sun, C., C. Sung, L. He, and C. Law (1999). Dynamics of weakly stretched flames : quantitative description and extraction of global flame parameters. *Combust. Flame 118*, 108–28.

Tabaczynski, R., C. Ferguson, and K. Radhakrishnan (1977). A turbulent entrainment model for spark ignition engine combustion. *SAE paper 770647*.

Tahtouh, T., F. Halter, E. Samson, and C. Mounam-Rousselle (2009). Effects of hydrogen addition and nitrogen dilution on the laminar flame characteristics of premixed methaneair flames. *Int. J. Hydrogen Energy 34*, 8329–38.

Takahashi, F., M. Mizomoto, and S. Ikai (1983). *Alternative energy sources III*. New York: McGraw-Hill.

Tanoue, K., S. Goto, F. Shimada, and T. Hamatake (2003). Effects of hydrogen addition on stretched premixed laminar methane flames. 1st report, effects on laminar burning velocity. *Transactions of the Japan Society of Mechanical 69*, 162–8.

Taylor, S. (1991). *Ph.D. dissertation*. Ph. D. thesis, The University of Leeds and Department of Fuel and Energy.

Tennekes, M. and J. Lumley (1972). A first course in turbulence. *M.I.T. Press, Cambridge, Mass.*.

Teraji, A., T. Tsuda, T. Noda, M. Kubo, and T. Itoh (2005). Development of a novel flame propagation model (ucfm : Universal coherent flame model) for si engines and its application to knocking prediction. *SAE paper 04-11-2005*.

Vagelopoulos, C. and F. Egolfopoulos (1994). Vagelopoulos cm, egolfopoulos fn. further consideration on the determination of laminar flame speeds with the counterflow twin-flame technique. *25th Symposium on Combustion and The Combustion Institute*, 13417.

Vagelopoulos, C. and F. Egolfopoulos (1998). Direct experimental determination of laminar flame speeds. *27th Symposium (International) on Combustion and The Combustion Institue*, 513–9.

van Oijen, J., F. Lammers, and L. de Goey (2001). *Combust. Flame 127*, 2124–34.

Verhelst, S., C. T'Joen, J. Vancoillie, and J. Demuynck (2011). A correlation for the laminar burning velocity for use in hydrogen spark ignition engine simulation. *Int J of Hydrogen Energy 36*, 95774.

Vermorel, O., S. Richard, O. Colin, A. Benkenida, C. Angelberger, and D. Veynante (2007). Multi-cycle les simulations of flow and combustion in a pfi si 4-valve production engine. *SAE transactions, J. of engines 116*, 152–164.

Vervisch, L., E. Bidaux, K. Bray, and W. Kollmann (1995). Surface density function in premixed turbulent combustion modeling, similarities between probability density function and flame surface approach. *Phys. Fluids A 7(10)*, 2496:2503.

Vervisch, P. (2012). *Modlisation de la formation de NOx et de suies dans les moteurs Diesel*. Ph. D. thesis, Ecole Centrale Paris.

Vervisch, P., O. Colin, J.-B. Michel, and N. Darabiha (2011). No relaxation approach (nora) to predict thermal no in combustion chambers. *Combust. Flame 158*, 148090.

Veynante, D. and T. Poinsot (1997). Reynolds averaged and large eddy simulation modeling for turbulent combustion.,. *J. F. O. Metais (Ed.), New tools in turbulence modelling. Lecture 5, Les editions de Physique*, 105–135.

Veynante, D. and L. Vervisch (2009). Turbulent combustion modeling. *von karman institute for fluid dynamics, lecture series, VKI*.

Wang, H., X. You, A. Joshi, S. Davis, A. Laskin, F. Egolfopoulos, and C. Law. *http* : $//ignis.usc.edu/usc_mech_i.htm$.

Wang, J., H. Chen, B. Liu, and Z. Huang (2008). Study of cycle-by-cycle variations of a spark ignition engine fuelled with natural gas-hydrogen blends. *Int. J. Hydrogen Energy 33*, 4876–83.

Weller, H. G., G. Tabor, A. D. Gosman, and C. Fureby (1998). Application of a flame-wrinkling les combustion model to a turbulent mixing layer. *Proc. Comb. Inst. 27(1)*, 899–907.

Wiebe, I. (1956). Halbempirische formel fur die verbrennungs-geschwindigkeit. *Verlag der akademie der Wissenschaften der Vd SSR and Moscow*.

Williams, F. (1985). *Combustion therory 2nd edition*.

Woschni, G. (1697). Universally applicable equation for the instantaneous heat transfer coefficient in the internal combustion engine. *SAE paper 670931*.

Wu, M., S. Kwon, J. Driscoll, and G. Faeth (1990). Turbulent premixed hydrogenair flames at high reynolds numbers. *Combust. Sci. Technol. 73*, 32750.

Wu, M., S. Kwon, J. Driscoll, and G. Faeth (1991). Preferential diffusion effects on the surface structure of turbulent premixed hydrogen/air flames. *Combust. Sci. Technol. 78*, 69–96.

Yates, A. D. B., A. Swart, and C. L. Viljoen (2005). Correlating auto-ignition delays and knock-limited spark-advance data for different types of fuel. *SAE paper 2005-01-2083*.

Yu, G., C. Law, and C. Wu. (1986). Laminar flame speeds of hydrocarbon + air mixtures with hydrogen addition. *Combust. Flame 63*, 339–47.

Zhao, Z., J. P. Conley, A. Zakarov, and F. L. Dryer (2003). Burning velocities of real gasoline fuel at 353 k and 500 k. *SAE Technical Papers Series 2003-01-3265*.

Ziegler, M. (1998). *Untersuchungen zur ausbreitung stationairer, turbulenter vormischflammen unter besonderer beruicksichtigung bevorzugter diffusion*. Ph. D. thesis, University of Karlsruhe.

Zimont, V. (2000). Gas premixed combustion at high turbulence. turbulent flame closure combustion model. *Exp. Thermal Fluid. Sci. 21*, 179–86.

End of the document